



**FACULTY
OF MATHEMATICS
AND PHYSICS**
Charles University

MASTER THESIS

David Němec

**Validation of the cloud and precipitation
microphysics scheme in the numerical
weather prediction model ALADIN**

Department of Atmospheric Physics

Supervisor of the master thesis: doc. Mgr. Michal Žák, Ph.D.

Study programme: Atmospheric Physics, Meteorology
and Climatology

Study branch: FAMKP

Prague 2023

I declare that I carried out this master thesis independently, and only with the cited sources, literature and other professional sources. It has not been used to obtain another or the same degree.

I understand that my work relates to the rights and obligations under the Act No. 121/2000 Sb., the Copyright Act, as amended, in particular the fact that the Charles University has the right to conclude a license agreement on the use of this work as a school work pursuant to Section 60 subsection 1 of the Copyright Act.

In Prague

2023-05-02

David Němec

I thank doc. Mgr. Michal Žák, Ph.D. for supervising my thesis.

I thank RNDr. Radmila Brožková, CSc. for patient guidance throughout this thesis, valuable insights, constant support, and great explanation of numerous aspects of numerical weather prediction.

I thank the Czech Hydrometeorological Institute and the whole NWP team at CHMI for helping me carry out this thesis.

I thank my parents and my brother for their support throughout my studies.

Title: Validation of the cloud and precipitation microphysics scheme in the numerical weather prediction model ALADIN

Author: David Němec

Department: Department of Atmospheric Physics

Supervisor: doc. Mgr. Michal Žák, Ph.D., Department of Atmospheric Physics

Abstract: This thesis aims to validate the microphysics scheme in the numerical weather prediction model ALADIN. The first part is focused on the parameterization of hydrometeors and microphysical processes in various microphysics schemes used in current numerical weather prediction models. The microphysics scheme used in ALADIN is discussed in detail, together with its parameterizations associated with the microphysics scheme. The main part of the thesis deals with an improved parameterization of graupel and improvements in the microphysical processes of all precipitating hydrometeors in the microphysics scheme in ALADIN. Alternative approaches to the parameterization of autoconversion and evaporation are tested. Results are validated using various objective statistical methods and compared with precipitation estimates based on a combination of data from gauges and radars.

Keywords: Numerical weather prediction, parameterization of processes, cloud and precipitation microphysics

Contents

Introduction	4
1 Hydrometeors and their representation in microphysics schemes	5
1.1 Hydrometeors	5
1.1.1 Liquid-phase hydrometeors	5
1.1.2 Ice-phase hydrometeors	6
1.2 Types of microphysics schemes	7
1.2.1 Bin and bulk microphysics schemes	8
1.2.2 Single-moment and multi-moment schemes	9
1.3 Representation of hydrometeors in microphysics schemes	9
1.3.1 The moment method	10
1.3.2 The Marshall-Palmer distribution	11
1.3.3 Mass-size and fall speed relations	13
2 Microphysical processes and their parameterizations	15
2.1 Precipitation production processes	15
2.1.1 The continuous growth model	16
2.1.2 Common autoconversion parameterizations	17
2.1.3 Parameterizations obtained from numerical simulations	20
2.2 Evaporation and condensation of precipitation	21
2.3 Melting and freezing	26
2.4 Sedimentation	27
3 NWP microphysics schemes	29
3.1 ICE3	29
3.2 WSM6	31
3.3 Thompson scheme	33
3.4 Microphysics scheme in MetUM	35
3.5 COSMO/ICON microphysics scheme	36
3.6 Microphysics scheme in JMA-LFM	39
4 ALARO and its microphysics scheme	41
4.1 A brief introduction to ALARO	41
4.2 Dynamics-physics interface	42
4.3 Cloud scheme	43
4.4 Microphysics scheme	44
4.4.1 Parameterization of microphysical processes	44
4.4.2 Extension for prognostic graupel	47
4.4.3 Computation of sedimentation	47
4.5 Cloud and precipitation geometry	49
4.6 3MT cascade	51
5 Model configuration, selected cases, and methods	54
5.1 Model configuration	54
5.2 Periods used for experiments	54
5.2.1 Severe convection in June 2021	54

5.2.2	Severe convection in June 2022	55
5.2.3	Convection in June 2009	55
5.2.4	Autumn stratocumulus period	56
5.2.5	Autumn/winter precipitating period	56
5.2.6	Additional selected cases	56
5.3	Methods	56
5.3.1	DDH diagnostic	56
5.3.2	Atmospheric scores	56
5.3.3	Fraction skill score	58
5.3.4	Other validation techniques	58
6	Enhancements of prognostic graupel	60
6.1	Effects of prognostic graupel	60
6.2	Improvements of prognostic graupel parameterization	63
6.2.1	Fall speed relation and mass-size distribution	63
6.2.2	Autoconversion	66
6.2.3	Conversion from snow to graupel	66
6.2.4	Collection efficiency	68
6.3	The final proposal for graupel	69
7	Further innovations of the microphysics scheme	76
7.1	Autoconversion	76
7.1.1	Coefficient for autoconversion to snow	76
7.1.2	Modification of the computation of the threshold value for autoconversion to snow	79
7.1.3	Nonlinear rain autoconversion	80
7.1.4	Modification of the threshold value of rain autoconversion	87
7.2	Evaporation	89
7.2.1	Behaviour of the Lopez scheme	91
7.3	Cloud overlap	94
8	Validation of microphysics developments	98
8.1	Summer period 2009	98
8.1.1	Influence of the assimilation cycle	102
8.2	Summer period 2022	103
8.2.1	Atmospheric scores	104
8.2.2	Validation of precipitation	107
8.2.3	Precipitation day by day	112
8.2.4	Evaluation of this period	123
8.3	Winter precipitation period	125
8.4	Autumn stratocumulus period	130
8.5	Snowfall on 2022-12-12	131
9	Summary and discussion	134
10	Conclusion	137
	Bibliography	138

List of Figures	151
List of Tables	156
List of symbols	157
List of abbreviations	163
A Appendix	165
A.1 Mass-weighted relation for fall speed	166
A.2 Collection	167
A.3 Evaporation in ALARO	168
A.4 Melting	170
A.5 Derivation of the Lopez evaporation parameterization for rain . .	171
A.6 Derivation of the Lopez evaporation parameterization for graupel	173

Introduction

Microphysics schemes are one of the essential parameterizations of current numerical weather prediction models, as they are responsible for precipitation production. Thus, physically argued formulas for microphysical processes are crucial for the correct prediction of precipitation accumulation and its phase. The precipitation accumulation forecast impacts the awareness level of alerts during floods or severe convection. Thus, correct forecasts protect our health and lives.

Many approaches to microphysics parameterization occurred. The first widely used scheme was introduced in 1967 by German physicist Kessler, who observed clouds and distinguished two categories of water - cloud and precipitating. His model was developed only for liquid water. The following logical step was extending this scheme for the solid phase, which was done in multiple ways. In 1983, American physicist Lin introduced a microphysical scheme with five hydrometeors as he extended the Kessler scheme for snow and graupel. Ruetledge and Hobbs developed a similar model in 1984. These two models are the base stones for many current microphysical schemes, which still evolve.

Although the types of microphysical processes being relatively well-known, the uncertainty in their parameterization is high. One reason is the uncertainties of the size spectra of hydrometeors, particularly of solid particles, which acquire a tapestry of irregular shapes. Another reason is the large population of particles within a grid box. Thus, particles experience many collisions, dependent on many factors, e.g., turbulence, vertical temperature gradient, or humidity. Also, the characteristic spatial and time scales are very small, making correct estimation of rates of microphysical processes in the laboratory difficult.

Finally, microphysics schemes are not stand-alone parameterizations. They must cooperate reasonably with other parameterizations in a numerical weather prediction model. The microphysics scheme mainly interacts with the parameterization of precipitating convection but also with radiation and turbulence.

The thesis is divided into ten chapters. The first chapter deals with the basic physical description of hydrometeors, their properties, and sizes. The second chapter describes common parameterizations of microphysical processes. The third chapter portrays various microphysics schemes in current numerical weather prediction models. The fourth chapter explains the microphysics scheme and associated parameterizations used in the canonical model configuration of ALADIN called ALARO. The fifth chapter describes methods and periods used for testing various modifications of microphysics, which are introduced and validated in chapters seven and eight. The former chapter focuses on the parameterization of graupel, and the latter on the general parameterization of microphysical processes for all precipitating hydrometeors. Results are discussed in chapter nine. Finally, chapter ten provides a brief conclusion.

1. Hydrometeors and their representation in microphysics schemes

Any product of condensation or deposition of atmospheric water vapour can be called a hydrometeor, no matter whether the condensation or deposition occurs on the ground or in the atmosphere (American Meteorological Society [2023]). This definition includes rainwater, snow aggregates, graupel, cloud water and cloud ice, which are hydrometeors simulated by many microphysics schemes. The term water species includes also water vapour.

There are two ways to describe the mass of hydrometeors in a volume of air in numerical weather prediction (NWP) models. The first one is the mixing ratio of hydrometeor j , denoted by r_j , and defined as (American Meteorological Society [2023])

$$r_j = \frac{m_j}{m_d}, \quad (1.1)$$

where m_j is the mass of hydrometeor j in a volume of air and m_d is the mass of dry air in the same volume of air. The other approach is to compute the specific content of hydrometeor j , defined as

$$q_j = \frac{m_j}{m_d + m_v + \sum_i m_i}, \quad (1.2)$$

where m_v is the mass of water vapour in the volume of air and $\sum_i m_i$ denotes the sum of masses of all hydrometeors present in the layer.

1.1 Hydrometeors

1.1.1 Liquid-phase hydrometeors

Liquid water is often divided into two separate categories, rainwater (drops) and cloud water (droplets). Processes involving these two types of particles are often called warm rain processes since the ice phase is not present (Straka [2009]). However, that does not mean that they occur only at temperatures above the melting point of water, $T_f = 0^\circ\text{C} = 273.15\text{ K}$.

The split of liquid water hydrometeors into cloud and rainwater is rather artificial. However, it is convenient as it allows for neglecting the fall speed of droplets, and the separation of certain properties of other processes is possible, as will be described later.

Shapes of liquid water hydrometeors are rather simple. Water droplets are almost perfectly spherical for diameters less than $280\ \mu\text{m}$. For larger diameters, they become ellipsoidal due to aerodynamic drag. For diameters over 1 mm , the deformation of drops is significant, and their bases become flat. Drops up to 8 mm in diameter have been reported, and drops larger than 1 cm are hydrodynamically unstable even in a laminar air stream (Pruppacher and Klett [1997]). In NWP

models are drops and droplets usually assumed to be spherical, therefore their mass follows a simple relationship

$$m(D) = \frac{\pi D^3}{6} \rho_w, \quad (1.3)$$

where D is the diameter of the particle and $\rho_w = 1000 \text{ kg} \cdot \text{m}^{-3}$ the density of liquid water.

Cloud droplets are often found at temperatures below T_f . Liquid water colder than T_f is called supercooled water. The existence of supercooled water is due to curvature effects and a dearth of ice nuclei (IN), which water can heterogeneously freezes onto (Řezáčová et al. [2007]).

Clouds are often made of liquid water even below T_f as a consequence of the existence of supercooled water. Stratocumulus clouds consist mainly of cloud droplets, altocumuli are often mixed clouds, so they consist of cloud droplets and ice crystals (World Meteorological Organization [2017]). Liquid water has been reported at the base of cirrostrati at temperatures between -35°C and -36°C (Sassen et al. [1985]). Liquid water was also observed at temperatures as low as -38°C in upper parts of cumulonimbi, while more than half of the total adiabatic water content (the water content of an air parcel when it is lifted adiabatically from cloud base with suppressed mixing (Khvorostyanov and Curry [2014])) was in the liquid phase at temperatures down to -37.5°C . For lower temperatures, cloud water vanished abruptly via homogeneous freezing in the measured convective clouds (Rosenfeld [2000]).

1.1.2 Ice-phase hydrometeors

As ice hydrometeors are classified, for example, cloud ice (also called ice crystals), snow aggregates, graupel (snow pellets) and hail (Straka [2009]). The shape of ice crystals and aggregates depends on the ambient temperature and oversaturation of air with respect to ice (Pruppacher and Klett [1997]). The variety of ice-phase hydrometeors shapes is much broader compared to liquid ones. Also, parameterizations of cold-rain (rain production at temperatures below T_f) and ice processes are more complicated than warm-rain processes (Straka [2009]).

As was mentioned before, the mixing ratio of ice water does not outweigh the mixing ratio of liquid water even at temperatures below T_f due to the lack of IN. The number of IN grows nearly exponentially with decreasing temperature (Pruppacher and Klett [1997]). Heterogeneous freezing is the freezing of liquid water due to contact with IN, and is the dominant process of freezing at temperatures down to around -40°C (Pruppacher and Klett [1997]). Homogeneous freezing is dominant for lower temperatures. Homogeneous freezing denotes a process whereby a drop freezes without contact with another solid surface or containing IN inside. It mostly occurs at temperatures from -38°C to -42°C . Smaller droplets freeze at lower temperatures due to curvature effects (Khvorostyanov and Curry [2014]).

A vital process for ice production is the Wegener-Bergeron-Findeisen (WBF) process; that is, the growth of ice to the detriment of liquid water due to lower equilibrium water vapour pressure with respect to ice than with respect to water (American Meteorological Society [2023]). Consequently, the saturation water

vapour pressure with respect to water is not reached while is exceeded with respect to ice at the same moment. This leads to evaporating liquid water and deposition onto ice crystals if the water vapour pressure is undersaturated with respect to liquid water and oversaturated with respect to ice.

Hail and graupel have two regimes of growth, wet and dry. The growth regime depends on whether all liquid water can freeze on the surface of the particle, which depends on the final temperature of the particle after accounting for the effect of latent heating. If the hypothetical final temperature of the particle exceeds T_f , then the particle grows in the wet regime; otherwise, it grows in the dry regime. This explains why hailstones often consist of multiple layers of transient (wet growth) and white shells (dry growth) with different densities (Pruppacher and Klett [1997]).

The shape of hailstones varies with their size. Small hails are usually spherical or conical, hails with $1\text{ cm} < D < 5\text{ cm}$ are usually ellipsoidal, and bigger hails are relatively spherical with many irregularities (Straka [2009]). The density of a hailstone decreases towards the center of the hailstone (Heymsfield et al. [2018]). Densities of hailstones range from 400 to $900\text{ kg} \cdot \text{m}^{-3}$ for hails of $D < 1\text{ cm}$ and from 700 to $900\text{ kg} \cdot \text{m}^{-3}$ for larger diameters (Straka [2009]).

Graupel can have many shapes; it can be spherical, irregular (lump) graupel, hexagonal or conical graupel, which usually has lower density and is less stable when falling than the lump graupel. Furthermore, more irregular shapes are often observed (Straka [2009]).

Graupel can be produced by heavy riming of cloud water on ice crystals or by freezing of raindrops (Pruppacher and Klett [1997]). Lump graupel origins from frozen drops, while conical graupel often develops from snow (Heymsfield et al. [2018]). Conical graupel can also develop when droplets start to freeze on a planar ice crystal (Straka [2009]). The density of graupel particles is influenced by their growth mechanism, growth time, liquid water content, size of collected droplets, and the growth mode (Heymsfield et al. [2018]). Consequently, the parameterization of graupel in microphysics schemes is challenging. Graupel densities fluctuate between 100 and $900\text{ kg} \cdot \text{m}^{-3}$ (Straka [2009]). A typical value of graupel density is $\rho_g = 400\text{ kg} \cdot \text{m}^{-3}$ (Heymsfield et al. [2018]). Unlike hailstones, melting graupel does not shed water (Straka [2009]).

1.2 Types of microphysics schemes

A microphysics scheme (or parameterization) aims to simulate microphysical processes occurring in nature as accurately as possible to deliver correct amounts of precipitation on the ground and interact well with other parameterizations in a model. However, a wide range of microphysical processes, which are rather complex, implies that some approximations have to be made and some less important processes have to be omitted for feasibility reasons. One of the difficulties is the large number of hydrometeors to be found in one model grid box.

A typical value of the number concentration of cloud droplets is a few tenths to hundreds of particles per cm^{-3} (Pruppacher and Klett [1997]). However, it is not feasible to simulate all particles explicitly for a typical NWP model with grid volumes of a few tenths of cubic kilometers (Igél et al. [2015]). Since hydrometeors in the grid volumes differ in size, the rate of microphysical processes

depends on droplet radii (e. g. evaporation) differs for smaller and for bigger particles (Pruppacher and Klett [1997]). This can be overcome by an assumption that the size distribution of a given hydrometeor follows a certain distribution function or by distributing particles to a defined number of bins (Straka [2009]).

Another obstacle is a vast variety of shapes of ice-phase hydrometeors shapes, which depend on the ambient temperature and the water vapour oversaturation with respect to ice (Pruppacher and Klett [1997]). Current operationally used microphysics schemes do not consider the wide variety of shapes of ice-phase hydrometeors, since the high computational complexity. Ice-phase hydrometeors are usually divided into two or three categories. Namely, cloud ice (also called ice crystals) with negligible or minimal gravitational fall speed, snow (aggregates), and some schemes set graupel aside (Straka [2009]). Some trials to include hails appeared (Lascaux et al. [2006], Bae et al. [2018]). To the best of the author’s knowledge, schemes including hail as a separate category have not been operationally used in NWP to date. However, they are still being developed.

1.2.1 Bin and bulk microphysics schemes

There are two most common approaches to the problem of estimating the spectra of sizes of hydrometeors, bin and bulk parameterizations. Bin parameterizations assume hydrometeor size spectra to be divided into bins. Usually, few tens or few hundreds of bins are used (Lee and Baik [2018]). The scale can be either linear or nonlinear. Typical sizes of hydrometeors span from $4 \cdot 10^{-6}$ m to $4 \cdot 10^{-3}$ m, and thus it is necessary to capture such a range of sizes (Straka [2009]). Smaller droplets must have narrower bins than larger droplets to be represented well. Therefore logarithmic or exponential scales are widely used (Straka [2009]).

In the bulk parameterizations, size distribution is assumed to follow a distribution function with few parameters. Usually, the gamma or the negative exponential distributions are used (Lee and Baik [2018]). Also, log-normal distributions are used (Khain et al. [2015]); for example, cloud ice can be approximated by the log-normal distribution (Cotton et al. [2013]).

Different kinds of combinations of bin and bulk approaches are possible. For example, liquid hydrometeors can be handled more precisely using the bin approach, while ice-phase hydrometeors are described using the bulk approach since there are much higher uncertainties in the formation of ice-phase hydrometeors than the liquid ones (Khain et al. [2015]).

A new approach has been developed in large-eddy simulations (LES) over the past few years, the Lagrangian cloud model (Khain et al. [2015]). The motion of individual droplets is calculated as they are advected in the flow of air. Because of the high number of individual droplets, the concept of superdroplets, when one superdroplet represents a large number of droplets having the same size and location, was introduced (Khain et al. [2015]). The accuracy of Lagrangian cloud models depends on the ability of an LES model to correctly simulate turbulent motion (Khain et al. [2015]). The LES models resolve larger turbulent eddies explicitly, while small ones are parameterized (Zhiyin [2015]). Thus, a significant proportion of the turbulence is explicitly resolved in LES models, in contrast to all operational NWP models, which use turbulence parameterizations as their grid size usually exceeds 1 km, which is above the size of turbulent whirls. Lagrangian

cloud models are not used in NWP models.

Bin parameterizations outperform bulk parameterizations regarding prediction accuracy (Lee and Baik [2018]). However, the computational cost of bin parameterizations is more than 5-20 times higher (Khain et al. [2015]), that is why bulk type parameterizations are currently widely used in operational runs of NWP models (Lee and Baik [2018]). Therefore, the following text is devoted to a description of different types of bulk microphysics parameterizations.

1.2.2 Single-moment and multi-moment schemes

Bulk microphysics schemes can be either single-moment or multi-moment ones. Usually, single-moment schemes are used in NWP. A single-moment scheme simulates only the mixing ratio or the specific content of hydrometeor species. Other quantities, such as the number concentration, are obtained diagnostically.

Double-moment schemes predict both the mixing ratio and the number concentration of each hydrometeor species allowing to simulate different types of clouds more accurately (Straka [2009]). However, they are not widely used in NWP due to their higher computational cost and minimal gains in the accuracy of weather forecasts under normal circumstances (Baldauf et al. [2011]). Also, the wide variety of ice-phase hydrometeors impedes their operational application due to the difficulty of computing their number concentration.

It is also possible to combine both methods. Thus, two moments are used for certain hydrometeor species, while only mixing ratios are computed for others. Such schemes are sometimes called 1.5-moment schemes. For example, Thompson et al. [2008] suggest computing rain, cloud ice, and optionally also cloud water using two moments (mixing ratio and number concentration), while for snow and graupel is only one moment used.

Also, triple-moment schemes exist, the radar reflectivity, which is related to the sixth moment of the distribution, can be the additional moment being predicted (Milbrandt and Yau [2005]). Nonetheless, triple-moment schemes are not used operationally.

1.3 Representation of hydrometeors in microphysics schemes

Most operationally used microphysics schemes simulate four or five hydrometeor species prognostically. Namely, cloud water, cloud ice, rainwater, snow, and some schemes also include graupel or a shared category of graupel and hail. Graupel is usually considered to be a middle-density particle with fall speed and density lower than rain and higher than snow of the same (characteristic) diameter (Straka [2009]). The wide range of graupel densities is often neglected (Thompson et al. [2008]).

The distinction between cloud and precipitating particles, following Kessler [1967], is somewhat artificial. However, it is very convenient since cloud particles are assumed to have negligible sedimentation or their gravitational fall speed is set to a certain value, while the fall speed of precipitating particles depends on their size. This split also simplifies the collection of particles because it does not

require any changes in the gravitational collection kernel of one category since the growth of cloud particles to precipitating ones is parameterized by a process called autoconversion. As an exception, the operationally used microphysics scheme of the Unified Model clusters cloud ice and snow into one category (Johnson et al. [2018]).

Since it is not sustainable to simulate every single particle, their spectra is assumed to follow a statistical distribution. In other words, an integrable probability density function is used for the description of their population (Straka [2009]). The size spectrum of precipitating particles $N(D)$ (D is the diameter of the particle) is usually described by the generalized gamma distribution or by its special cases (with the gamma distribution or with the negative exponential distribution, which is also called the Marshall-Palmer distribution (Marshall and Palmer [1948])). The generalized gamma distribution can be written as (Laboratoire d'Aérodynamique and CNRM-GAME [2022])

$$N(D) = N_T \frac{\iota}{\Gamma(\nu)} \lambda^\nu D^{\nu-1} e^{-(\lambda D)^\iota} \quad (1.4)$$

where $\Gamma()$ is the gamma function, and ι and ν are parameters that can be computed or prescribed. It is normalized by the total number of particles, N_T , to obtain the number concentration of particles as the zeroth moment. From the generalized gamma distribution can be easily obtained the negative exponential distribution setting $\nu = 1$ and $\iota = 1$ or the gamma distribution setting $\iota = 1$. The intercept parameter

$$N_0 = \frac{N_T}{\Gamma(\nu)} \lambda^\nu, \quad (1.5)$$

is often kept constant in single-moment schemes (Milbrandt and Yau [2005]).

1.3.1 The moment method

The moments of a distribution can be used to compute its parameters. This method is called the moment method (Straka [2009]). The system of equations for the moments of a distribution is not closed; the p -th moment includes terms with $(p+1)$ -th moment (Khain et al. [2015]). Therefore, a closure of the scheme has to be defined. The number of computed moments determines the order of the closure (Milbrandt and Yau [2005]).

The p -th moment of a distribution is defined as (Milbrandt and Yau [2005])

$$M(p) = \int_0^\infty D^p N(D) dD. \quad (1.6)$$

The zeroth moment is the number concentration (Straka [2009]). This quantity is predicted by double-moment schemes. In single-moment schemes, the number concentration is diagnostically obtained from the number-size relation, such as the Marshall-Palmer law. The first moment is related to the mean diameter of particles. The mean volume diameter for any distribution can be written as (Straka [2009])

$$\overline{D_j^V} = \left(\frac{6\rho_a r_j}{\pi\rho_j N_j} \right)^{\frac{1}{3}}, \quad (1.7)$$

where ρ_j and N_j are the density of hydrometeor species j and its number concentration, respectively. The second moment is related to the surface area. The mass is the third moment and the most often computed one. Usually, it is described by the mixing ratio or specific content. Since mass is related to volume, it is computed using the third moment of the distribution (Straka [2009]). The mixing ratio of rain can be expressed as (Abel and Boutle [2012], with a correction)

$$r_j = \frac{1}{\rho_a} \int_0^\infty V_j(D_j) D_j^3 N_j(D_j) dD_j, \quad (1.8)$$

where ρ_a is the density of air and $V_j(D_j)$ is the volume of one particle j . For the rainfall rate one has (Pruppacher and Klett [1997])

$$\mathcal{R}_j = \int_0^\infty V_j(D_j) D_j^3 N_j(D_j) v_j(D_j) dD_j. \quad (1.9)$$

with $v_j(D_j)$ the terminal velocity of particle j . Since the reflectivity depends on D^6 , the sixth moment is related the radar reflectivity, which is used as the additional moment in some triple-moment schemes (Milbrandt and Yau [2005]).

Alternatively, the p -th moment of a distribution can be also defined in terms of the mass of the particle m as

$$M(p) = \int_0^\infty m^p N(m) dm, \quad (1.10)$$

with $N(m)$ is the particle size distribution dependent on its mass. Thus, the number concentration is obtained for $p = 0$, mass content for $p = 1$ and the reflectivity for $p = 2$ (Khain et al. [2015]). That is consistent with values $p = 0$, $p = 3$ and $p = 6$ in Equation (1.6), since the mass of a spherical hydrometeor is proportional to the third power of its diameter.

1.3.2 The Marshall-Palmer distribution

Many schemes use the negative exponential distribution, also called the Marshall-Palmer size distribution, written as

$$N(D) = N_0 e^{-\lambda D}, \quad (1.11)$$

where N_0 is the intercept parameter of the exponential distribution and λ is the slope of the distribution (Straka [2009]). The slope parameter λ can be obtained from Equation (1.8) as

$$\lambda_j = \left(\frac{\pi \rho_w N_0}{\rho_a r_j} \right)^{\frac{1}{4}}. \quad (1.12)$$

Typical values of the intercept parameter are $N_0^r = 8 \cdot 10^6 \text{ m}^{-3} \cdot \text{m}^{-1}$ for rain, as suggested by Marshall and Palmer [1948]. This value is not often questioned. However, some variations to this constant parameter were examined by Wainwright et al. [2014]. A more realistic field of radar reflectivities, reduced cold pool, and better number concentration was obtained with $N_0^r = 4 \cdot 10^5 \text{ m}^{-3} \cdot \text{m}^{-1}$

in a simulation of a tornadic supercell. A value of $N_0^s = 2 \cdot 10^6 \text{ m}^{-3} \cdot \text{m}^{-1}$ is commonly used for snow (Lin et al. [1983], Lopez [2002], Hong and Lim [2006]). For snowstorms over Lake Michigan, the span of N_0^s was experimentally estimated as $N_0^s \in (4 \cdot 10^5, 8.75 \cdot 10^6) \text{ m}^{-4}$ (Pruppacher and Klett [1997]). Some schemes (Doms et al. [2021], Hong and Lim [2006]) use for graupel $N_0^g = 4 \cdot 10^6 \text{ m}^{-3} \cdot \text{m}^{-1}$ following Rutledge and Hobbs [1984]. However, the coefficient for graupel varies even more than that of snow. In the case of hail, the intercept parameter would be much lower since hails usually have a low number concentration and bigger particles (Thompson et al. [2008]).

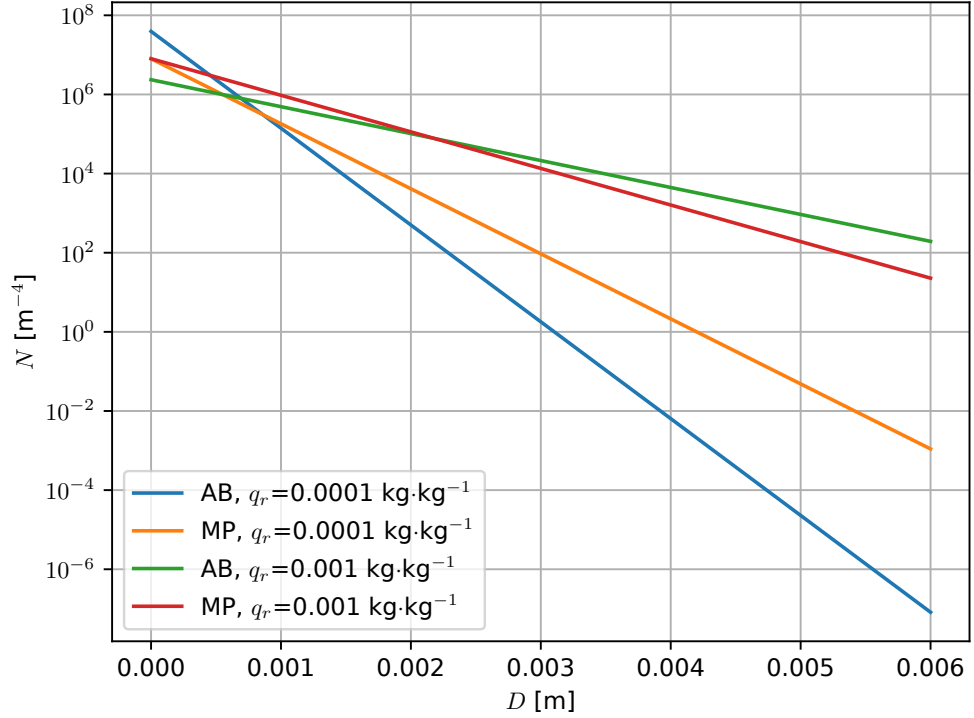


Figure 1.1: Comparison of drop sizes approximated by the Marshall-Palmer distribution using the fixed value of $N_0 = 8 \cdot 10^6 \text{ m}^{-4}$ (MP), and with the modification proposed by Abel and Boutle [2012] (AB). Two rainwater specific contents are plotted. Note that while for $q_r = 0.1 \text{ g} \cdot \text{kg}^{-1}$ is more smaller particles estimated by AB, for $q_r = 1 \text{ g} \cdot \text{kg}^{-1}$ is more small particles estimated by MP.

Despite the undeniable popularity of the Marshall-Palmer distribution, numerous deficiencies were revealed. Firstly, the Marshall-Palmer distribution overestimates the size of drizzle particles (Abel and Boutle [2012]). That causes too high precipitation rates in the case of drizzle because it takes more time for a larger drop to evaporate fully. The overestimation of the size of drizzle drops was corrected by a modification of the intercept parameter proposed by Abel and Boutle [2012], written for the exponential distribution as

$$N_0 = x_1 \lambda^{x_2}, \quad (1.13)$$

where

$$\lambda = \left[\frac{\pi \rho_w x_1}{\rho_a r_r} \right]^{\frac{1}{4-x_2}}, \quad (1.14)$$

$x_1 = 0.22 \text{ m}^{-1.8}$ and $x_2 = 2.20$. Both values were obtained from an analysis of aircraft measurements of cloud droplets in stratocumulus and trade winds cumulus clouds (Abel and Boutle [2012]). This modification of the intercept parameter is more suitable for the simulation of drizzle since it allows more efficient evaporation due to smaller drops with higher number concentration. Thus, it reduces the area covered by light precipitation (Wilkinson et al. [2013]). Figure 1.1 shows that the number concentration of little drops is higher in case of low mixing ratios of rain. In contrast, for higher mixing ratios it delivers even bigger drops than the typical fixed value, which might be beneficial, as was found by Igel et al. [2015].

Secondly, combined with the assumed constant density of ice particles, it does not correctly match the spectra of snow and graupel. The exponential distribution tends to overestimate the size of small ice particles but underestimate the size of bigger ones (Thompson et al. [2008]). However, the Marshall-Palmer distribution is widely used since the spectra of sizes and shapes of hydrometeors depend on temperature, relative humidity and other factors, e.g. turbulence (Khvorostyanov and Curry [2014]). As a result, it is only feasible to simulate some of these effects in a NWP model (Thompson et al. [2004]).

1.3.3 Mass-size and fall speed relations

The other ingredients needed to be determined are the mass of a particle and its fall speed relation. The mass-size relation is usually considered to follow a power law, written as

$$m(D) = a_1 D^{a_2} \quad (1.15)$$

with a_1 and a_2 parameters, which are usually prescribed (Straka [2009]).

Many schemes use the power law also for the fall speed relation,

$$w(D) = b_1 D^{b_2} \left(\frac{\rho_0}{\rho_a} \right)^{b_3}, \quad (1.16)$$

where ρ_0 is the reference density and b_1 , b_2 and b_3 are parameters (Straka [2009]). Another approach is to multiply the power law by the exponential function, for example the JMA-LSM model used for the certain period of time (Ikuta et al. [2021], Japan Meteorological Agency [2022])

$$w(D) = \sum_{k=1}^2 b_{k,1} D^{b_{k,2}} \left(\frac{\rho_0}{\rho_a} \right)^{b_{k,3}} e^{-b_{k,4} D} \quad (1.17)$$

with b_4 a parameter. Also, Thompson et al. [2008] uses a different expression for the fall speed relation, which can be written as

$$w(D) = b_1 D^{b_2} \left(\frac{\rho_0}{\rho_a} \right)^{0.5} e^{-b_4 D}. \quad (1.18)$$

The two latter expressions should better represent fall speeds for larger particles (Thompson et al. [2008]). On the other hand, more complex expression leads to higher computational expense, especially the evaluation of the exponential function. While the power law always delivers higher fall speed for bigger diameters, the observed fall speed of large drops remains almost invariable

with respect to their diameter because of the effect of turbulence, which is important for $D > 1.5 - 2$ mm, and higher aerodynamic drag, which rapidly increases for $D > 4$ mm and can cause even decrease of fall speed for larger diameters (Khvorostyanov and Curry [2014]). That is the reason why the exponential part can be beneficial.

2. Microphysical processes and their parameterizations

The previous chapter described basic methods for approximating hydrometeor spectra within one hydrometeor category, yet interactions between hydrometeor categories were not discussed. Thus, this chapter provides a little excursion into microphysical processes and their parameterizations. Definitions of selected microphysical processes are listed in Table 2.1.

Table 2.1: Description of various microphysical processes. References are abbreviated for readability: AMS for American Meteorological Society [2023], PK97 for Pruppacher and Klett [1997], KC14 for Khvorostyanov and Curry [2014] and eMS for Česká meteorologická společnost [2023]

process	description	reference
Coalescence	process when two colliding drops (or droplets) merge into one	AMS
Collection	process when a particle (collector) grows due to collision and coalescence with other particles	PK97
Self-collection	collection of particles within one category	KC14
Autoconversion	conversion from cloud water/ice to precipitating hydrometeors due to their self-collection.	AMS
Accretion	collection of cloud droplets by rain drops	AMS
Riming	collection of cloud water by graupel or snow	PK97
Aggregation	collection of cloud ice or snowflakes by snow	PK97
Evaporation	phase transition from liquid to gas	eMS
Condensation	phase transition from gas to liquid	AMS
Melting	phase transition from solid to liquid	AMS
Freezing	phase transition from liquid to solid	AMS
Sublimation	phase transition from solid to gas; colloquially also called evaporation	AMS
Deposition	phase transition from gas to solid	AMS

2.1 Precipitation production processes

For the initiation of precipitation are crucial processes broadening the size spectrum of droplets (Pruppacher and Klett [1997]). There are multiple processes leading to broadening of their spectrum; namely, self-collection, autoconversion and accretion (American Meteorological Society [2023]). All these processes are similar in nature, since they all describe collisions between particles.

Coalescence occurs due to multiple factors. Gravitational coalescence describes a process when the difference between the fall velocity of droplets and drops leads to the collection of smaller droplets by larger drops (Česká meteorologická společnost [2023]). Also, turbulent and electrostatic coalescence exists. Finally, Brownian coalescence describes the growth of small droplets due to Brownian motion (Česká meteorologická společnost [2023]). A hydrometeor category's final growth or detriment is due to the collection of particles, which accounts for coalescence and collisions.

Two models describe the process of collection based on the scientific knowledge of processes, the continuous growth model and the stochastic model. Also, data from bin microphysics schemes in LES models or other numerical simulations are available and they can be used for the parameterization of collection. In NWP models, collection and autoconversion is parameterized either by the continuous growth model or using results from LES models. The autoconversion process is also parameterized as there must be a process for converting cloud water to rainwater. Autoconversion can be viewed as a subgroup of collection since its physical essence is the self-collection of droplets. By definition, autoconversion leads to broadening the drop spectrum, so some droplets become large enough to be converted to the precipitating category (Seifert and Beheng [2001]).

2.1.1 The continuous growth model

The continuous growth model describes the collection of droplets with radius a_l by drops with radius a_r deterministically by the continuous collection equation (Pruppacher and Klett [1997], Řezáčová et al. [2007])

$$\begin{aligned} \frac{dm(a_r)}{dt} &= \int_0^{a_r} K(a_r, a_l) m(a_l) N(a_l) da_l \\ &= \int_0^{a_r} E(a_r, a_l) (a_r + a_l)^2 \pi (w_r - w_l) m(a_l) N(a_l) da_l, \end{aligned} \quad (2.1)$$

where $K(a_r, a_l)$ is the gravitational collection kernel, which describes the physical properties of the collection process (Khvorostyanov and Curry [2014]). It is often considered to be $a_l \ll a_r$ and $w_l \ll w_r$ for raindrops collecting cloud droplets, so these terms are usually neglected and Equation (2.1) becomes

$$\frac{dm(a_r)}{dt} = \int_0^{a_r} E(a_r, a_l) a_r^2 \pi w_r m(a_l) N(a_l) da_l. \quad (2.2)$$

where $E(a_r, a_l)$ is the collection efficiency of particle r collecting particle l ; that is, the ratio of the number of merged particles to the number of collided particles. The approximation $a_l \ll a_r$ and $w_l \ll w_r$ is not valid if the fall speed of both particles is comparable, e.g. for raindrops collecting hydrometeors. Then, the full form of Equation (2.1) must be used.

The collection kernel $K(a_r, a_l)$ is proportional to $(a_r + a_l)$ for the Brownian collection kernel and to $(a_r + a_l)^2$ for the gravitational collection kernel. Thus, it is another rationale for splitting liquid water into two categories besides the before-mentioned discrimination of fall speeds.

The collection efficiency E is often divided into two separate efficiencies, the coalescence and collision efficiency, denoted by E_{coal} and E_{colli} . The collection efficiency E is defined as (American Meteorological Society [2023])

$$E = E_{colli}E_{coal}. \quad (2.3)$$

The collection efficiency E is the only experimentally accessible quantity, as it is impossible to differentiate between coalescence and collision in the experimental environment (Pruppacher and Klett [1997]).

In spite of the possibility of measuring the collection efficiency E , it is a hardly known quantity since there are many uncertainties, e.g., the influence of turbulence. Estimating E is especially challenging for ice-phase hydrometeors (Laboratoire d'Aérodynamique and CNRM-GAME [2022]). The complex shapes and the secondary motion of hails and graupels make the value even more uncertain for them (Řezáčová et al. [2007]).

Equations (2.1) and (2.2) are the most widely used collection parameterizations in NWP models (Pinty and Jabouille [1998], Thompson et al. [2008], Hong and Lim [2006], Doms et al. [2021]). Equation (2.1) is used for the parameterization of the collection of precipitating particles by precipitating particles, while Equation (2.2) is used for the collection of cloud particles by precipitating particles.

2.1.2 Common autoconversion parameterizations

A complete rigorous theory of autoconversion is still absent due to uncertainties in observations of gravitational self-collection of cloud droplets within a narrow size spectrum (Khvorostyanov and Curry [2014]). Nevertheless, autoconversion is successfully parameterized in numerous NWP microphysics schemes.

Typically, the autoconversion from cloud water to rain and from cloud ice to snow is included in microphysics schemes in NWP models.

The traditional way how to parameterize autoconversion, following Kessler [1967], is to assume a constant rate of conversion from cloud water to rainwater as

$$\frac{dr_r}{dt} = k_r (r_l - r_l^{crit}) \mathcal{H}(r_l - r_l^{crit}) \quad (2.4)$$

where k_r is a constant, $\mathcal{H}()$ is the Heaviside step function and r_l^{crit} is an arbitrarily chosen threshold of cloud water mixing ratio above which autoconversion occurs.

For studying the properties of this autoconversion parameterization, Equation (2.4) can also be expressed as

$$\frac{dr_r}{dt} = \widetilde{k}_r r_l \mathcal{H}(r_l - r_l^{crit}), \quad (2.5)$$

where \widetilde{k}_r can be obtained from a comparison with Equation (2.4) as

$$\widetilde{k}_r = k_r \left(1 - \frac{r_l^{crit}}{r_l}\right). \quad (2.6)$$

This shows that increasing k_r affects the autoconversion rate in a similar way as does lowering or rising the value of r_l^{crit} (Liu and Daum [2004]).

It can be shown (Liu and Daum [2004]) that

$$\frac{dr_r}{dt} = K(a_{r,k}, a_{l,k}) N_l r_l = c_k r_l \quad (2.7)$$

with $K(a_{r,k}, a_{l,k})$ the average gravitational collection kernel and N_l the number concentration of cloud droplets. Comparing equations (2.7) and (2.4) shows that the averaged gravitational collection kernel is expressed as

$$K(a_{r,k}, a_{l,k}) = k_r \left(1 - \frac{r_l^{crit}}{r_l} \right) N_l^{-1}, \quad (2.8)$$

which is not the observed behaviour because the collection kernel is not independent of droplet radius in nature (Liu and Daum [2004]).

The Kessler autoconversion parameterization was later modified by Sundqvist [1978] in order to prevent the on-off behaviour of the Kessler parameterization and make the transition smooth. This modification delivers more physical realism (Liu et al. [2006]). Thus, the equivalent of Equation (2.5) is written as (Sundqvist [1978])

$$\frac{dr_r}{dt} = k_r r_l \left[1 - e^{-\left(\frac{r_l}{r_l^{crit}} \right)^2} \right]. \quad (2.9)$$

This formula can be further generalized as (Liu et al. [2006])

$$\frac{dr_r}{dt} = k_r r_l \left[1 - e^{-\left(\frac{r_l}{r_l^{crit}} \right)^\sigma} \right], \quad (2.10)$$

where $\sigma > 0$ is a real parameter to be empirically determined. The formulation of the threshold function is the only difference between the Kessler and Sundqvist type of autoconversion parameterization.

Many microphysics schemes use Kessler or Sundqvist autoconversion parameterizations despite their assumptions violate observed properties of forming water drops. Both parameterizations assume that the gravitational collection kernel is independent of the cloud droplet radius and also that the cloud water droplet size distribution is monodisperse (Liu and Daum [2004]). The error of the autoconversion rate estimation can be even around 1000 % (Phillips and Yano [2015]). However, for the onset of precipitation is essential the value of r_l^{crit} , then the collection of smaller droplets outweighs the influence of autoconversion on the evolution of rain. Thus, the poor quantitative accuracy of the Kessler type of autoconversion is not so detrimental (Phillips and Yano [2015]). The Kessler and Sundqvist parameterizations are proven to work successfully in many NWP models for many years.

A more physically realistic approach was presented by Manton and Cotton [1977], and further discussed by Tripoli and Cotton [1980]. This parameterization is based on the assumption that autoconversion follows

$$\frac{dr_r}{dt} = E_l \rho_l \mathcal{H}(\rho_l - \rho_{lt}), \quad (2.11)$$

where E_l is the mean collision efficiency between cloud water droplets, ρ_l is the density of cloud water in the air, and ρ_{lt} is the threshold density of cloud water, which can be expressed as

$$\rho_{lt} = \frac{4\pi\rho_w}{3}a_{lt}^3N_l, \quad (2.12)$$

where a_{lt} is the threshold radius of cloud droplets. The mean collision efficiency is given as

$$E_l = \pi a_l^2 \rho_w N_l w_l, \quad (2.13)$$

where w_l is the terminal velocity of water droplets. Droplets are small enough to allow the air flow around the drop, which is considered laminar, but they are also big enough to neglect molecular effects. Therefore, the terminal velocity follows Stokes' law

$$w_l = \frac{2\rho_w g}{9\mu} a_{lt}^2 = \frac{2\rho_w g}{9\mu} \left(\frac{3\rho_l}{4\pi\rho_w N_l} \right)^2, \quad (2.14)$$

where μ is the viscosity of air, g is the magnitude of the gravity of Earth, and for r_{lt} is substituted from Equation (2.12). Substituting Equation (2.14) into (2.13) and then (2.13) and (2.12) into (2.11) yields

$$\frac{dr_r}{dt} = E_l \frac{2g}{9\mu} (\pi\rho_w N_l)^{-\frac{1}{3}} \left(\frac{3}{4} \right)^{\frac{4}{3}} \rho_l^{\frac{7}{3}} \mathcal{H} \left(\rho_l - \frac{4\pi}{3} \rho_w a_{lt}^3 N_l \right). \quad (2.15)$$

This parameterization uses the droplet concentration as a dependent variable, and the threshold value of r_l^{crit} is based on the mean volume diameter of the droplet instead of the liquid water content. This allows for distinguishing different air masses, unlike the approach suggested by Kessler (Manton and Cotton [1977]). Still, this parameterization assumes a monodisperse spectrum of cloud droplets, constant collection efficiency, and fixed Stokes terminal velocity (Liu and Daum [2004]).

Some more complex proposals appeared. They are usually designed for multi-moment microphysics schemes. Here we limit the text to describe common approaches used in NWP. One such approach was proposed by Seifert and Beheng [2001]. The autoconversion parameterization is written as

$$\frac{dr_r}{dt} = \frac{k_r}{20m^*} \frac{(\nu+2)(\nu+4)}{(\nu+1)^2} r_l^2 \bar{m}_l^2 \quad (2.16)$$

where ν is the shape parameter of the gamma distribution for cloud droplets, $\bar{m}_l = r_l/N_l$ is the mean mass of one cloud droplet, and m^* is a threshold beyond which a significant number of droplets does not occur; it can be set as the mean mass of raindrops assuming $m_l \ll m^*$. The value of k_r can significantly differ from typical values used in Equation 2.4 as the functional dependence on r_l is non-linear. Using a two-moment parameterization in a single-moment scheme is possible, but the number concentration of droplets must be prescribed.

More sophisticated parameterization of autoconversion were proposed in various articles (e.g. Liu and Daum [2004]), which suppress the deficiencies of the ones mentined above. However, to the best of the author's knowledge, they are not operationally used in any NWP model.

While there are multiple autoconversion parameterizations for the so-called warm processes used across the microphysics parameterizations in NWP, autoconversion from cloud ice to snow is usually parameterized following Lin et al. [1983]

$$\frac{dr_s}{dt} = k_s r_i \mathcal{H}(r_i - r_i^{crit}), \quad (2.17)$$

often with $k_s = 10^{-3} \text{ s}^{-1}$. Eventually, Equation (2.17) can be expressed in the form of Equation (2.9) with the smooth transition function.

2.1.3 Parameterizations obtained from numerical simulations

The use of numerical simulations to assess the evolution of the growth of droplets is not only a phenomenon of a few past years. This method was used, for example, by Berry and Reinhardt [1974a], who solved the evolution of the growth of droplets in the stochastic model numerically. Results were used to obtain a formula for autoconversion (Berry and Reinhardt [1974b]), which is currently used in the Thompson scheme (Thompson et al. [2004]) and in the ICE-T scheme (Engdahl et al. [2022]), written as

$$\frac{dr_r}{dt} = \frac{0.0027 \cdot r_l \left[\frac{1}{16} \cdot 10^{20} (\overline{D_j^V})^4 (1 + \nu)^{-0.5} - 0.4 \right]}{\frac{3.7}{\rho_a r_l} \left[0.5 \cdot 10^6 \overline{D_j^V} (1 + \nu)^{-1/6} - 7.5 \right]^{-1}}, \quad (2.18)$$

where $\overline{D_j^V}$ is computed from Equation (1.7) and ν is again the shape parameter of the gamma distribution. This autoconversion parameterization should be more physically accurate than the Kessler one (Thompson et al. [2004]).

Another approach for autoconversion and collection parameterization was proposed by Khairoutdinov and Kogan [2000], who used data from simulations of the stable boundary layer using four different LES models with bin microphysics. Khairoutdinov and Kogan [2000] proposed three double-moment expressions for autoconversion. The final expressions are obtained by linear regression using the least square method. The one used in certain NWP models can be written as

$$\frac{dr_r}{dt} = 1350 r_l^{2.47} (N_l \cdot 10^{-6})^{-1.79} \quad (2.19)$$

where N_l is the cloud droplets concentration. All variables are in SI units.

Albeit this parameterization is a double-moment one, it is used in single-moment schemes as well, for example, in IFS (ECMWF [2021]) or Harmonie-Arome (Bengtsson et al. [2017]) with prescribed number concentrations. This parameterization delivers much lower autoconversion rates than the Kessler or Manton parameterization. This effect is compensated by higher collection rates, as noted in the next section. Also, Khairoutdinov and Kogan [2000] state that this autoconversion is from cloud water to drizzle rather than to rain, which explains the difference in the rates between this parameterization and the typical parameterization by Equation (2.4) and Equation (2.1).

Complementary to the autoconversion parameterization described by Equation (2.19), collection parameterization from cloud water to rainwater proposed

by Khairoutdinov and Kogan [2000] can be written as

$$\frac{dr_r}{dt} = 67 (r_r r_l)^{1.15}. \quad (2.20)$$

This equation can be linearized to

$$\frac{dr_r}{dt} = 3.7 r_r r_l. \quad (2.21)$$

However, Equation (2.21) has a tendency to overestimate higher collection rates (Khairoutdinov and Kogan [2000]). Equations (2.20) and (2.21) deliver higher collection rates compared to Equation (2.2), which compensates for the lower autoconversion rates delivered by Equation (2.19).

The full Khairoutdinov and Kogan [2000] parameterization (autoconversion and collection) is used in IFS (ECMWF [2021]) and the Unified Model configuration used at the Met Office (Wilkinson et al. [2013]).

As analytical derivations are sensitive to initial assumptions, data from numerical experiments are influenced by chosen cloud regimes because they produce different rates. Kogan [2013] used the same approach as Khairoutdinov and Kogan [2000] but used data for shallow cumuli. The resulting autoconversion rate obtained using the same procedure is:

$$\frac{dr_r}{dt} = 7.98 \cdot 10^{10} r_l^{4.22} (N_l \cdot 10^{-6})^{-3.01}, \quad (2.22)$$

which is a much stronger dependence on cloud water mixing ratio and droplet number concentration than for stratocumuli. By contrast, the collection parameterization is more similar:

$$\frac{dr_r}{dt} = 8.53 r_r^{1.05} r_l^{0.98}. \quad (2.23)$$

2.2 Evaporation and condensation of precipitation

First of all, it is worth emphasizing that evaporation and condensation occur simultaneously on the molecular scale. The observed macroscopic result is determined by which process predominates. Also, the parameterization of sublimation is referred to as evaporation parameterization.

In order to derive an equation for the condensation and evaporation rate of a drop, one can start from the distribution of water vapour around the drop. It is possible to analytically compute the distribution of water vapour around a spherical drop. The equation for the flux density of water vapour mass \vec{j}_v yields

$$\vec{j}_v = -D_v \nabla \rho_v + \rho_v \vec{u}, \quad (2.24)$$

where D_v is the diffusivity of water vapour in the air, ρ_v the density of water vapour, and \vec{u} is the relative velocity of the drop to the surrounding flow. After substituting \vec{j}_v into the continuity equation, which can be written as

$$\frac{\partial \rho_v}{\partial t} = -\nabla \cdot \vec{j}_v, \quad (2.25)$$

one gets the convective diffusion equation for water vapor

$$\frac{\partial \rho_v}{\partial t} + \vec{u} \rho_v = D_v \nabla^2 \rho_v \quad (2.26)$$

with ∇^2 the Laplace operator. Term $\nabla D_v \nabla \rho_v$ was neglected as is considered to be insignificant, and term $\rho_v \nabla \vec{u}$ is zero for incompressible flow. If one considers the stationary case, $\vec{u} = 0$, Equation (2.26) becomes Laplace's equation, which can be easily solved in spherical coordinates with prescribed boundary conditions of the water vapour density at the drop surface $\rho_{v,a}$ and $\rho_{v,\infty}$ the water vapour density in the infinite distance limit.

Using the Gauss-Ostrogradsky theorem, the flux of water vapour evaluated at the drop surface with area S is equal to the change of the drop mass as

$$\frac{dm}{dt} = - \int_S \vec{j}_v|_{r=a} dS = 2\pi D D_v (\rho_{v,\infty} - \rho_{v,a}) = \frac{2\pi D D_v}{R_v} \left(\frac{e_{sat,\infty}}{T_\infty} - \frac{e_{sat,a}}{T_a} \right), \quad (2.27)$$

where R_v is the specific gas constant of water vapour, $e_{sat,\infty}$ is the saturation water vapour pressure in the infinite distance limit, and $e_{sat,a}$ is the saturation water vapour pressure at the drop surface.

To account for ventilation, it is necessary to solve the complete set of Navier-Stokes equations of the flow around the drop. However, this is not feasible in NWP. Consequently, the average ventilation factor of mass, \bar{f}_c , is estimated. The typical empirical expression for raindrops is (Pruppacher and Klett [1997]):

$$\bar{f}_c = 0.78 + 0.308 \cdot Sc^{\frac{1}{3}} \cdot Re^{\frac{1}{2}}, \quad (2.28)$$

where Sc is the Schmidt number and Re is the Reynolds number. Thus, it is possible to proceed with the derivation in the same manner as for the stationary case, only adding the ventilation factor.

The next step is to account for the latent heat. Since water vapour condenses on the drop surface, latent heat is released and the temperature of a drop is raised. In analogy to Equation (2.27), the balance of heat released by condensation and the rate of heat conducted away from the particle is (Srivastava and Coen [1992])

$$L_v \frac{dm}{dt} = 2\pi D k_a \bar{f}_h (T_\infty - T_a), \quad (2.29)$$

where L_v is the latent heat of evaporation, k_a is the thermal conductivity of air, \bar{f}_h is the average ventilation coefficient of heat, T_a is the drop temperature, and T_∞ is the temperature in the infinite distance limit, but it is considered to be the ambient temperature. It can be undoubtedly better to consider the temperature at a certain point between the drop surface and ∞ . Nevertheless, it is hard to determine such a point, and the error caused by this approximation is at worst few percent (Srivastava and Coen [1992]).

Finally, the water vapour density at the particle surface, $\rho_{v,a}$, is to be determined, which can be written as

$$\rho_{v,a} = \rho_{v,a,sat}(T_a) (1 + s_a), \quad (2.30)$$

where $\rho_{v,sat}(T_a)$ is the saturation water vapour density at T_a and s_a is the equilibrium supersaturation over the drop due to salute effects and effects of curvature (Srivastava and Coen [1992]).

Equations (2.27), (2.29), (2.30) must be solved simultaneously (Srivastava and Coen [1992]). However, such an iterative technique is too computationally expensive to be used in NWP. Therefore, approximate explicit solutions must be found. The usual way is to approximate the saturation water vapour density difference between the particle and the ambient air using the first-order Taylor series, which yields

$$\rho_{v,sat}(T_a) \approx \rho_{v,sat}(T_\infty) + \frac{\delta\rho_{v,sat}}{\delta T}(T_\infty)(T_\infty - T_a). \quad (2.31)$$

This means that $\rho_{v,sat}$ is a linear function of $(T_\infty - T_a)$, which works well if the temperature difference $T_\infty - T_a$ is small. However, the evaporation rate is too low for some situations, such as for droplets in downdraughts, so it is better to use a quadratic approximation of T_a (Srivastava and Coen [1992]).

After a few steps, we can get an equation for the mass change in the form

$$\left(\frac{dm}{dt}\right)_{evap} = \frac{2\pi D D_v \rho_{v,sat}(T_\infty)(s - s_a)\overline{f_c}}{1 + H_w}, \quad (2.32)$$

where H_w is called the Howell factor (Köhler and Seifert [2015]), which can be easily derived from (Khvorostyanov and Curry [2014])

$$\frac{dm}{dt} = \frac{2\pi D (s - s_a) \overline{f_c}}{\frac{L_v}{k_a T} \left(\frac{L_v}{R_v T} - 1\right) + \frac{R_v T}{D_v e_{w,sat}}}, \quad (2.33)$$

where the first term in the denominator describes the thermal conduction of humid air, and the second one describes the diffusivity of water vapour in the air with precipitation (Lopez [2002]). Equation (2.33) is the most widely used equation for evaporation of drops in NWP models (Doms et al. [2021], Hong and Lim [2006], Lopez [2002], Japan Meteorological Agency [2022], Laboratoire d'Aérodynamique and CNRM-GAME [2022]). The term -1 in parenthesis is often omitted to reduce computation time and usually also $s_a = 0$ (Khvorostyanov and Curry [2014]).

Another approach was proposed by Kessler [1967]. This proposal is based on data taken from Smithsonian Meteorological Tables (List [1951]), wherein the formula consists of two terms in square brackets:

$$\frac{dm}{dt} = \underbrace{\left[2\pi D \left(1 + \frac{FD}{2v}\right)\right]}_{\text{first term}} \underbrace{\left[D_v (\rho_{v,a} - \rho_{v,\infty})\right]}_{\text{second term}}, \quad (2.34)$$

where v is the equivalent thickness of the transition shell outside the drop and F is a dimensionless factor. This equation was derived from Equation 2.27. Both parts were tabulated separately by Kinzer and Gunn [1951], based on data from an experiment using a chamber in which the evaporation of single falling drops was studied. These tabulated data were approximated by Kessler [1967]. The first part was approximated as

$$2\pi D \left(1 + \frac{FD}{2v}\right) = 2240 \cdot D^{1.6}. \quad (2.35)$$

Table 2.2: Coefficients of the approximation of the first term in Equation (2.34).

	T=0 °C	T=10 °C	T=20 °C	T=30 °C	T=40 °C
coefficient	41959	40531	25651	23606	15772
power	2.10	2.10	2.03	2.02	1.96
coefficient if $D^{1.6}$	2295	2217	2114	2049	1963

Table 2.3: Coefficients of the approximation of the second term in Equation (2.34). Values of $\rho_{v,sat}$ are taken from Nave [2023]

	T=0 °C	T=10 °C	T=20 °C	T=30 °C	T=40 °C
$\rho_{v,sat} [\text{g} \cdot \text{m}^{-3}]$	4.85	9.4	17.3	30.4	51.1
$D_v \cdot 10^{-5} [\text{m}^2 \text{s}^{-1}]$	1.40	1.15	0.942	0.732	0.575

Very similar results can be obtained using the least squares method if the power is kept at 1.6.

The second part was approximated by Kessler [1967] as

$$D_v (\rho_{v,a} - \rho_{v,\infty}) = 10^{-5} \chi, [\text{g} \cdot \text{m}^{-1} \cdot \text{s}^{-1}], \quad (2.36)$$

where χ is the absolute humidity deficit. As Ghosh and Jonas [1998] pointed out, coefficient 10^{-5} significantly underestimates the evaporation rate by a factor of around two. On the other hand, the product of both terms can possibly compensate for this effect.

For a more precise estimation of values given by Kessler [1967], data from the Smithsonian meteorological tables (tables 117a and 117b) are refitted using the least squares method. Obtained coefficients for the first term are given in Table 2.2 and coefficients for the second expression are given in Table 2.3. For completeness, also values of the saturation water vapour density are listed.

Plotting the Kessler approximation against measured values in the Smithsonian meteorological tables provides useful information. It is evident from Figure 2.1 that the power of $D^{1.6}$ chosen by Kessler in the first part of Equation (2.34) is not optimal. Much better agreement is obtained using values close to D^2 . The fit of the second part by Kessler is reasonably accurate, as shown in Figure 2.2. Hence, the fit of the second term needs to be significantly improved.

The main advantage of the Kessler evaporation parameterization is its lower computational cost compared to Equation (2.33).

Because of the irregular shapes of snow crystals, one cannot analytically find the distribution of water vapour around them. Therefore, the electrostatic analogy must be fully used (Khvorostyanov and Curry [2014]). However, it leads to the same equation as Equation (2.33); only the diameter D must be substituted for the crystal capacitance \mathcal{C} . The crystal capacitance \mathcal{C} depends on the shape of the crystal. Circular discs have $\mathcal{C} = D/\pi$, and spheres $\mathcal{C} = D/2$ (Pruppacher

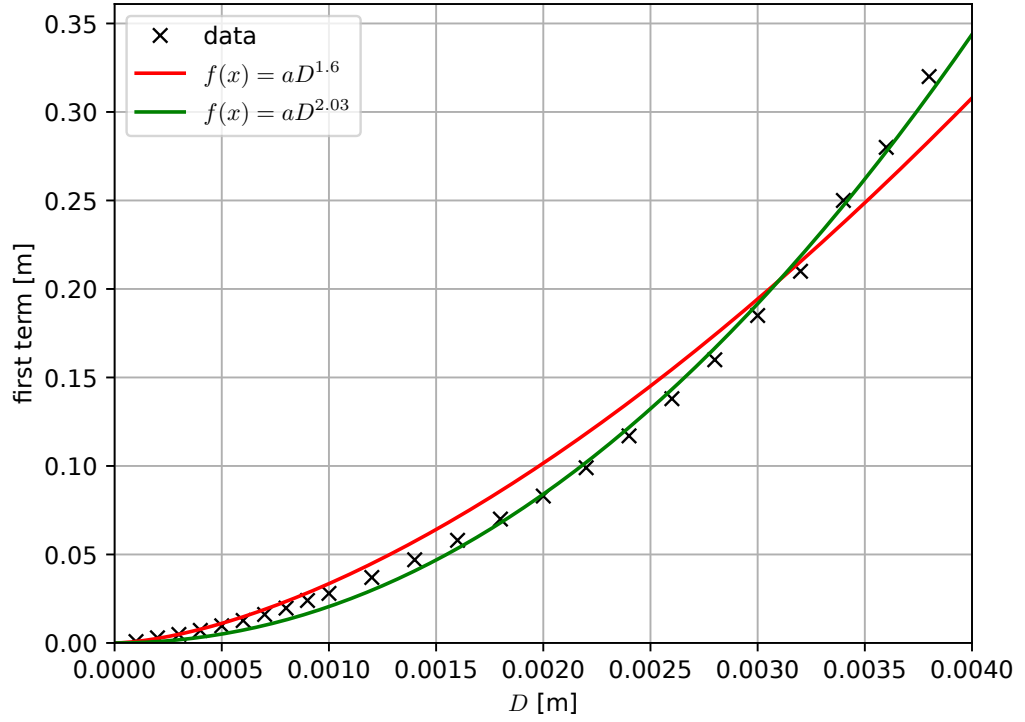


Figure 2.1: Least square approximation of the first term in Equation (2.34) at $T = 20^{\circ}\text{C}$

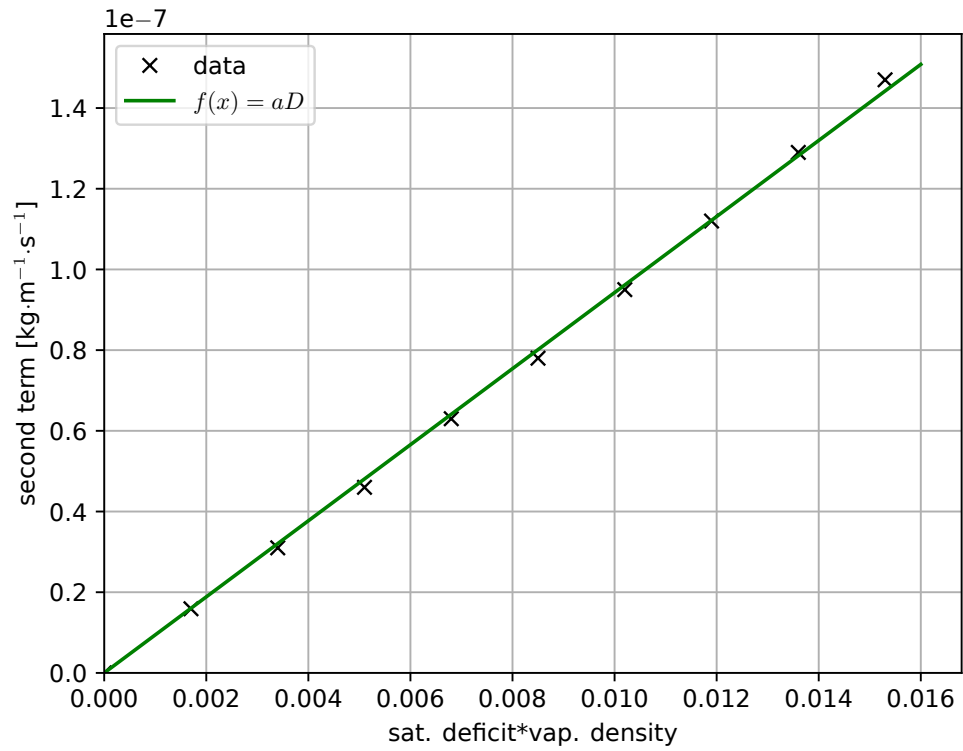


Figure 2.2: Least square approximation of the second term in Equation (2.34) at $T = 20^{\circ}\text{C}$

and Klett [1997]). Their orientation and shape determine the direction of their depositional growth. This is impossible to handle in NWP models; therefore, $\mathcal{C} = D/\pi$ is usually used for snowflakes (Lopez [2002], Hong and Lim [2006], Doms et al. [2021], Laboratoire d'Aérodynamique and CNRM-GAME [2022]). The Thompson scheme assumes a linear decrease from 0.5 to 0.3 as temperature increase from -30 to -15 °C. Graupel is often considered to be spherical (Doms et al. [2021], Laboratoire d'Aérodynamique and CNRM-GAME [2022]).

2.3 Melting and freezing

The most typical way to parameterize melting is similar to evaporation described by Equation (2.27). It is considered a spherical ice particle (it can be a graupel particle) with diameter a_i and a layer of water of uniform thickness $a - a_i$. Also, no shedding, evaporation, or internal circulation of liquid water is assumed. Then, the rate of released latent heat is equivalent to the rate at which is heat transferred though the water layer (Pruppacher and Klett [1997]). It leads to equation

$$4\pi\rho_i L_f a_i^2 \frac{da_i}{dt} = \frac{4\pi a a_i k_w [T_f - T_a(a_i)]}{a - a_i}, \quad (2.37)$$

where L_f is the latent heat of melting (fusion), and k_w is the thermal conductivity of water.

In reality, one cannot neglect the effect of water evaporation from the water shell and the convection of heat in the layer of liquid water. Thus, Equation (2.37) is modified to

$$\begin{aligned} \frac{4\pi a a_i k_w [T_f - T(a_i)]}{a - a_i} &= 4\pi a k_a [T_\infty - T(a_i)] \overline{f_h} \\ &+ 4\pi a D_v \frac{L_f M_w}{R^*} \left[\frac{e_\infty}{T_\infty} - \frac{e_a}{T_a(a_i)} \right] \overline{f_v}, \end{aligned} \quad (2.38)$$

where $\overline{f_h}$ and $\overline{f_v}$ are the average ventilation coefficient of heat and mass, R^* is the universal gas constant, M_w is the molar mass of water, and $e_\infty = \phi_v e_{sat,w}(T_\infty)$, wherein ϕ_v is the fractional relative humidity of the air. The first term on the right-hand side is the same as the right-hand side of Equation (2.27).

As evaporation cools the particle, Equation (2.38) gives lower melting rates than Equation (2.37). The critical temperature of the air at which melting begins is (Pruppacher and Klett [1997])

$$T_{crit} = T_f + \frac{D_v L_f M_w}{k_a R^*} \left[\frac{e_{w,sat}(T_f)}{T_f} - \frac{\phi_v e_{w,sat}(T_\infty)}{T_\infty} \right]. \quad (2.39)$$

Consequently, the lower the relative humidity, the higher the temperature required to trigger melting. For example, at a relative humidity of 50 %, melting of such spherical particles begins at $+4$ °C (Pruppacher and Klett [1997]), demonstrating that the latent heat transfer effects are not negligible.

As stated in Subsection 1.1.1, homogeneous water freezing is a rare phenomenon. However, the tangible value of the temperature of the homogeneous freezing used in NWP varies around -35 °C or -38 °C (Laboratoire d'Aérodynamique

and CNRM-GAME [2022], Thompson et al. [2004], Doms et al. [2021]). Micro-physics schemes also differ in how they split the condensate mass into solid and liquid phases for $T < T_f$.

It is essential to remember that the melting of a falling particle is a relatively fast process, and when the time step of a model is long, the particle can melt within one time step. Consequently, simpler parameterizations were developed. One of them is implemented in the IFS model and also in the JMA-GSM (global Japanese model), written as (ECMWF [2021])

$$\frac{dr_s}{dt} = -\frac{c_p}{L_f} \frac{T_w - T_f}{\tau_m}, \quad (2.40)$$

where

$$\tau_m = \frac{\tau_c}{1 + 0.5 \cdot (T_w - T_f)}, \quad (2.41)$$

T_w is the wet-bulb temperature, and τ_c is a constant. The IFS cycle cy47R3 uses $\tau_c = 11\,800$ s, while the current version of the global model used by the Japan Meteorological Agency uses $\tau_c = 7\,200$ s. The choice of values by ECMWF [2021] can cause slower melting than observed. However, it is kept this way since it should account for sub-grid scale air flow delaying the melting process.

Another approach is the Kessler-type of melting. Its derivation is similar to the derivation of Kessler-type of evaporation; the only additional quantities are the ratio of the molecular diffusion of heat to the molecular diffusion of water vapour and the ratio of the molecular heat capacity of dry air to the latent heat of fusion. Since this parameterization is used in ALARO, its detailed description can be found in Appendix A.4.

2.4 Sedimentation

Historically, models had coarse grids and long time steps. Thus, using non-prognostic hydrometeors was justified by assuming the fall speed of particles to be infinite. Consequently, precipitating particles reached the ground within one time step. This assumption was based on the fact that the time step of models was longer than the lifetime of particles. However, the fall speed of hydrometeors varies. Snow falls much slower than rain, which can violate this condition. With a significant improvement of computational resources, it was possible to introduce prognostic treatment of hydrometeors. As a consequence, terminal velocities of particles are considered finite. They are kept constant or follow some kind of relationship described in Subsection 1.3.3 (typical for LAMs).

Solving the particles sedimentation introduces the necessity to find a numerically stable scheme. It is well-known that the explicit Euler method requires the inverse Courant number Z to satisfy relation

$$Z = \frac{\delta z}{\bar{w} \delta t} \geq 1. \quad (2.42)$$

Thus, the explicit computation of precipitation sedimentation requires, for a typical depth of a high-resolution model layer of $\delta z = 30$ m in the surface layer of

the atmosphere and a typical raindrop average fall speed of $\bar{w}_r = 5 \text{ m}\cdot\text{s}^{-1}$, time step less than

$$\delta t < \frac{\delta z}{\bar{w}_r} = \frac{30}{5} \text{ s} = 6 \text{ s}. \quad (2.43)$$

Otherwise, the Courant-Friedrichs-Lewy (CFL) stability condition is violated, and the scheme becomes numerically unstable. Thus, time steps can be significantly shortened, especially for models with semi-Lagrangian semi-implicit advection schemes, which allow for much longer time step than the CFL condition permits in the horizontal.

There are two most common approaches to overcome this restriction, both relying on advection schemes. One possibility is to use the Lagrangian method. The second one is the time-splitting method, which computes the sedimentation explicitly using Eulerian method with smaller time steps than time steps used for the rest of the computations.

As an alternative to advection schemes, statistical sedimentation schemes are based on the probabilities at which a particle stays in layer, exit the layer or is created (or destructed) within the layer. Such a scheme was firstly used in ALARO (Geleyn et al. [2008b]) and its speacial case is also used in AROME (Bouteloup et al. [2011]). The sedimentation scheme used in the ALARO model will be described in Subsection 4.4.3.

3. NWP microphysics schemes

This chapter discusses various microphysics schemes with three ice hydrometeors (cloud ice, snow and graupel/hail) used in NWP models. Historically, models had coarse grids and long time steps that justified using non-prognostic water species except for water vapour. Today, all widely used NWP models handle water species prognostically. More sophisticated schemes arise with finer resolutions of model grids and shorter time steps, with goes hand in hand with significantly increased computational resources. This making possible to handle the complex effects of particle interaction within one time step in LAMs as well as in global models. Modern LAMs have time steps typically of the order of tens of seconds.

The first widely used microphysics scheme was developed by Kessler [1967] and it is still the foundation stone of current microphysics parameterizations. This scheme includes only warm-rain processes. It was later extended for solid phase hydrometeors by Lin et al. [1983] and Rutledge and Hobbs [1984].

This chapter aims to briefly expound the unique characteristics of the schemes, not to deliver a complete description of all schemes, which is over the scope of this text. The microphysics scheme used in ALARO will be discussed more in-depth in Section 4.4.

3.1 ICE3

The first described scheme is the ICE3 scheme since it is used in AROME, which is one of the canonical model configurations of the ALADIN system (besides ALARO and HARMONIE-AROME). The ICE3 microphysics scheme was developed in the Meso-NH model, which is a non-hydrostatic mesoscale atmospheric model. Later, it was adapted for use in NWP models by implementing the statistical sedimentation scheme allowing for longer time steps.

The generalized gamma distribution function (Equation 1.4) is used for the size distribution for every hydrometeor. However, the combination of parameters for precipitating hydrometeors ($\iota = 1$, $\nu = 1$) leads to the Marshall-Palmer distribution (Pinty and Jabouille [1998]). The parameter N_T is set as

$$N_T = c\lambda^x. \quad (3.1)$$

The values of coefficients c and x for rain, snow, and graupel are listed in Table 3.1.

Table 3.1: Coefficients for Equation (3.1) used in the ICE3 scheme (Pinty and Jabouille [1998]).

parameter	rain	snow	graupel
c	$8 \cdot 10^6$	5	$5 \cdot 10^5$
x	-1	1	-0.5

The full set of prognostic equations can be written as (Laboratoire d'Aérodologie and CNRM-GAME [2022]):

$$\frac{dr_v}{dt} = -\Delta_{cond}^{v \rightarrow l} + \Delta_{eva}^{r \rightarrow v} - \Delta_{het}^{v \rightarrow i} - \Delta_{dep}^{v \rightarrow r} - \Delta_{dep}^{v \rightarrow s} - \Delta_{dep}^{v \rightarrow g} \quad (3.2a)$$

$$\begin{aligned} \frac{dr_l}{dt} = & -\Delta_{aco}^{l \rightarrow r} - \Delta_{col}^{l+r \rightarrow r} + \Delta_{cond}^{v \rightarrow l} - \Delta_{hom}^{l \rightarrow i} - \Delta_{fre}^{l \rightarrow i} - \Delta_{col}^{l \rightarrow s} \\ & - \Delta_{col}^{l+s \rightarrow g} - \Delta_{dry}^{l \rightarrow g} - \Delta_{wet}^{l+g \rightarrow g+r} + \Delta_{melt}^{i \rightarrow l} \end{aligned} \quad (3.2b)$$

$$\begin{aligned} \frac{dr_i}{dt} = & +\Delta_{het}^{v \rightarrow i} + \Delta_{hom}^{l \rightarrow i} + \Delta_{fre}^{l \rightarrow i} + \Delta_{dep}^{v \rightarrow i} - \Delta_{melt}^{i \rightarrow l} - \Delta_{aco}^{i \rightarrow s} \\ & - \Delta_{col}^{i \rightarrow s} - \Delta_{fre}^{i+r \rightarrow g} - \Delta_{dry}^{i \rightarrow g} - \Delta_{wet}^{i \rightarrow g} \end{aligned} \quad (3.2c)$$

$$\begin{aligned} \frac{dr_r}{dt} = & +\Delta_{aco}^{l \rightarrow r} + \Delta_{col}^{l \rightarrow r} - \Delta_{eva}^{r \rightarrow v} - \Delta_{fre}^{r \rightarrow g} + \Delta_{fre}^{i+r \rightarrow g} - \Delta_{col}^{r \rightarrow s} \\ & - \Delta_{dry}^{r \rightarrow g} - \Delta_{wet}^{i+r \rightarrow g} + \Delta_{melt}^{g \rightarrow r} + \Delta_{wet,shed}^{l+g \rightarrow g+r} - \Delta_{col}^{r+s \rightarrow g} + \Delta_{dep}^{v \rightarrow r} \end{aligned} \quad (3.2d)$$

$$\begin{aligned} \frac{dr_s}{dt} = & -\Delta_{rim}^{s+l \rightarrow g} - \Delta_{col}^{s+r \rightarrow g} - \Delta_{dry}^{s \rightarrow g} - \Delta_{wet}^{s \rightarrow g} - \Delta_{convmel}^{s \rightarrow g} + \Delta_{col}^{r \rightarrow s} \\ & + \Delta_{col}^{l \rightarrow s} + \Delta_{col}^{i \rightarrow s} + \Delta_{aco}^{i \rightarrow s} + \Delta_{dep}^{v \rightarrow s} - \Delta_{col}^{r+s \rightarrow g} \end{aligned} \quad (3.2e)$$

$$\begin{aligned} \frac{dr_g}{dt} = & +\Delta_{fre}^{r \rightarrow g} + \Delta_{dep}^{v \rightarrow g} + \Delta_{fre}^{i+r \rightarrow g} + \Delta_{col}^{l+s \rightarrow g} + \Delta_{col}^{r+s \rightarrow g} + \Delta_{convmel}^{s \rightarrow g} \\ & + \Delta_{dry}^{(i,l,s,r) \rightarrow g} + \Delta_{wet}^{(i,s,r) \rightarrow g} + \Delta_{wet}^{l+g \rightarrow g+r} - \Delta_{melt}^{g \rightarrow r}. \end{aligned} \quad (3.2f)$$

The meaning of symbols is explained in The autoconversion parameterization follows Kessler [1967] for rain and Lin et al. [1983] for snow. Both parameters k_s and r_i^{crit} for autoconversion from cloud ice to snow are temperature dependent.

Collecting precipitating particles by precipitating particles is allowed, and even three particle processes are present (Pinty and Jabouille [1998]). The collection efficiency of cloud ice by graupel is set to $E_{gi} = 0.01e^{0.1(T-T_t)}$ (T_t the temperature is the triple point of water), while the collection efficiency of cloud water by graupel is set to $E_{gl} = 1$. So, graupel is assumed to be a very effective collector of cloud water while very poor collector of cloud ice. This setting improves the representation of cirrus clouds (Laboratoire d'Aérodologie and CNRM-GAME [2022]).

Snow cannot melt directly to rain; the intermediate particle is graupel. That is based on the idea that as a snowflake contains a lot of spaces of air, water start to fulfill some of them, increasing the density of the whole particle. Graupel has a higher density than snow, so it is a logical successor. This process is called conversion melting (Laboratoire d'Aérodologie and CNRM-GAME [2022]). Conversion melting does not release latent heat since graupel is also a solid particle. In nature, graupel also contains many pores that can be filled with water. This effect is neglected; graupel always follows the mass-size relation $m_g(D) = 19.6D^{2.8}$ taken from Locatelli and Hobbs [1974]. Then graupel melts to water if the environment is favorable for it.

Graupel can be produced by freezing rainwater; snow can grow into graupel due to heavy riming when snow is converted to the graupel category if its diameter is more than 0.7 mm (Laboratoire d'Aérodologie and CNRM-GAME [2022]). The collection of cloud ice by rain can produce graupel. Finally, graupel can be created by collisions of rain and snow.

The specific characteristic of this scheme is the treatment of graupel. There are two modes of collection growth, wet and dry. Wet growth occurs when liquid water cannot freeze on the surface of the graupel particle because the final temperature of such a particle can exceed T_f . Consequently, water cannot stay on the particle's surface and sheds, producing rain. Graupel grows more efficiently in the wet mode than in the dry mode (Pinty and Jabouille [1998]).

An effort to include hail in the ICE3 microphysics schemes appeared; the scheme is called ICE4 (Lascaux et al. [2006]). In the ICE4 scheme, hail grows via wet growth, while graupel grows exclusively via dry growth. However, the ICE4 scheme does not deliver superior results of hail prediction over the hail diagnostics with the ICE3 scheme used operationally in AROME (Seity and Riette [2017]). To the author's knowledge, schemes including hail as a separate category have yet to be operationally used in NWP.

Also a double-moment version of the ICE3/ICE4 scheme is developed. It is called LIMA, which stands for Liquid Ice Multiple Aerosols (Vié et al. [2016]). Autoconversion follows Equation (2.18). The collection kernels for accretion and self-collection are parametrized as (D_1 is the diameter of the collector, and D_2 is the diameter of the collected drop or droplet):

$$K(D_1, D_2) = \begin{cases} K_1(D_1^6 + D_2^6) & D_1 < 100 \mu\text{m} \\ K_2(D_1^3 + D_2^3) & D_1 > 100 \mu\text{m}. \end{cases} \quad (3.3)$$

Otherwise, LIMA is purely based on the ICE4 scheme, except that it includes specific terms for the double-moment treatment of hydrometeors (e.g., secondary ice production).

3.2 WSM6

The WSM6 (WRF Single Moment, Hong and Lim [2006]) scheme is a commonly used options for microphysics parameterization in WRF. For example, the WSM6 scheme is operationally used by the NOAA's National Weather Service Forecast Office, Raleigh, North Carolina (Weather Forecast Office Raleigh [2023]).

The WSM6 scheme relies upon the Lin model (Lin et al. [1983]) and the work of Rutledge and Hobbs [1984] with some changes. For example, graupel is assumed to have a constant density of $\rho_g = 500 \text{ kg}\cdot\text{m}^{-3}$. If the hail option is enabled, the density of graupel/hail is set to $\rho_g = 700 \text{ kg}\cdot\text{m}^{-3}$, contrary to Lin et al. [1983], where $\rho_g = 917 \text{ kg}\cdot\text{m}^{-3}$ is used.

The size distribution for every particle is the exponential distribution. The intercept parameters for rain and for snow are the typical ones. For snow, the intercept parameter is temperature dependent, $N_0^s = 2 \cdot 10^6 e^{0.12(T-T_f)} \text{ m}^{-4}$. The intercept parameter of graupel is $N_0^g = 4 \cdot 10^6 \text{ m}^{-4}$.

The complete set of prognostic equations can be written as follows:

$$\frac{dr_l}{dt} = -\Delta_{aco}^{l \rightarrow r} - \Delta_{col}^{l \rightarrow r} + \Delta_{cond}^{v \rightarrow l} - \Delta_{hom}^{l \rightarrow i} - \Delta_{het}^{l \rightarrow i} - \Delta_{col}^{l \rightarrow s} - \Delta_{col}^{l \rightarrow g} + \Delta_{melt}^{i \rightarrow l} \quad (3.4a)$$

$$\frac{dr_i}{dt} = -\Delta_{aco}^{i \rightarrow s} - \Delta_{col}^{i \rightarrow r} - \Delta_{col}^{i \rightarrow s} - \Delta_{col}^{i \rightarrow g} + \Delta_{dep}^{v \rightarrow i} + \Delta_{cond}^{v \rightarrow i} \quad (3.4b)$$

$$+ \Delta_{hom}^{l \rightarrow i} + \Delta_{het}^{l \rightarrow i} - \Delta_{melt}^{i \rightarrow l} \quad (3.4c)$$

$$\frac{dr_r}{dt} = +\Delta_{aco}^{l \rightarrow r} + \Delta_{col}^{l \rightarrow r} - \Delta_{col}^{r \rightarrow i} - \Delta_{col}^{r \rightarrow g} - \Delta_{col}^{r \rightarrow s} - \Delta_{fre}^{r \rightarrow g} - \Delta_{eva}^{r \rightarrow v} + \Delta_{melt}^{g \rightarrow r} \quad (3.4d)$$

$$+ \Delta_{melt}^{s \rightarrow r} + \Delta_{melt,enhcd}^{g \rightarrow r} + \Delta_{melt,enhcd}^{s \rightarrow r} \quad (3.4e)$$

$$\frac{dr_s}{dt} = +\Delta_{aco}^{i \rightarrow s} - \Delta_{aco}^{s \rightarrow g} + (1 - \delta_3) \Delta_{col}^{r+i \rightarrow s} + \Delta_{col}^{i \rightarrow s} \quad (3.4f)$$

$$- \Delta_{col}^{s \rightarrow g} - \delta_2 \Delta_{col}^{s+r \rightarrow g} + (1 - \delta_2) \Delta_{col}^{r \rightarrow s} + \Delta_{dep}^{v \rightarrow s} - \Delta_{melt}^{s \rightarrow r} - \Delta_{melt,enhcd}^{s \rightarrow r} \quad (3.4g)$$

$$\frac{dr_g}{dt} = +\Delta_{aco}^{s \rightarrow g} + \delta_3 \Delta_{col}^{r+i \rightarrow g} + \delta_2 \Delta_{col}^{r+s \rightarrow g} + \Delta_{col}^{i \rightarrow g} + \Delta_{col}^{l \rightarrow g} + \Delta_{col}^{r \rightarrow g} \quad (3.4h)$$

$$+ \Delta_{col}^{s \rightarrow g} + \Delta_{col}^{s+l \rightarrow g} + \Delta_{dep}^{v \rightarrow g} + \Delta_{fre}^{r \rightarrow g} - \Delta_{melt,enhcd}^{g \rightarrow r} - \Delta_{melt}^{g \rightarrow r}. \quad (3.4i)$$

Collisions of rain and ice can produce graupel but also snow. That is decided upon the value of the critical values of r_r and r_s , which are defined as

$$\begin{aligned} \delta_2 &= \mathcal{H}(r_r - r_r^{thres}) \quad r_r^{thres} = 10^{-4} \text{ kg} \cdot \text{kg}^{-1} \\ \delta_3 &= \mathcal{H}(r_{r,s} - r_{r,s}^{thres}) \quad r_{r,s}^{thres} = 10^{-4} \text{ kg} \cdot \text{kg}^{-1}. \end{aligned} \quad (3.5)$$

If the mixing ratio of rain is higher than $10^{-4} \text{ kg} \cdot \text{kg}^{-1}$, it is converted to graupel when it collects cloud ice. Collecting rain by snow (or vice versa) leads to graupel production if the mixing ratio of both exceeds $10^{-4} \text{ kg} \cdot \text{kg}^{-1}$. A term that differs this scheme from others is the enhanced melting by the collection of rainwater, which is for graupel parameterized as

$$\Delta_{melt,enhcd}^{g \rightarrow r} = \left(\frac{dr_g}{dt} \right)_{melt,enhcd} = \frac{-C_w}{L_f} (T - T_f) (\Delta_{col}^{r \rightarrow g} + \Delta_{col}^{l \rightarrow g}), \quad (3.6)$$

where C_w is the heat capacity of water and L_f is the latent heat of fusion. An analogous equation holds for the enhanced melting of snow.

The autoconversion parameterization for rain is taken from Manton and Cotton [1977], the critical diameter of a droplet to be converted to drop is $a_{crit} = 8 \cdot 10^{-6} \text{ m}$, and the number concentration of cloud droplets is $N_l = 3 \cdot 10^8 \text{ m}^{-3}$. According to Equation (2.12), this choice of r_{crit} yields the value of $r_l^{crit} = 6.43 \cdot 10^{-4} / \rho_a$. Autoconversion to snow follows Equation (2.17). Graupel is produced by autoconversion from snow. The formula is of the Kessler type

$$\frac{dr_g}{dt} = k_s (r_s - r_s^{crit}) \quad (3.7)$$

with $k_s = 10^{-3} e^{0.09(T-T_i)}$ and $r_s^{crit} = 6 \cdot 10^{-4} \text{ kg} \cdot \text{kg}^{-1}$ (Hong and Lim [2006]).

Collection of cloud ice by precipitating particles is temperature dependent. While for snow and graupel collecting cloud ice, the collection efficiency $E_{si} = E_{gi} = e^{0.07(T-T_i)}$, for graupel collecting snow $E_{gs} = e^{0.09(T-T_i)}$.

This scheme has several variants: the WSM5 scheme without graupel or a simpler WSM3 scheme, which simulates cloud water, cloud ice, and rainwater.

Also, a new version with hail placed into a separate category, called WSM7, is available (Bae et al. [2018]).

Schemes WSM5, WSM6, and WSM7 also have double-moment versions called WDM5, WDM6 and, WDM7 (WRF Double Moment), respectively (Skamarock et al. [2021]).

Tests of the WSM3 and WSM5 schemes on a coarse grid with a horizontal resolution of 45 km deliver similar rainfall rates, WSM6 tends to deliver higher rainfall rates and consequently rainfall accumulations due to higher fall speed of graupel compared to snow (Lim et al. [2004]).

3.3 Thompson scheme

The Thompson scheme (Thompson et al. [2004], Thompson et al. [2008], Thompson and Eidhammer [2014]) is another microphysics scheme available in the WRF model. The newest version of this scheme is also aerosol-aware (Thompson and Eidhammer [2014]). This option is kept under `mp_physics=28`, while the version without aerosols is option `mp_physics=8` in the microphysics setting in the WRF-ARW model version 4 (Skamarock et al. [2021]).

The Thompson scheme is a two-moment one for selected hydrometeors. Two moments are used for cloud ice, rainwater, and optionally for cloud water. This scheme is operationally used in the Rapid Refresh (RAP) and High-Resolution Rapid Refresh (HRRR) Weather Research and Forecast (WRF) models run at the National Center for Environmental Prediction (NCEP) in the USA (Alexander et al. [2020]).

The size distribution follows the generalized gamma distribution for every hydrometeor except for snow, for which is used a combination of the generalized gamma and the exponential distribution function. The intercept parameters of distributions are also complex, for rain one has (Thompson et al. [2008])

$$\begin{aligned}
 N(D) &= N_0 D^\mu e^{-\lambda D} \\
 N_0 &= \frac{N_1 - N_2}{2} \tanh\left(\frac{r_{r0} - r_r}{4r_{r0}}\right) + \frac{N_1 + N_2}{2} \\
 N_1 &= 9 \cdot 10^9 \text{ m}^{-4} \quad N_2 = 2 \cdot 10^6 \text{ m}^{-4}
 \end{aligned} \tag{3.8}$$

where N_0 is the intercept parameter, N_1 and N_2 an upper (lower) intercept limit, $r_{r0} = 10^{-4} \text{ kg} \cdot \text{kg}^{-1}$ is the transition value between the two limits. While the terminal velocity of smaller drops, f.e. drizzle, is decreased, the fall speed of large drops is high enough. Indeed, the effect is very similar to the modification of the intercept parameter introduced by Abel and Boutle [2012]. Moreover, suppose there is snow or graupel one layer above the uppermost melting layer and a rain layer below this melting layer. In that case, these raindrops will have a bigger mean volume diameter than raindrops created in warm rain processes, drizzle in particular (Thompson et al. [2008]).

In a similar way to rain, the intercept parameter of graupel varies with the graupel mixing ratio as (Thompson et al. [2008]):

$$N_{0g} = \max\left[10^4, \min\left(\frac{200}{r_g}, 5 \cdot 10^6\right)\right] m^{-4}, \tag{3.9}$$

which ensures higher fall speeds for large mixing ratios of graupel, approaching hail fall speeds. On the other hand, for low mixing ratios of graupel, the fall speed should be close to that of low-density graupel.

The full set of equations can be written as (UCAR [2023]):

$$\begin{aligned} \frac{dr_v}{dt} = & -\Delta_{cond}^{v \rightarrow l} + \Delta_{eva}^{r \rightarrow v} - \Delta_{het}^{v \rightarrow i} - \Delta_{dep}^{v \rightarrow i} - \Delta_{dep}^{v \rightarrow s} - \Delta_{dep}^{v \rightarrow g} \\ & - \Delta_{dep}^{i+v \rightarrow s} - \Delta_{fre}^{a \rightarrow i} \end{aligned} \quad (3.10a)$$

$$\frac{dr_l}{dt} = +\Delta_{cond}^{v \rightarrow l} - \Delta_{aco}^{l \rightarrow r} - \Delta_{col}^{l \rightarrow r} - \Delta_{col}^{l \rightarrow s} - \Delta_{col}^{l \rightarrow g} - \Delta_{col}^{s+l \rightarrow g} - \Delta_{fre}^{l \rightarrow i} \quad (3.10b)$$

$$\frac{dn_l}{dt} = +\Delta_{cond}^{v \rightarrow l} - \Delta_{aco}^{l \rightarrow r} - \Delta_{col}^{l \rightarrow r} - \Delta_{col}^{l \rightarrow s} - \Delta_{col}^{l \rightarrow g} - \Delta_{fre}^{l \rightarrow i} \quad (3.10c)$$

$$\begin{aligned} \frac{dr_i}{dt} = & +\Delta_{dep}^{v \rightarrow i} + \Delta_{HM}^{s \rightarrow i} + \Delta_{HM}^{g \rightarrow i} + \Delta_{fre}^{l \rightarrow i} + \Delta_{fre}^{r \rightarrow i} + \Delta_{dep}^{v \rightarrow i} - \Delta_{col}^{i \rightarrow r} \\ & + \Delta_{fre}^{a \rightarrow i} - \Delta_{col}^{i \rightarrow s} - \Delta_{aco}^{i \rightarrow s} \end{aligned} \quad (3.10d)$$

$$\begin{aligned} \frac{dn_i}{dt} = & +\Delta_{dep}^{v \rightarrow i} + \Delta_{HM}^{s \rightarrow i} + \Delta_{HM}^{g \rightarrow i} + \Delta_{fre}^{l \rightarrow i} + \Delta_{fre}^{r \rightarrow i} + \Delta_{dep}^{v \rightarrow i} - \Delta_{col}^{i \rightarrow r} \\ & - \Delta_{aco}^{i \rightarrow s} + \Delta_{col}^{i \rightarrow i} + \Delta_{fre}^{a \rightarrow i} \end{aligned} \quad (3.10e)$$

$$\begin{aligned} \frac{dr_r}{dt} = & +\Delta_{aco}^{l \rightarrow r} + \Delta_{col}^{l \rightarrow r} + \Delta_{col}^{s \rightarrow r} + \Delta_{col}^{g \rightarrow r} + \Delta_{melt}^{s \rightarrow r} + \Delta_{melt}^{g \rightarrow r} + \Delta_{col}^{i \rightarrow r} \\ & - \Delta_{fre}^{r \rightarrow g} - \Delta_{fre}^{r \rightarrow i} - \Delta_{eva}^{r \rightarrow v} \end{aligned} \quad (3.10f)$$

$$\begin{aligned} \frac{dn_r}{dt} = & +\Delta_{aco}^{l \rightarrow r} + \Delta_{col}^{s \rightarrow r} + \Delta_{col}^{g \rightarrow r} + \Delta_{melt}^{s \rightarrow r} + \Delta_{melt}^{g \rightarrow r} + \Delta_{col}^{i \rightarrow r} - \Delta_{eva}^{r \rightarrow v} \\ & + \Delta_{col}^{r \rightarrow r} - \Delta_{fre}^{r \rightarrow g} - \Delta_{fre}^{r \rightarrow i} \end{aligned} \quad (3.10g)$$

$$\begin{aligned} \frac{dr_s}{dt} = & +\Delta_{dep}^{i+v \rightarrow s} + \Delta_{dep}^{v \rightarrow s} + \Delta_{col}^{i \rightarrow s} - \Delta_{col}^{s \rightarrow r} + \Delta_{col}^{l \rightarrow s} - \Delta_{HM}^{s \rightarrow i} \\ & + \Delta_{dep}^{v \rightarrow s} - \Delta_{melt}^{s \rightarrow r} \end{aligned} \quad (3.10h)$$

$$\begin{aligned} \frac{dr_g}{dt} = & +\Delta_{col}^{i+r \rightarrow g} + \Delta_{col}^{s+l \rightarrow g} + \Delta_{dep}^{v \rightarrow g} + \Delta_{fre}^{r \rightarrow g} - \Delta_{melt}^{g \rightarrow l} + \Delta_{col}^{l \rightarrow g} \\ & + \Delta_{col}^{s+r \rightarrow g} + \Delta_{col}^{r \rightarrow g} - \Delta_{HM}^{g \rightarrow i}. \end{aligned} \quad (3.10i)$$

Since this scheme is a double-moment one for certain hydrometeors, there are unique terms, namely $\Delta_{fre}^{a \rightarrow i}$ representing freezing of aqueous aerosols and $\Delta_{HM}^{s, g \rightarrow i}$ denoting the Hallet-Mossop process of secondary ice production. Also, aerosols washout by precipitation is considered, but it is not stated in the system of equations above since it does not change the mass of any hydrometeor.

Autoconversion to rain is parameterized following Equation (2.18). Instead of the classical type of autoconversion from ice to snow, cloud ice is converted to snow if the size of ice crystals exceeds $200 \mu\text{m}$, denoted by $\Delta_{dep}^{i+v \rightarrow s}$ in the budget equations. Data for a fraction of cloud ice exceeding this threshold are tabulated in lookup tables (Thompson et al. [2008]).

The collection efficiencies depend on the median volume diameter of particles. Lookup tables for them are created at the start of integration to reduce the time needed for the computation (Thompson et al. [2008]). It is worth noting that the collection efficiency of graupel collecting cloud ice is zero.

Evaporation follows the formula proposed by Srivastava and Coen [1992], using the cubic relationship between the water vapour of the saturation water

vapour density difference between the particle and the ambient air temperature. This ensures a better representation of evaporation than the more common linear approximation of the drop surface temperature and ambient temperature difference when the drop temperature differs from the ambient temperature significantly, especially in downdraughts.

The freezing of rain, rain collecting cloud ice, and rimming of cloud water on snow can produce graupel. Graupel is produced if the rimming rate of cloud water on snow outweighs the depositional growth of snow. If rain freezes, it can be converted to cloud ice if the particle is small enough (Thompson et al. [2008]).

Compared to the WSM6 and Morrison schemes, which can also be used in the WRF model, the Thompson scheme deliver less graupel in convective storms (Bao et al. [2019]).

Some parts of the Thompson scheme are being incorporated into the ICE3 scheme; the resulting scheme is named ICE-T (Engdahl et al. [2019], Engdahl et al. [2022]).

3.4 Microphysics scheme in MetUM

The microphysics scheme used in the Unified Model is based on Wilson and Ballard [1999]. However, many changes have been applied since then (Wilkinson et al. [2013]). The set of equations, according to Wilson and Ballard [1999], is

$$\frac{dr_r}{dt} = +\Delta_{aco}^{l \rightarrow r} + \Delta_{col}^{l \rightarrow r} + \Delta_{col}^{r \rightarrow i} + \Delta_{melt}^{i \rightarrow r} - \Delta_{eva}^{r \rightarrow v} \quad (3.11a)$$

$$\frac{dr_l}{dt} = -\Delta_{aco}^{l \rightarrow r} - \Delta_{col}^{l \rightarrow r} - \Delta_{WBF}^{l \rightarrow i} - \Delta_{col}^{l \rightarrow i} + \Delta_{cond}^{v \rightarrow l} \quad (3.11b)$$

$$\frac{dr_i}{dt} = +\Delta_{col}^{r \rightarrow i} + \Delta_{col}^{l \rightarrow i} + \Delta_{nucl}^{v \rightarrow i} + \Delta_{dep}^{v \rightarrow i} + \Delta_{WBF}^{l \rightarrow i} \quad (3.11c)$$

$$\frac{dr_v}{dt} = \Delta_{eva}^{i \rightarrow v} + \Delta_{eva}^{r \rightarrow v} - \Delta_{nucl}^{v \rightarrow i} + \Delta_{cond}^{v \rightarrow l} - \Delta_{cond}^{v \rightarrow i}. \quad (3.11d)$$

The unique property is only one category for ice, shared by cloud ice and snow. The fraction of snow within this category f_{agg} is obtained diagnostically from

$$f_{agg} = 1 - \exp\left(-T_0 \Delta T \frac{r_i}{r_i^{crit}}\right), \quad (3.12)$$

where $T_0 = 0.0384 \text{ K}^{-1}$, $r_i^{crit} = 10^{-4} \text{ kg} \cdot \text{kg}^{-1}$ and ΔT represents the positive temperature difference from the cloud top (Cotton et al. [2013]).

The fall speed relation for rain follows Equation (1.17), a combination of two terms that are a product of a power law and an exponential (Walters et al. [2019]).

The intercept parameter of the size distribution of rain follows Abel and Boutle [2012]. The modifications of the intercept parameter combined with the auto-conversion parameterization proposed by Khairoutdinov and Kogan [2000], and prognostic computation of aerosol concentration lead to a better representation of stratocumulus clouds (Boutle and Abel [2012]).

The parameterization of autoconversion follows Khairoutdinov and Kogan [2000] with a threshold function in the form of

$$\frac{dr_r}{dt} = 1350 r_l^{2.47} (N_l \cdot 10^{-6})^{-1.79} \mathcal{H}(\overline{R_j} - R_0), \quad (3.13)$$

where R_0 is the critical diameter of cloud water to be converted to rainwater and $\overline{R_j^V} = 0.5 \cdot \overline{D_j^V}$ defined by Equation (1.7). The collection of particles by rain also follows the Khairoutdinov and Kogan [2000] model. Since the microphysics scheme is single-moment, the droplet number concentration is prescribed. Originally, constant values of $N_l = 3 \cdot 10^8 \text{ m}^{-3}$ over the land and $N_l = 0.5 \cdot 10^8 \text{ m}^{-3}$ over the ocean were used. These values cause the autoconversion rate to be almost 25 times higher over the ocean than the land with the same cloud water mixing ratio. Consequently, it leads to artificial rain structures on the coastline of Great Britain when there is not negligible rainfall accumulation over the ocean while no rainfall occurs over the land. This issue was solved by implementing a prognostic calculation of aerosol concentrations. Thus, aerosols are advected from continental Europe over the North Sea, and the droplet number concentration is consequently higher, significantly improving model results in the vicinity and over Great Britain. Such a scheme delivers much higher aerosol concentration over the North Sea, resulting in higher cloud droplet concentration than the prescribed values mentioned above (Wilkinson et al. [2013]). Without incorporating the prognostic computation of aerosol concentration into the model, too little drizzle precipitation is predicted. Consequently, the stratocumulus thickens, causing a positive 2-metre temperature bias (Wilkinson et al. [2013]).

A double moment aerosol aware scheme CASIM (Shipway and Hill [2012]) will be used for the following operational configuration (Field [2022]). This scheme accounts for more processes since double moment schemes require much more processes to be simulated. Even if they do not contribute to a significant mass change, they can impact the number concentration of particles. This scheme simulates five hydrometeors prognostically; the concept of one category for all ice hydrometeors used in the single is not retained. Graupel has a density of $250 \text{ kg} \cdot \text{m}^{-3}$, which provides the best agreement with radar measurements (Miltnerberger et al. [2018]).

3.5 COSMO/ICON microphysics scheme

Originally, ICON was a global model, and COSMO was a limited-area model. Recently, Deutscher Wetterdienst, in cooperation with the Max-Planck Institute for Meteorology, started to develop a limited-area version of ICON. The complete transition to ICON-LAM is ongoing (COSMO [2022]). However, ICON uses the same microphysics package as COSMO (ICON [2022]). Some changes beyond the standard COSMO microphysics scheme have been made for operational use in Deutscher Wetterdienst (Seifert [2008]). The standard COSMO/ICON microphysics scheme is a single-moment one.

The Marshall-Palmer law is used for rain, snow, and graupel. For rain, the typical value of $N_0^r = 8 \cdot 10^6 \text{ m}^{-4}$ is used, for graupel is used $N_0^g = 4 \cdot 10^6 \text{ m}^{-4}$ (Doms et al. [2021]). The intercept parameter of snow is currently (Seifert [2008])

$$N_{0,s} = \frac{27}{2} a(3, T) \frac{r_s^{4-3b(3, T)}}{0.069}, \quad (3.14)$$

This computation replaced the prescribed value of $N_0^s = 8 \cdot 10^5 \text{ m}^{-4}$. Functions $a(3, T)$ and $b(3, T)$ are temperature dependent, and their values are tabulated.

This modification of the intercept parameter leads to smaller snowflakes, especially at lower temperatures (Seifert [2008]).

The fall speed of snow is parameterized as

$$v_s = 15D^{\frac{1}{2}}, \quad (3.15)$$

which delivers lower values than observed, and fall speed is decreased compared to the standard COSMO scheme. This choice is justified by the fact that the vertical motions generated by orographic forcing might be resolved poorly in some models with grids with resolutions of a few kilometers (Seifert [2008]), based on the findings of Garvert et al. [2005].

The full set of equations is written as (Doms et al. [2021])

$$\frac{dr_v}{dt} = -\Delta_{cond}^{v \rightarrow l} + \Delta_{eva}^{r \rightarrow v} - \Delta_{het}^{v \rightarrow i} - \Delta_{dep}^{v \rightarrow i} - \Delta_{dep}^{v \rightarrow s} - \Delta_{dep}^{v \rightarrow g} \quad (3.16a)$$

$$\begin{aligned} \frac{dr_l}{dt} = & -\Delta_{aco}^{l \rightarrow r} - \Delta_{col}^{l \rightarrow r} + \Delta_{cond}^{v \rightarrow l} - \Delta_{fre}^{l \rightarrow i} + \Delta_{melt}^{i \rightarrow l} - \Delta_{col}^{l \rightarrow s} \\ & - \Delta_{col}^{l \rightarrow g} - \Delta_{shed}^{l+s \rightarrow r} - \Delta_{shed}^{l+g \rightarrow r} \end{aligned} \quad (3.16b)$$

$$\begin{aligned} \frac{dr_i}{dt} = & +\Delta_{dep}^{v \rightarrow i} + \Delta_{fre}^{l \rightarrow i} + \Delta_{dep}^{v \rightarrow i} - \Delta_{melt}^{i \rightarrow l} - \Delta_{aco}^{i \rightarrow s} - \Delta_{dep}^{i+v \rightarrow s} \\ & - \Delta_{col}^{i \rightarrow s} - \Delta_{col}^{i \rightarrow g} - \Delta_{col}^{r+i \rightarrow g} \end{aligned} \quad (3.16c)$$

$$\begin{aligned} \frac{dr_r}{dt} = & +\Delta_{aco}^{l \rightarrow r} + \Delta_{col}^{l \rightarrow r} - \Delta_{eva}^{r \rightarrow v} + \Delta_{shed}^{s+l \rightarrow r} + \Delta_{shed}^{g+l \rightarrow r} - \Delta_{col}^{r+i \rightarrow g} \\ & - \Delta_{fre}^{r \rightarrow g} + \Delta_{melt}^{s \rightarrow r} + \Delta_{melt}^{g \rightarrow r} \end{aligned} \quad (3.16d)$$

$$\begin{aligned} \frac{dr_s}{dt} = & +\Delta_{aco}^{i \rightarrow s} + \Delta_{dep}^{i+v \rightarrow s} + \Delta_{col}^{i \rightarrow s} + \Delta_{col}^{l \rightarrow s} + \Delta_{dep}^{v \rightarrow s} - \Delta_{melt}^{s \rightarrow r} \\ & - \Delta_{col}^{s+l \rightarrow g} + \Delta_{col}^{r+i \rightarrow s} \end{aligned} \quad (3.16e)$$

$$\begin{aligned} \frac{dr_g}{dt} = & +\Delta_{col}^{i \rightarrow g} + \Delta_{col}^{l \rightarrow g} + \Delta_{dep}^{v \rightarrow g} + \Delta_{fre}^{r \rightarrow g} - \Delta_{melt}^{g \rightarrow l} + \Delta_{col}^{s+l \rightarrow g} \\ & + \Delta_{col}^{r+i \rightarrow g} - \Delta_{shed}^{g+l \rightarrow r}. \end{aligned} \quad (3.16f)$$

The autoconversion from ice to snow can occur due to the deposition of water vapour onto ice crystals or growth through the aggregation of ice crystals. The autoconversion parameterization follows Equation (2.16). Since the scheme is single-moment, a constant cloud droplet concentration $N_l = 5 \cdot 10 \text{ m}^{-3}$ is assumed (Seifert [2008]).

Melting and sublimation are parameterized with respect to the critical temperature described by Equation (2.39). Suppose the ambient temperature is lower than the critical temperature. In that case, no melting occurs, and deposition or sublimation drives the loss or gain of the mass of a given ice particle besides collection and autoconversion. If the ambient temperature exceeds the critical temperature, the particle melts, and liquid water evaporates or condenses on the particle's surface. Therefore, neither sublimation nor deposition is assumed as the particle is entirely coated with liquid water.

Two processes produce graupel. Firstly, the freezing of raindrops and collisions of raindrops with cloud ice lead to graupel production. The other process is converting snow to graupel due to heavy riming, which occurs if the mass fraction of rimmed water on snow is more than 12 % (Doms et al. [2021]).

ICON also offers a double-moment microphysics scheme proposed by Seifert and Beheng [2006]. This scheme is suitable for use in models with very fine resolution using short time steps. More processes are considered since the correct number concentrations of hydrometeors is essential. Therefore, collision breakup and self-collection must be parameterized. Also, the enhanced melting is considered, following Equation (3.6). Naturally, for a double-moment scheme, secondary ice production is taken into account. The double-moment scheme was later extended for hails, and some parameterizations were changed (Baldauf et al. [2011]).

Fall speed relations follow Equation (1.15), for rain are used less common values of $b_1 = 159 \text{ m}^{1/3} \cdot \text{s}^{-1}$ and $b_2 = 2/3$ (Seifert and Beheng [2006]). An interesting part of this scheme can be perceived in the computation of the mean collection efficiencies of snow, graupel, and cloud ice collecting cloud water, which are assumed to follow

$$E = E_l(\overline{D_l^V})E_j(\overline{D_j^V}) \quad (3.17)$$

with $\overline{D_j^V}$ the volume mean diameter of collector and $\overline{D_l^V}$ the volume mean diameter of cloud droplets. The value of $E_l(\overline{D_l^V})$ is computed as

$$E_l(\overline{D_l^V}) = \begin{cases} 0 & \overline{D_l^V} < \overline{D_{l,0}^V} \\ \frac{\overline{D_l^V} - \overline{D_{l,0}^V}}{\overline{D_{l,1}^V} - \overline{D_{l,0}^V}} & \overline{D_{l,0}^V} \leq \overline{D_l^V} \leq \overline{D_{l,1}^V} \\ 1 & \overline{D_l^V} > \overline{D_{l,1}^V} \end{cases}, \quad (3.18)$$

where $\overline{D_{l,0}^V} = 15 \mu\text{m}$ and $\overline{D_{l,1}^V} = 40 \mu\text{m}$ are constants. The value of $E_e(\overline{D_j^V})$ is computed as

$$E_j(\overline{D_j^V}) = \begin{cases} 0 & \overline{D_j^V} \leq \overline{D_{j,0}^V} \\ E_j^{max} & \overline{D_j^V} > \overline{D_{j,0}^V} \end{cases} \quad (3.19)$$

with $\overline{D_{j,0}^V} = 150 \mu\text{m}$ for snow, graupel and cloud ice and $E_s^{max} = 0.8$ for snow and cloud ice, while for graupel $E_g^{max} = 1$. The collection efficiency $E_{gs} = e^{0.09(T-T_f)}$ is used for graupel and snow collisions. The collection efficiency of collisions between raindrops and ice particles is assumed to be one. The collection efficiency of graupel collecting ice crystals is set to zero (Seifert and Beheng [2006]).

Baldauf et al. [2011] showed that the difference between the results obtained using a single or double-moment scheme is not so significant on a mesh with a horizontal resolution of 2.8 km, to be advantageous to use the double-moment one since it demands more resources than a single-moment one. Since there were only a few cases with significant differences between simulations with the double-moment scheme and the single-moment scheme between June and August 2007, the single-moment scheme was later used operationally (Baldauf et al. [2011]). Moreover, in the case of the double-moment scheme, the sensitivity of results to the assumed aerosol mass and cloud condensation nuclei was also not significant. Similar results were obtained from sensitivity studies of the LIMA scheme (Homonnai [2016]). However, as the mesh size becomes finer, the double-moment scheme might also benefit climate modeling (Baldauf et al. [2011]).

3.6 Microphysics scheme in JMA-LFM

The microphysics scheme of the Local Forecast Model of the Japan Meteorological Agency (JMA-LFM) is described in Ikawa and Saito [1991]. The microphysics scheme itself is based on Lin et al. [1983]. However, the list of simulated processes has changed since then. For example, Ikawa and Saito [1991] permit autoconversion from cloud ice to graupel, which is omitted based on Japan Meteorological Agency [2022].

The full set of equations can be written as (Japan Meteorological Agency [2022]):

$$\frac{dr_v}{dt} = -\Delta_{cond}^{v \rightarrow l} + \Delta_{eva}^{r \rightarrow v} - \Delta_{het}^{v \rightarrow i} - \Delta_{dep}^{v \rightarrow i} - \Delta_{dep}^{v \rightarrow s} - \Delta_{dep}^{v \rightarrow g} \quad (3.20a)$$

$$\begin{aligned} \frac{dr_l}{dt} = & -\Delta_{aco}^{l \rightarrow r} - \Delta_{col}^{l \rightarrow r} + \Delta_{cond}^{v \rightarrow l} - \Delta_{col}^{g \rightarrow l \rightarrow r} - \Delta_{col}^{s \rightarrow l \rightarrow r} - \Delta_{dep}^{l \rightarrow i} - \Delta_{hom}^{l \rightarrow i} \\ & - \Delta_{col}^{l \rightarrow s} - \Delta_{dep}^{l \rightarrow s} - \Delta_{dep}^{l \rightarrow g} - \Delta_{col}^{l \rightarrow g} \end{aligned} \quad (3.20b)$$

$$\begin{aligned} \frac{dr_i}{dt} = & -\Delta_{aco}^{i \rightarrow s} - \Delta_{col}^{r \rightarrow i \rightarrow g} - \Delta_{col}^{i \rightarrow g} - \Delta_{melt}^{i \rightarrow r} + \Delta_{dep}^{v \rightarrow i} + \Delta_{cond}^{v \rightarrow i} - \Delta_{col}^{i \rightarrow s} \\ & + \Delta_{het}^{v \rightarrow i} + \Delta_{hom}^{l \rightarrow i} + \Delta_{dep}^{l \rightarrow i} \end{aligned} \quad (3.20c)$$

$$\begin{aligned} \frac{dr_r}{dt} = & +\Delta_{aco}^{l \rightarrow r} + \Delta_{col}^{l \rightarrow r} - \Delta_{col}^{r \rightarrow g} - \Delta_{col}^{r \rightarrow s} - \Delta_{col}^{i \rightarrow r \rightarrow g} - \Delta_{fre}^{r \rightarrow g} - \Delta_{eva}^{r \rightarrow v} \\ & + \Delta_{melt}^{s \rightarrow r} + \Delta_{melt}^{g \rightarrow r} + \Delta_{melt}^{i \rightarrow r} + \Delta_{col}^{g \rightarrow l \rightarrow r} + \Delta_{col}^{s \rightarrow l \rightarrow r} - \Delta_{col}^{s \rightarrow r \rightarrow g} \end{aligned} \quad (3.20d)$$

$$\begin{aligned} \frac{dr_s}{dt} = & +\Delta_{aco}^{i \rightarrow s} + \Delta_{dep}^{v \rightarrow s} + \Delta_{col}^{i \rightarrow s} + \Delta_{col}^{l \rightarrow s} + \Delta_{col}^{r \rightarrow s} - \Delta_{col}^{s \rightarrow g} - \Delta_{col}^{r \rightarrow s \rightarrow g} \\ & - \Delta_{melt}^{s \rightarrow r} - \Delta_{col}^{l \rightarrow s \rightarrow g} + \Delta_{dep}^{l \rightarrow s} \end{aligned} \quad (3.20e)$$

$$\begin{aligned} \frac{dr_g}{dt} = & +\Delta_{col}^{i \rightarrow g} + \Delta_{col}^{l \rightarrow g} + \Delta_{col}^{l \rightarrow s \rightarrow g} + \Delta_{dep}^{v \rightarrow g} + \Delta_{fre}^{r \rightarrow g} + \Delta_{col}^{r \rightarrow g} + \Delta_{col}^{s \rightarrow r \rightarrow g} \\ & + \Delta_{col}^{r \rightarrow i \rightarrow g} - \Delta_{melt}^{g \rightarrow r} + \Delta_{dep}^{l \rightarrow g} + \Delta_{col}^{s \rightarrow g}. \end{aligned} \quad (3.20f)$$

The size distributions of rain, cloud ice, and graupel follow the Marshall-Palmer distribution. For rain is used the typical value of $N_{0,r} = 8 \cdot 10^6 \text{ m}^{-4}$, for graupel $N_{0,g} = 1.1 \cdot 10^6 \text{ m}^{-4}$. No size distribution function is used for snow; only its moments are computed (Japan Meteorological Agency [2022]). For some time, the computation of the intercept parameter proposed by Abel and Boutle [2012] was used (Japan Meteorological Agency [2019]). Coefficients x_1 and x_2 had different values of $x_1 = 26.2$ and $x_2 = 1.57$, which were formerly used in the MetUM Global Atmosphere model version 3.0 (Abel and Boutle [2012]). However, unlike many other models, it suffered too little weak precipitation (Boutle and Abel [2012]). Consequently, this concept is abandoned as it delivers less drizzle than observed (Ikuta et al. [2021]).

Besides rainwater and cloud water, also graupel is considered spherical, with a constant density of $\rho_g = 300 \text{ kg} \cdot \text{m}^{-3}$ (Japan Meteorological Agency [2022]). Graupel can be produced by the freezing of rainwater, rain collecting cloud ice collisions of snow and graupel, and converting snow to graupel due to heavy riming. Collisions of rain and snow lead either to snow or graupel production.

The fall speed relations for rain, snow, and graupel follow a simple power law relationship (Equation (1.15)). A product of a power law and an exponential

described by Equation (1.17) was used in previous model configurations (Japan Meteorological Agency [2019]).

The parameterization of autoconversion to form rain follows the Kessler approach with coefficients in Equation (2.4) $k_r = 10^{-3} \text{ s}^{-1}$ and $r_l^{crit} = 10^{-5} \text{ kg} \cdot \text{kg}^{-1}$ (Ikuta et al. [2021]). Autoconversion from cloud ice to snow is parameterized as

$$\frac{dr_s}{dt} = \max \left[k_s (r_i - r_i^{crit}) \mathcal{H}(r_i - r_i^{crit}), f_{agg} \frac{r_i}{\Delta t} \right], \quad (3.21)$$

where Δt is the time step, $k_s = 10^{-3} e^{0.025(T-T_f)} \text{ s}^{-1}$, $r_i^{crit} = 10^{-4} \text{ kg} \cdot \text{kg}^{-1}$ and f_{agg} is given by Equation (3.12).

A different approach was chosen to parameterize melting and evaporation for the global model. Melting is parameterized similarly to the IFS parameterization described by Equation (2.40) with minor changes, e.g., using a different value of the typical timescale τ .

4. ALARO and its microphysics scheme

4.1 A brief introduction to ALARO

ALARO (the name is derived from a combination of ALADIN and AROME) is one of the three canonical model configurations of the ALADIN System (Aire Limitée Adaptation Dynamique Développement International), which is a limited area numerical weather prediction system developed by the international ALADIN consortium (Termonia et al. [2018]). ALARO is suitable for a wide range of horizontal mesh resolutions.

The dynamical core is spectral. Both non-hydrostatic and hydrostatic versions are available. The numerical scheme is a two-time level semi-implicit semi-Lagrangian. This choice allows for using long time steps. The model domain is projected onto a map. Multiple projections are possible. The Lambert conformal conic (LCC) map projection provides the lowest distortion in mid-latitudes (Batka [2002]). Moreover, the Mercator and polar stereographic projections are available. The vertical coordinate is of the η -type described in Laprise [1992] for the non-hydrostatic case, an analogue of the η -coordinate used in the hydrostatic case following Simmons and Burridge [1981].

After quantities are advected in dynamics, physics computations take place. Used parameterizations are listed in Table 4.1.

Turbulence is parameterized using the TOUCANS scheme. TOUCANS use a third-order closure and two prognostic turbulent kinetic energies (Ďurán et al. [2018]).

Radiation is computed using the ACRANEB2 scheme (Mašek et al. [2016]). It uses one interval for the shortwave radiation, which means that wavelengths of incoming solar radiation are not divided into bins like in, e.g., RRTMG. The parameterization of long-wave radiation also uses only one broadband. It uses the net exchange rate decomposition with bracketing, which evaluates the gaseous optical saturation based on the exchange rate between layers rather than the emissions and absorptions per emitter (Geleyn et al. [2017]). The advantage of this approach is that it allows for splitting the computation of the interaction with cloudiness and gas transmissions. Therefore, it allows for selective intermittency, which means that the interaction with cloudiness is computed in every time step. In contrast, the computationally expensive computations of gas transmissions are computed only in selected time steps.

The gravity wave drag parameterization follows Catry et al. [2008]. However, it might not be used with finer resolutions and better topography databases.

Parameterizations relevant to cloud and precipitation microphysics are described in the following sections.

Table 4.1: ALARO parameterizations, according to Termonia et al. [2018].

parameterization	scheme	references
turbulence & shallow convection	TOUCANS	Řurán et al. [2018]
radiation	ACRANEB2	Mašek et al. [2016], Geleyn et al. [2017]
deep convection	3MT	Gerard et al. [2009]
surface	ISBA	Noilhan and Planton [1989]

4.2 Dynamics-physics interface

The dynamics-physics interface is mass-weighted and flux-conservative using the Gauss-Ostrogradsky theorem described in Catry et al. [2007]. This approach benefits from the additivity of fluxes. There are six tenets taken into account as simplifying hypotheses (Catry et al. [2007]):

1. The atmosphere is permanently in the thermodynamic equilibrium.
2. The volume of all hydrometeors is assumed zero; thus, they have infinite density and are incompressible.
3. Both prognostic gases present in the model, dry air and water vapour, obey Boyle–Mariotte law and Dalton’s law.
4. All specific heat values are independent of temperature.
5. All hydrometeor species in one grid box have the same temperature. This includes falling precipitation, of which temperature may differ in reality. However, the accuracy is sufficient and the computation time is reduced.
6. Mass loss due to falling precipitation does not have to be compensated by a fictitious upward flux of dry air. However, it was experimentally verified that the distinction between runs with and without such compensation is minimal, even in extreme events. Thus, this compensation is used in the operational model configuration since it does not require modifications of the continuity equation in model’s dynamical core.

Microphysics is computed in one vertical column starting at the uppermost level of the model. It is assumed that there are no fluxes from the sides of grid boxes in all physics parameterizations as the horizontal scales of the size of grid boxes noticeably surpass the vertical scale. Thus, hydrometeors can be horizontally advected to another grid box only in the computation of dynamics, which precedes the computation of physics.

Without loss of generality, all phase changes are computed such that the original phase is firstly converted to water vapour and then to the final phase. This path is thermodynamically equivalent to the direct one and allows for elegant code.

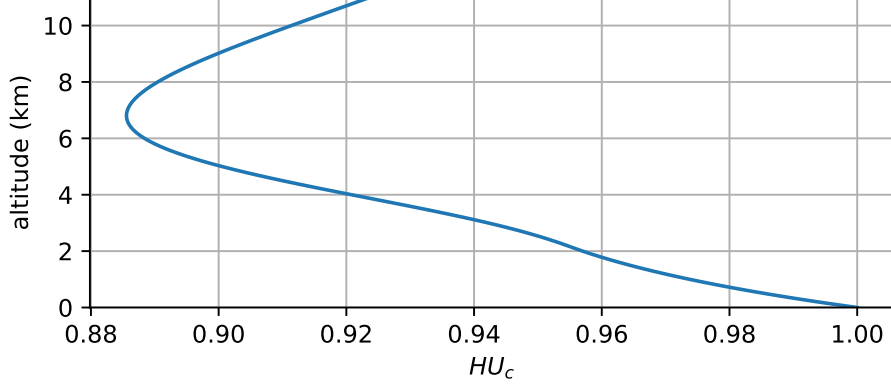


Figure 4.1: Vertical dependence of HU_c used in microphysics in the standard atmosphere for a horizontal resolution of 2.325 km.

4.3 Cloud scheme

Cloud schemes drive the amount of grid-scale cloudiness. In nature, condensation occurs at relative humidity close to 1 (usually slightly higher). However, the model grid is too coarse to capture small nuances in the humidity field; thus, the relative humidity within a grid box cannot be assumed homogeneous. Therefore, the concept of critical relative humidity is introduced. The critical relative humidity is the value of relative humidity above which condensation occurs.

There are multiple proposals for cloud schemes. The simplest one is the all-or-nothing scheme. However, such a scheme is suitable only for very fine resolutions (e.g., LES models). In NWP, there are two main categories: the statistic and relative humidity cloud schemes (Machulskaya [2015]). The statistic ones have a prescribed probability density function (PDF) of $q_l + q_i$. Some schemes modify parameters of the PDF due to the sub-grid variance of the mass of condensates due to turbulence, convection, or microphysics (e.g., Tompkins [2002] or Chaboureaud and Bechtold [2002]). The relative humidity schemes are based on the assumption of the critical relative humidity above which condensation occurs without considering the statistical distribution of condensates. However, the distinction between these schemes is very fine since many statistical schemes can be formulated as relative humidity ones and vice versa (Tompkins [2002]). Moreover, statistical schemes also benefit from the concept of critical relative humidity.

The cloud scheme used in ALARO is based on the work of Xu and Randall [1996] with some simplifications. This scheme is a relative humidity one. However, it can also be formulated as a statistical one with an unknown probability density function (Tompkins [2002]). The resolved cloudiness is calculated as (Geleyn et al. [2008a])

$$C = \left(\frac{q_v}{q_w}\right)^r \left[1 - \exp\left(-\alpha \frac{q_c}{(q_w - q_v)^\delta}\right)\right] \approx \left(\frac{q_v}{q_w}\right)^r \frac{\alpha q_c}{\alpha q_c (q_w - q_v)^\delta}, \quad (4.1)$$

where $q_c = q_l + q_i$ and q_w is the equilibrium water content in the case of the exact saturation, which differs from q_v^{sat} by assuming the effects of condensation or evaporation on the environment through latent heat release or storage (Geleyn

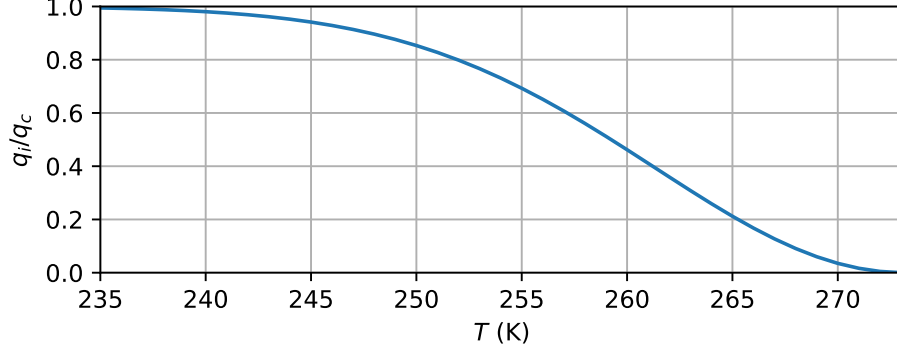


Figure 4.2: Temperature dependence of $(q_i/q_c)_{cond}$.

et al. [2008a]). Values taken from Xu and Randall [1996] are $r = 0.25$ and $\alpha = 0.5$ (rounded from 0.49). Finally, δ is a tunable parameter of the order of 100. Moreover, the following equations must be fulfilled:

$$q_v = q_w [HU_c (1 - N) + N] \quad (4.2)$$

$$q_c = q_t - q_v, \quad (4.3)$$

where q_t is the total water content, and HU_c is the critical relative humidity. The profile of the critical relative humidity is height and resolution-dependent. The vertical dependence of HU_c is shown in Figure 4.1. The critical relative humidity is always assumed with respect to liquid water.

The ratio of the ice condensate specific content to the total condensate specific content follows

$$\left(\frac{q_i}{q_c}\right)_{cond} = 1 - \exp\left(-\frac{(T_t - T)^2}{2(T_t - T_x)^2}\right), \quad T < T_t, \quad (4.4)$$

where $q_c = q_i + q_l$ and T_x is the temperature of the maximum difference between the saturation vapor pressures with respect to ice and liquid water, respectively (Gerard et al. [2009]). The shape of this function ensures enough supercooled liquid water.

4.4 Microphysics scheme

4.4.1 Parameterization of microphysical processes

The microphysics scheme in ALARO is based on the work of Lopez [2002] with many modifications. A single-moment microphysics scheme is used. In the original ALARO microphysics scheme, which is described in this subsection, four hydrometeors are predicted prognostically, the specific content of graupel is obtained diagnostically. Extension for prognostic graupel is described in Subsection 4.4.2.

Both precipitating hydrometeor species are assumed to follow the negative exponential distribution. The modification of the intercept parameter proposed by Abel and Boutle [2012] is used for rain.

The fall speed relation for rain is

$$w_r(D) = 654.5 \left(D \frac{\rho_0}{\rho_a} \right)^{0.7706}. \quad (4.5)$$

This expression is used to derive the average mass-weighted fall speed relation, which the model internally uses. Its derivation can be found in Appendix A.1. The fall speed relation for snow is not derived from a unique fall speed relation, but it is based on the ratio between the rain and snow fall speed relation used in Lopez [2002]. Its value is 3.959 at the triple point of water. Also, the ratio of collection efficiencies of snow and rain and temperature dependencies of various microphysical processes are taken from Lopez [2002]. Since many similar coefficients for the temperature dependence of various processes are introduced in Lopez [2002], the average one having a value of $e^{0.0231(T-T_i)}$ is chosen (Geleyn et al. [2007]).

Specific contents of hydrometeors, denoted by q , are used instead of their mixing ratios. The complete set of prognostic equations is

$$\frac{dq_r}{dt} = +\Delta_{aco}^{l \rightarrow r} + \Delta_{col}^{l \rightarrow r} + \Delta_{col}^{i \rightarrow r} + \Delta_{melt}^{s \rightarrow r} - \Delta_{eva}^{r \rightarrow v} - \Delta_{fre}^{r \rightarrow s} \quad (4.6a)$$

$$\frac{dq_s}{dt} = +\Delta_{aco}^{i \rightarrow s} + \Delta_{aco}^{l \rightarrow s} + \Delta_{col}^{l \rightarrow s} + \Delta_{col}^{i \rightarrow s} - \Delta_{melt}^{s \rightarrow r} - \Delta_{eva}^{s \rightarrow v} + \Delta_{fre}^{r \rightarrow s} \quad (4.6b)$$

$$\frac{dq_l}{dt} = -\Delta_{aco}^{l \rightarrow r} - \Delta_{aco}^{l \rightarrow s} - \Delta_{col}^{l \rightarrow r} - \Delta_{col}^{l \rightarrow s} + \Delta_{cond}^{v \rightarrow l} \quad (4.6c)$$

$$\frac{dq_i}{dt} = -\Delta_{aco}^{i \rightarrow s} - \Delta_{col}^{i \rightarrow r} - \Delta_{col}^{i \rightarrow s} + \Delta_{cond}^{v \rightarrow i} \quad (4.6d)$$

$$\frac{dq_v}{dt} = +\Delta_{eva}^{s \rightarrow v} + \Delta_{eva}^{r \rightarrow v} - \Delta_{cond}^{v \rightarrow l} - \Delta_{cond}^{v \rightarrow i}. \quad (4.6e)$$

Autoconversion follows Sundqvist [1978] for both autoconversion from cloud water to rain and from cloud ice to snow, written as

$$\left(\frac{dq_{l/i}}{dt} \right)_{aco} = -k_{r/s}(T) q_{l/i} \left\{ 1 - \exp \left[-\frac{\pi}{4} \left(\frac{q_{l/i}}{q_{l/i}^{crit}(T)} \right)^2 \right] \right\}. \quad (4.7)$$

Unlike k_r , k_s is dependent on temperature; for lower temperatures it is less efficient with the above-mentioned functional dependence $e^{0.0231(T-T_i)}$.

One unusual term is the autoconversion from cloud water to snow in the presence of cloud ice, which is not present in other schemes mentioned above. This autoconversion represents the Wegener-Bergeron-Findeisen (WBF) process and is parameterized as

$$\left(\frac{dq_l}{dt} \right)_{WBF} = -k_s F_{WBF}^a q_l \frac{q_l q_i}{(q_l + q_i)^2} \left\{ 1 - \exp \left[-\frac{\pi}{4} \left(\frac{q_l q_i}{q_l^{crit} q_i^{crit}(T) (F_{WBF}^b)^2} \right) \right] \right\}, \quad (4.8)$$

where F_{WBF}^a and F_{WBF}^b are tuning parameters with recommended values of $F_{WBF}^a = 300$ and $F_{WBF}^b = 4$ (Geleyn et al. [2007]).

Collection occurs only between a precipitating particle and a cloud particle. It always leads to the growth of the precipitating category, and the precipitating particle never changes its category; it means that no three-particle processes are considered. Thus, all precipitating particles collect both cloud ice and cloud water.

The formula for the collection rate is derived from the continuous collection equation. Its final shape of the equation for collection is

$$\frac{dq_r}{dt} = C_E^r E_r \mathcal{R}^{\frac{4}{5}} q_l, \quad (4.9)$$

where C_E^r is a constant consisting of multiple quantities. The complete derivation of Equation (4.9) is given in Appendix A.2. Collection efficiencies are taken from Lopez [2002]. They are the same for cloud water and cloud ice, except that the collection efficiency of cloud ice is temperature dependent with the abovementioned dependency. For rain is used $E_r = 0.2$, and $E_s = 0.1$ for snow.

The current evaporation parameterization is of the Kessler type. This parameterization was derived for cloud drops only. Consequently, coefficients for different kinds of hydrometeors must be determined. Two main processes come under consideration. A less dense particle is more extensively evaporated since the ratio of the area to the volume of the particle is higher than for denser particles. Contrarily, such a particle also falls slower, so its ventilation is less. Because these processes are assumed to cancel each other out, the coefficients of the Kessler-type evaporation parameterization of rain and snow are equal in ALARO except for the consideration of the ratio between the specific latent heat of sublimation to the specific latent heat of evaporation, which lowers the sublimation rates for ice hydrometeors (Geleyn et al. [2011]). The final equation describing evaporation and sublimation in the flux form is written as

$$\frac{d\sqrt{\mathcal{R}}}{d(1/p)} = E_{vap}(q_w - q), \quad E_{vap} = 4.8 \cdot 10^6. \quad (4.10)$$

The full derivation of Equation (4.10) can be found in Appendix A.3.

The Kessler-type parameterization of melting (and freezing) is very similar to the parameterization of evaporation. However, the ratio of the specific heat of melting to the heat capacity of water must be considered. The final equation yields

$$\frac{dm_i}{d(1/p)} = \frac{F_{ont}}{\sqrt{R}} (T_t - T), \quad F_{ont} = 2.4 \cdot 10^4, \quad (4.11)$$

where m_i is the fraction of ice precipitation. Its derivation in Appendix A.4.

Finally, the description of diagnostic graupel and its effects follows. Diagnostic graupel is a subcategory of snow, and its amount is described by the ratio of the precipitation flux of diagnostic graupel to the total snow precipitation flux, denoted by \widetilde{r}_g . Diagnostic graupel is produced exclusively via the WBF process described by Equation (4.8). Its fall speed relation is that of rain (Catry [2007]). The influence on the fall speed of snow (the fall speed of snow and rain are considered at the same precipitation flux) is (Catry [2007]):

$$\frac{w_r}{w_{s+g}} = \widetilde{r}_g + (1 - \widetilde{r}_g) \frac{w_r}{w_s}, \quad (4.12)$$

where w_{s+g} is later used as the fall speed of snow. Similarly, the collection efficiency of diagnostic graupel is assumed to be the same as of rain. Thus, the collection efficiency of snow with diagnostic graupel is modified to

$$\frac{E_r}{E_{s+g}} = \widetilde{r}_g + (1 - \widetilde{r}_g) \frac{E_r}{E_{s+g}}. \quad (4.13)$$

After the collection computation, \widetilde{r}_g is modified to (Catry [2007])

$$\widetilde{r}_g' = \frac{\widetilde{r}_g}{\widetilde{r}_g + (1 - \widetilde{r}_g) (E_{ff}^s / E_r)}, \quad (4.14)$$

because diagnostic graupel collects less than snow since its fall speed is higher. The effect of diagnostic graupel diminish after the computation of evaporation and sublimation.

4.4.2 Extension for prognostic graupel

Recently, prognostic graupel was added to the microphysics scheme in ALARO. Graupel is produced by the freezing of rain and by autoconversion of cloud water in the presence of cloud ice, mimicking the WBF process. The WBF process leads to snow production in the case without prognostic graupel, but no snow is produced by the WBF process when prognostic graupel is used. Graupel can collect cloud ice and cloud water and its sink terms are sublimation and melting.

Thus, the prognostic equation for graupel is

$$\frac{dq_g}{dt} = +\Delta_{aco}^{l \rightarrow g} + \Delta_{col}^{l \rightarrow g} + \Delta_{col}^{i \rightarrow g} - \Delta_{melt}^{g \rightarrow r} - \Delta_{eva}^{g \rightarrow v} + \Delta_{fre}^{r \rightarrow g}. \quad (4.15)$$

As a consequence, prognostic equations for other water species are modified to

$$\frac{dq_r}{dt} = +\Delta_{aco}^{l \rightarrow r} + \Delta_{col}^{l \rightarrow r} + \Delta_{col}^{i \rightarrow r} + \Delta_{melt}^{s \rightarrow r} + \Delta_{melt}^{g \rightarrow r} - \Delta_{eva}^{r \rightarrow v} - \Delta_{fre}^{r \rightarrow g} \quad (4.16a)$$

$$\frac{dq_s}{dt} = +\Delta_{aco}^{i \rightarrow s} + \Delta_{col}^{l \rightarrow s} + \Delta_{col}^{i \rightarrow s} - \Delta_{melt}^{s \rightarrow r} - \Delta_{eva}^{s \rightarrow v} \quad (4.16b)$$

$$\frac{dq_l}{dt} = -\Delta_{aco}^{l \rightarrow r} - \Delta_{aco}^{l \rightarrow g} - \Delta_{col}^{l \rightarrow r} - \Delta_{col}^{l \rightarrow s} - \Delta_{col}^{l \rightarrow g} + \Delta_{cond}^{v \rightarrow l} \quad (4.16c)$$

$$\frac{dq_i}{dt} = -\Delta_{aco}^{i \rightarrow s} - \Delta_{col}^{i \rightarrow r} - \Delta_{col}^{i \rightarrow s} - \Delta_{col}^{i \rightarrow g} + \Delta_{cond}^{v \rightarrow i} \quad (4.16d)$$

$$\frac{dq_v}{dt} = +\Delta_{eva}^{g \rightarrow v} + \Delta_{eva}^{s \rightarrow v} + \Delta_{eva}^{r \rightarrow v} - \Delta_{cond}^{v \rightarrow l} - \Delta_{cond}^{v \rightarrow i}, \quad (4.16e)$$

where the new terms are marked in blue.

The parameterization of microphysical processes keeps the idea used for the diagnostic graupel. Thus, the graupel mechanical properties (fall speed and collection efficiency) are that of rain, and the thermodynamic properties (melting and sublimation) of graupel are that of snow.

4.4.3 Computation of sedimentation

A vital part of any microphysics scheme is the computation of sedimentation. ALARO uses a statistical sedimentation scheme (Geleyn et al. [2008b]). This

scheme is unconditionally stable, so it permits using a wide range of inverse Courant numbers $Z \ll 1$, thus avoiding the time step restriction given by the CFL condition. The essence of this scheme are the three probability functions P_1 , P_2 , and P_3 . The probability function P_1 denotes the probability that drops are inside the layer at the beginning of the time step. Probability P_2 is used for drops coming from the layer above. Finally, P_3 is the probability of drops being created or destructed within the layer during the time step. Thus, the flux at the bottom of the layer \mathcal{R}_{bot} is obtained from

$$\mathcal{R}_{bot} = q_r \frac{\delta p}{g \delta t} P_1 + \mathcal{R}_{top} P_2 + (\Delta_{aco} - \Delta_{evap}) \frac{\delta p}{g \delta t} P_3, \quad (4.17)$$

where $\frac{\delta p}{g \delta t}$ is the transformation term from specific contents to fluxes, and \mathcal{R}_{top} is the precipitation flux at the top of the layer.

The probability functions are defined as (Geleyn et al. [2008b]):

$$P_0(z, t) = e^{-\frac{\delta z}{\bar{w} \delta t}} \quad (4.18)$$

$$P_1(\delta z, \delta t) = \frac{1}{\delta z} \int_0^{\delta z} P_0(z, \delta t) dz = \frac{\bar{w} \delta t}{\delta z} \left(1 - e^{-\frac{\delta z}{\bar{w} \delta t}}\right) \quad (4.19)$$

$$P_2'(\delta z, \delta t) = \frac{1}{\delta t} \int_0^{\delta t} P_0(\delta z, t) dt = \frac{1}{\delta t} \int_0^{\delta t} e^{-\frac{\delta z}{\bar{w} \delta t}} dt = E_2(Z) \approx \frac{P_0(Z)}{Z + 1 + X} \quad (4.20)$$

$$\begin{aligned} P_3(\delta z, \delta t) &= \frac{1}{\delta z \delta t} \int_0^{\delta z} \int_0^{\delta t} P_0(\delta z, \delta t) dt dz = \frac{1}{\delta z} \int_0^{\delta z} E_2\left(\frac{z}{\bar{w} \delta t}\right) dz \\ &= \frac{1}{Z} [1 - E_3(Z)] = \frac{1}{2} [E_2(Z) + P_1(Z)] = \frac{1}{2} [P_2'(Z) + P_1(Z)] \end{aligned} \quad (4.21)$$

$$P_2 = P_2' + \frac{(1 - P_2') P_3}{1 + P_3}, \quad (4.22)$$

where

$$X = \frac{\sqrt{(1 + Z)^2 + 4Z} - (1 + Z)}{2}.$$

Although the scheme is unconditionally stable, it is crucial to deliver physically correct results. Suitable values of Z can be derived from the equation for the stationary case, which is written as

$$(\Delta_{aco} - \Delta_{evap}) \frac{\delta p}{g \delta t} = \mathcal{R}_{bot} - \mathcal{R}_{top}. \quad (4.23)$$

Substituting this equation into Equation 4.17 yields

$$\mathcal{R}_{bot} (1 - P_3) = q_r \frac{\delta p}{g \delta t} P_1 + \mathcal{R}_{top} (P_2 - P_3). \quad (4.24)$$

This provides physically correct solutions only for $(P_2 - P_3) \geq 0$; otherwise, decreasing of \mathcal{R}_{top} leads to raising \mathcal{R}_{bot} . For this case, $Z \leq 0.96$ is required to fulfill this constraint (Geleyn et al. [2008b]).

4.5 Cloud and precipitation geometry

Since the distribution of condensates within a grid box is uneven, a specific cloud and precipitation geometry, which divides every grid box into four parts, is implemented. Its introduction is further motivated by convection, which deliver even more inhomogenities into gridbox. However, this aproach can be used regardless the moist deep convection scheme is active or not.

For each of these four parts, the precipitation flux densities are computed for every precipitating hydrometeor separately. The respective precipitation flux densities are denoted by

1. F_{SO} for the seeded cloudy part,
2. F_{RO} for the non-seeded cloudy part,
3. F_{SE} for the seeded clear sky part,
4. F_{RE} for the non-seeded clear sky part.

Precipitation flux densities in all four geometric areas are computed, since all parts, even the non-seeded ones, can contain precipitation from the previous time step. Areas are denoted by C for the cloudy part (consequently $(1 - C)$ for the clear sky part), α for the seeded clear sky part ($1 - \alpha$ for the non-seeded clear sky part), β for the seeded part of C , and $1 - \beta$ for the non-seeded part of the cloudy part (see Figure 4.3). In other words, area C represents cloudiness; that is, the total cloud fraction, which are merged the stratiform and convective cloud fractions if the most deep convection parameterization is active. Microphysics then performs only one computation on the resulting cloud fraction. Thus, also the cloud geometry computation does not distinguish between them. The saturation deficit is concentrated only in the clear sky part.

The total precipitation flux of particle j is given by

$$\mathcal{R}_j = (1 - C)(1 - \alpha)F_{RE} + (1 - C)\alpha F_{SE} + C(1 - \beta)F_{RO} + C\beta F_{SO}. \quad (4.25)$$

In the following, variables with an asterisk are considered at the top of the current layer, and variables without an asterisk are considered at the bottom of the layer (at the top of the layer below). No changes in precipitation flux due to microphysical processes are considered on the interface of these layers. Thus, all changes in the specific contents of hydrometeors are done within the layer.

The cloud overlap is usually maximal or random. The maximal cloud overlap denotes when clouds in two consecutive layers share as much area as possible. The random overlap means that the positions of the clouds in two consecutive layers are uncorrelated. The maximal-random overlap is often used when clouds in two consecutive layers are overlapped maximally. At the same time, if at least one layer is without clouds between two layers containing clouds, then random overlap is used.

However, based on observations, the assumption of the maximal overlap is not often observed (Tompkins and Giuseppe [2015]). The first approach in ALARO to deliver more randomness was the epsilon-maximal-random overlap (Van den Bergh et al. [2011]). Later, this approach was extended to account for seasonal variations of sun angle as used in radiation.

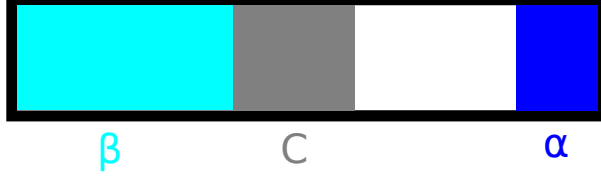


Figure 4.3: Cloud and precipitation geometry. Symbols are explained in the main text.

Firstly, the decorrelation depth is given by

$$\varepsilon = \exp\left(\frac{p^* - p}{\psi}\right). \quad (4.26)$$

where ψ is the decorrelation parameter, which is the atmosphere's depth for computing the overlap's randomness coefficient. Its value can be prescribed or computed according to the seasonal variations of the maximum sun elevation to capture different cloud regimes in winter and summer. In the case of maximum-random overlap, $\varepsilon = 1$ ($\psi \rightarrow \infty$), and $\varepsilon = 0$ ($\psi \rightarrow -\infty$) in the case of random overlap. Therefore, εC overlaps maximally and $(1 - \varepsilon)C$ overlaps randomly with C^* .

The two seeded geometric areas α and β , where α is the seeded part of the clear sky part, and β is the seeded part of the cloudy part, are given by

$$\begin{aligned} \alpha &= \frac{[\max(\varepsilon C, C^*) - \varepsilon C] + \alpha^* [1 - \max(\varepsilon C, C^*)]}{1 - \varepsilon C}, \\ \beta &= \frac{C(1 - \varepsilon) [C^* + \alpha^* (C - C^*)] + [\min(\varepsilon C, C^*) (1 - \alpha^*) + \alpha^* C] (1 - C)}{C (1 - \varepsilon C)}. \end{aligned} \quad (4.27)$$

Specific hydrometeors are not distinguished in the following text as the computation is separately performed on each of them in the same manner. After the estimation of α and β , the precipitation flux densities for the four geometric parts are computed in the following order. Firstly, the precipitation flux densities for each hydrometeor species in the non-seeded clear sky are recomputed as

$$F_{RE} = F_{RE}^* = \mathcal{R}_{bot} - \frac{\delta p}{g \cdot \delta t} P_3 (\Delta_{evap} + \Delta_{melt}), \quad (4.28)$$

where the multiplication by $\delta p / (g \cdot \delta t)$ again ensures correct units when it transforms fluxes to specific contents.

Secondly, for the seeded areas, the precipitation flux density is updated to

$$F_{SO} + F_{SE} = R^* - (1 - C^*) (1 - \alpha^*) F_{RE}^* = (1 - C^*) \alpha^* F_{SE}^* + C^* F_{SO}^*. \quad (4.29)$$

It is assumed that new precipitation is created only in the cloudy part, and the precipitation from above is mixed in the cloudy part. Consequently, homogeneous precipitation is produced in the cloudy part at the bottom of the layer (Van den Bergh et al. [2011]). Therefore, $\beta^* = 1$ and consequently $C^* (1 - \beta^*) F_{RO}^* = 0$.

After that, two options are considered. One of them is chosen based on a simple test $\mathcal{Z} = \mathcal{H}(\varepsilon C - C^*)$. If $\mathcal{Z} = 1$ ($\varepsilon C > C^*$), then $\alpha = \alpha^*$ because the

precipitation coming from the cloudy part does not seed the clear sky part, since the maximally overlapped part of C (εC) is greater than C^* . The precipitation flux density from the clear sky part is distributed randomly between the increment of the cloudy part and the clear sky part. Therefore, the seeded fraction of the clear sky part F_{RE} remains unchanged, which yields

$$\begin{aligned} F_{SO} &= \frac{\alpha(1 - C^*) - \alpha(1 - C)}{\beta C} F_{SE}^* + \frac{C^*}{\beta C} F_{SO}^* = \frac{\alpha(C - C^*)}{\beta C} F_{SE}^* + \frac{C^*}{\beta C} F_{SO}^*, \\ F_{SE} &= F_{SE}^*. \end{aligned} \quad (4.30)$$

If $\mathcal{Z} = 0$ ($\varepsilon C < C^*$), then F_{SO} is obtained from

$$\begin{aligned} F_{SO} &= \frac{\alpha^*(1 - \varepsilon)(1 - C^*) F_{SE}^* + [\varepsilon(1 - C) + (1 - \varepsilon)C^*] F_{SO}^*}{(1 - \varepsilon)[C^* + \alpha^*(C - C^*)] + (1 - C)[\varepsilon C(1 - \alpha^*) + \alpha^*C] \frac{1}{C}} = \\ &= \frac{\alpha^*(1 - \varepsilon)(1 - C^*)}{\beta(1 - \varepsilon C)} F_{SE}^* + \frac{\varepsilon(1 - C) + (1 - \varepsilon)C^*}{\beta(1 - \varepsilon C)} F_{SO}^*, \end{aligned} \quad (4.31)$$

and F_{SE} is given by

$$\begin{aligned} F_{SE} &= \frac{\alpha^*(1 - C^*) F_{SE}^* + C^* F_{SO}^* - \beta C F_{SO}}{\alpha(1 - C)} = \\ &= \frac{\alpha^*(1 - C^*)}{\alpha(1 - \varepsilon C)} F_{SE}^* + \frac{C^* - \varepsilon C}{\alpha(1 - \varepsilon C)} F_{SO}^*. \end{aligned} \quad (4.32)$$

After all precipitation evaporates in the seeded clear-sky part, the extent of this part is set to zero, $\alpha = 0$. Consequently, the non-seeded part is stretched and F_{RE} must be recomputed as

$$F_{RE} = F_{RE}(1 - \alpha) \quad (4.33)$$

to protect against artificial precipitation.

Cloud geometry has quite a significant feedback in microphysics. For example, evaporation cannot occur in the cloudy part since the environment is saturated. Consequently, values of ε influence evaporation rates. The bigger the decorrelation, the higher evaporation rates can occur since drops fall more likely into clear-sky parts, making these parts more humid.

Due to the specific cloud and precipitation geometry, autoconversion is computed only in the cloudy part and is called only once. The collection parameterization is called twice, separately for the seeded cloudy part and for the non-seeded cloudy part. Finally, evaporation and melting are grouped in one routine, called three times. Firstly, for the seeded clear-sky part, secondly, for the non-seeded clear-sky part, and finally, for the cloudy part, where is computed only melting.

4.6 3MT cascade

The Modular Multi-scale Microphysics and Transport (3MT) scheme (Gerard et al. [2009]) is the moist deep convection parameterization used in ALARO. The 3MT scheme is specially designed for the so-called grey zone of moist deep

convection when moist deep convection is partially resolved; that is, for horizontal resolutions ranging approximately from 1 to 10 km, the borderline is not well-marked (Gerard [2015]). Models with such resolutions are called convection-permitting models. The 3MT scheme is highly prognostic and unique in that the microphysics scheme is called only once, using the sum of condensates from the cloud scheme and the convection scheme. Consequently, the difference between the convective and resolved part of precipitation diminishes in microphysics. Another uniqueness is that downdraughts can be in a grid box without updraughts. This is favored by many observations, as downdraughts can be produced far from updraughts.

It is necessary to call parts of the parameterization sequentially for satisfactory performance of such a prognostic scheme, hence the name cascade. This sequential approach protects against double counting of physical processes. In the following, it is assumed that the necessary condition for triggering the moist deep convection scheme based on the moisture convergence is fulfilled. After the saturation adjustment computed by the cloud scheme, the 3MT cascade consists of (Gerard et al. [2009]):

1. *Updraught calculations* which compute vertical fluxes of convective condensation and transport. Variables T , q_v , q_l , and q_i of the cascade are updated. Moreover, the updraught velocity and updraught mesh fraction are computed. The detrainment fraction is computed diagnostically. The convective cloudiness covers the updraught mesh fraction and the detrainment fraction.
2. *Call of microphysics*. The sum of the convective and resolved condensation fluxes is used on input. The total precipitation flux, pseudo-fluxes (flux-dimensioned vertical integrals of rates of microphysical processes like autoconversion or evaporation (Brožková [2007])), and fall speeds of particles are ones of the outputs.
3. *Update after microphysics*, where contributions from microphysics to 3MT are calculated; thus, T , q_v , q_l and q_i are updated again and q_r , q_s and q_g are also updated. In addition, the contribution of evaporation to the saturation deficit and corrections of the precipitation flux and temperature are computed. Moreover, the temperature sink due to the evaporation of precipitation is computed for the downdraught closure, which allows for triggering the downdraught calculations.
4. *Downdraught calculations*, where the computation of convective transport fluxes is based on the prognostically computed downdraught velocity and downdraught mesh fraction. Also, additional evaporation of precipitation in downdraught is computed.
5. *Update after downdraught*, where precipitation fluxes due to additional evaporation in downdraught, water species of the cascade, temperature, and transport fluxes are updated.

Thus, updraught calculations contribute only to the condensation to cloud particles, while microphysics and downdraught calculations update specific contents of falling species.

The condensates from the convective part must be protected against evaporation in the saturation adjustment; otherwise, the condensates from 3MT could be evaporated in the saturation adjustment as the cloud scheme assumes a different distribution of water within the grid box.

5. Model configuration, selected cases, and methods

5.1 Model configuration

All experiments were performed using the operational ALADIN model configuration at the Czech Hydrometeorological Institute (CHMI). The model configuration is described in Brožková et al. [2019] with several recent modifications.

The domain is shown in Figure 5.1 and consists of 1080x864 points in the horizontal (extension and coupling zones included) with 87 vertical levels. The domain is projected onto the Lambert conformal conic map projection. The horizontal grid resolution is 2.325 km in the map projection. Despite the relatively fine horizontal resolution, the moist deep convection scheme 3MT is active. The gravity wave drag parameterization is not used as the level of sub-grid details from the topography database Ecoclimap 2 allows to determine sub-grid scale topography characteristics.

The lateral boundary conditions are provided by the global model ARPEGE and they are updated every three hours with quadratic time interpolation in between.

5.2 Periods used for experiments

Several periods are used to test parameters and modifications of the microphysics scheme. It is important to deliver good results in all seasons. Therefore, multiple ten days periods and a few more selected cases are used for tests.

5.2.1 Severe convection in June 2021

This period lasts from 2021-06-21 to 2021-06-30 and can be characterized by a flat low over Central Europe with a distinct temperature gradient between warmer Eastern Europe and colder Western Europe. Thus, combined with enough humidity at lower atmospheric levels, several severe storms occurred over Czechia. In the first four days of this period, mainly mesoscale convective systems and supercells occurred. Between 2021-06-25 and 2021-06-27, storms were relatively weak, single-cell. A shallow cyclone appeared over France and influenced weather over Central Europe during the last three days of this period delivering squall-lines over Czechia on the nights of June 28-29 and 29-30. Before running all these experiments for full three days integrations all days, a shorter 24-hour integration starting at 00 UTC on 2021-06-29 is often tested to obtain a preview of the behaviour of the experiment. A severe mesoscale convective system (derecho) developed that day and crossed Czechia in the evening with wind gust $29.2 \text{ m} \cdot \text{s}^{-1}$ in Hradec Králové, rainfall 29.1 mm/0.5 hour in Kadov in Vysočina and hail up to 5 cm in diameter near Hranice (European Severe Storms Laboratory [2023]).

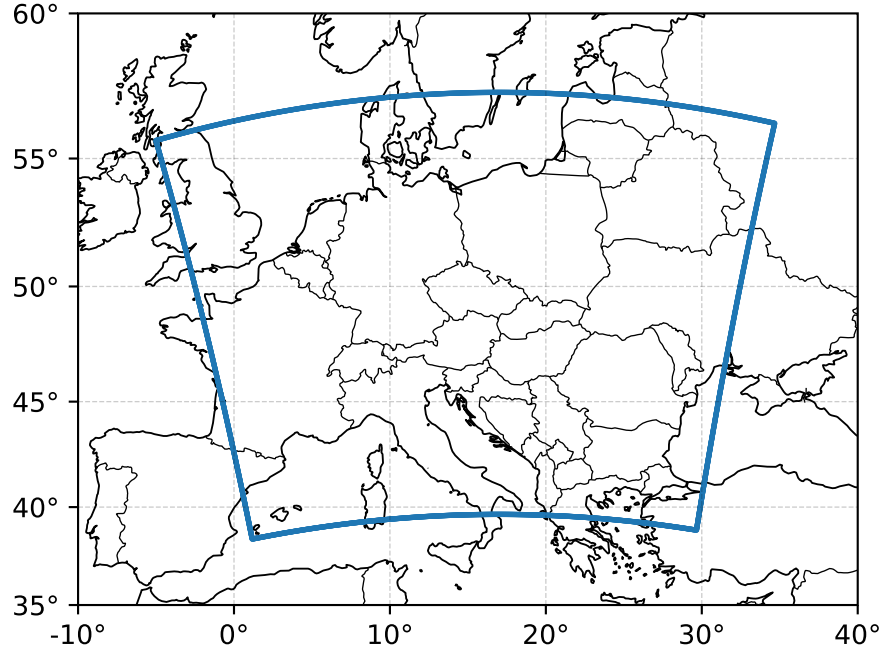


Figure 5.1: Model domain in projection CRS84.

5.2.2 Severe convection in June 2022

This period lasts from 2022-06-20 (or alternatively 2022-06-21) to 2022-06-30. The period starts with a storm on a cold front on 2022-06-20. A waving front influenced the weather regime for the next three days when on 2022-06-24, a mesoscale convective system occurred with rainfall 109,7 mm in Praha, Komořany (Stašová and Sedláková [2022]) that day and the rain continued overnight. A waving front slowly moving from Germany through Czechia to Poland dominated the weather for the rest of the period delivering severe storms on June 27th, 28th and 29th. This period was later extended until the 10th of June. This part of the period is characterized by an anticyclone westerly of the United Kingdom and France, whose ridge of high pressure influenced weather over Czechia in combination with a regenerating cyclone over Scandinavia, of which fronts crossed Czechia multiple times. Only weaker storms and showers appeared over Czechia except for the 1st of July, the last day of the period with severe convection, and the 5th of July. However, there was enough precipitation over the model domain to evaluate changes in microphysics.

5.2.3 Convection in June 2009

This period lasts from 2009-06-24 to 2009-07-04 and is exceptional because there was a shallow cyclone over the Mediterranean Sea and an anticyclone over Scandinavia for most of the period bringing eastern winds to Central Europe with relatively weak pressure gradients. Thus, with enough moisture in the lower troposphere, conditions were favorable for thermal convection. This period is helpful for evaluating the diurnal cycle of precipitation in convection because convection is not triggered by frontal forcing, unlike in the previous two periods.

5.2.4 Autumn stratocumulus period

The period between 2021-11-11 and 2021-11-20 is a good example of temperature inversion over Czechia with stratocumulus. The ALARO model suffers from overestimation of the precipitation accumulation in the case of drizzling stratocumulus. This period is suitable for testing approaches to overcome this shortcoming. Anticyclonic weather conditions persisted for most of the period; however, on 2021-11-13, a shallow cyclone in the dissipation stage crossed Czechia. Finally, a weaker cold front crossed Czechia on 2021-11-18.

5.2.5 Autumn/winter precipitating period

The period from 2021-11-25 to 2021-12-04 was chosen as a precipitating period for an autumn/winter case. Multiple cyclones crossed Central Europe and delivered both snow and rain precipitation to Czechia. Snowfall occurred in Prague on 2021-12-04.

5.2.6 Additional selected cases

Snowfall occurred in Austria on 2019-01-04. It can be a valuable case for validating the sublimation of solid hydrometeors since it is known that AROME underestimated the snow accumulation in Inntal valley and ALARO overestimated precipitation accumulations on the lee side of the Alps.

2022-12-12 is another useful day to validate snow precipitation. The operational run slightly overestimated the precipitation accumulation. In addition, the precipitation shadow behind the Ore Mountains, Krkonoše, and Hrubý Jeseník was too weak as too high precipitation accumulations were predicted in these areas.

5.3 Methods

5.3.1 DDH diagnostic

Diagnostics in Horizontal Domains, abbreviated as DDH (Joly et al. [2019]), is a valuable tool that diagnoses the contributions of processes to the total tendency of meteorological fields in every model layer to the final tendency of the quantity. The main budgets are for temperature (enthalpy) and water species. Abbreviations used in graphs are listed in Table 5.1.

5.3.2 Atmospheric scores

The evaluation of experiments on the atmospheric scores is based on their comparison with synoptic data and data from radiosondes (Janoušek and Mládek [2008]). The corners of the domain of verification in the Lambert projection are 40N,2E for the SW one, and 55.6N, 29E for the northeast one. There are three

Table 5.1: List of abbreviations used for contributors in graphs in the DDH diagnostics.

abbreviation	meaning
auto-cv	convective autoconversion
auto-rs	resolved autoconversion
condev	condensation in updraught
condrs	resolved condensation
conev-cv	convective condensation and evaporation
dynam	dynamics
evapcv	evaporation in downdraft
evaprs	resolved evaporation
micro	microphysics
neg	correction for negative values
prec-cv	convective precipitation
prec-rs	resolved precipitation
rad-sol	solar radiation
rad-ther	thermal radiation (Earth irradiation)
resid	residuals
(sum)tend	total tendency
turconv	vertical convective transport
turdiff	vertical turbulent transport

basic statistics methods used:

$$\text{BIAS} = \frac{1}{N} \sum_1^N (F_i - O_i), \quad (5.1)$$

$$\text{RMSE} = \sqrt{\frac{1}{N} \sum_1^N (F_i - O_i)^2}, \quad (5.2)$$

$$\text{STDE} = \sqrt{\sum_1^N (\text{RMSE}^2 - \text{BIAS}^2)}, \quad (5.3)$$

$$(5.4)$$

where N is the number of observations, F_i is the value from model and O_i is the observed value of a given quantity.

On top of that, the statistical significance of results is tested using a t-test with the null hypothesis such that the mean value of the differences in their statistics are equal to zero. The differences in their statistics are assumed to follow the Gaussian distribution in the limit for infinite samples (Student's distribution for discrete cases). Therefore, the necessary condition for using t-test is met. Three significance levels are considered, roughly 68 %, 95 %, and 99.73 %, corresponding to one, two, and three multiples of variance of the Gaussian distribution. BIAS is also evaluated as the difference of the BIAS of the run with proposed changes (experiment) and the BIAS of the reference run. To evaluate

which model configuration is closer to BIAS=0, also

$$|\text{BIAS}| = \frac{1}{N_{inits}} \left[\left| \sum_1^{N_{inits}} (\text{BIAS}_{i,new}) \right| - \left| \sum_1^{N_{inits}} (\text{BIAS}_{i,ref}) \right| \right], \quad (5.5)$$

where $\text{BIAS}_{i,new}$ and $\text{BIAS}_{i,ref}$ are the bias of the new experiment and the reference one, respectively, at one forecast range for one model initialization. Finally, it is averaged over all model initializations.

The term surface scores mean that the meteorological fields are evaluated at their typical height above the ground at synoptic meteorological stations. That is, temperature and relative humidity are measured at 2 m (thus, often abbreviated as T2m and RH2m), and wind at 10 m (often abbreviated as w10m for wind speed and wdir10m for wind direction). Geopotential is validated against such stations, of which measured pressure is reduced at the mean sea level, so the geopotential at the mean sea level is validated (Janoušek and Mládek [2008]).

As fewer radiosondes are released at 06 and 18 UTC than at 00 and 12 UTC, these terms are less reliable due to the lack of observations. Errors caused by this can be seen in plots as rhomboidal structures around a single level at 06 or 18 UTC.

5.3.3 Fraction skill score

The Fraction skill score (FSS) is a new method for the verification of precipitation following Roberts and Lean [2008]. Standard statistics like STDE and RMSE are prone to favour smoother precipitation fields over coarser ones, which might better capture the observed reality (Bučánek [2020]). This phenomenon is often called a double penalty, and its origin is that there are compared data point by point without considering the spatial distribution of precipitation. On the contrary, FSS evaluates results in square boxes of specific areas, of which lengths of their sides usually increase in powers of 2. At CHMI, observational data are provided by the MERGE product (Novák and Kyznarová [2016]), which combines the data from rain gauges and radar estimates of precipitation based on CAPPI 2km; that is, from the elevation of 2 km above mean sea level (Bučánek [2020]).

5.3.4 Other validation techniques

Besides the above-described methods, the model output provides an extensive set of meteorological fields that can be compared with model runs with different settings and observations. Precipitation can be validated against data from MERGE, which provides data over Czechia. MERGE can also be used to evaluate the diurnal cycle of precipitation and total precipitation accumulation. For the sake of it, precipitation accumulations are summed over the whole MERGE domain and compared with the summed simulated precipitation over the same domain. Especially, simulated radar reflectivities and brightness temperatures are valuable tools as they can be compared with satellites and range height indicator (RHI) radar measurements. In addition, plan position indicator (PPI) radar measurements were provided by the Radar department of CHMI for the storm on 2021-06-29. They also contain the Vaisalla hydroclass product, which

classifies hydrometeors into six classes using fuzzy logic. Moreover, vertical cross-sections through relevant fields deliver valuable information. Finally, it is also important to validate results subjectively on weather maps as then can reveal many characteristics not detected by the objective methods described above.

6. Enhancements of prognostic graupel

Recently, the transition from diagnostic to prognostic graupel in ALARO was prepared, which is the initial state of the microphysics scheme before modifications are introduced in this work. Its description provides Subection 6. The original approach to the parameterization of microphysical processes of graupel is based on the idea used for diagnostic graupel. It means that the graupel mechanical properties (fall speed and collection efficiency) are that of rain, and the thermodynamic properties (melting and sublimation) of graupel are that of snow. However, this approach is rare across microphysics schemes. Hence, one of this thesis aims is to collect information on the graupel parameterization in various microphysics schemes and, if convenient, introduce a more complex concept of the treatment of graupel. Proposed modifications of the set of parameters for graupel are introduced and tested in the following subsections.

6.1 Effects of prognostic graupel

Before modifying the set of parameters for prognostic graupel, it is convenient to compare the key differences between experiments with prognostic graupel (configuration denoted by **GRAU**) and without it (denoted by **NOGR**) to identify the main characteristics of the transition and find possible deficiencies of **GRAU** as it serves as the reference for further modifications of the parameterization of graupel.

After introducing prognostic graupel, the amount of snow is reduced. Also, the specific content of snow, q_s , reaches maxima higher in the atmosphere, as shown in Figure 6.1. Higher fall speed of graupel leads to slightly more solid precipitation reaching the ground when temperatures are slightly above the temperature of fusion. On top of that, there are four main differences between the model configuration with prognostic graupel and without it.

The first impact of prognostic graupel is that the atmosphere is less stable, as shown in the temperature budget for a summer convection case (Figure 6.2). There is a warm bias near the surface and a cold bias near the tropopause. The destabilization of the atmosphere is caused by less sublimation (included in evaporation) due to faster-falling graupel compared to snow. Also, the temperature budget reveals a significant difference in the split between contributions of convective condensation and evaporation (**conv-cv**) and microphysics (**micro**). The water vapour budget for the same day (Figure 6.3) shows that it is caused by different ratios of convective and resolved condensation. Finally, dynamics and convective transport modify the vertical distribution of water vapour as they compensate for the changes caused by prognostic graupel.

The second impact is that higher precipitation maxima on windward sides and over mountainous areas appeared. This pattern is observed mainly in winter and it is caused by the higher fall speed of graupel compared to snow and the consequent lack of time to sublimate. This pattern is more distinct over the Alps than over Czechia, where it is also present, but the tendency of precipitation accumulation maxima can vary.

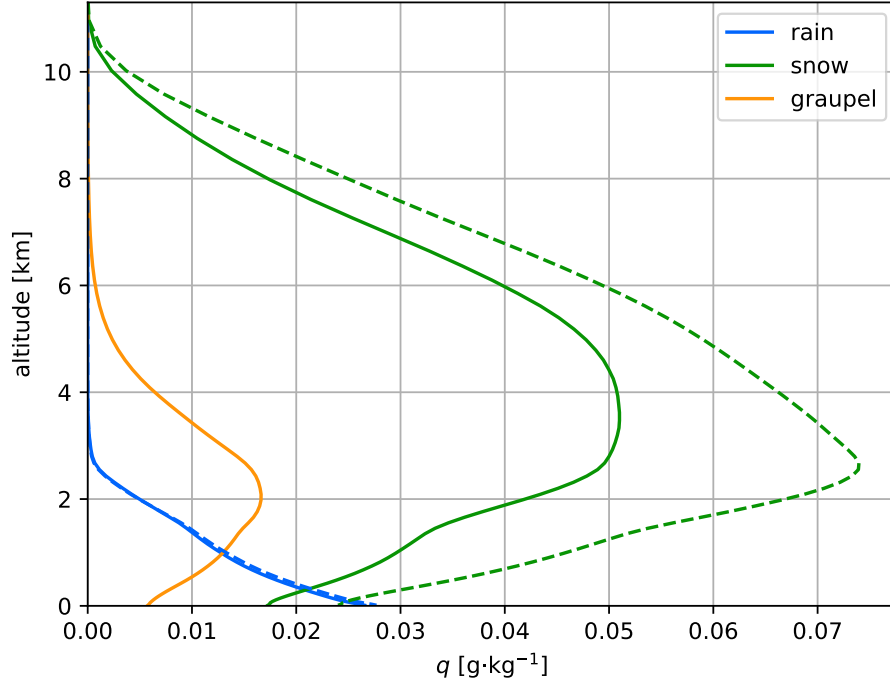


Figure 6.1: Vertical profiles of the specific content of hydrometeors for a winter case. The simulation without prognostic graupel is dashed.

The third difference is higher precipitation maxima observed in convective storms and showers. The higher precipitation maxima do not imply higher precipitation accumulations over the whole domain, which stay roughly the same or are even slightly reduced. One possible explanation for this phenomenon might be the higher fall speed of graupel. Due to consequently lessened sublimation, graupel can accumulate in a higher amount close to the melting layer, fall through it, and melt to rain. This can cause higher instantaneous precipitation flux than was simulated in the case without prognostic graupel on 2021-06-29 and 2022-06-24. However, the observed instantaneous fluxes are not unrealistically high. They are usually below $0.05 \text{ kg} \cdot \text{m}^{-2} \cdot \text{s}^{-1}$ (equivalent to 180 mm/h). This does not exceed the observed intensity of the 5-minute precipitation accumulation on 2022-06-20 in Praha-Komořany. Hence, the reason why accumulations of precipitation over 3 or 6 hours are sometimes overestimated when prognostic graupel is used remains unknown. It probably interacts with the moist deep convection parameterization. Also, more efficient evaporation of precipitation might help. Moreover, precipitation accumulations are highly sensitive to small changes in the trajectories of cells and the general movement of storms. If a storm moves slower than observed, the same precipitation flux delivers higher precipitation accumulations.

The fourth difference is that simulated reflectivities of convective storms were decreased since there is less snow in the atmosphere, as shown in Figure 6.4. Snow has higher simulated reflectivity than graupel when the precipitation flux is conserved since reflectivity is dependent on the radii of particles, not on precipitation flux. The reflectivity field matches observations better after adding prognostic graupel. Without prognostic graupel, the highest reflectivities are of-

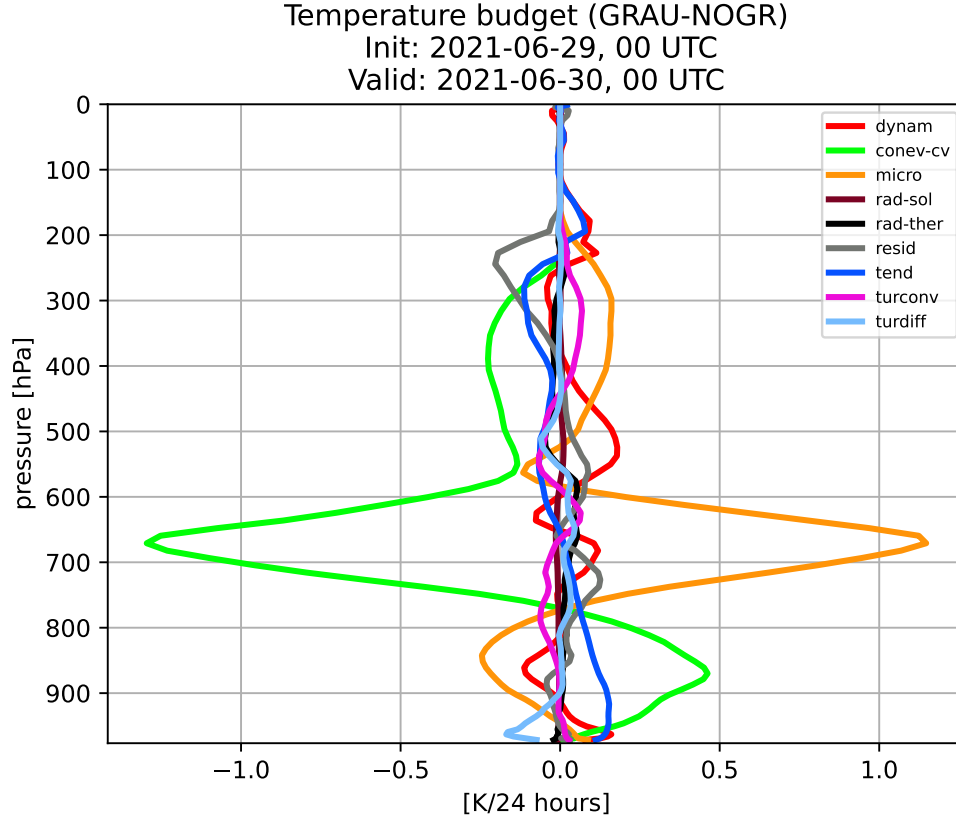


Figure 6.2: The difference temperature budget for 2021-06-29. The version without prognostic graupel (NOGR) is used as a reference for a run with prognostic graupel (GRAU).

ten simulated in cumulonimbus anvils. In addition, the cloud tops are usually a bit higher with prognostic graupel.

The benefit of the introduction of prognostic graupel was evaluated using the atmospheric forecast scores. Firstly, the autumn/winter precipitation period from 2021-11-25 to 2021-12-04 is discussed. Runs without prognostic graupel (model configuration NOGR) were taken from the archive. Runs with prognostic graupel (GRAU) were run with the assimilation cycle, which started a few days prior to the first forecast run. While STDE and RMSE of temperature and relative humidity are substantially improved, mainly at the surface, the STDE and RMSE of geopotential are slightly worsened for later stages of integrations. A distinct warm bias below 700 hPa appeared. Scores of other meteorological fields are relatively neutral.

For the summer period between 2021-06-21 and 2021-06-30, the overall impression of the scores is the same as for the winter case. Only the STDE and RMSE of upper air temperature are neutral. The statistically significant improvement of 2-metre temperature is still present.

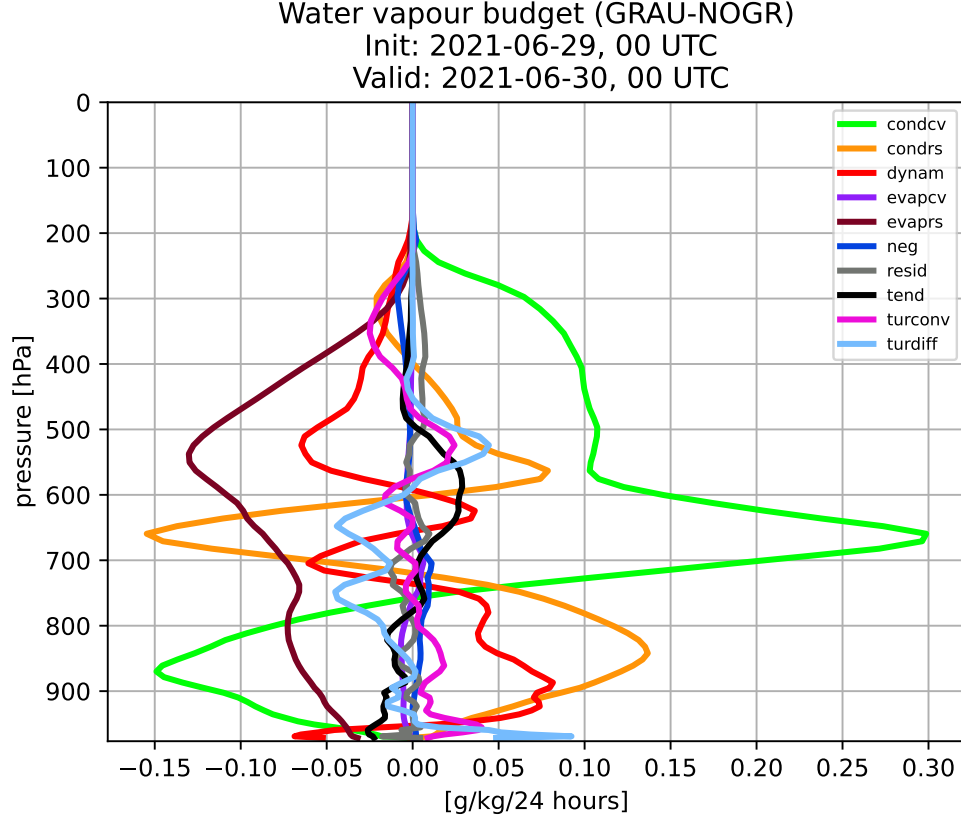


Figure 6.3: The difference water vapour budget for 2021-06-29. The version without prognostic graupel (NOGR) is used as a reference for a run with prognostic graupel (GRAU).

6.2 Improvements of prognostic graupel parameterization

6.2.1 Fall speed relation and mass-size distribution

The observed terminal fall speed of graupel particles is lower than that of rain when the precipitation flux is identical (Locatelli and Hobbs [1974], Heymsfield et al. [2018]). Therefore, the aim is to reduce the fall speed of graupel.

As the mass-weighted fall speed relation is tightly connected to the size distribution of particles, two options are possible. Firstly, one can keep the currently used mass-size distribution of rain and multiply the fall speed relation used for rain by a coefficient. Secondly, a new mass-size distribution and fall speed relation can be adopted. Both options were tested. After some tuning, four experiments were designed:

1. FVG1 using the fall speed relation for graupel $w_g = 0.62w_{AB}$, where w_{AB} is the fall speed computed from the fall speed relation for rain with the intercept parameter proposed by Abel and Boutle [2012]. The value of 0.62 is based on the ratio of rain, snow, and graupel fall speeds used in the IFS model for lightning diagnostics.

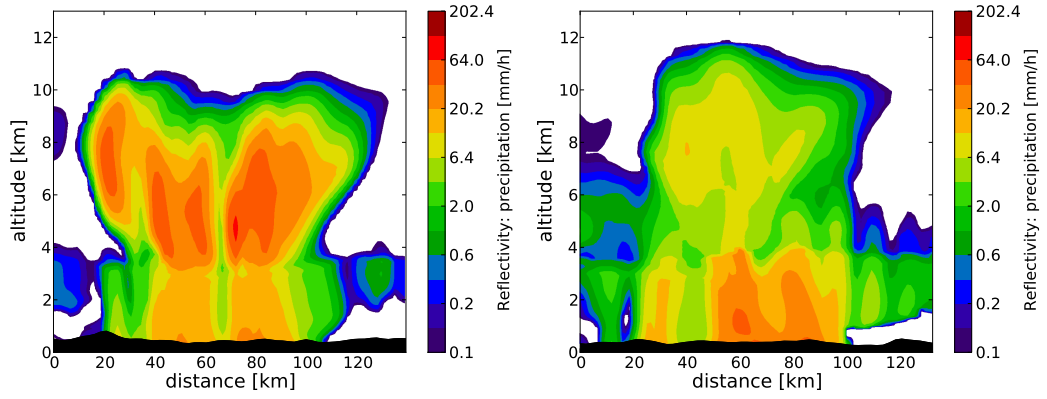


Figure 6.4: Vertical cross section of reflectivity through a multicellular storm of a run without prognostic graupel (left) and with prognostic graupel (right). Note the difference in the reflectivity above 4 km and also the difference in the top cloud height.

2. **FVG2** using $w_g = 0.62w_{r,MP}$, where $w_{r,MP}$ is the fall speed computed from the fall speed relation for rain with the Marshall-Palmer distribution with $N_0^r = 8 \cdot 10^6 \text{ m}^{-4}$.
3. **FVG3** using $w_g = 330D^{0.8}(\rho_0/\rho_a)^{0.5}$, used in the WSM6 scheme (Hong and Lim [2006]). The Marshall-Palmer distribution is used with $N_0^g = 4 \cdot 10^6 \text{ m}^{-4}$. Graupel is assumed spherical with a constant density $\rho_g = 400 \text{ kg} \cdot \text{m}^{-3}$.
4. **FVG4** using $w_g = 124D^{0.66}(\rho_0/\rho_a)^{0.4}$, following (Locatelli and Hobbs [1974]), which is also used in the ICE3 scheme (Pinty and Jabouille [1998]). The size distribution of graupel and its density are the same as for **FVG3**.

The dependence of the fall speed on the precipitation rate is shown in Figure 6.5.

Firstly, all experiments were tested on summer convection cases. The period from 2021-06-21 to 2021-06-30 was chosen. Before running all these experiments for full 72 hours forecast runs for all days, shorter 24-hour integrations starting at 00 UTC, mainly on 2021-06-29, were tested to obtain a preview of the behaviour of the experiments.

All these experiments deliver more evaporation in summer convective cases than the reference. Thus, they partially compensate for the destabilization of the atmosphere caused by introducing prognostic graupel. This means there is a lower temperature below 500 hPa than predicted by the reference. However, a warm bias is still observed at these levels compared to observations.

The higher precipitation maxima over the Alps are partially compensated by all new fall speed relations, which allow for more graupel sublimation. Also, convective storms reach slightly further in the direction of their movement since the time that graupel requires to reach the melting level is longer; consequently, graupel is advected further, causing rainfall to occur later. However, precipitation maxima are still overestimated compared to observations, mainly in convection.

These modifications were evaluated on atmospheric scores for the summer period from 2021-06-21 to 2021-06-29. The upper air scores indicate a cold bias

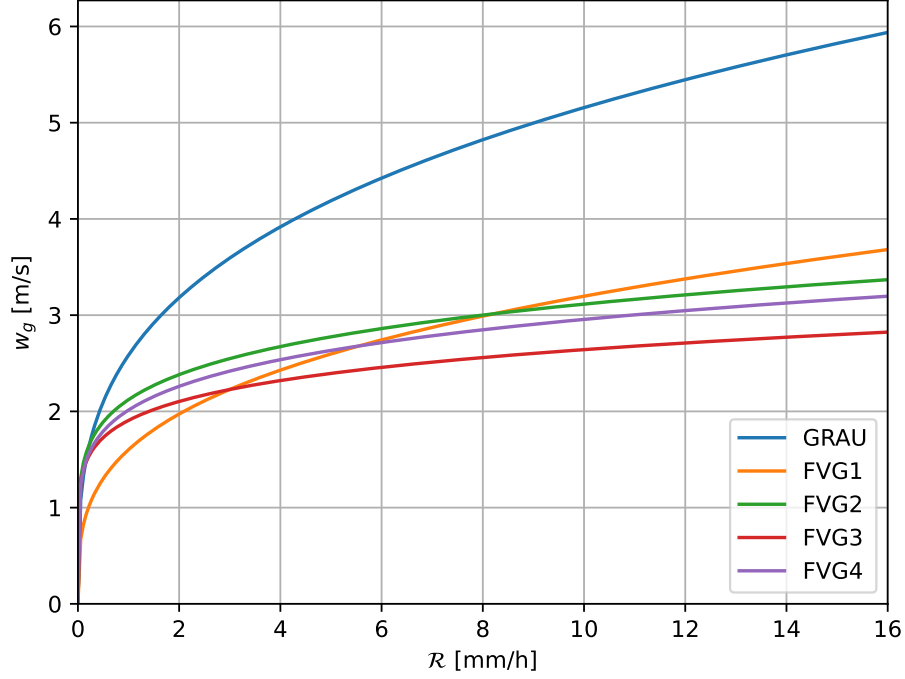


Figure 6.5: Dependence of the graupel fall speed on the precipitation rate for various proposals. The density of air is $\rho_a = 1 \text{ kg} \cdot \text{m}^{-3}$.

below 700 hPa, which is especially pronounced at 18 UTC for all three days of the model forecast. The cold bias is caused by enhanced evaporation. The cooling is connected to the positive bias of geopotential below 700-850 hPa. The RMSE and STDE of many meteorological fields indicate that decreasing fall speed just by multiplication by constant leads to little improvement as they are worsened for many meteorological fields, both the upper air and surface ones.

By contrast, **FVG3** and **FVG4** do not experience such detriment of scores showing that it is more suitable to release the idea of the similarity of mechanical properties of graupel and rain and implement a new set of parameters for graupel. Hence, only **FVG3** and **FVG4** are further examined in more detail.

The difference between results delivered by **FVG3** and **FVG4** is relatively tiny. Experiment **FVG4** delivers better results at later stages of the 72-hour forecast. In particular, the STDE and RMSE of the upper-air temperature are improved mainly in the later stages of the integration time. Moreover, **FVG4** outperforms **FVG3** in the upper air temperature and the STDE and RMSE of wind direction. Experiment **FVG3** delivers better results for geopotential, mainly in the first half of the integration time. Other fields are similar.

For the winter precipitation period from 2021-11-25 to 2021-12-04, both **FVG3** and **FVG4** show similar tendencies compared to the reference. The RMSE of geopotential is worsened at night and is neutral during the day. The RMSE and STDE of the upper-air temperature are worsened. The magnitudes of RMSE and STDE differences between both fields are small. To conclude, both simulations deliver comparable results for the winter period.

The precipitation field is very similar for both experiments, and no significant difference are found both for winter and summer cases. Compared to the refer-

ence, the too high maxima of precipitation accumulations in convection storms are usually slightly reduced, as well as the orographic effect.

Overall, experiment FVG4 delivers slightly better results than FVG3, so it is chosen for further testing.

6.2.2 Autoconversion

The coefficient for graupel autoconversion, k_g , has a standard value of 10^{-3} s^{-1} . Since $k_r = 5 \cdot 10^{-4} \text{ s}^{-1}$ for rain and $k_s = 2 \cdot 10^{-3} \text{ s}^{-1}$ for snow are used in the referential model configuration with the first implementation of prognostic graupel, both these boundary values were tested for k_g . However, neither of the values improved the model results. These modifications were tried on three cases of summer convection between 2020-06-07 and 2020-06-09. If $k_g = 2 \cdot 10^{-3} \text{ s}^{-1}$, then there is a positive bias of temperature below 400 hPa and a negative bias of geopotential below 500 hPa. As expected, $k_g = 5 \cdot 10^{-4} \text{ s}^{-1}$ causes the opposite: a negative bias of geopotential compared to the reference below 500 hPa and a warm bias of temperature in the troposphere. Overall, the influence of this parameter on model results is rather weak. Atmospheric scores show no improvement and sometimes worsened RMSE and STDE; mainly, the higher value ($k_g = 2 \cdot 10^{-3} \text{ s}^{-1}$) is not beneficial. Therefore, the standard value of $k_g = 10^{-3} \text{ s}^{-1}$ will be used for further tests.

6.2.3 Conversion from snow to graupel

Graupel is commonly produced by snow-to-graupel conversion in various microphysics schemes. The WSM6 scheme uses autoconversion from snow to graupel. Some other schemes, for example, ICE3 or the microphysics scheme used in COSMO, convert snow to graupel when snow collects enough cloud water. For the first tests, autoconversion from snow to graupel, as is used in the WSM6 scheme (Equation (3.7)), was implemented.

Firstly, an experiment with the WBF process leading to snow production instead of graupel production was tested. Thus, graupel is produced exclusively from snow. However, this combination does not deliver good results. Graupel then prevails in a horizontal layer rather than near updraughts (slightly behind them), where the highest specific amount of graupel is expected according to the Vaisala HydroClass product, which is one of the products provided by the double polarized C-band weather radars used in Czechia. Generally, it produces too little graupel. Hence, various combinations of the coefficient for autoconversion from snow to graupel, k_s , and threshold values of snow autoconversion, q_s^{crit} , were tested. Neither of them solved the problem.

Therefore, experiments were tested using the WBF process for graupel production and autoconversion from snow. Multiple sets of parameters were examined. However, it does not deliver a significant change of precipitation and reflectivity. Contrarily, if the autoconversion rate from snow to graupel is high enough, a horizontal layer of graupel appears again regardless of the presence of updraughts. Consequently, the idea of employing autoconversion from snow to graupel was rejected.

Another approach to converting snow to graupel is to produce graupel when

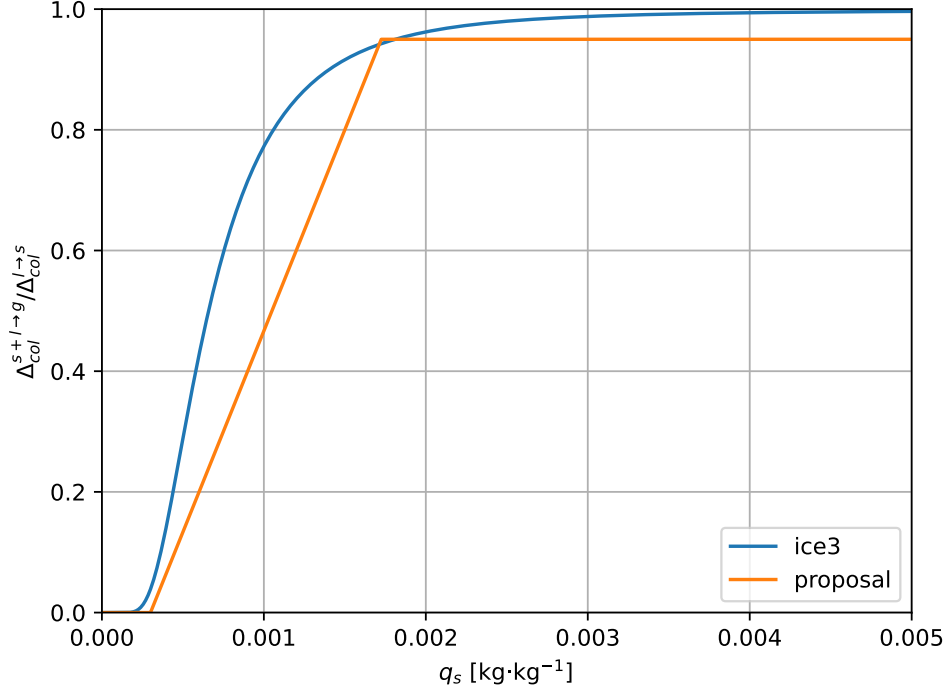


Figure 6.6: The shape of the transition function of the ratio between snow and graupel production by snow collecting cloud water. The transition function used in ICE3 is compared to the function proposed for ALARO.

the collection rate of snow collecting cloud water is high. A transition function based on the amount of snow was implemented. Its shape is depicted in Figure 6.6. When there is enough snow, a significant fraction of snow created by the collection of q_l is converted to graupel. There could also be a constraint for the minimum amount of q_l . If the minimum amount of q_l is not implemented, areas of significantly lower reflectivity in the central parts of storms appear. It is caused by abrupt conversion from snow to graupel, leading to a locally decreased amount of snow. This produces “stripes” in the snow field because the simulated reflectivity of snow is higher than graupel with the same precipitation flux as snow falls slower. Consequently, the minimum value of $q_l = 2 \cdot 10^{-4} \text{ kg} \cdot \text{kg}^{-1}$ is used. The final expression for snow to graupel conversion due to heavy rimming, which is used for further tests, is:

$$\Delta_{col}^{l+s \rightarrow g} = K \Delta_{col}^{l \rightarrow s} \mathcal{H}(q_l - 2 \cdot 10^{-4}) \quad (6.1)$$

$$K = \min \left[0.95, \max \left(0, \frac{q_s}{1.5 \cdot 10^{-3}} - 0.2 \right) \right].$$

As expected, this modification does not have a significant impact on the temperature and water vapour budgets, although there is a subtle tendency to warm lower levels. The magnitude is tiny, around 0.02 K on average. There was one case for the summer period 2021 when the temperature was even lowered near the surface. Atmospheric scores confirm the warming effect near the surface. After all, it is not a surprising result as graupel falls faster. Thus, its sublimation, which

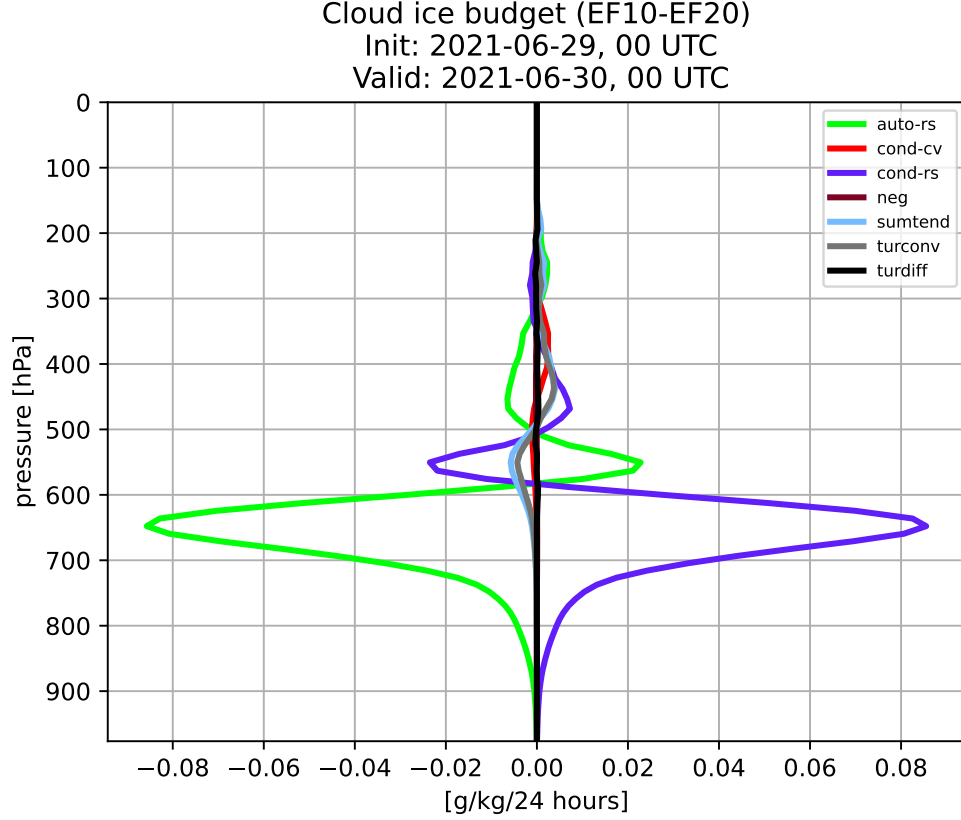


Figure 6.7: The cloud ice budget of the difference between a run with $E_{ff}^g = 0.1$ (EF10) and EF20 with $E_{ff}^g = 0.2$ (as a reference) for a summer convection case.

is of the same efficiency as the sublimation of snow, is lower. This also subtly reduces the positive bias of RH2m at lower levels. Another effect is a reducing the specific content of snow and higher specific content of graupel between 500 and 700 hPa. However, there is also very small reduction of graupel between the tropopause and 500 hPa, so there is less hydrometeors overall.

Scores for the period from 2021-06-21 to 2021-06-30 show that there are only minor changes. The subtle warming of T2m is confirmed. However, scores are generally neutral or without a clear signal. Also, this process has little impact on scores for the winter period from 2021-11-25 to 2021-12-04. Moreover, there is no significant impact on precipitation accumulations, their spatial distribution, and their diurnal cycle.

The effect of this process is minimal. This configuration does not change results much, so it is redundant. Thus, the production term of graupel is not changed.

6.2.4 Collection efficiency

The collection efficiency E_{ff}^g is another parameter to be determined. For rain, a value of 0.2 is used, whereas a value of 0.1 is used for snow. The value of the collection efficiency of graupel is expected to stay within these boundaries. Three experiments are proposed with collection efficiencies of 0.1, 0.15, and 0.2.

Table 6.1: The proposed set of parameters for graupel.

parameter	proposed value
fall speed relation	$w_g = 124D^{0.66} \left(\frac{\rho_0}{\rho_a}\right)^{0.4}$
density of graupel	$\rho_g = 400 \text{ kg} \cdot \text{m}^{-3}$
size distribution	$N_g(D) = N_0^g e^{-\lambda D}$
intercept parameter	$N_0^g = 4 \cdot 10^6 \text{ m}^{-4}$
mass-size relation	$m_g(D) = \frac{\pi D^3}{6} \rho_g$
collection efficiency	$E_{ff}^g = 0.15$
autoconversion coefficient	$k_g = 10^{-3} \text{ s}^{-1}$
first WBF coefficient	$F_{WBF}^a = 300$
second WBF coefficient	$F_{WBF}^b = 4$

The results are surprising. There is less cloud water and cloud ice for $E_{ff}^g = 0.1$ than for $E_{ff}^g = 0.15$ and $E_{ff}^g = 0.2$, as shown in Figure 6.7 for a summer convection case. Despite the primary contributions coming from less autoconversion and collection (grouped into **auto-rs**) and less resolved condensation (**cond-rs**), their contributions cancel out. Instead, the change of the total cloud ice tendency follows the contribution of the convective transport tightly. Thus, the main difference in the total cloud ice tendency is caused by convective transport.

Moreover, there is no distinct tendency of the temperature or water vapour budgets. Thus, the adjustments of the collection efficiency does not seem to have a noticeable impact on results. Consequently, $E_{ff}^g = 0.15$ was chosen in the spirit of the assumption that graupel is an intermediate particle between snow and rain.

6.3 The final proposal for graupel

A new set of parameters for graupel is proposed based on the results discussed in the previous subsections. The values of the coefficients are listed in Table 6.1. The fall speed relation closely follows the one used in ICE3 in AROME. However, its mass-size relation differs, a spherical graupel with a constant density is proposed here. This approach is similar to those used in the WSM6 scheme or the JMA-LFM model. The intercept parameter is the widely used one following Rutledge and Hobbs [1984]. The autoconversion coefficient remains $k_g = 10^{-3} \text{ s}^{-1}$, and both F_{WBF}^a and F_{WBF}^b use their recommended values. The collection efficiency is set between the values used for snow and rain. The sublimation and melting formulae for graupel remain unchanged as it follows the spirit of the evaporation parameterization in ALARO described earlier.

The performance of the proposed set of parameters for graupel (**OPGR**, which stands for optimized graupel) is evaluated against the reference runs with prognostic graupel (**GRAU**) and also against simulations without prognostic graupel (**NOGR**).

For a summer convection case, the temperature budget reveals a tendency to cool the lower troposphere while slightly warming up the upper troposphere. There is warming above 700 hPa caused by condensation and evaporation in the

deep convection scheme due to the melting of graupel occurring over a shallower layer with reduced fall speed.

Evaluation of scores for the summer period in June 2021 confirms the cold bias of temperature below 700 hPa due to higher evaporation rates (Figure 6.8). Its RMSE and STDE are slightly reduced. The change of temperature results in a more pronounced already existing positive bias of geopotential below 700 hPa (Figure 6.9). The STDE of geopotential is also worsened, which, combined with higher bias, leads to raised RMSE. However, the deterioration of geopotential in later stages of integrations is decreased, and the STDE and RMSE of geopotential are improved. In addition, the STDE and RMSE of relative humidity are reduced while its bias is almost untouched.

The surface cards (Figure 6.10) show a negative bias of temperature and a positive bias of geopotential at the surface. shows that there is a cold bias at surface as well as a positive bias of geopotential. The RMSE and STDE of relative humidity are slightly reduced. The difference on other fields is relatively small, except for cloudiness, which might be misleading as the grid box size is small and the observer at a station considers the cover over the whole sky. Moreover, there are few professional meteorological stations. To conclude, the results for the summer period are neutral, maybe slightly positive.

For the winter precipitation period of 2021, the upper air scores are mostly neutral except for the cold bias and the linked positive bias of geopotential below 700 hPa, which are still present. Although the magnitude is relatively small, the STDE and RMSE of temperature, geopotential, and relative humidity are worsened. The surface scores show detriment for this winter period (Figure 6.10). However, although the changes are statistically significant, their magnitude is small. Overall, the performance in winter is slightly worsened, although the differences are subtle.

To conclude, the difference delivered by this modification is slight both in summer and winter. The whole package seems to have a neutral impact on scores except the negative bias of 2-metre temperature, which is beneficial for the summer period but detrimental for the winter period. The differences in STDE and RMSE are quite small, so even if they are statistically significant for these periods, they might differ for other weather regimes. The only significant outputs from scores are the cooling below 700 hPa, raising geopotential at the same levels as a result, and delivering more moisture, which is beneficial for the upper air.

Scores are a handy tool but can hide small nuances, so verifying the results on weather maps is important. A slight reduction of occasionally exaggerated maxima of accumulated precipitation is observed in convective storms. This is demonstrated in Figure 6.11, where simulations are compared with the MERGE product. The precipitation maxima are overestimated with both graupel parameterizations compared to observations. The modification of parameters for graupel partially reduces the overestimation. This time, the version without prognostic graupel matches the observations best. However, runs with graupel usually deliver a better agreement with observations than runs without prognostic graupel.

It is important to remember that the occurrence of overestimated precipitation accumulation maxima is a volatile feature that differs a lot between times of initialization of model integration, so it is hard to tell a random success from an improvement. However, the reduction of the precipitation maxima with the new

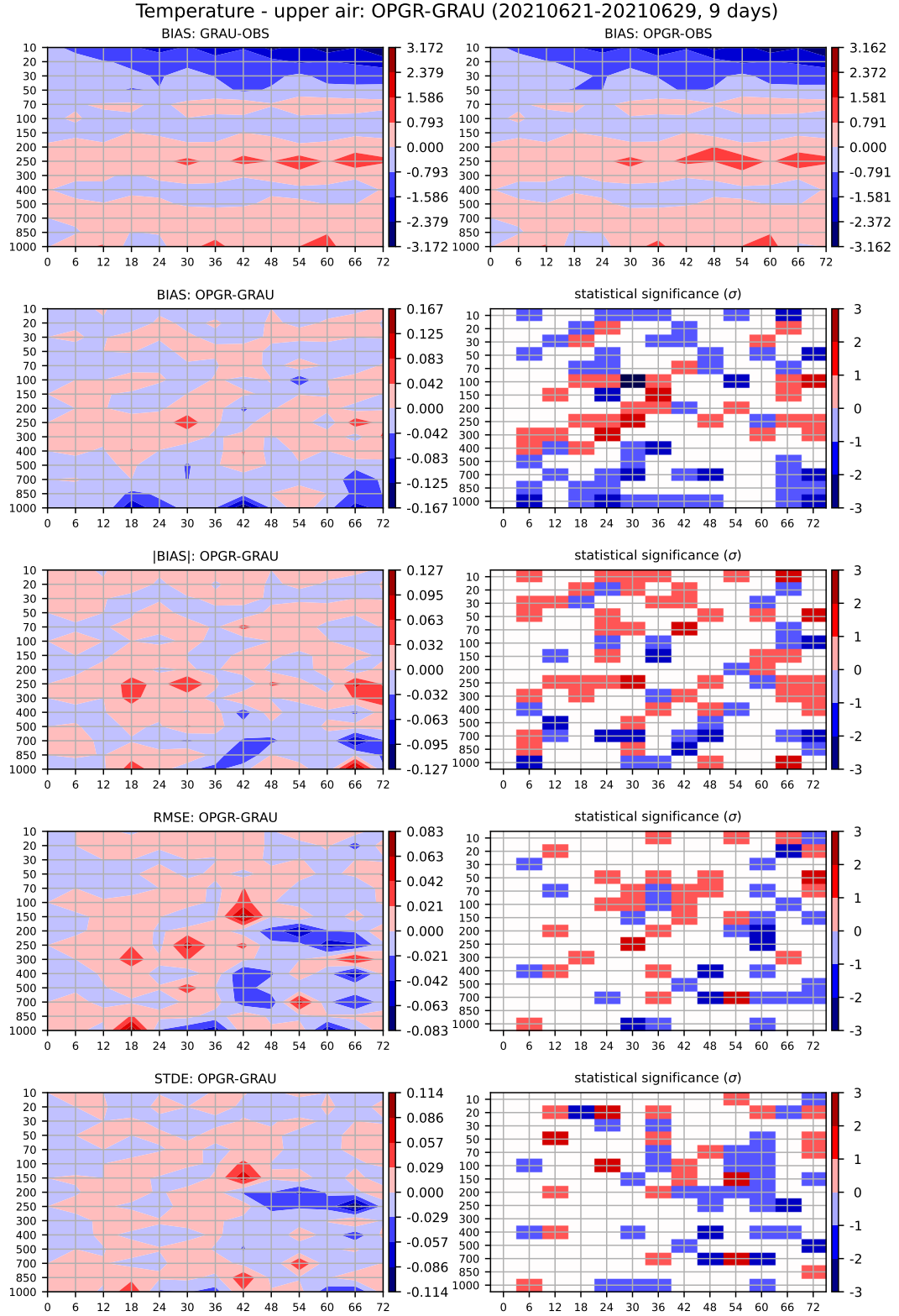


Figure 6.8: The difference of the upper air atmospheric scores of temperature for the period from 2021-06-21 to 2021-06-29 between OPGR and GRAU (reference). Terms 06 and 18 UTC are less reliable for the upper air observations as there is much less radiosondes released compared to terms 00 UTC and 12 UTC, which can make artefacts at 06 and 18 UTC.

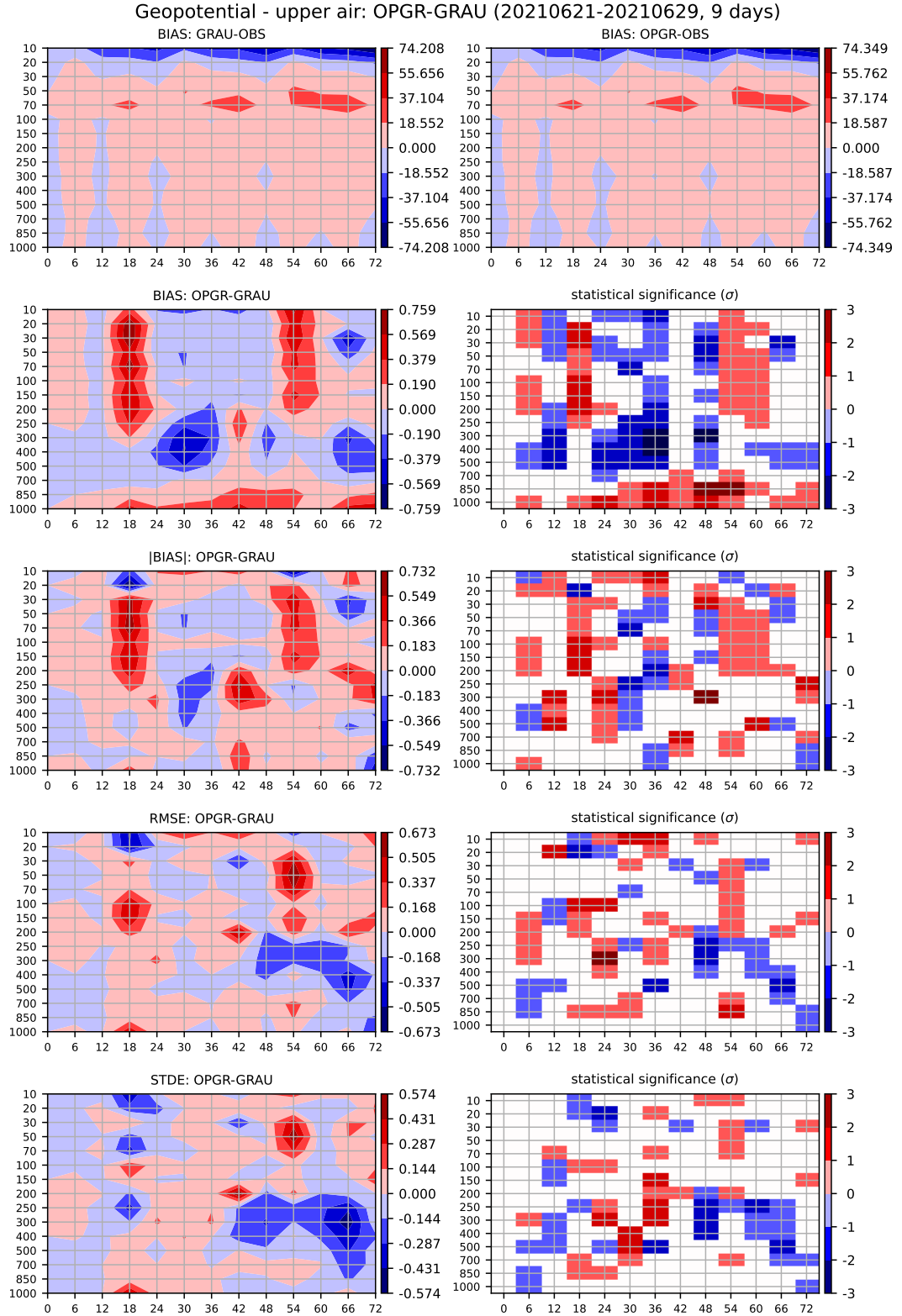
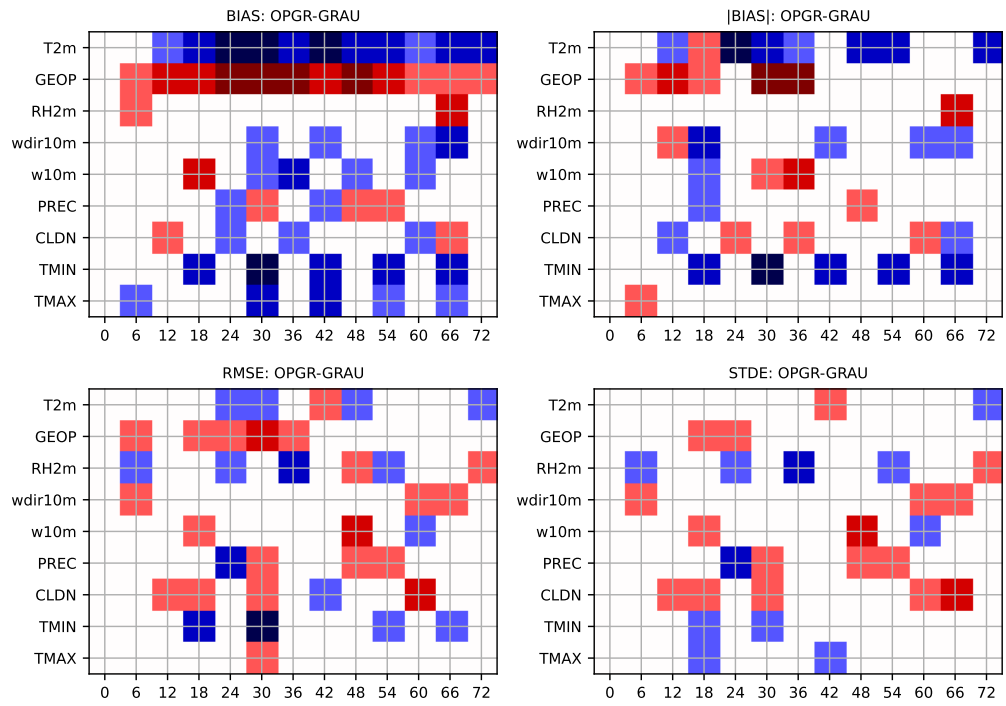


Figure 6.9: The difference of the upper air atmospheric scores of geopotential for the period from 2021-06-21 to 2021-06-29 between OPGR and GRAU.

Surface score difference: OPGR-GRAU (20210621-20210629, 9 days)



Surface score difference: OPGR-GRAU (20211125-20211204, 10 days)

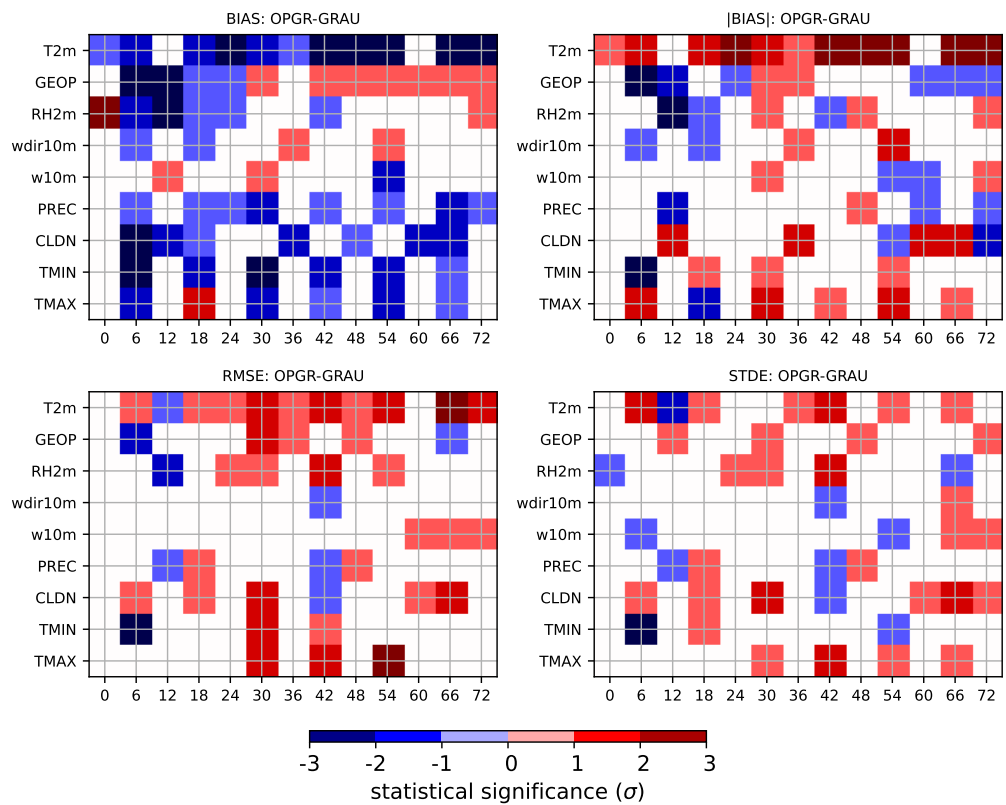


Figure 6.10: The statistical significance of trends of various statistics at surface for the period from 2022-06-21 to 2022-06-29 (upper) and from 2021-11-25 to 2021-12-04 (lower). Configuration OPGR is compared to GRAU.

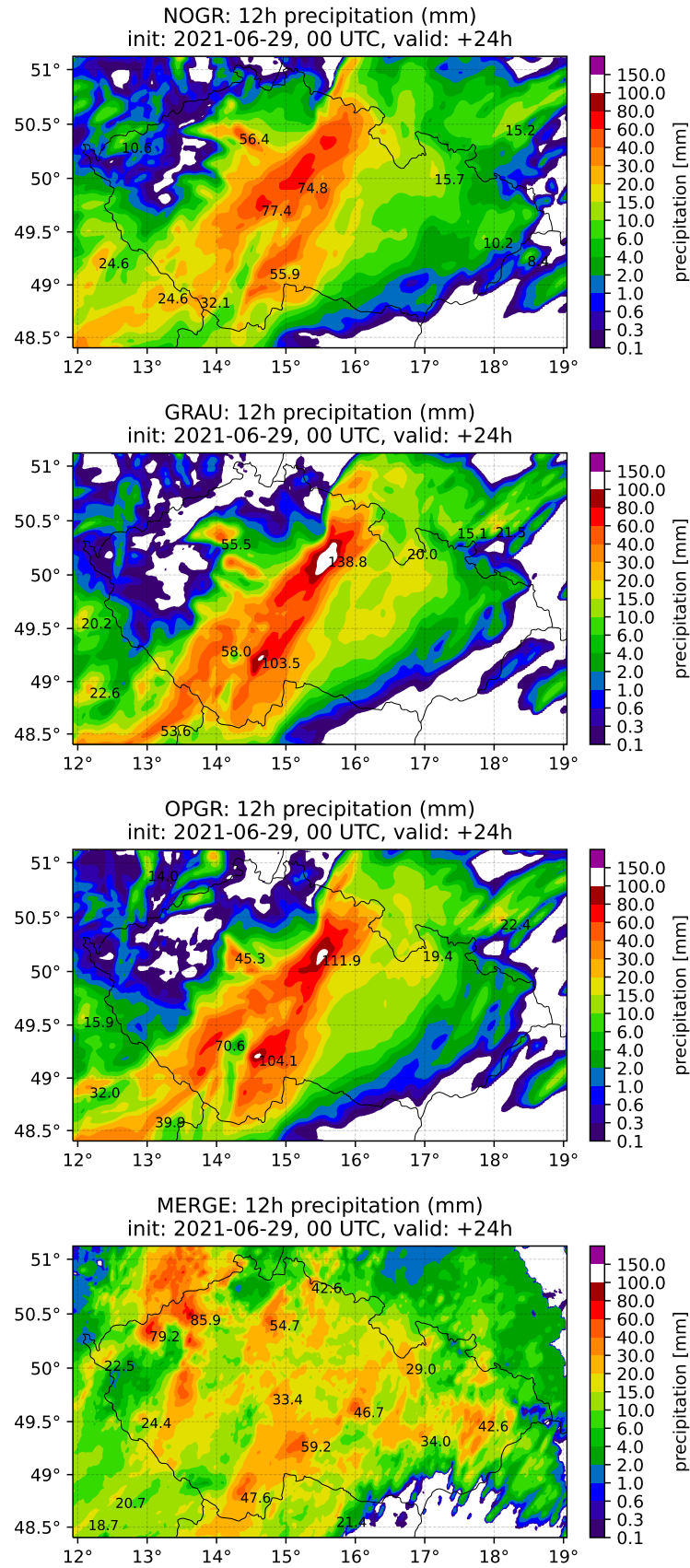


Figure 6.11: 12-hour precipitation accumulation ending on 2021-06-30 at 00 UTC. In descending order: NOGR, GRAU, OPGR, and MERGE (observations).

proposal was observed in multiple cases. The orographic effect is also slightly reduced, and precipitation reaches farther leeward mountain ranges as graupel fall speed is reduced.

To conclude, the difference made by introducing prognostic graupel exceeds the influence of the modified parameters for graupel. The final set of parameters delivers only a slight improvement but a more physically realistic graupel parameterization. The most significant influence has the new fall speed relation. A slight improvement is delivered in the case of severe convection, while very subtle detriment of results appears in winter. Another enhancement are the reduced precipitation maxima. As a side effect, this change substantially improves the underestimation of predicted maxima by the lightning diagnostic, which was observed before (Němec).

This model configuration (denoted by **OPGR**) will be used for further experiments as a reference.

7. Further innovations of the microphysics scheme

This chapter presents proposals for innovations in the microphysics scheme. The aim is not to focus only on the microphysical processes touching graupel but also on microphysical processes of rain and snow.

7.1 Autoconversion

7.1.1 Coefficient for autoconversion to snow

One of the known deficiencies of the model is the underestimation of the optical thickness of anvils and the overestimation of brightness temperatures of cloud tops of cumulonimbi (Sokol et al. [2022]). It is important to emphasize that the cloud scheme in radiation, which is used for the brightness temperature diagnostic, differs from the one used in microphysics. The unification of cloud schemes in microphysics and radiation is theoretically possible for the grid-scale cloud scheme. Nonetheless, parameters of cloud schemes differ in the model configuration used at CHMI, which is common across NWP models. Moreover, non-precipitating shallow convection cloudiness must be considered in radiation, unlike in microphysics. However, changes in microphysics can influence the cloud cover in the radiation scheme via feedbacks.

A possibility for enhancing the optical thickness of anvils is to lower the coefficient for autoconversion to snow from $k_s = 2 \cdot 10^{-3} \text{ kg} \cdot \text{kg}^{-1}$ to $k_s = 10^{-3} \text{ kg} \cdot \text{kg}^{-1}$. This experiment is hereafter denoted by **AKS1**. Figure 7.1 compares the brightness temperature delivered by **OPGR** and **AKS1** on a selected area around the storm over Czechia on 2022-06-24 at 21 UTC. There is not a big difference in the lowest brightness temperatures. However, there is a rather significant difference between 225 and 240 K, where **AKS1** delivers a larger area fraction of brightness temperature lower than a threshold value compared to **OPGR**. This tendency is widely observed. Also, **AKS1** delivers more high clouds in radiation in such cases.

This modification does not significantly impact precipitation fields, except that a slight reduction of predicted precipitation accumulation maxima is sometimes observed. It might be caused by less snow sublimation, which causes less condensation to cloud water, thus leading to less active autoconversion to graupel. However, the difference is rather subtle, and even results for individual cases sometimes differ. Another positive influence of this change is a reduction of the positive bias of precipitation in the summer and winter precipitation periods of 2021. Consequently, there is more moisture in the troposphere. Thus, less precipitation is created, and less precipitation reaches the ground.

As a consequence of this adjustment, there is less autoconversion from cloud ice to snow except near the tropopause for summer convection cases. As feedback, there is less condensation to cloud ice. Its final tendency shows less cloud ice above 400 hPa and slightly below 400 hPa. This tendency mostly follows the contribution of convective transport. The budget of cloud water is usually roughly the same. The amount of snow is slightly raised above 400 hPa and slightly



Figure 7.1: The area fraction of brightness temperature lower than a threshold value $T_{b,thr}$ for AKS1 and OPGR on 2022-06-24 at 21 UTC.

reduced below 400 hPa. The probable reason for more snow near the tropopause is that the lower autoconversion rates cause more cloud ice to reach the tropopause in updraughts; thus, more snow is produced there.

Figure 7.2 shows the atmospheric scores for the summer period from 2021-06-21 to 2021-06-30. The atmospheric scores reveal that the geopotential is lowered below 700 hPa and raised between 700 hPa and the tropopause. Its RMSE is neutral. The upper air temperature is raised below 500 hPa due to less evaporative cooling by the sublimation of snow. There is more moisture above 500 hPa and less below. Its RMSE and STDE at 500 hPa and 700 hPa are worsened.

Regarding the surface scores, the positive bias of geopotential is reduced. The bias of T2m evinces a subtle diurnal cycle when the temperature is decreased during the day and raised at night. The magnitude is about 0.03 K for warming at 00 UTC and 0.03-0.04 K for cooling at 12 and 18 UTC. This is caused by enhanced cloudiness, mainly middle and high; thus, there is less outgoing longwave radiation at night and less incoming shortwave radiation during the day.

For the winter precipitation period from 2021-11-25 to 2021-12-04, the bias of geopotential shows the same dipole pattern as in summer, only the boundary line is lower, between 700 and 850 hPa. This reduces the positive bias of geopotential for the first 36 hours of integration while it enhances the negative bias for the rest of the integration time. The RMSE and STDE of geopotential are worsened in the later stages of integrations while slightly improved at the beginning. Relative humidity shows the same dipole pattern of bias as in summer; the borderline is again lower, around 850 hPa. The RMSE and STDE of relative humidity are improved. The improvement is statistically significant. Temperature is raised

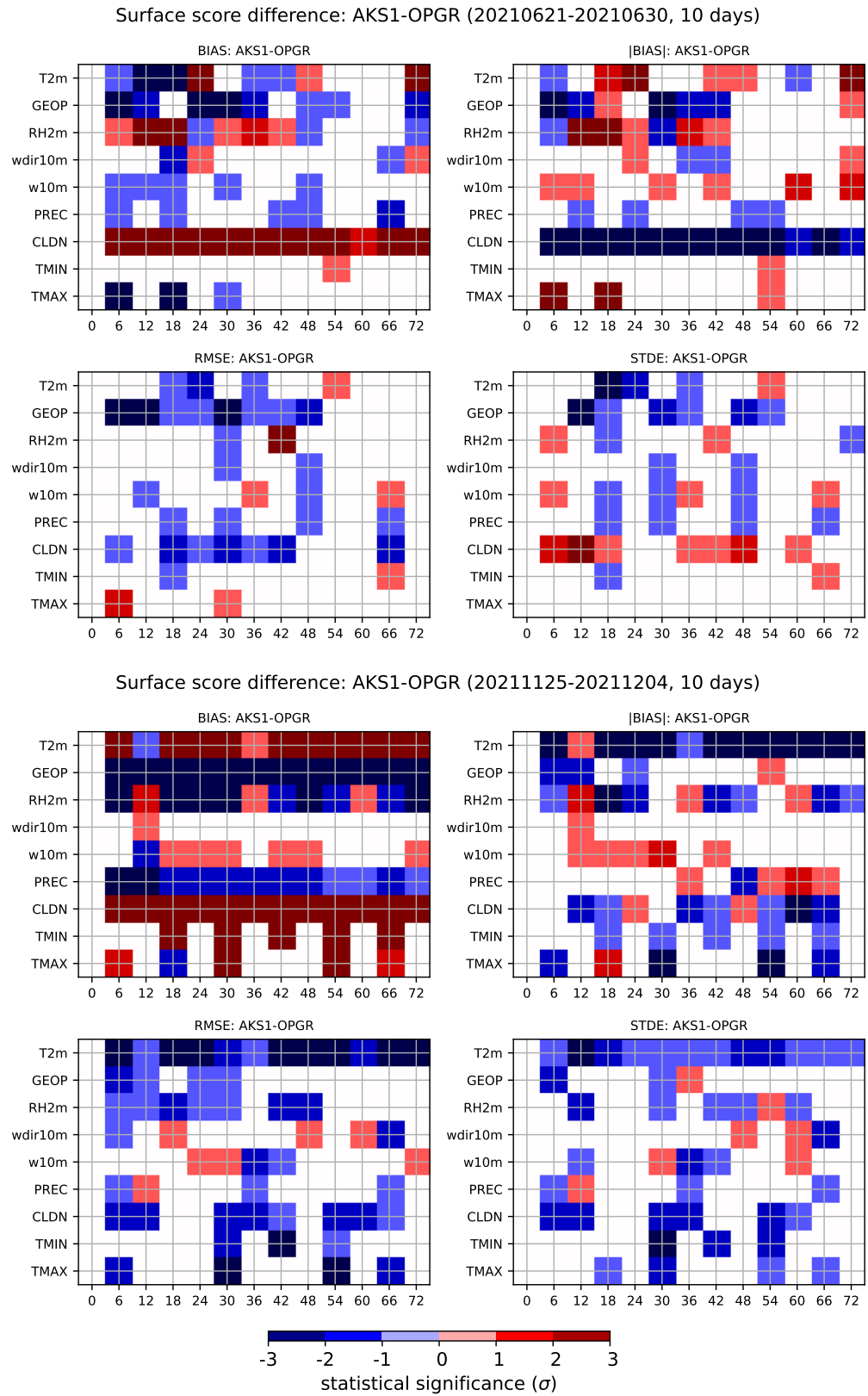


Figure 7.2: The statistical significance of trends of various statistics at the surface for the summer 2021 (upper) and winter precipitation (lower) periods for AKS1 with OPGR as the reference.

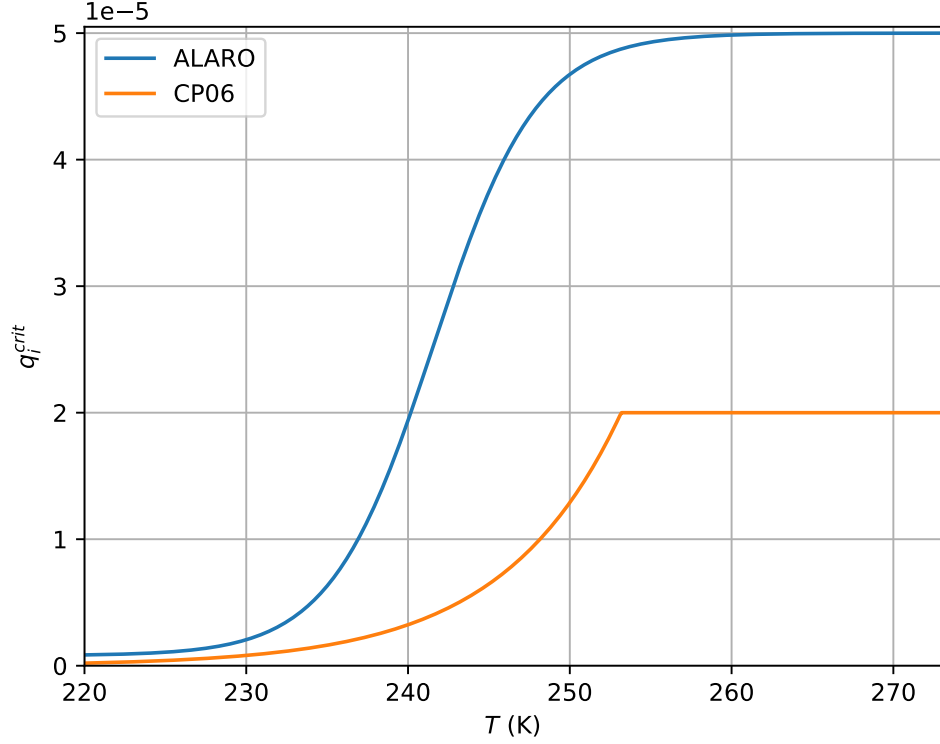


Figure 7.3: Temperature dependence of Equation 7.1 (ALARO) and Equation 7.2 (CP06).

below 500 hPa. This is probably caused by the decreased evaporation from less precipitation. The RMSE and STDE of the upper air temperature are neutral, maybe slightly worse at the later stages of integrations.

The surface scores are improved, except that the already too high w10m is further raised, and the results of wdir10m are neutral. Especially, T2m is statistically significantly improved for all forecast ranges except for its bias at 12 UTC of the first days of integrations.

Figure 7.2 shows improved surface scores for both the summer and winter periods. This modification is beneficial as the maxima of precipitation in convection are sometimes slightly reduced, and the surface scores are improved. Consequently, it is one of the proposed changes of the parameters of the microphysics scheme.

7.1.2 Modification of the computation of the threshold value for autoconversion to snow

A different computation of the threshold value of the autoconversion from cloud ice to snow, q_i^{crit} , is tested. The current parameterization use

$$q_i^{crit} = q_i^{crit,min} + (q_i^{crit,max} - q_i^{crit,min}) \cdot e^{0.0231 \cdot (T - T_t)}, \quad (7.1)$$

where the two tunable parameters are currently set to $q_i^{crit,min} = 8 \cdot 10^{-7} \text{ kg} \cdot \text{kg}^{-1}$ and $q_i^{crit,max} = 5 \cdot 10^{-5} \text{ kg} \cdot \text{kg}^{-1}$. The new proposal, which follows Chaboureau

and Pinty [2006], uses

$$q_i^{crit} = \min \left(k_1, 10^{k_2 \cdot (T - T_i) - k_3} \right), \quad (7.2)$$

where the tunable parameters have recommended values of $k_1 = 2 \cdot 10^{-5} \text{ kg} \cdot \text{kg}^{-1}$, $k_2 = 0.06$ and $k_3 = 3.5$ (Chaboureau and Pinty [2006]). This function was proposed to represent well cirri in tropical areas and is based on the comparison with satellite data. Figure 7.3 compares the shapes of the functional dependence given by Equation (7.1) and Equation (7.2).

Runs with the computation of q_i^{crit} following Chaboureau and Pinty [2006] are denoted by CP06. For tests, $k_s = 10^{-3} \text{ kg} \cdot \text{kg}^{-1}$ is used; therefore, AKS1 is used as the reference.

Typical summer convection case's enthalpy and water species budgets reveal interesting feedback. The cloud ice budget (Figure 7.4) shows that cloud ice is removed around 600 hPa by autoconversion to snow as the autoconversion is now more efficient. Due to this, there is more sublimation of snow around 600-650 hPa. This causes a more stable atmosphere in the layer between 650 and 550 hPa. Moreover, the stabilization effect is enhanced by more condensation just at the top of this stable layer, around 550 hPa. As the condensation is less effective at higher levels, it causes a subtle destabilization of this layer between 550 hPa and 300 hPa. The less stable layer causes enhancement of the convective transport of q_i , thus delivering more q_i to the upper troposphere.

Despite the mechanism mentioned above, observed for multiple cases, the difference in atmospheric scores is minimal without a distinct tendency. However, it explains why there is higher cloud ice specific content with lower q_i^{crit} , which might be counter-intuitive.

The effect of this parameterization is negligible in winter. As this parameterization leads to a slightly better representation of anvils, it will be included in the final proposal for changes to the microphysics scheme.

7.1.3 Nonlinear rain autoconversion

One of the model's deficiencies are too high precipitation accumulations in autumn stratocumulus inversion situations. A way to improve the representation of these events in microphysics might be implementing a non-linear autoconversion parameterization.

As the first attempt, the autoconversion parameterization following Equation (2.15) was implemented. Values of parameters for the first tuning were taken from the WSM6 scheme:

$$\frac{dq}{dt} = 7.03 \cdot q_l \cdot \mathcal{H} \left(q_l - \frac{6.43 \cdot 10^{-4}}{\rho_a} \right); \quad (7.3)$$

that is, $q_l^{crit} = 6.43 \cdot 10^{-4} / \rho_a \text{ kg} \cdot \text{kg}^{-1}$ and $k_r = 7.03 \text{ s}^{-1}$. However, this equation does not deliver a reduction of the precipitation accumulation for selected cases from the period from 2021-11-11 to 2021-11-20. Consequently, multiple modifications of parameters q_l^{crit} and k_r were tested. Nevertheless, only a small reduction of precipitation accumulation is reached unless q_l^{crit} is set to a very high value or k_r is significantly reduced. This leads to too broad areas of high q_l in stratocumuli and mainly to too much q_l in the lowermost model layer.

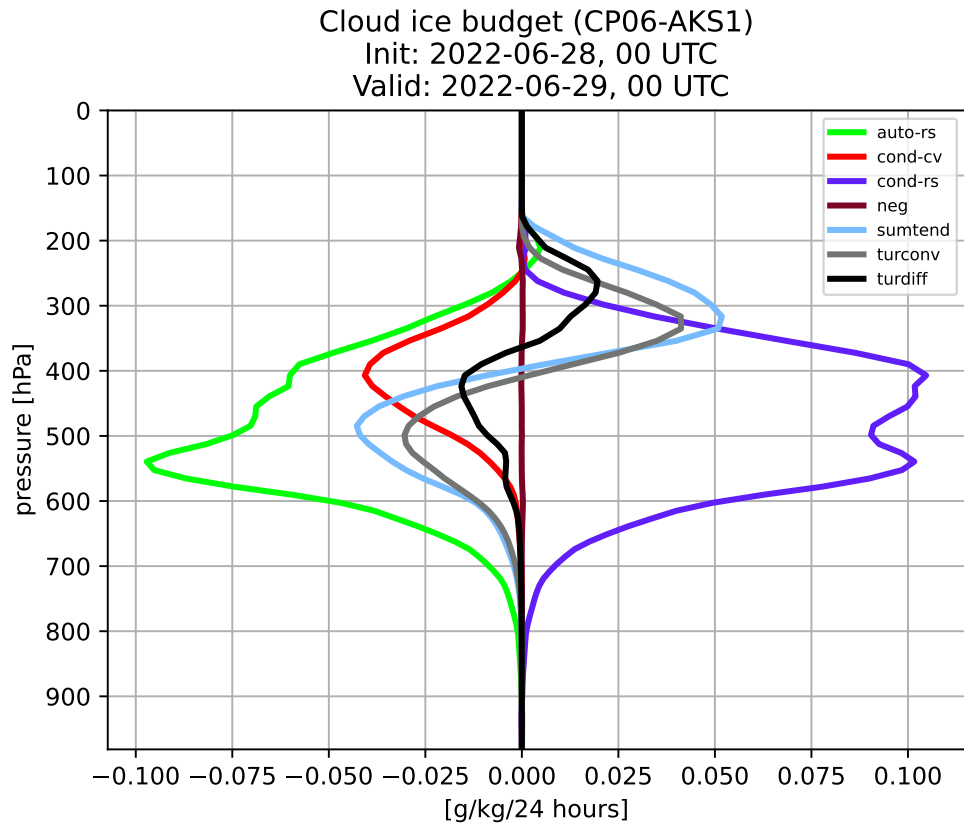
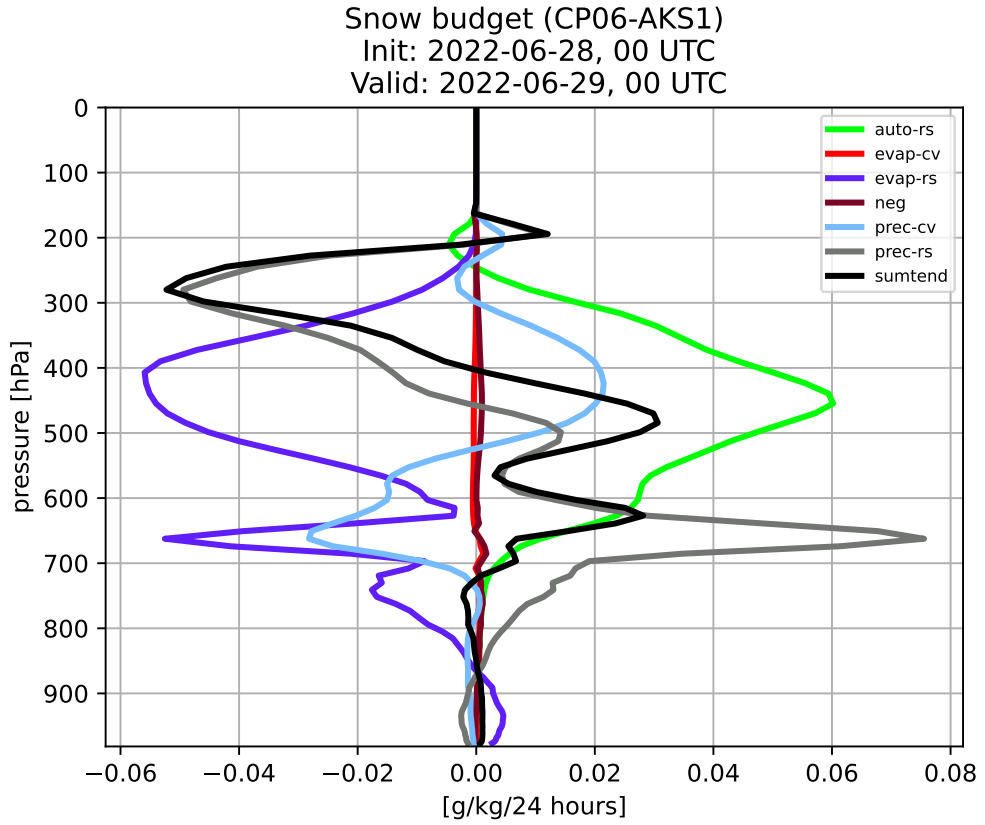


Figure 7.4: The snow (top) and cloud ice (bottom) budget difference between CP06 and AKS1 for a summer convection case.

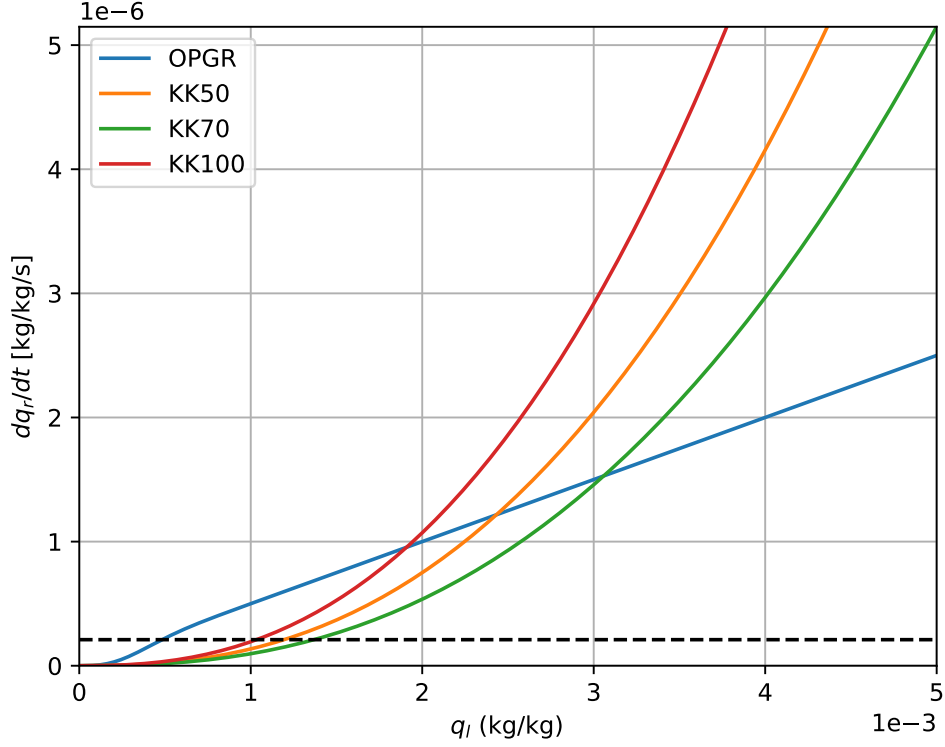


Figure 7.5: Multiple tested coefficients for the autoconversion parameterization following Khairoutdinov and Kogan [2000]. The number in the name of the experiment denotes the value of the multiplication coefficient. Black line roughly denotes the empirically discovered (from various simulations) required autoconversion rate at which stratocumuli typically start to precipitate with the operational collection parameterization in the current ALARO configuration. Thus, the black dashed line roughly denotes the specific water content of thick stratocumuli.

The Khairoutdinov and Kogan [2000] autoconversion or possibly the whole model for rain with the collection parameterization, was chosen as another suitable adept. Stratocumuli in autumn exclusively consist of water droplets; therefore, a better representation of the so-called warm-rain processes might help.

Firstly, only the autoconversion parameterization following Equation (2.19) was tested. The autoconversion rate for a given amount of q_l delivered by this equation is significantly lower than the rate given by the Kessler or Sundqvist parameterization. Thus, a tunable parameter multiplies its value for its solitary use without the collection parameterization described by Equation (2.20). Figure 7.5 shows multiple tested options for this coefficient. The most suitable proposal was to set the value to 70. Also, values of 50 and 100 were tested. If the multiplication factor is 100, there is no observed decrease in the precipitation accumulation on the 14th and 15th of November. Neither of the versions delivers a reduction of the precipitation accumulation on the 11th of November. The value of 50 appeared to reduce also higher precipitation rates in some cases, which is not desired. Consequently, the value of 70 was chosen for further testing and KK70 denotes this experiment. Overall, a little reduction of precipitation accumulation during this

period is observed, although the change is not as significant as was expected. The change is similar to the change reached when using the previous adept for the autoconversion parameterization following Equation (2.15). In this case, there is a reduction of q_l in the lowermost model layer as no positive threshold value q_l^{crit} is used.

However, precipitation accumulations on fronts are also slightly reduced, although undesirable as it slightly underestimates observed precipitation accumulations. Moreover, KK70 suffers from too high q_l in stratocumuli. Overall, the effects of this autoconversion parameterization are similar to the previously tested parameterization following Equation (2.15). It seems that small variations of the power of q_l do not significantly impact model results.

Finally, the full parameterization following Khairoutdinov and Kogan [2000] was implemented. Thus, the collection parameterization follows Equation (2.20), and autoconversion follows Equation (2.19). The number concentration of cloud droplets was set to $N_l = 3 \cdot 10^8 \text{ m}^{-3}$, which is the value used by the IFS (ECMWF [2021]) over the land, and it was also used by Wilkinson et al. [2013] in the MetUM model before the prognostic aerosol computation was implemented. This experiment is denoted by KK00.

As shown in Figure 7.6, the precipitation accumulation is reduced compared to the operational run. On the other hand, the precipitation bias is almost unchanged for a part of the winter precipitation period from 2021-11-26 to 2021-12-01 (Figure 7.7). Thus, the full Khairoutdinov and Kogan [2000] parameterization delivers better results than only the solitaire use of their autoconversion.

The atmospheric scores do not show a significant difference. However, the boundary layer is slightly colder than in the case of OPGR, which further strengthens the already present cold bias of 2-metre temperature from 2021-11-26 to 2021-12-01. The RMSE of temperature is slightly worsened while its STDE is rather unchanged. The cold bias corresponds with a positive bias of geopotential below 700 hPa.

The influence on the temperature profile is rather complex, as shown in Figure 7.8 for an autumn case. There is a positive contribution of radiation to the temperature budget below 850 hPa due to thicker stratocumuli. The positive contribution of radiation abruptly transforms into a negative contribution at the top of the boundary layer, caused by outgoing longwave radiation from cloud tops of jailed stratocumuli at the top of the boundary layer. The resulting temperature tendency at the lowermost layer is often around zero or slightly lower as the diurnal cycle is present. The difference is negligible at night, but the temperature is lower during the day than in the case of OPGR. The change is due to feedback from the thicker stratocumulus, which prevents the shortwave radiation from reaching the ground during the day while impeding outgoing longwave radiation at night. This feedback was also observed by Wilkinson et al. [2013].

In correspondence with the findings of Khairoutdinov and Kogan [2000], enhanced precipitation evaporation causes the cooling contribution to microphysics. This autoconversion parameterization produces lower precipitation rates; thus, smaller drops, which evaporate quicker than big ones. The fact that there is also enhanced condensation may suggest that the evaporated precipitation is again condensed to cloud water in the saturation adjustment. After that, probably a little rain is created, and the loop continues.

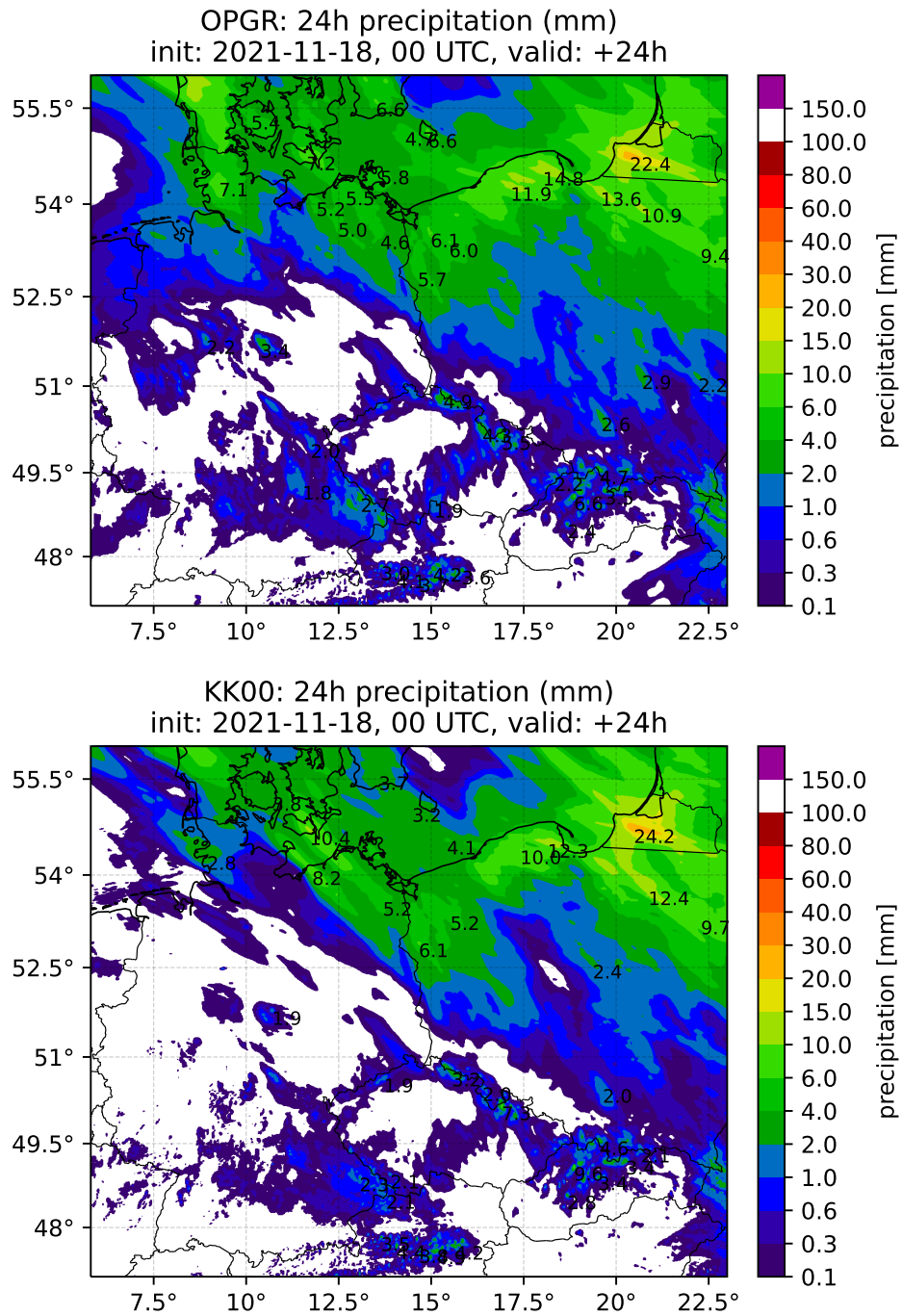


Figure 7.6: Comparison of the 24-hour precipitation accumulation ending on 2021-11-19 at 00 UTC of OPGR (upper) and KK00 (lower).

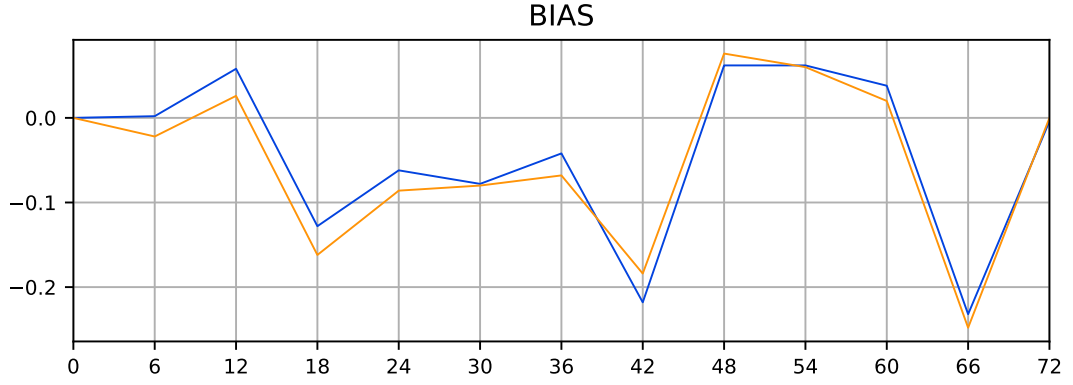


Figure 7.7: Comparison of the precipitation bias of OPGR (blue) and KK00 (orange) for the period from 2021-11-26 to 2021-12-01.

On the contrary, their effect changes in the lowermost layer, where less condensation to cloud particles and enhanced evaporation of precipitation appears, which contributes to the budget as strong cooling. Lowered temperature by microphysics is compensated by turbulent transport. Unusually for a winter case, condensation and evaporation in the deep convection scheme contribute significantly to the temperature budget, which is most probably caused by intensive showers over Croatia.

For a shortened summer period, there is a noticeable detriment of all scores except the temperature one, of which STDE and RMSE are improved. On the other hand, T2m is lowered (Figure 7.9). Generally, the model has a tendency to underestimate 2-metre temperature, so further cooling is not desired. As the bias of precipitation and cloudiness is almost unchanged for summer cases, a significant change of 2-metre temperature is not expected when this modification is incorporated into the assimilation cycle, which was not tested. If the precipitation bias were changed, feedback via the groundwater reservoir would lead to lower latent heat consumption due to lower evaporation rates from the surface.

Nonetheless, there is a possibility of one positive feedback. The autoconversion rates of KK00 are higher than of OPGR in cumulonimbi. As OPGR has locally too high q_l (according to values found in Pruppacher and Klett [1997] and Khvorostyanov and Curry [2014]), the amount of cloud water vertically advected to higher altitudes is lower. This effect leads to less specific cloud water content in the strongest updraughts and possibly suppresses the exaggeration of the maxima of accumulated precipitation in convection. However, the phenomenon of overestimating precipitation maxima is susceptible to subtle changes in initial conditions, so it must be thoroughly investigated. So far, the precipitation accumulation for the runs initialized on 2022-06-24 at 12 UTC and 2022-06-29 at 00 UTC is reduced. However, more than two cases are needed to be sure of this behaviour. Also, it does not help for lighter, relatively stationary showers, of which precipitation accumulations are also sometimes exaggerated.

For the case 2021-11-18, there is a rather significant difference in precipitation accumulation (Figure 7.6), which is taken under investigation. The vertical cross section of the specific cloud water content (q_l) through this area is shown in Figure 7.10. There is a significant difference in q_l . The observed liquid water con-

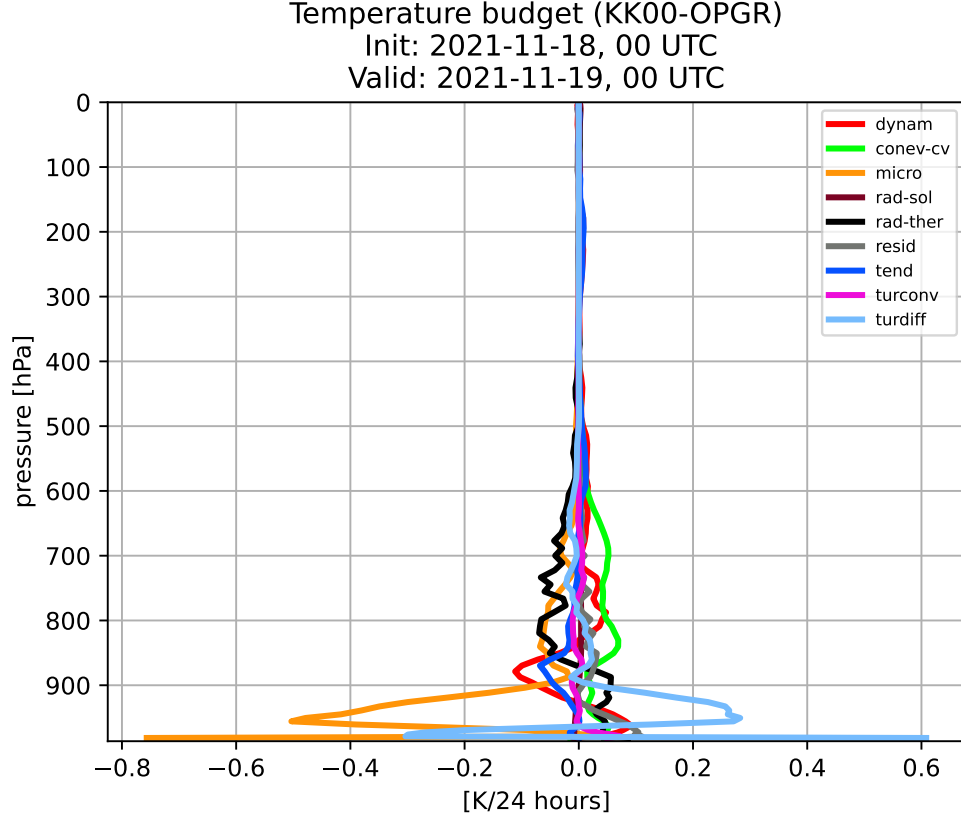


Figure 7.8: The temperature budget difference between KK00 and OPGR for an autumn case.

tent w_L of stratocumuli varies between 0.1 and 0.5 g/m^3 (Pruppacher and Klett [1997]) or $0.05 - 0.3 \text{ g/m}^3$ (Khvorostyanov and Curry [2014]). Both values are significantly lower than w_L predicted by KK00, where a broad area of q_l exceeding $1 \text{ g} \cdot \text{kg}^{-1}$ is present. Since the density of air in these layers is close to unity, it is evident that there is a significant detriment in the accuracy of the simulated amount of cloud water in stratocumuli. That is not the case for OPGR, which delivers a realistic value of q_l in stratocumuli. Moreover, there is a significant amount of cloud water in the lowermost layer, which is also not observed for stratocumuli in such conditions.

Sadly, the unrealistically high liquid water content in strati and stratocumuli occurs repeatedly. This experience is in correspondence with findings of Wilkinson et al. [2013], who described thickens of stratocumulus in the MetUM model. The suggested solution, which is to use prognostic equations for aerosol concentrations, is yet to be implemented in the ALARO microphysics.

For ALARO, it seems that there is required a specific autoconversion rate at which clouds start to precipitate, and the corresponding q_l in the cloud stays close to this value in the case of very little precipitation. The empirically observed autoconversion rate necessary for a cloud to start to precipitate is depicted in Figure 7.5 by the black dashed line. The intersection of this line with the lines denoting different autoconversion parameterizations shows the expected q_l in stratocumuli just before they start to precipitate.

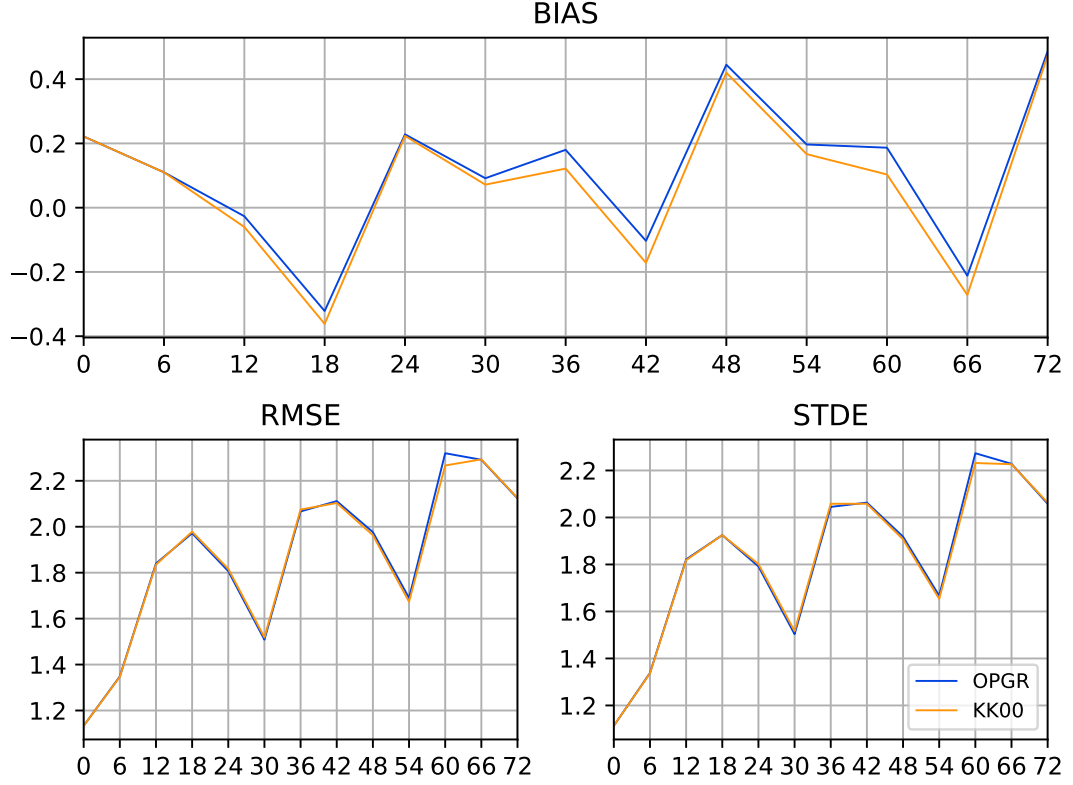


Figure 7.9: Bias, STDE and RMSE of temperature for the period from 2021-06-21 to 2021-06-26. Configuration OPGR in blue and KK00 in orange.

Consequently, after considering all the above-mentioned deficiencies, the proposal of non-linear autoconversion parameterization was declined. Even modifications of the parameters for KK00 were tested (multiplying by a constant, which is equivalent to changing the value of N_l) to reduce the overestimation of q_l in stratocumuli. Also, the tested modifications of parameters of HUc do not lead to any noticeable changes in q_l .

7.1.4 Modification of the threshold value of rain autoconversion

As an alternative to a non-linear autoconversion parameterization, the Sundqvist type of autoconversion for rain with a higher threshold value of the specific content of cloud water (q_l^{crit}) can also reduce the precipitation accumulation for the stratocumulus period. Also, a combination with a different value of the coefficient k_r can be beneficial.

Multiple values of q_l^{crit} were tested; they are listed in Table 7.1. Rainfall accumulations are decreased for all experiments; however, not as much as for KK00. If $q_l^{crit} = 0.5$, the specific cloud water content is too high in stratocumuli. Therefore, experiments AKR2 and AKR4 are not found to be suitable. Experiment AKR3 reduces locally too high specific cloud water content in cumulonimbi (over $8 \text{ g} \cdot \text{kg}^{-1}$) caused by too ineffective autoconversion due to too low k_r . However, the reduction of precipitation in autumn is very low. Therefore, AKR1 seems to

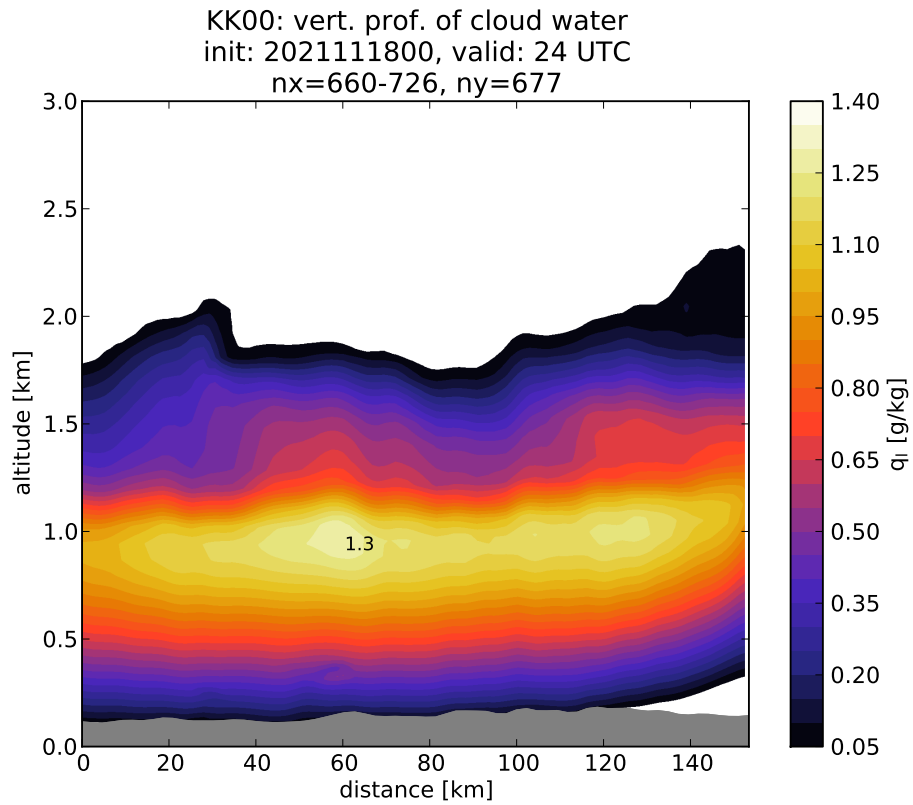
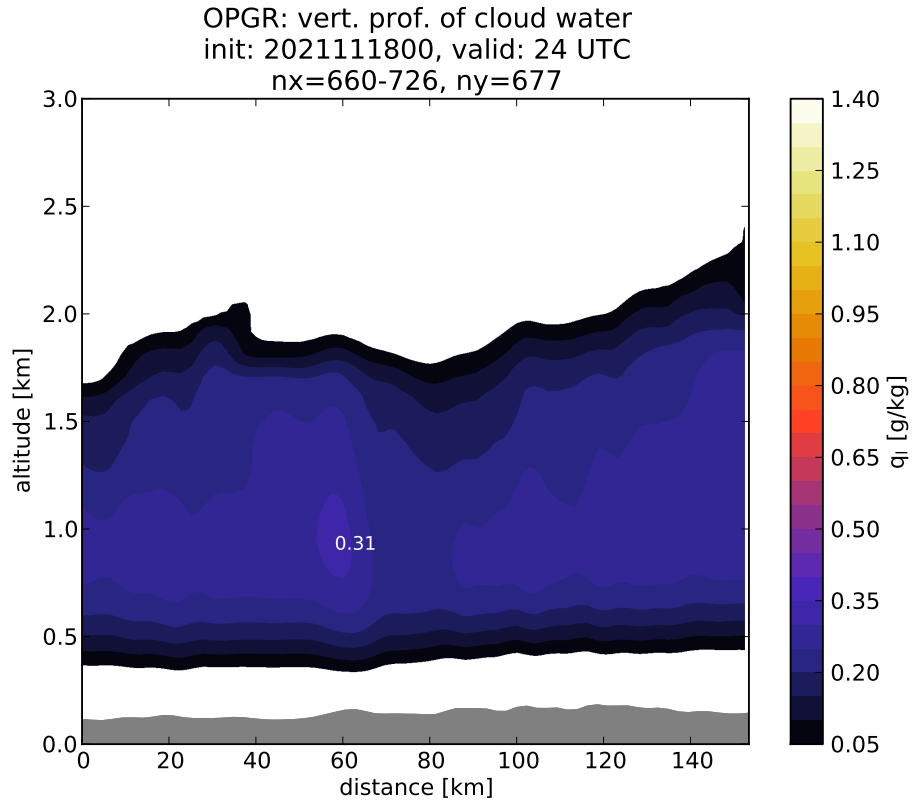


Figure 7.10: Vertical cross section of the specific content of cloud water through a stratocumulus cloud, which produced very little precipitation in the case of OPGR (upper) and no precipitation in case of KK00 (lower).

Table 7.1: Experiments with Sundqvist autoconversion.

experiment	k_r	r_l^{crit}
OPGR	0.5	0.3
AKR1	0.5	0.4
AKR2	0.5	0.5
AKR3	1	0.4
AKR4	1	0.5

be the best option as the overestimation of q_l is only local in the strongest cores of updraughts.

This modification does not significantly impact model results in summer convection cases because the liquid water content in cumulonimbi is significantly higher than the autoconversion threshold. Thus, as it improves model results in autumn, this modification is found beneficial and is included in the final proposal for microphysics modifications.

7.2 Evaporation

Another process to investigate is evaporation. As mentioned in Section 4.4, ALARO currently uses the Kessler-type of evaporation parameterization. There is also a possibility to use another evaporation scheme following Lopez [2002], who used the typical parameterization of evaporation following Equation (2.33). The evaporation parameterization following Lopez [2002] should deliver more evaporation. Thus, cooling of lower levels and lower precipitation accumulations are expected, which might be beneficial mainly in autumn and winter.

In the standard ALARO code, this parameterization is available only for rain and snow with parameters taken directly from Lopez [2002]. In this thesis, this parameterization was extended for rain with the fall speed relation used in ALARO (which differs from that used by Lopez [2002]), rain with the modification of the intercept parameter proposed by Abel and Boutle [2012], and graupel. The final equation for evaporation is in the form

$$\frac{dq_j}{dt} = \frac{(1 - RH)(1 - f_c)}{\rho_a(\mathcal{K}_r + \mathcal{D}_r)} \cdot \left[C_1 (\rho_a q_r)^{C_2} + C_3 (\rho_a q_r)^{C_4} p^{\frac{1}{3}} \right], \quad (7.4)$$

where \mathcal{K}_r describes the thermal conduction in humid air, \mathcal{D}_r describes the diffusion of water vapour in the air in the presence of precipitation Lopez [2002]. Finally, C_j ($j \in \{1, 2, 3, 4\}$) are coefficients of which values are listed in Table 7.2, both the newly derived and the original for snow.

The untypical shape of the dependency of the evaporation rate of rain on the specific content of rain for the modification of the intercept parameter following Abel and Boutle [2012] is shown in Figure 7.11. There are higher evaporation rates for tiny particles because the low specific content of rainwater delivers a lot of little drops. The full derivation of these formulae can be found in Appendix A.5, which also explains the shape of this dependency.

Table 7.2: List of parameters used in the evaporation parameterization following Lopez [2002]. Superscripts r , s and g stand for the corresponding parameters of rain, snow (unchanged), and graupel, respectively. MP stands for the Marshall-Palmer size distribution and AB for the modification of the intercept parameter by Abel and Boutle [2012]. New graupel is graupel with the new set of parameters introduced in Chapter 6 and old graupel is graupel parameterized in the original way; that is, mechanical properties of rain and thermodynamic of snow.

coefficient	rain with MP	rain with AB12	snow
C_1	$0.0874 \cdot (N_0^r)^{1-C_2^r}$	2.2295	$9.736(1 - N_0^s)^{C_2^s}$
C_2	0.5	$-1/9$	$2/3$
C_3	$1.437 \cdot (N_0^r)^{1-C_4^r}$	8.738	2373.7
C_4	0.721	0.3807	1

coefficient	new graupel	old graupel
C_1	$0.115 \cdot (N_0^g)^{1-C_2^g}$	$0.833 \cdot C_1^r$
C_2	0.5	C_2^r
C_3	$1.75 \cdot (N_0^g)^{1-C_2^g}$	$1.419 C_3^r$
C_4	0.7075	$1.419 \cdot C_4^r$

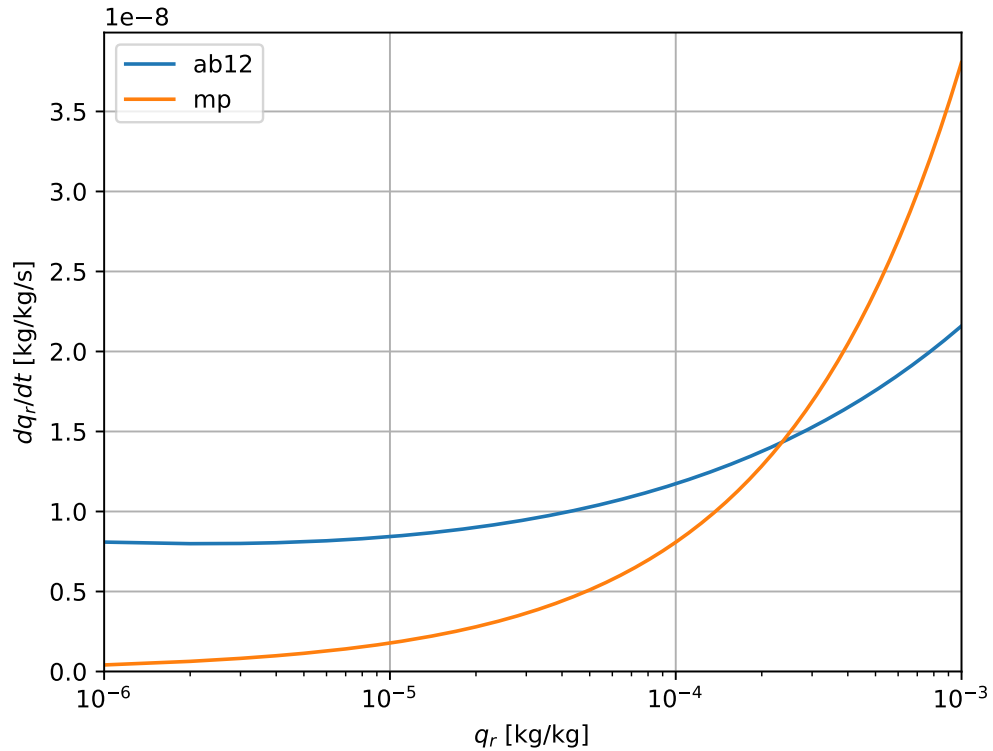


Figure 7.11: The shape of the Lopez evaporation function for rain with the Abel-Boutle size distribution (AB) and with the Marshall-Palmer distribution (MP).

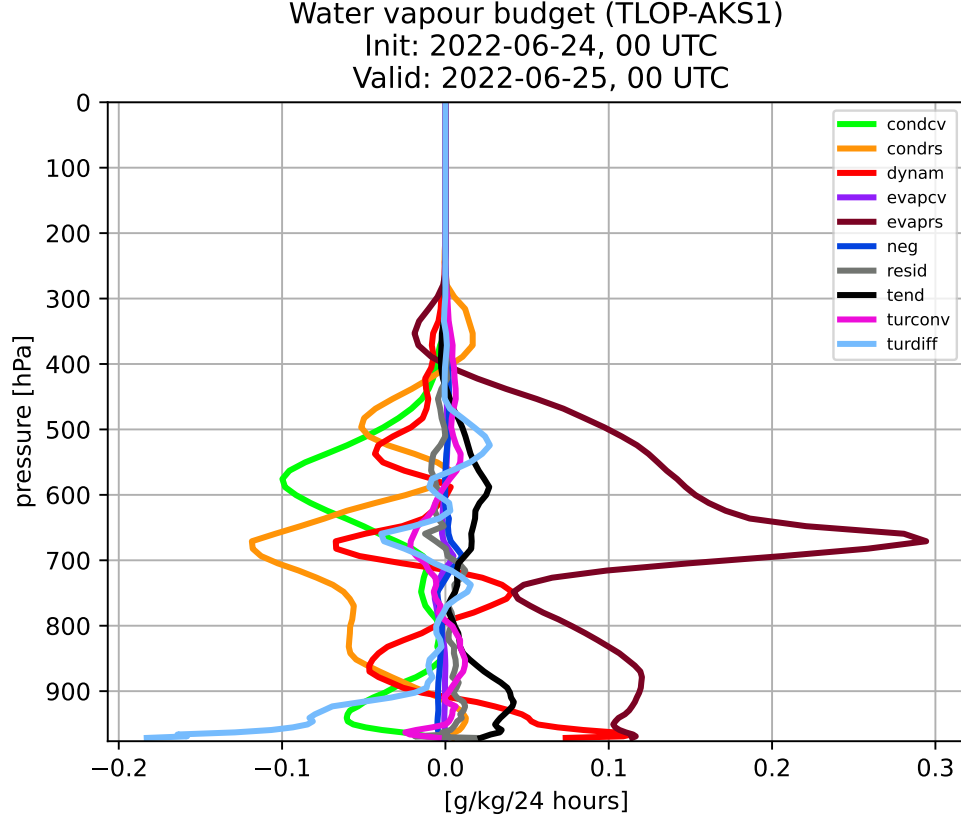


Figure 7.12: The water vapour budget difference between TLOP and AKS1 for a summer convection case.

7.2.1 Behaviour of the Lopez scheme

The Lopez evaporation scheme was tested with the coefficient of ice to snow autoconversion $k_s = 10^{-3} \text{ s}^{-1}$. Thus, it is compared with AKS1.

The water vapour budget for a summer convection case (Figure 7.12) shows enhancement of the resolved evaporation of precipitation, which leads to more active resolved condensation. The convective condensation slightly compensates for the effect of the resolved one, but the absolute value of its magnitude is smaller. There is an apparent influence of the turbulence and dynamics, which compensates for the enhanced evaporation. This is caused by less vertical transport due to the colder surface. It also causes the shape of the contribution of turbulence to the temperature budget. The contribution of microphysics to the temperature budget is driven by which process of evaporation or condensation prevails. However, the majority of the troposphere is significantly cooled by microphysics (Figure 7.13), meaning that evaporation predominates for most vertical levels. In a few lowermost layers is a different contribution of turbulence and dynamics to the temperature budget due to the modified vertical temperature profile.

One of the implications of this modification is more graupel due to the sublimation of snow, especially just above the melting layer in the later stages of storm development, as shown in Figure 7.14. The mechanism is such that the enhanced sublimation of snow saturates the air with water vapour; thus, condensation occurs. Because in this regions are higher temperatures than in the area where

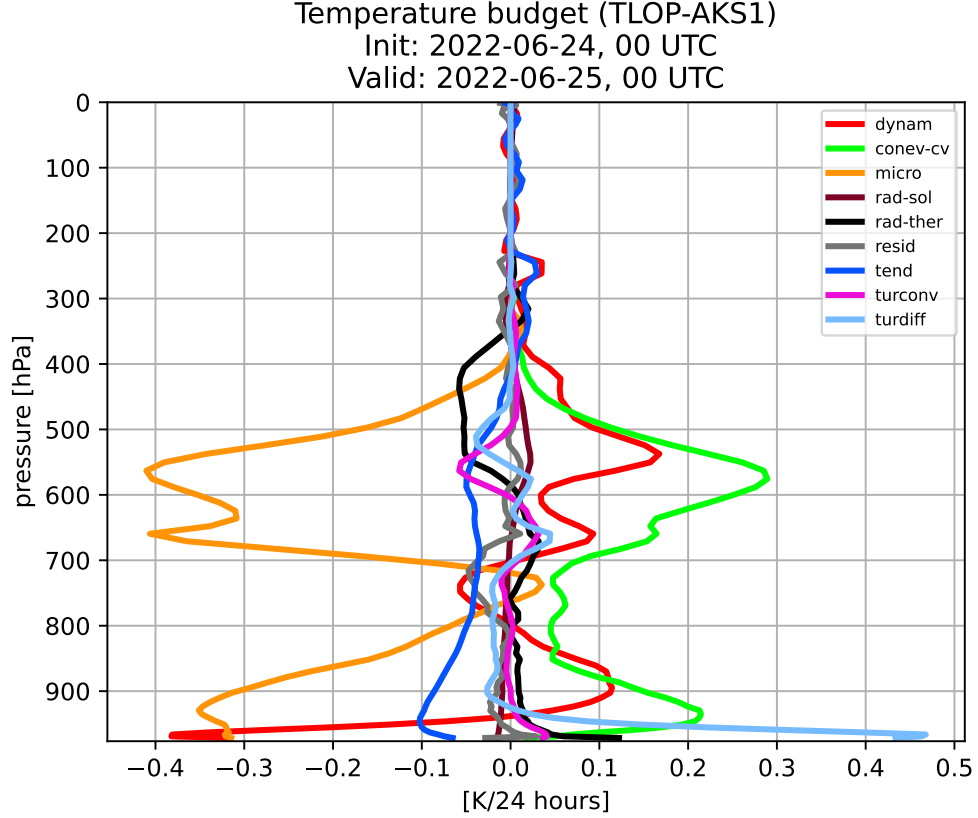


Figure 7.13: The temperature budget difference between TLOP and AKS1 for a summer convection case.

the sublimated snow was produced, often more than half of the condensates are liquid (see Figure 4.2). Therefore, more autoconversion to graupel and less to snow occurs, leading to more graupel and less snow in these layers.

Also, this modification leads to decreased precipitation accumulations in autumn and winter, especially when the cloud base is higher, making the rain shadow more pronounced. Because of the shape of the dependence of evaporation rates on q_l , weak precipitation is evaporated efficiently. Of course, drizzling stratus or stratocumulus touching the ground are not affected by this modification of evaporation if the whole grid box is filled with a cloud ($C = 1$).

The precipitation maxima are reduced. This tendency was observed in several cases. Nonetheless, the maxima of the instantaneous fluxes are not necessarily decreased. The same holds for 1-hour precipitation accumulations, which are not significantly decreased. On the other hand, 6-hour accumulation maxima are decreased in the case of mesoscale convective systems (MCS). However, the tendency to lower precipitation maxima is not always observed in the case of single-cellular storms. Thus, for the summer period in 2009, a significant decrease in the precipitation accumulation maxima is not observed, although it is observed for the summer periods of 2021 and 2022.

Another feedback is that convective storms occasionally reach further as a stronger cold pool is created, causing the storms to move slightly faster. This was observed on 2021-06-29, when a MSC crossed Czechia (Figure 7.15). This

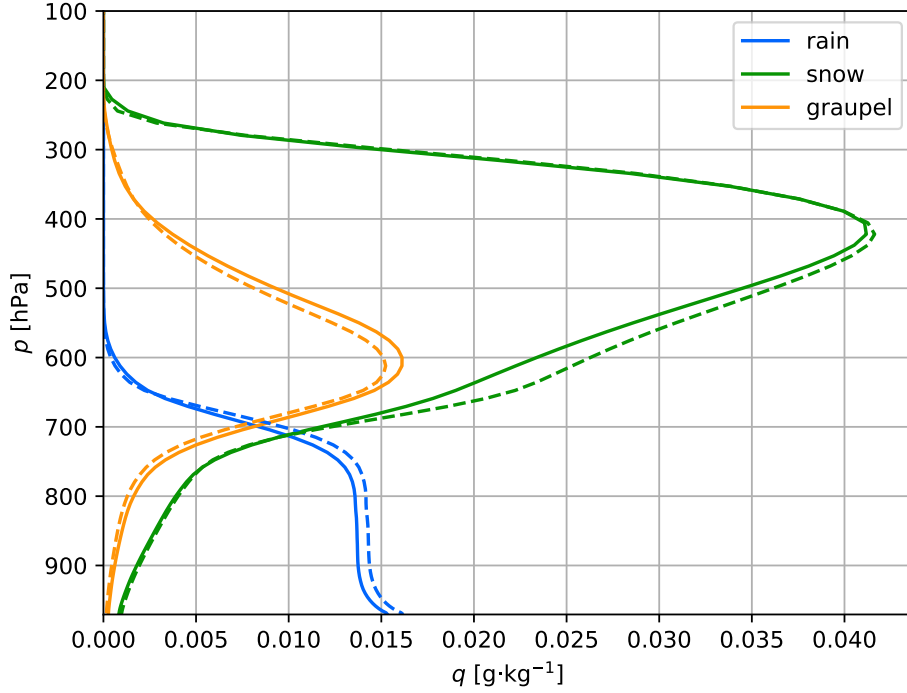


Figure 7.14: Vertical profiles of the specific content of hydrometeors for the convection case 2022-06-24 at 18 UTC. Solid lines are used for TLOP and dashed lines for AKS1.

can also contribute to the reduction of precipitation maxima.

This modification significantly lowers 2-metre temperature with a magnitude of around 0.1 K. This is caused by the overall decrease in the temperature of the troposphere. However, there is still present a warm bias in the troposphere all the way down to 850 hPa compared to observations. However, at the surface, the 2-metre temperature is usually predicted lower than observed and is further decreased by this modification. This can be compensated by reducing the positive precipitation bias, which consequently causes reducing the amount of water in the ground water reservoir. Thus, the latent heat flux is reduced and the 2-metre temperature is raised. Nonetheless, this mechanism works only if there is enough precipitation.

A case which is significantly improved using this parameterization is the case of snowfall in Austria. In this case, ALARO overestimates snowfall on the lee side of the Alps, while AROME underestimated snowfall in Inntal valley, where no snow was predicted, while non-negligible snow accumulation was reported in Innsbruck. The precipitation accumulation (all in solid phase) is shown in Figure 7.16. The Lopez evaporation parameterization provides the most realistic results of those three options.

The impact of this modification is significant, but not always positive. It worsens the surface scores of wind (both speed and direction) and the bias of 2-metre temperature and geopotential at the surface. Conversely, the majority of the upper air scores is improved. Fundamentally, it improves the precipitation field. Therefore, it is included in the proposal for the modifications of microphysics.

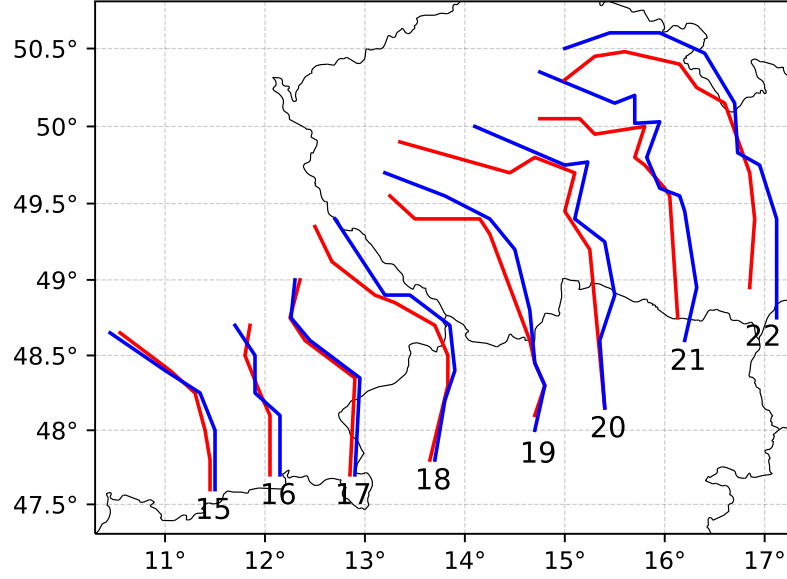


Figure 7.15: Evolution of the leading edge of the MSC on 2021-06-29. Configuration OPGR is denoted by red lines, ELOP by blue lines. Note that ELOP moves a little bit faster.

7.3 Cloud overlap

As was described in Section 4.5, a specific approach to the parameterization of cloud overlap with the decorrelation parameter ε is applied in ALARO. In radiation, ε is operationally computed according to the seasonal variations of sun angle, and it is proven to work well. This option is also available in microphysics. Thus, it is tested here, and CLOV denotes this model configuration.

Since the influence of the decorrelation depth ε has a higher impact on convection, the summer period from 2021-06-21 to 2021-06-30 was chosen for tests. The temperature budget (Figure 7.17) shows that while microphysics significantly cools below 800 hPa and strongly heats up above 750 hPa, the convective condensation and evaporation compensate for this effect. As expected, there is more evaporation of precipitation; thus, the specific humidity q_v is raised. There is not a big difference in the hydrometeor's budgets; only graupel is more concentrated around 600 hPa.

Atmospheric scores for this period confirm the rather extensive influence of this modification on meteorological fields. Sadly, most of the statistics were worsened. Geopotential shows a clear dipole pattern, where higher geopotential is from the surface to 600 hPa and lower elsewhere. Its RMSE and STDE are worsened. Temperature is decreased throughout the whole troposphere, more in lower layers. The bias of upper air relative humidity is improved as there is more moisture. Its STDE is subtly worsened, while its RMSE is neutral due to the improved bias. Quite interesting is the feedback to wind speed, which is predominantly decreased below 700 hPa, which is beneficial as its bias is reduced. In spite of this improvement, wind speed STDE and RMSE are worsened. The upper air RMSE and STDE of wind direction are slightly worsened.

Regarding the surface scores, the RMSE and STDE of geopotential are wors-

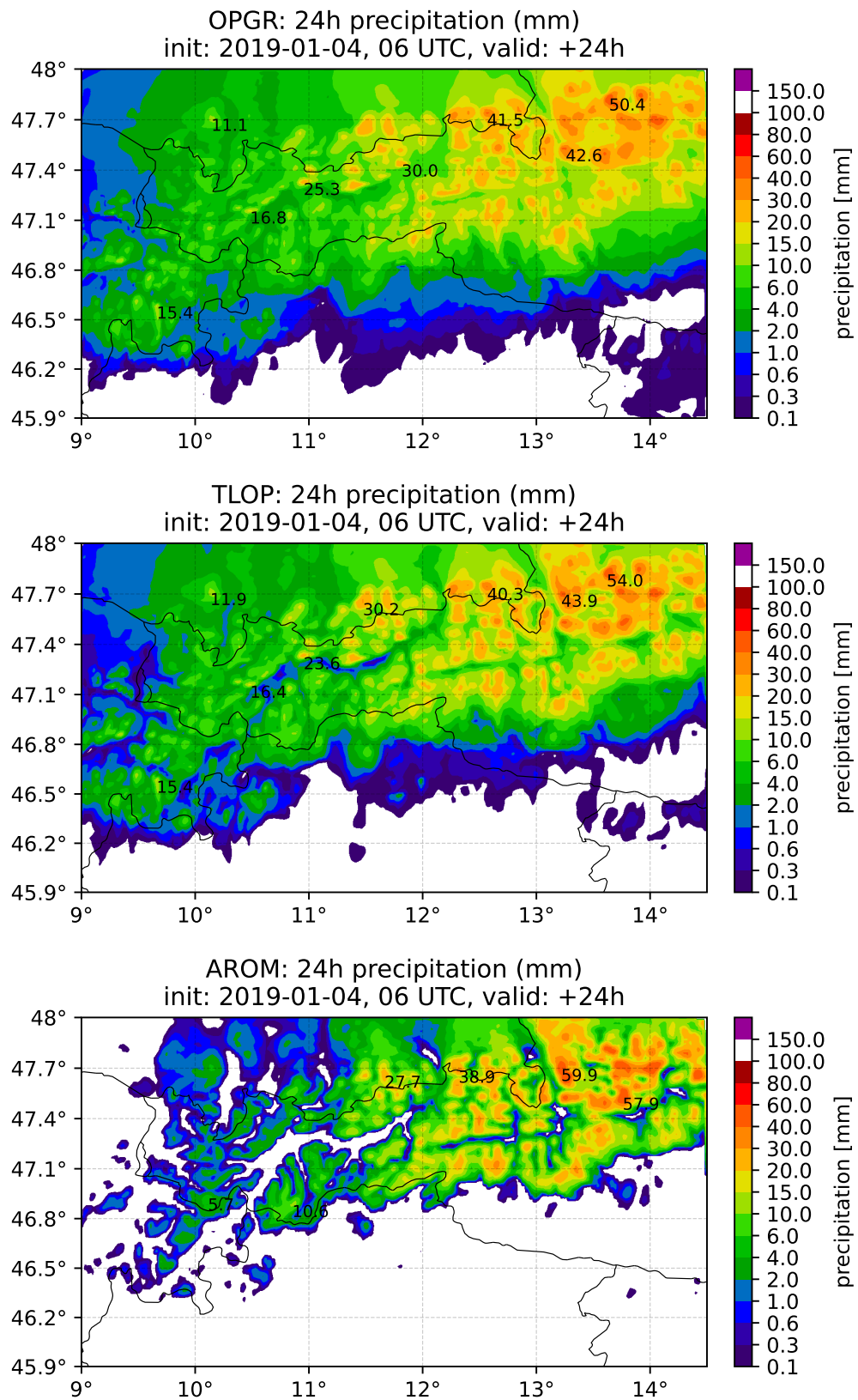


Figure 7.16: 24 hour precipitation accumulation for the case of snowfall over Austria.

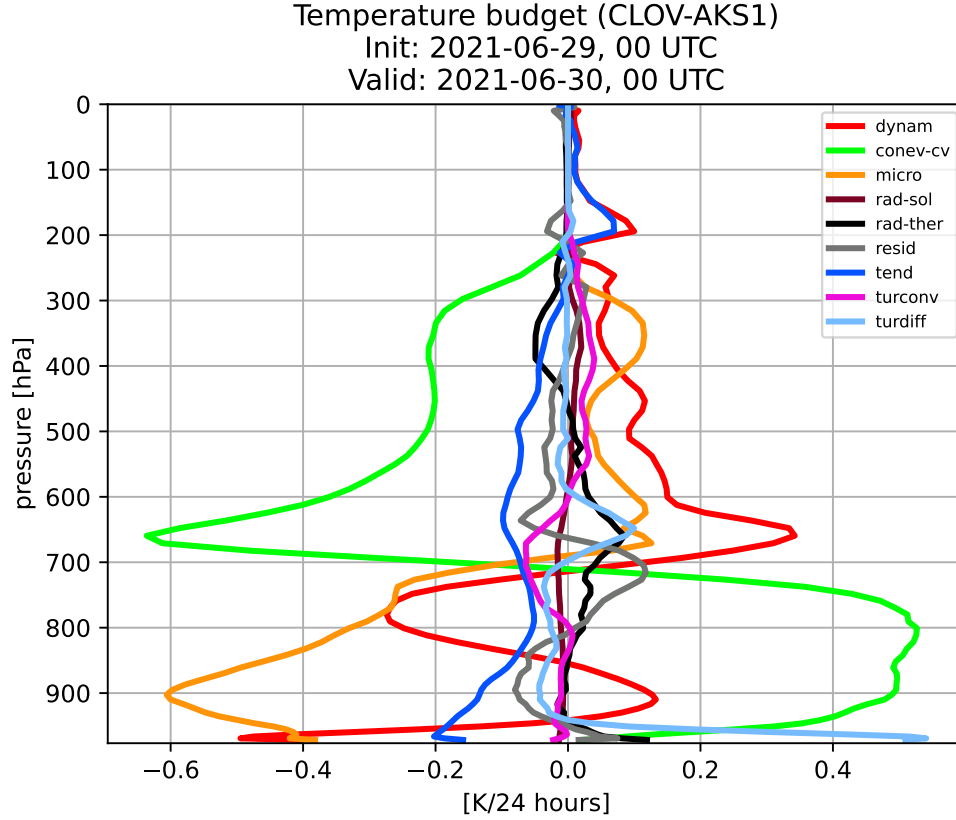


Figure 7.17: Temperature budget difference between CLOV and AKS1 for a summer convection case.

ened, and its already positive bias is more pronounced. The difference in the temperature bias shows cooling up to 0.2 K at the surface at 18 UTC, 42 UTC, and 66 UTC (Figure 7.18). Otherwise, the cooling is around 0.1 K. As expected, the p-value of the t-test at the surface exceeds the probability threshold of 0.9973 for all forecast ranges. The RMSE and STDE of temperature are again worsened. The bias of RH2m is accentuated during the daytime, while its negative bias at night is damped. The wind direction is turned more to the meridional direction at the surface, which reduces the present bias. The bias of precipitation is unchanged. There is more cloudiness. The STDE and RMSE of cloudiness and precipitation are improved.

Sadly, it seems that despite delivering more physical realism, this modification worsens model results. Thus, it is not used further.

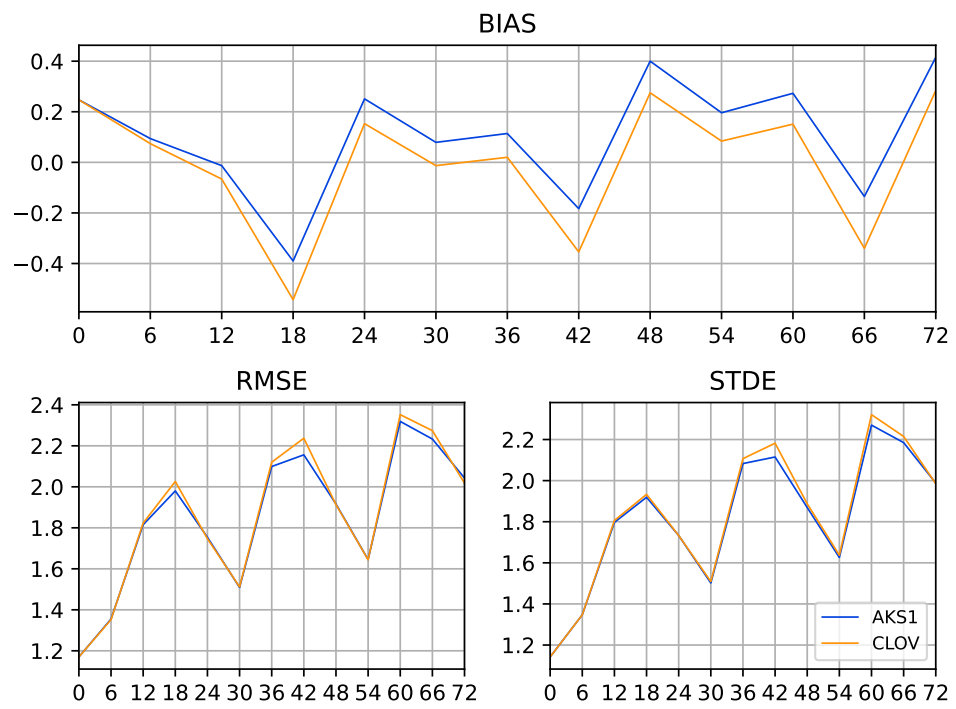


Figure 7.18: Precipitation bias, RMSE and STDE of CLOV and AKS1 for the summer period from 2021-06-21 to 2021-06-30.

8. Validation of microphysics developments

Following the tests in the previous chapter, the set of modified parameters for autoconversion, which is $k_s = 10^{-3} \text{ s}^{-1}$, $q_i^{crit} = 4 \cdot 10^{-4} \text{ kg} \cdot \text{kg}^{-1}$, the computation of q_i^{crit} following Chaboureaud and Pinty [2006], and the parameterization of evaporation used by Lopez [2002] are grouped into one package. This package is evaluated in this chapter for selected periods and cases introduced in Section 5.2. In the following, model configurations with the new package with the assimilation cycle are denoted by MPKA, and runs of the new package without assimilation by MPKN. The model configuration OPGR is used as a reference.

8.1 Summer period 2009

As mentioned in Section 5.2, the period from 2009-06-24 to 2009-07-04 is unique because of many single-cellular storms. Therefore, it is still useful despite the lower quality of the boundary and initial conditions. The assimilation cycle was rerun for both model configurations, OPGR and MPKA. The assimilation cycle of MPKA started ten days prior to the first production, and its first assimilation run started from the already prepared analysis for OPGR. All model integrations were initialized at 00 UTC.

The simulated diurnal cycle of precipitation match observations almost perfectly (Figure 8.1), thanks to the well-adjusted deep convection parameterization. The precipitation magnitude is irrelevant as the data were summed over the MERGE domain, which exceeds Czech borders, where its quality declines as there is no information from rain gauges. However, model configurations can still be compared with each other. The diurnal cycle is very similar for all experiments (OPGR, MPKA, and MPKN (not shown)); only the runs with the new evaporation parameterization have a subtle tendency to terminate rainfall earlier. This shows that the diurnal cycle is not much influenced by these microphysics changes, unlike the precipitation bias.

The upper air atmospheric scores of temperature show that the troposphere is colder (Figure 8.2). This improves the temperature bias for the majority of the troposphere. The RMSE of temperature is improved throughout the troposphere. Its STDE is also a little bit improved.

Figure 8.3 shows that geopotential evinces the typical dipole with more mass below 700 hPa and less above 700 hPa. The |BIAS| of geopotential is improved for 850 hPa and 700 hPa, neutral higher, and slightly worse in the upper troposphere at 300 and 250 hPa. The RMSE and STDE of geopotential are improved throughout the troposphere except for the forecast range of +48h.

The troposphere is moister due to the enhanced evaporation and lowered first coefficient of ice-to-snow autoconversion k_s . This tendency reduces the bias of relative humidity below 400 hPa, except for the lowermost layers and near the tropopause. Its RMSE and STDE are slightly worsened above the boundary layer and more significantly in the boundary layer.

The tendency of the bias of wind speed is not clear. However, its RMSE

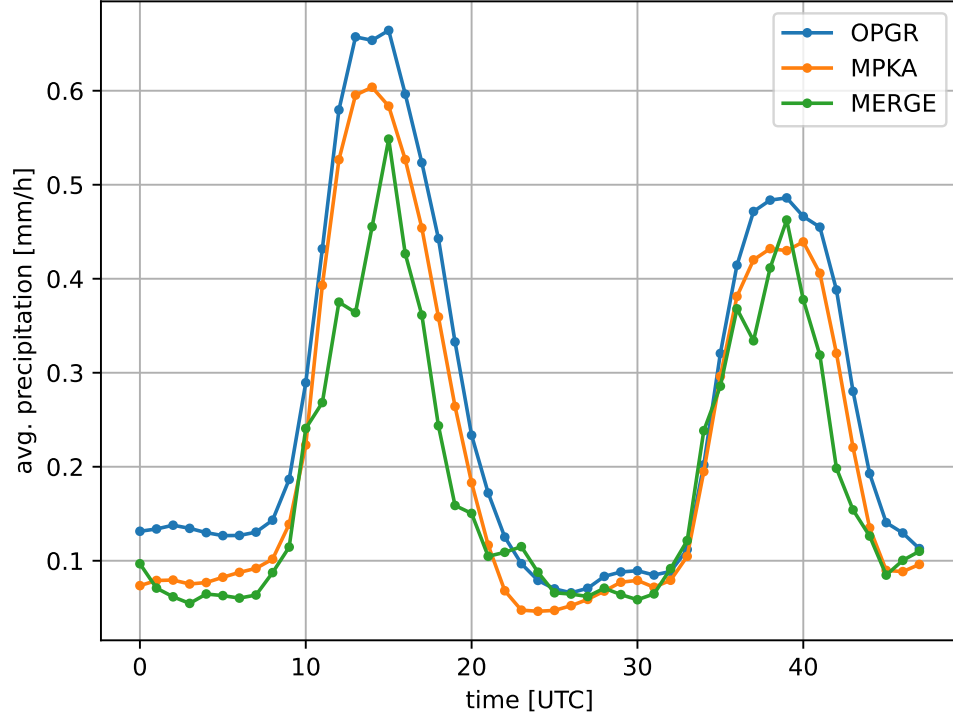


Figure 8.1: The diurnal cycle of precipitation in the summer period of 2009 from June 24th to July 4th. Model configurations MPKA (orange) and OPGR (blue) are compared to MERGE (green).

and STDE are reduced for most forecast ranges. The bias of wind direction is neutral, as well as its RMSE and STDE. Interestingly, the RMSE and STDE of both wind components are improved in the upper air, although the change is rarely statistically significant (not shown).

Unlike the upper air scores, the surface ones are worsened, as shown in Figure 8.4. Starting with T2m, its STDE and RMSE are statistically significantly worsened on the first day. Its bias is higher at 18 UTC for both days (at forecast ranges of +18 and +42 hours). The RMSE, STDE, and bias of geopotential and relative humidity are also worsened, as well as wdir10m and w10m, although the latter two are not worsened that much.

In addition, there is more cloudiness due to the change in k_s . Figure 8.5 shows that the positive bias of precipitation is significantly reduced.

The model configurations MPKA and MPKN modify the surface energy budget due to less precipitation and more cloudiness. Figure 8.6 shows the difference in various contributions to the surface energy budget between MPKA and OPGR for a summer convection case. Three contributors are changed significantly: the shortwave radiation, the sensible heat flux, and the latent heat flux. The leading cause is more clouds due to the adjustment of k_s . This results in cooling due to less shortwave radiation, lowering the latent heat flux, and making the surface warmer. The sensible heat flux approximately returns the budget to equilibrium by cooling. The most significant difference among these three budgets is shortly after 12 UTC. Generally, the resulting tendency shows warming in the morning and cooling during the day. The warming in the morning sometimes does not

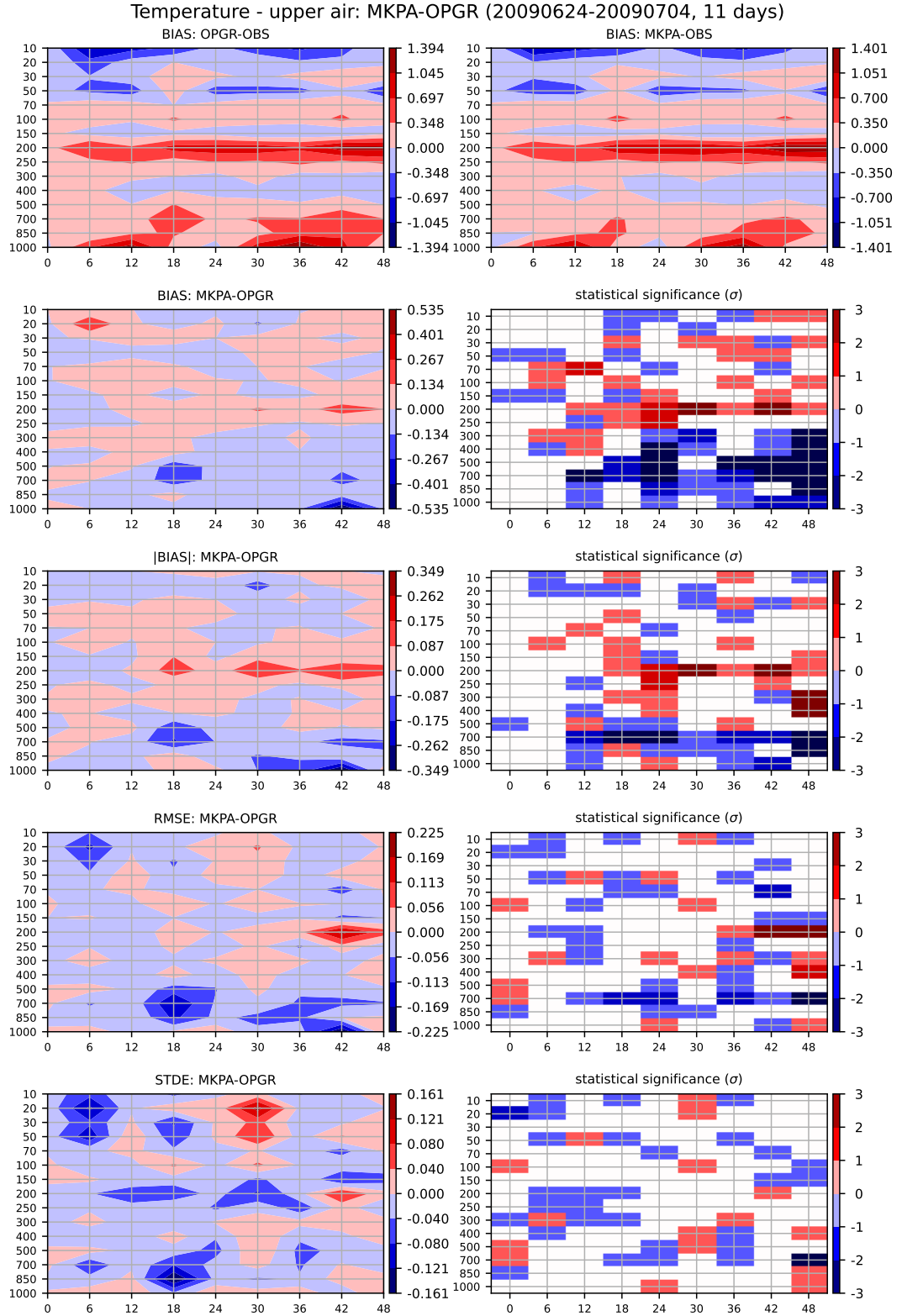


Figure 8.2: The upper air scores of temperature for the period from 2009-06-24 to 2009-07-04. Experiment MPKA is compared with OPGR, which is used as reference.

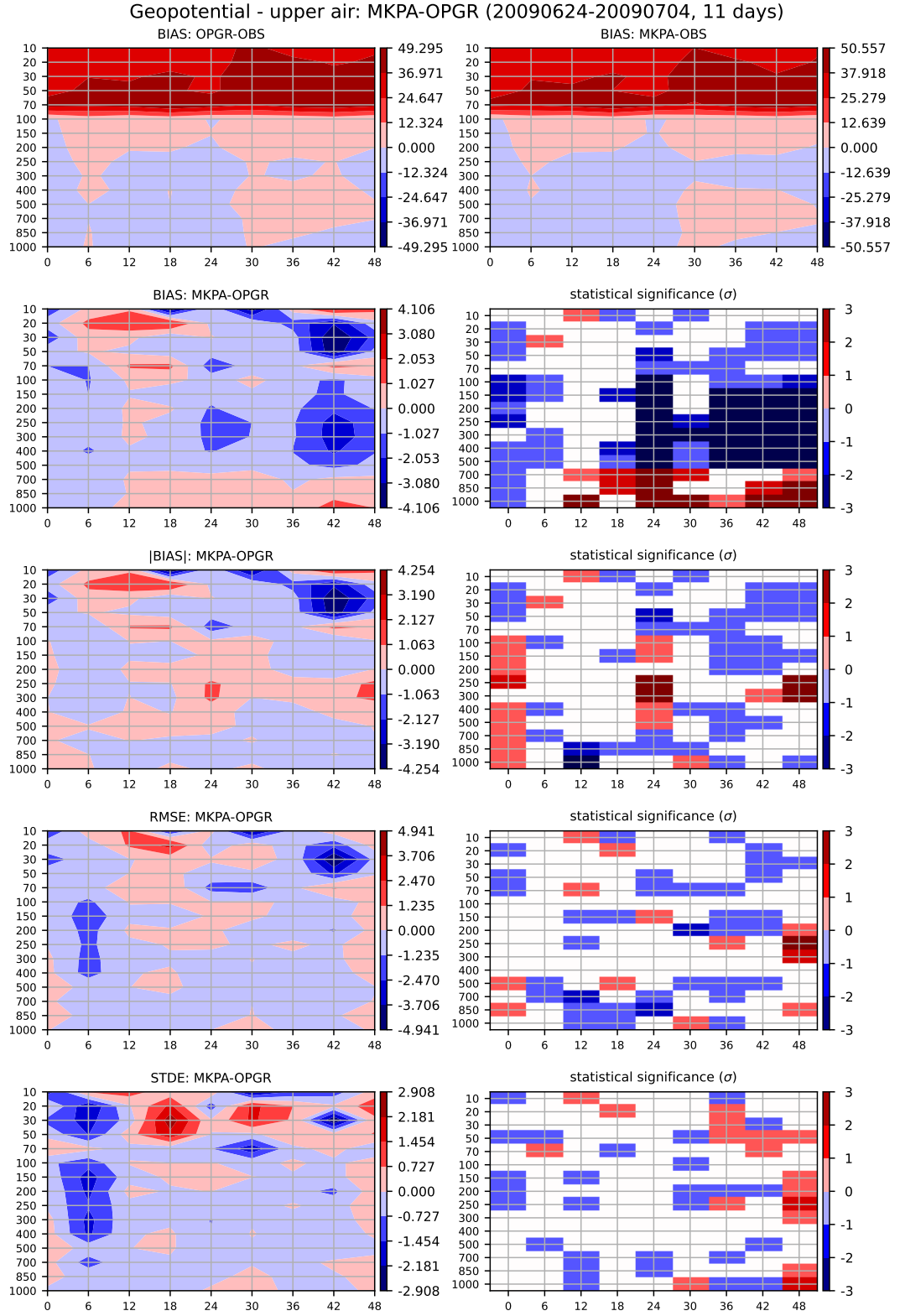


Figure 8.3: The upper air scores of geopotential for the period from 2009-06-24 to 2009-07-04. Experiment MPKA is compared with OPGR, which is used as reference.

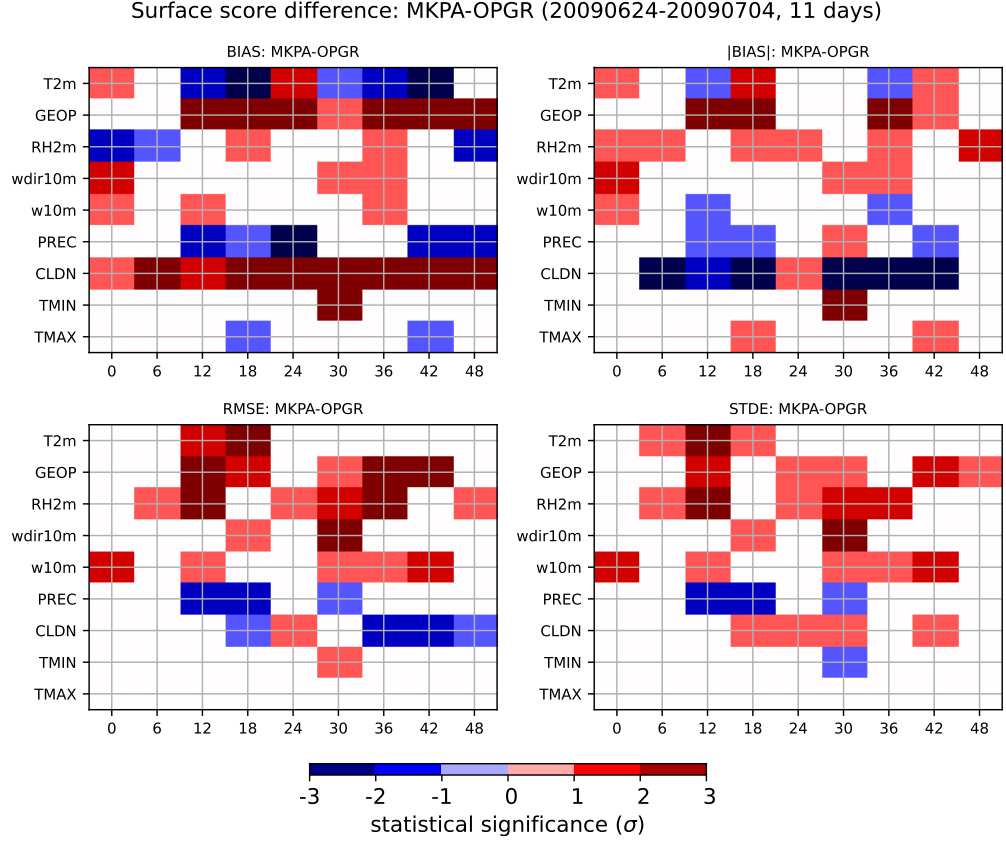


Figure 8.4: Surface scores for the period from 2009-06-24 to 2009-07-04. Experiment MPKA is compared with OPGR, which is used as reference.

occur, while cooling during the day is present regularly.

Various changes in parameters of the cloudiness scheme in radiation were tested to reduce the errors in the surface scores. The amount of cloudiness was raised by this modification as feedback to the higher autoconversion coefficient k_s ; thus, the aim is to reduce cloudiness. The amount of cloudiness in radiation can be lowered by adjusting the vertical profile of its critical relative humidity. However, none of the tested adjustments reduced errors, and results were usually even worse. The main objective was to reduce the temperature bias at 18 UTC and reduce the RMSE and STDE of temperature, which is worsened mainly at 12 and 18 UTC of the first days of model integrations. However, there was not reached a significant change in T2m at 18 UTC because the more the surface is heated up by shortwave radiation, the higher the sensible and latent heat fluxes are.

8.1.1 Influence of the assimilation cycle

As the assimilation cycle was run, it is possible to compare the difference in the groundwater reservoir as it evolved in the assimilation cycle (Figure 8.7). As this period delivered enough precipitation over the domain, the amount of groundwater was reduced by less precipitation as a consequence of more effective evaporation of precipitation.

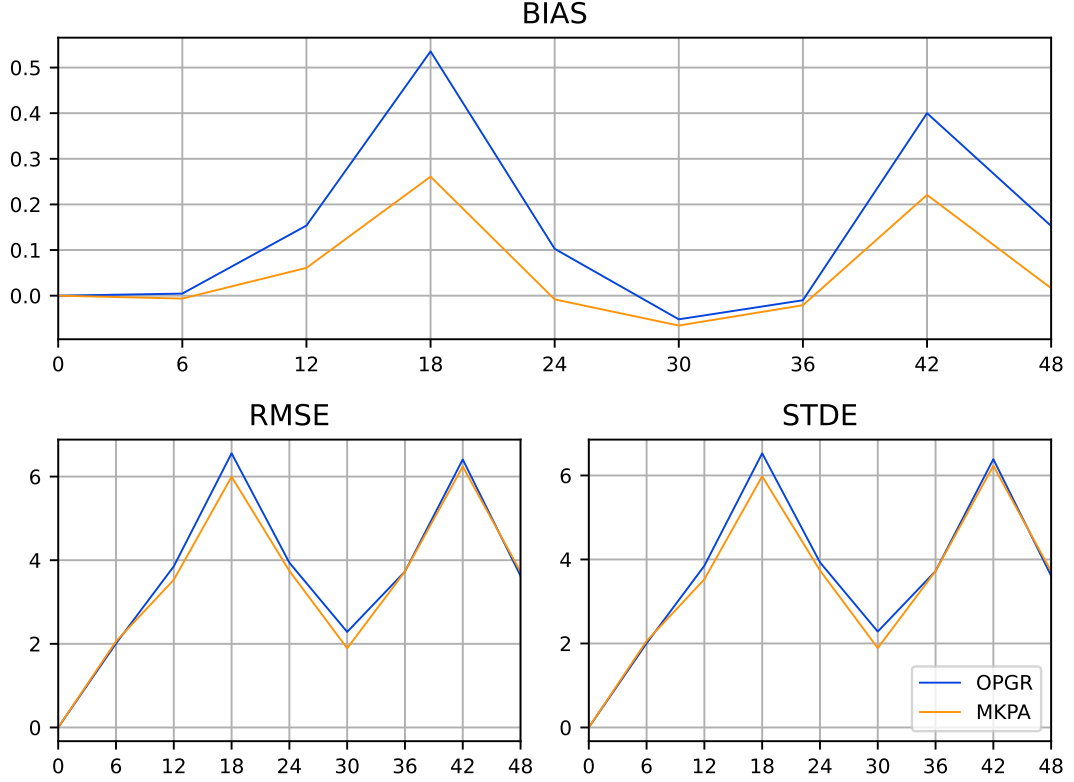


Figure 8.5: Bias, RMSE and STDE of precipitation in the summer period of 2009 between 2009-06-24 and 2009-07-04.

As there is less groundwater, less evaporation from the surface occurs. Thus, the effect of the latent heat cooling at the surface is lowered. This helps to partially reduce the bias of T2m. However, it does not significantly modify the RMSE and STDE of T2m. It affects RH2m similarly, which confirms that there is less evaporation from the surface. The positive bias of RH2m at terms 12 UTC and 18 UTC is reduced, while its RMSE and STDE are almost untouched. The surface energy flux budget confirms this.

8.2 Summer period 2022

Experiment MPKN was run for the period from 2022-06-21 to 2022-06-30. Later, the assimilation cycle was also run starting from 2022-06-10 to deliver better initial conditions for MPKA. In this case, forecasts from 2022-06-20 were run, and the period was later extended till 2022-07-10. All forecast integrations were initialized at 00 UTC. For most of this section, only MPKA is compared to OPRG, as the results of MPKN are generally slightly improved by the assimilation cycle.

This time, the groundwater reservoir is less influenced as this period was preceded by a dry period with high temperatures and almost no precipitation over the domain. Thus, the amount of groundwater was mostly the same. It was even temporarily raised as the decreased first coefficient of ice to snow autoconversion delivers more clouds, which lessen evaporation from the ground.

Firstly, general characteristics based on various statistical methods are dis-

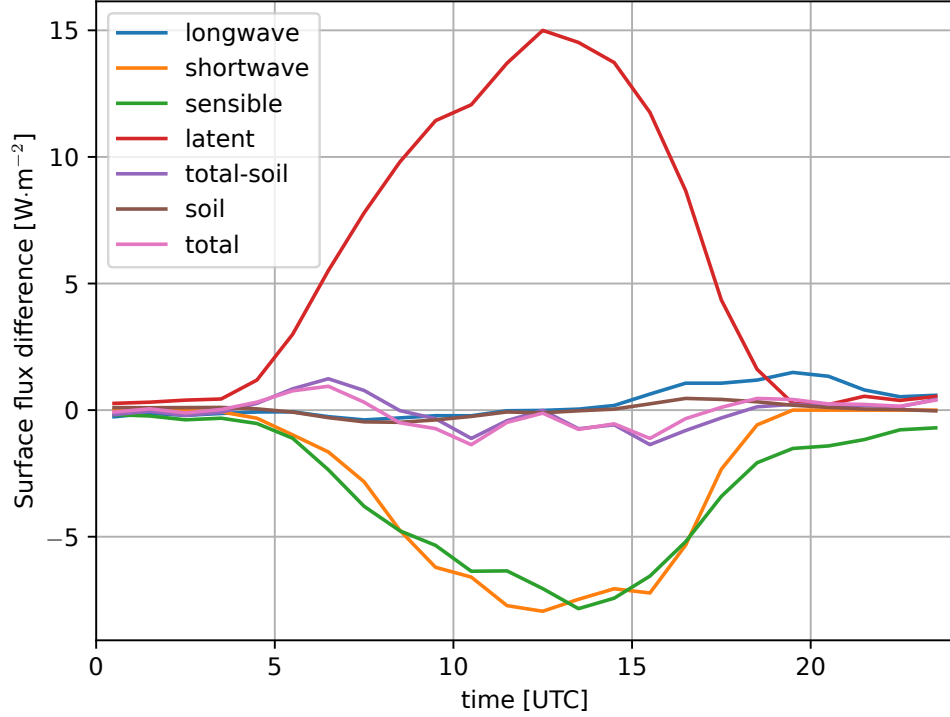


Figure 8.6: The difference of components of the surface energy budget between MPKA and OPGR (used as reference) on 2009-07-02. The flux towards the surface is positive. Data are averaged over the domain.

cussed. For this period, the forecasts of the precipitation field are later subjectively evaluated day by day.

8.2.1 Atmospheric scores

The only significantly worsened upper air score is the geopotential one (Figure 8.8). It is noticeably worsened below around 500 hPa (all statistics). The biggest detriment is in ranges $\in \{18 + 24i \text{ UTC}, i = 0, 1, 2\}$. On the other hand, its RMSE, and bias are significantly improved higher above, and STDE is there rather neutral.

There is a statistically significant reduction of $|\text{BIAS}|$ of the upper air temperature for almost all elevations between 1000-400 hPa and all ranges except +24h. The RMSE of temperature is slightly improved except for ranges of +24h and +48h. The biggest and most statistically significant reduction is again for the later stages of the forecast. In contrast, the STDE of temperature is slightly worsened, mainly at 700 hPa, which is close to the melting layer. However, the change is minimal, and most of the slightly worsened elevations and ranges are not statistically significant. It is evident that the change in the evaporation parameterization greatly outweighs the effect of autocnversion modifications, which have a warming or neutral effect.

The changes of bias, $|\text{BIAS}|$, RMSE, and STDE of the wind speed are statistically insignificant. The statistics of wind components are neutral. The $|\text{BIAS}|$ of wind direction is reduced for the upper air scores, mainly in the later stages of

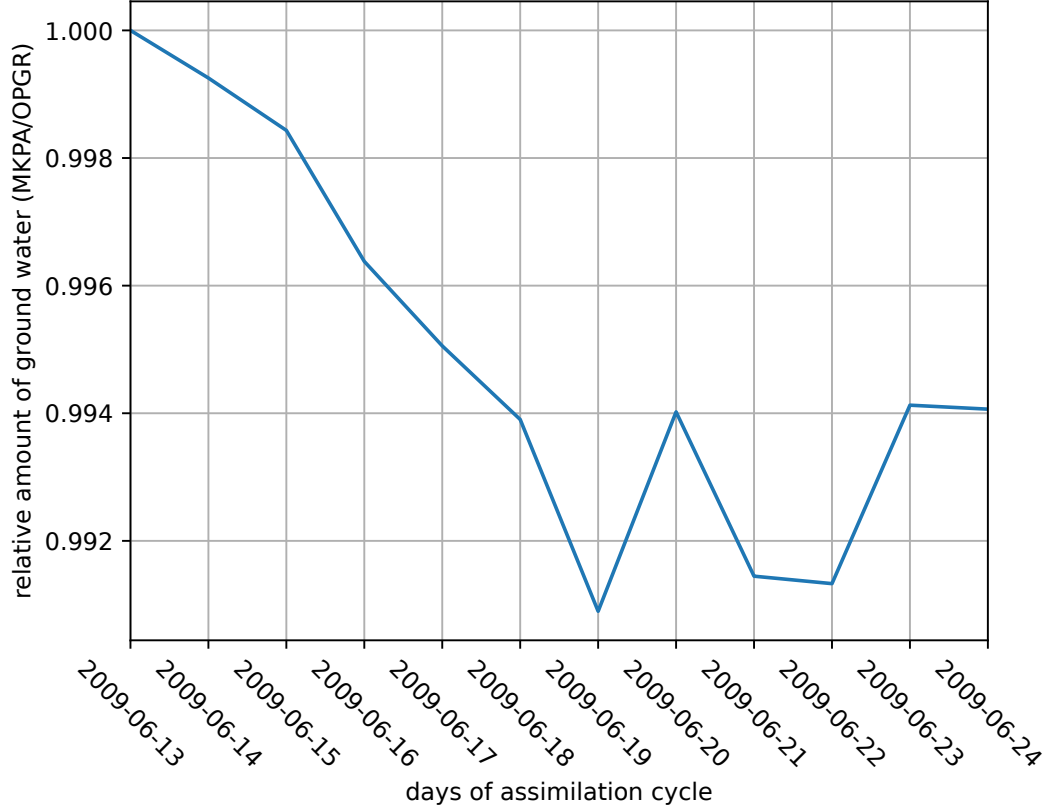


Figure 8.7: The evolution of the ratio of the amount of groundwater in MPKA to the amount of groundwater in OPGR during the assimilation cycle. Values are spatially averaged over the domain. Values over sea are filtered out.

the forecast range, where the improvement is throughout the troposphere. The RMSE and STDE of wind direction are improved for the latest forecast ranges.

There is a significantly reduced $|\text{BIAS}|$ of RH throughout the troposphere except for 1000 hPa. The magnitude of this change is around 0.5-1 % for ranges $\in \{18 + 24i \text{ UTC}, i = 0, 1, 2\}$ and elevations 850-400 hPa. Its RMSE is slightly improved, and its STDE is neutral.

Regarding the surface scores, there is a positive bias of geopotential. The RMSE and STDE of T2m are reduced for the period from 2022-06-20 to 2022-06-30 with many convective storms. There is the expected cold bias even with the assimilation since the 10th of June. However, for the extended period to the 10th of July, the reduction of the RMSE and STDE is rather subtle, and the tendency is not distinct; the negative bias remains. The bias of RH2m is worsened. The STDE and RMSE of wind speed and wind direction are worsened at the surface. Overall, the surface scores are very similar to those for the summer period of 2009.

There is more cloudiness due to modifying the autoconversion coefficient k_s , which is the only characteristic not dominated by the new evaporation parameterization.

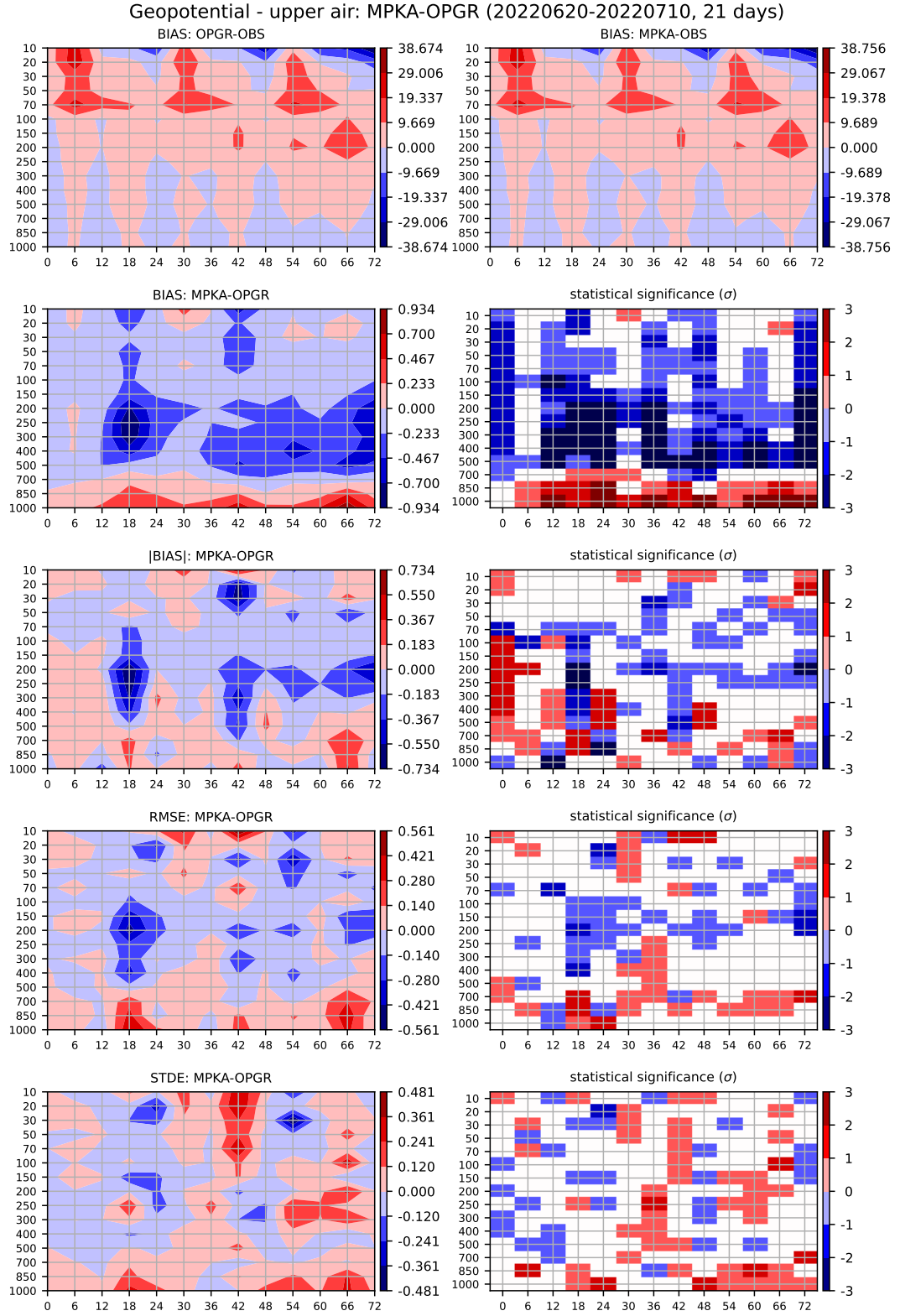


Figure 8.8: The upper air scores of geopotential for the period from 2022-06-20 to 2022-07-10. Experiment MPKA is compared with OPGR, which is used as reference.

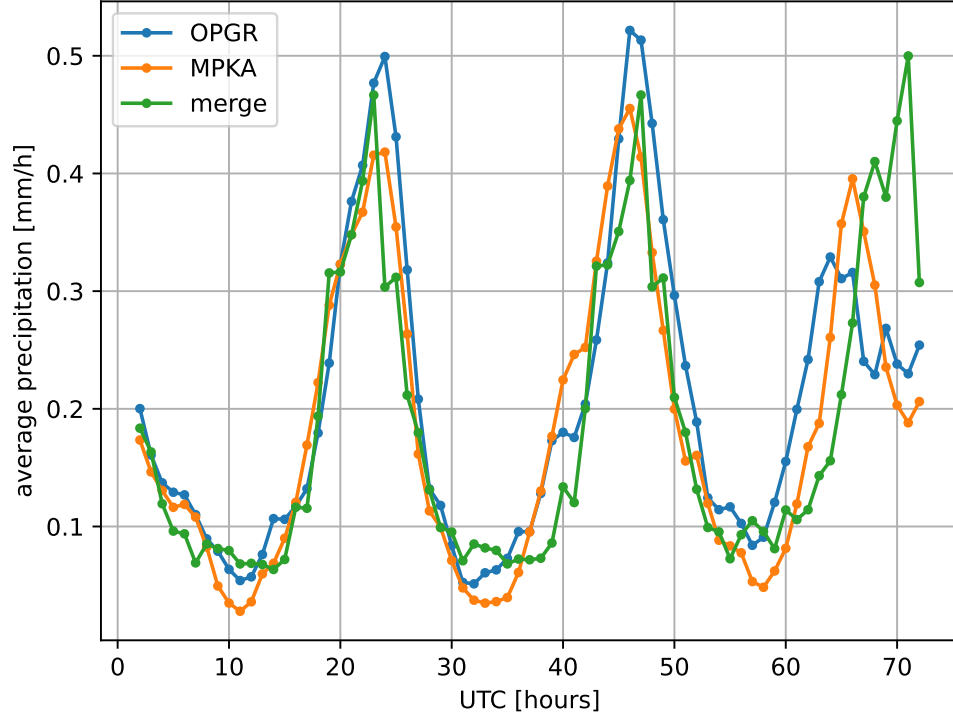


Figure 8.9: The diurnal cycle of precipitation in the summer period of 2022 from June 21st to June 29th. Model configurations MPKA (orange) and OPGR (blue) are compared to MERGE (green).

8.2.2 Validation of precipitation

The atmospheric scores confirm the tendency of less precipitation; lower precipitation accumulations are a stable feature. The positive bias of precipitation for the first day is reduced. However, in this case, the other days of integration suffered from a slight negative precipitation bias even for OPGR, which MPKA further intensifies.

The diurnal cycle of precipitation is not much modified by this change (Figure 8.9). The difference between model configurations and MERGE is subtle for the second day. The last day has the lowest uncertainty of the forecast; therefore, there are also the most significant differences between the model and observations. The diurnal cycle of convection is strongly determined by the deep convection parameterization; this only verifies that these modifications of microphysics do not much influence the diurnal cycle of precipitation.

The fractional skill score was computed for the period from 2022-06-21 to 2021-06-29. The results substantially differ for different forecast ranges. However, FSSs at the most crucial forecast ranges at 18, 24, 42, 48, and 66 UTC are slightly improved. Only the FSS at the forecast range of +72h is worsened. The FSSs for +18h and +42h are similar, and FSSs for forecast ranges +24h and +48h are similar. Figure 8.10 shows the averaged FSS over all forecast runs for six-hour accumulations ending at 18 UTC on the first day of forecasts. There is almost no change in FSS for the lowest three thresholds, less than 1 mm/6h. For thresholds 2 mm/6h and 5 mm/6h, the positioning of such precipitation seems

Mean FSS of range +18h for several precip. thresholds

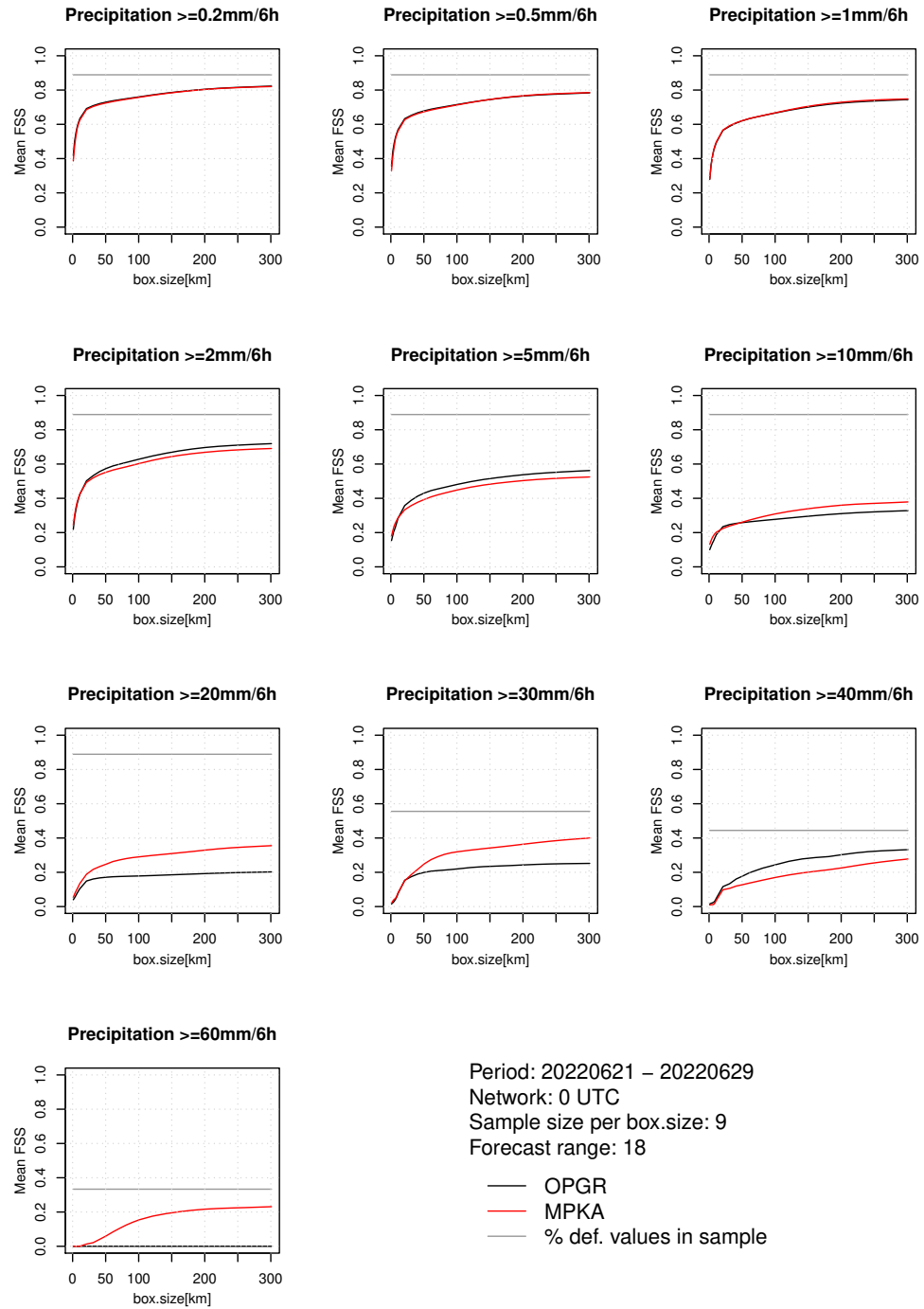


Figure 8.10: The mean FSS of precipitation accumulation for the forecast range 12-18 UTC.

Mean FSS of range +24h for several precip. thresholds

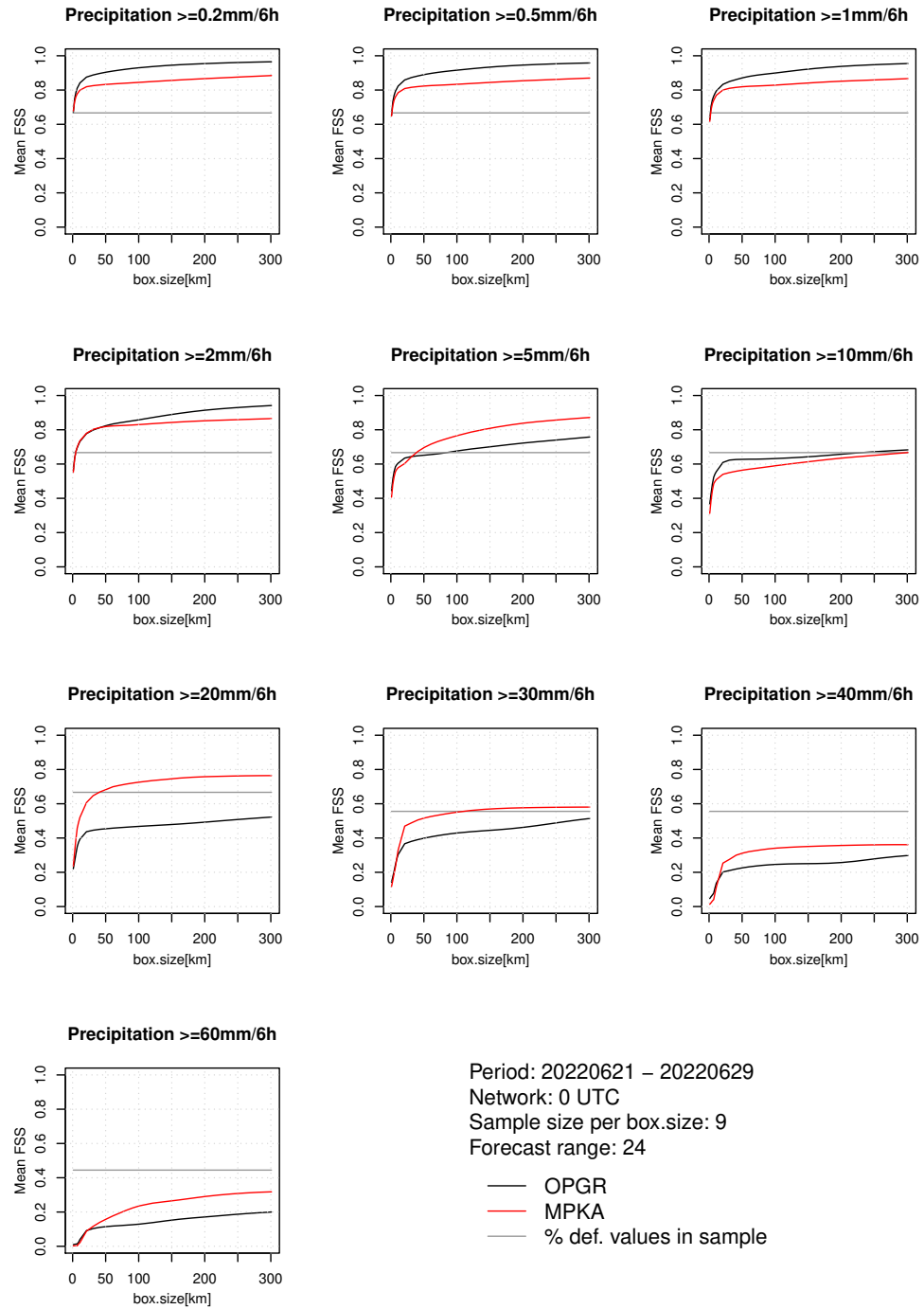


Figure 8.11: The mean FSS of precipitation accumulation for the forecast range 18-24 UTC.

Mean FSS of range +30h for several precip. thresholds

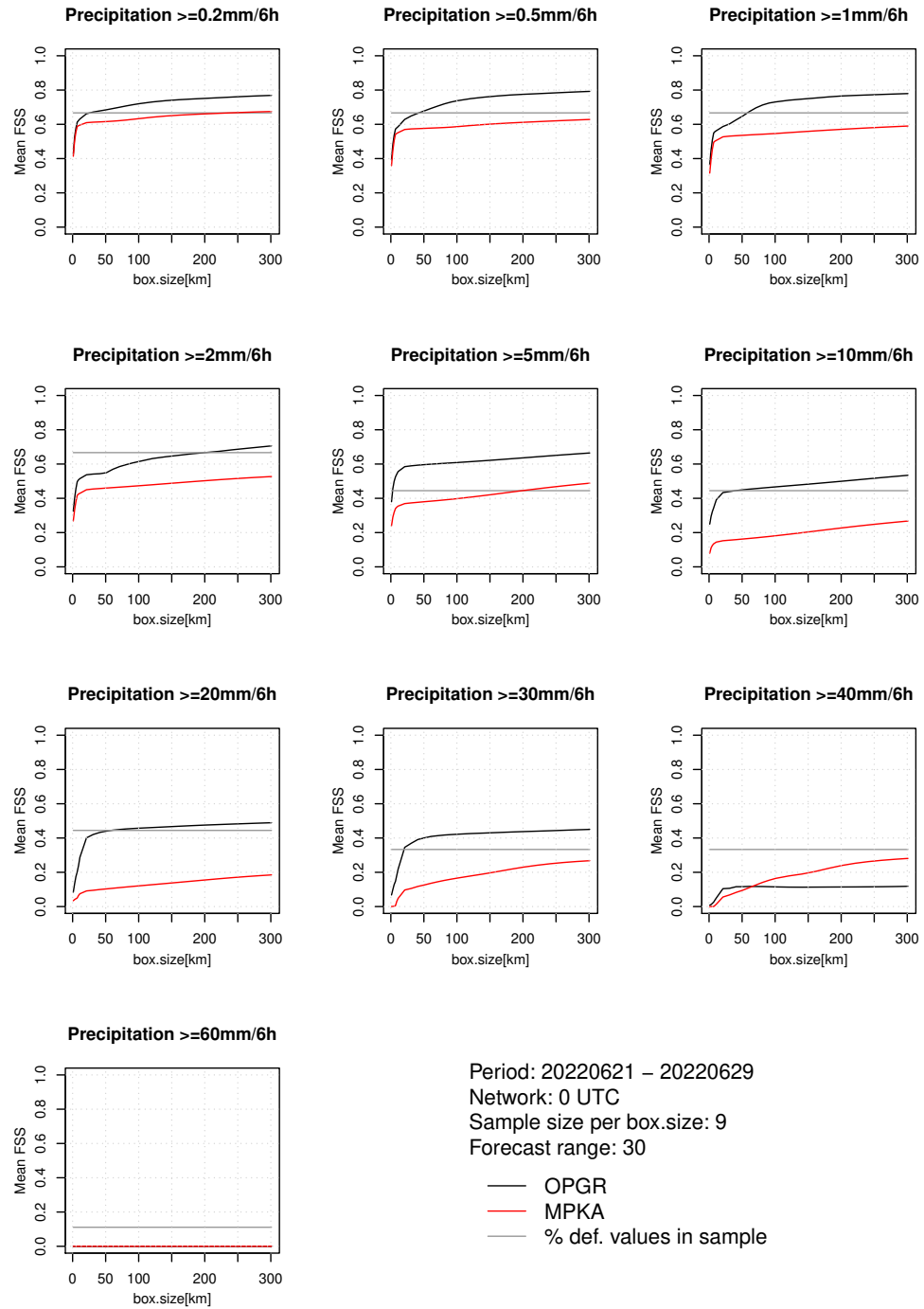


Figure 8.12: The mean FSS of precipitation accumulation for the forecast range 24-30 UTC.

Mean FSS of range +36h for several precip. thresholds

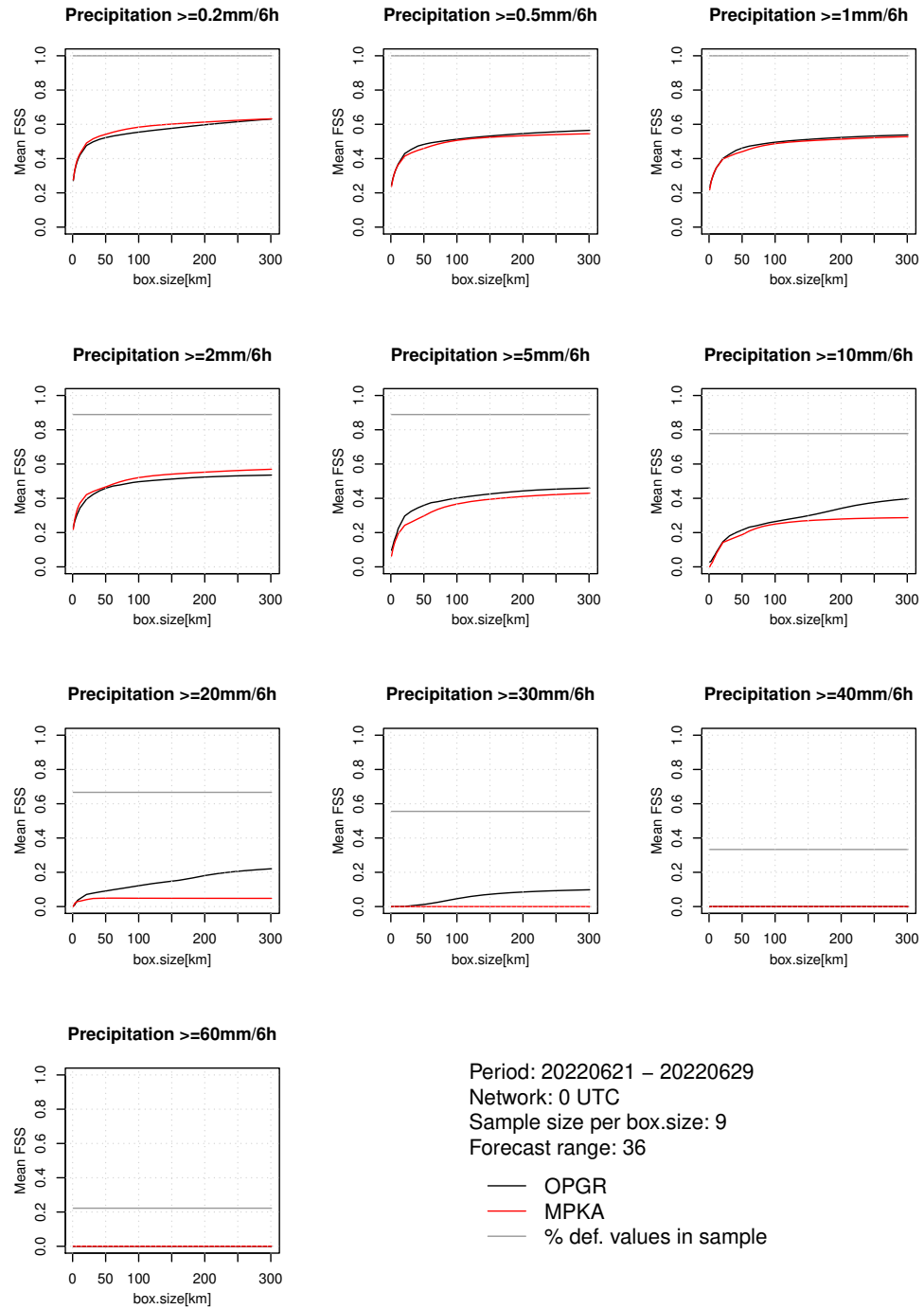


Figure 8.13: The mean FSS of precipitation accumulation for the forecast range 30-36 UTC.

correct. However, there is a bias of the precipitation field depicted by the lower FSS for the grid box size 301 km (probably too little precipitation exceeding such a threshold). On the other hand, positioning (for 20 mm/6h) and mainly bias of higher thresholds (10, 20, 30, and 60 mm/6h) MPKA scores higher, except for precipitation accumulations exceeding 40 mm/6h. It is essential to score well on the FSS of these precipitation thresholds as they show the performance of the forecasts of heavy rainfall. For the forecast range +42h, there are improved FSSs for almost all thresholds and box sizes, although the difference is less than for the forecast range +18h.

Figure 8.11 shows the averaged FSS over all forecast runs for six-hour accumulations ending at 24 UTC on the first day of forecasts. Again, there is a detriment of the FSSs of lower precipitation accumulations below 2 mm/6h and also an improvement of the FSS of higher precipitation accumulations exceeding 20 mm/6h. There is not so much deteriorated FSS for precipitation less than 1 mm/6h for the range +48h, but there are no improved results for the threshold of 5 mm/6h.

By contrast, OPGR performs better than MPKA in the case of weaker precipitation (ranges 06 and 12 for all days). Figure 8.12 shows the mean FSS for the forecast range of +30h, and Figure 8.13 shows the mean FSS for the forecast range of +36h. The results for the range +36h are quite the opposite to those at +18h and +24h, as OPGR performs better for higher precipitation thresholds, while MPKA scores higher on the FSS of lower precipitation thresholds. The limitation of these ranges is that there is much less area of precipitation that exceeds higher thresholds; thus, the comparison is made against fewer observations. However, it seems that MPKA tends to underestimate precipitation accumulations for these ranges.

8.2.3 Precipitation day by day

Finally, precipitation is subjectively validated on weather maps to assess the essential impacts of these model modifications on the precipitation field.

The precipitation fields for 2022-06-20 are very similar for both OPGR and MPKA without significant changes, except for the morning storm, for which MPKA delivers more precipitation than OPGR. The accumulations still remain underestimated. There was no significant precipitation over Czechia on 2022-06-21.

On 2022-06-22, a narrow band of stationary storms was created in Western Czechia. The 12h precipitation accumulation (Figure 8.14) shows an improvement in the precipitation position when the assimilation cycle is employed. It is tough to capture such structures, but all model configurations capture it quite well. The best position match of the precipitation maxima is delivered by MPKA, which correctly delivers the highest precipitation accumulation to the northern end of the precipitation band. On the other hand, the precipitation accumulation maximum is overestimated. The predicted value is 48.2 mm, while the observed is 40.2 mm. The structure of the narrow band was partially lost in MPKA, unlike in both MPKN and OPGR. The precipitation field of MPKA at the southern border match observations best as experiments OPGR and MPKN carry precipitation too far. Overall, MPKA delivers a slight improvement over OPGR. Also, results are modified by including the microphysical modifications in the assimilation cycle.

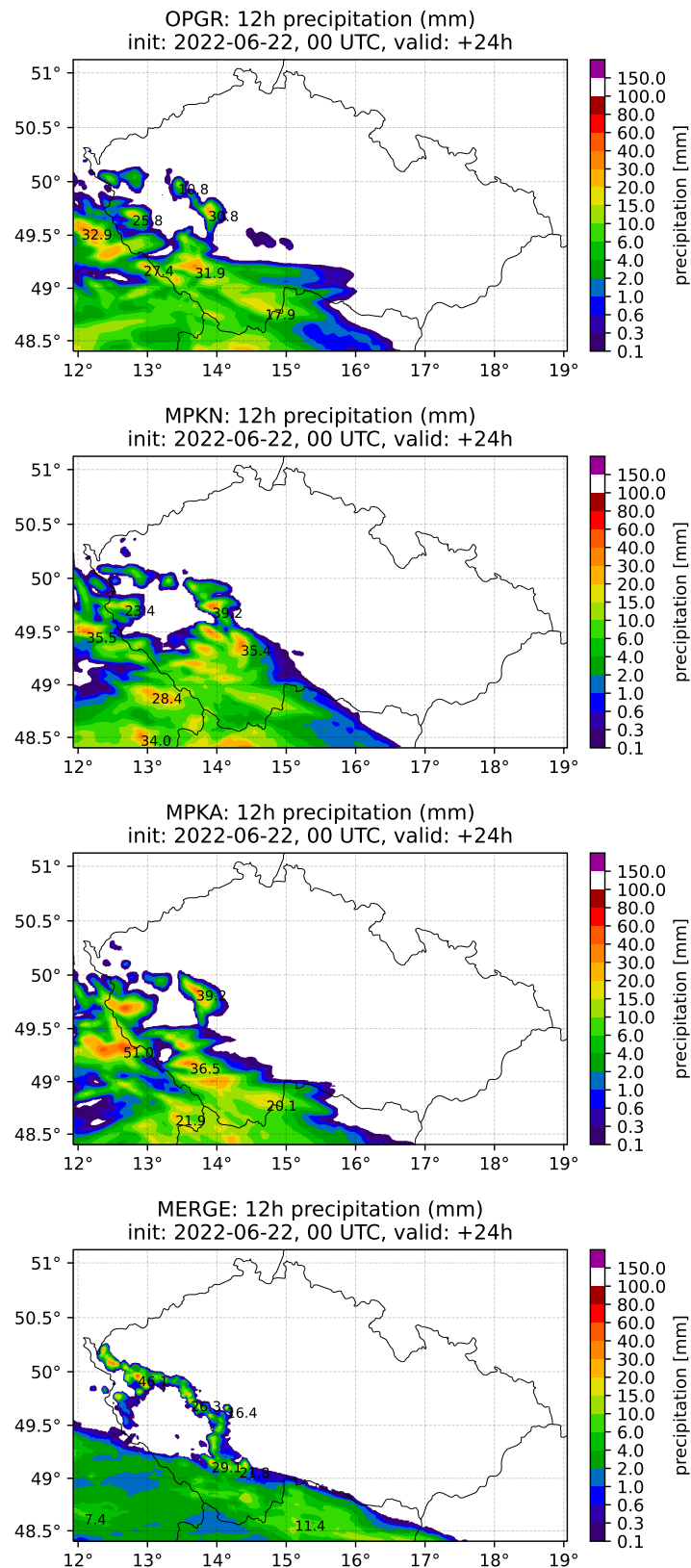


Figure 8.14: 12-hour precipitation accumulation ending on 2022-06-23 at 00 UTC. In descending order: OPGR, MPKN, MPKA, and observations (MERGE).

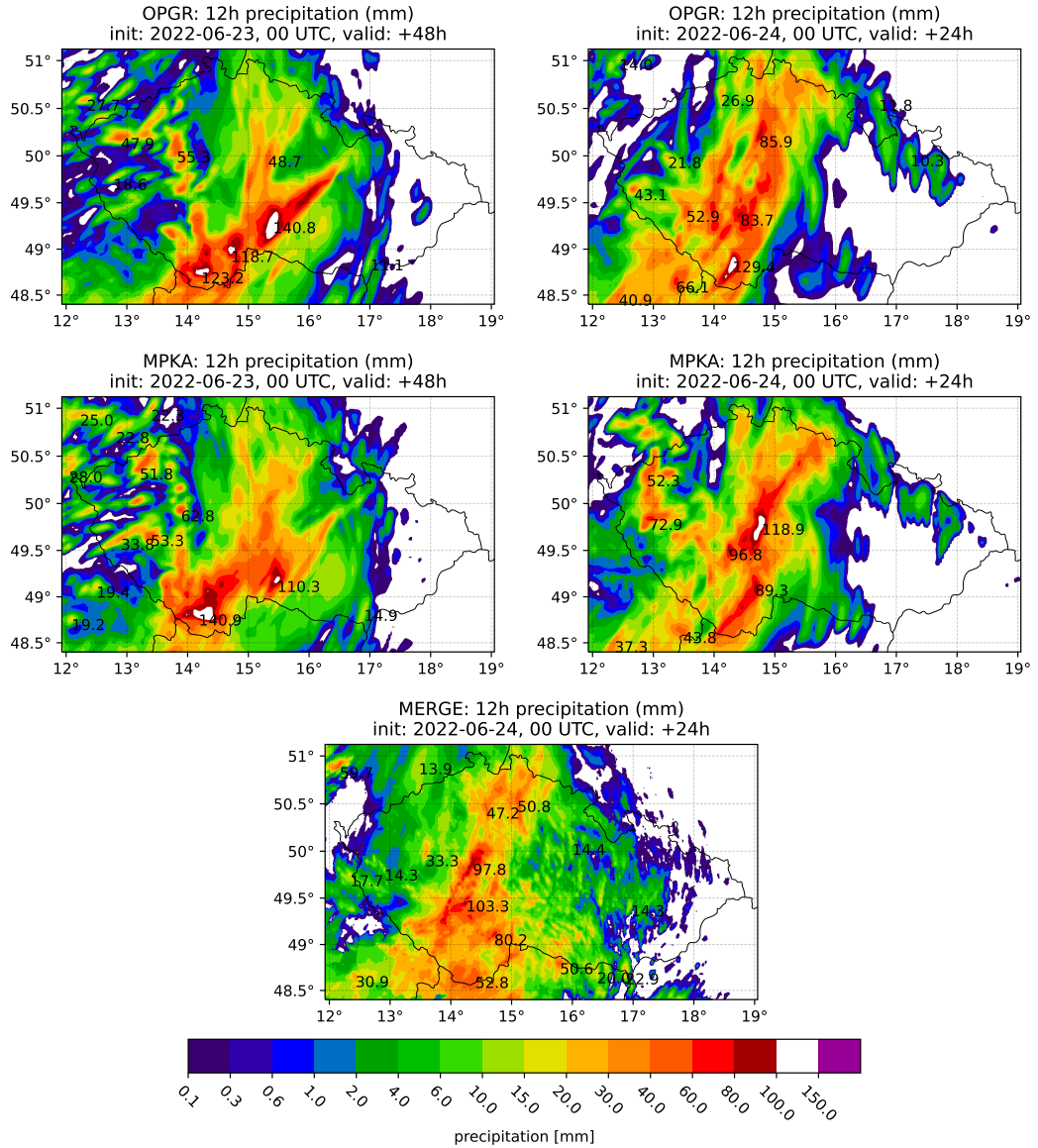


Figure 8.15: 12-hour precipitation accumulation on 2022-06-25 at 00 UTC predicted by model runs initialized on 2022-06-23 at 00 UTC (left) and model runs initialized on 2022-06-24 at 00 UTC (right). Left column is OPGR, right MPKA. Observations are shown in the lowermost row.

After 2022-06-23 without significant precipitation, 2022-06-24 and 2022-06-25 delivered heavy rainfall, when a well-developed MCS reached Czechia and slowly dissipated over Czechia. This MCS delivered heavy rainfall. Several model runs are discussed as the prediction of precipitation accumulation varies with time.

The precipitation accumulation delivered by the model initialization on 2022-06-23 at 00 UTC is similar for both configurations (Figure 8.15 left). Maxima are equal (142 mm), just their position differs. The highest maximum of MPKA in southern Czechia comes mostly (130 mm) from the six-hour precipitation accumulation between the 42nd and 48th hour of the model integration.

The most precise is the model forecast initialized on 2022-06-24 at 00 UTC (Figure 8.15 right), which delivered a precipitation maximum of 120 mm over

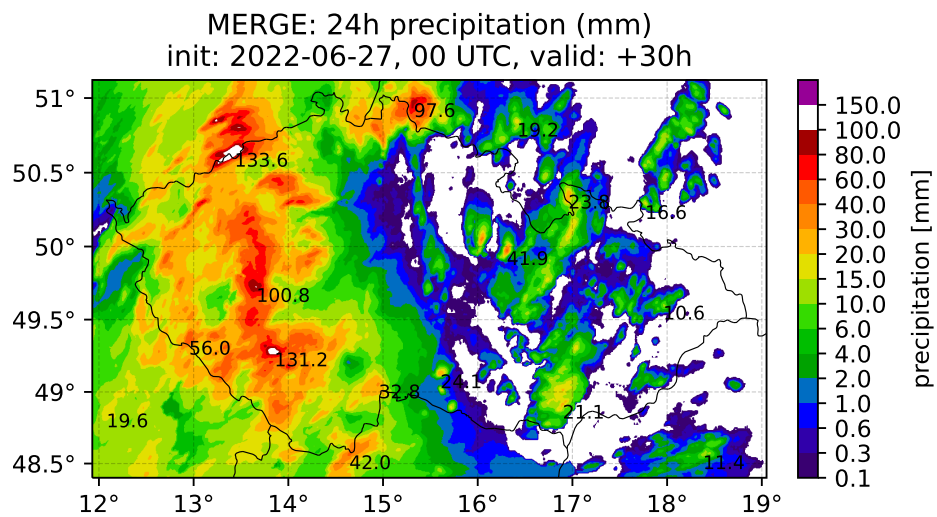
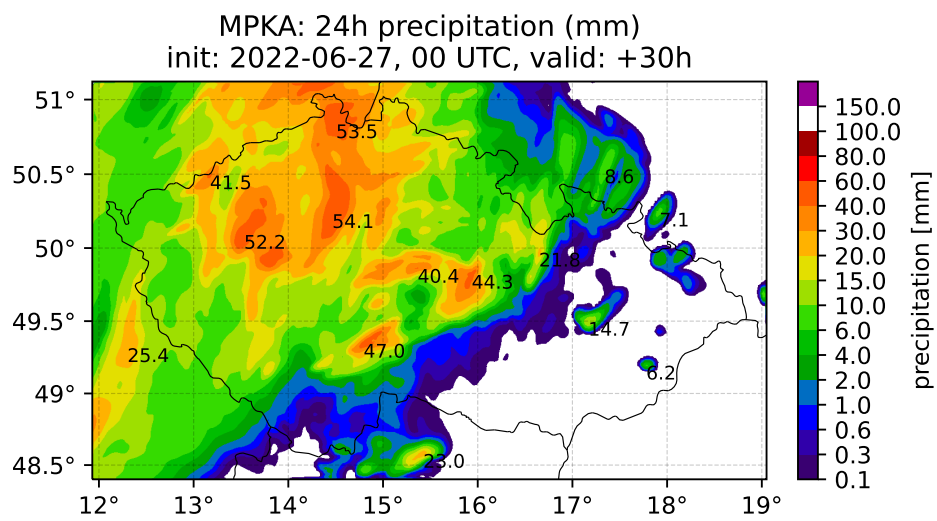
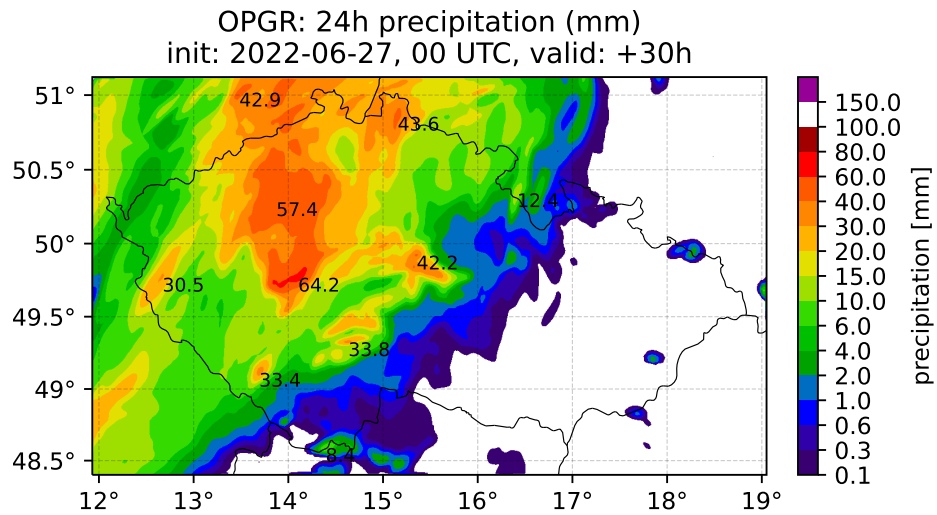


Figure 8.16: 24-hour precipitation accumulation on 2022-06-28 at 06 UTC. There are shown OPGR (top), MPKA (middle), and MERGE (bottom).

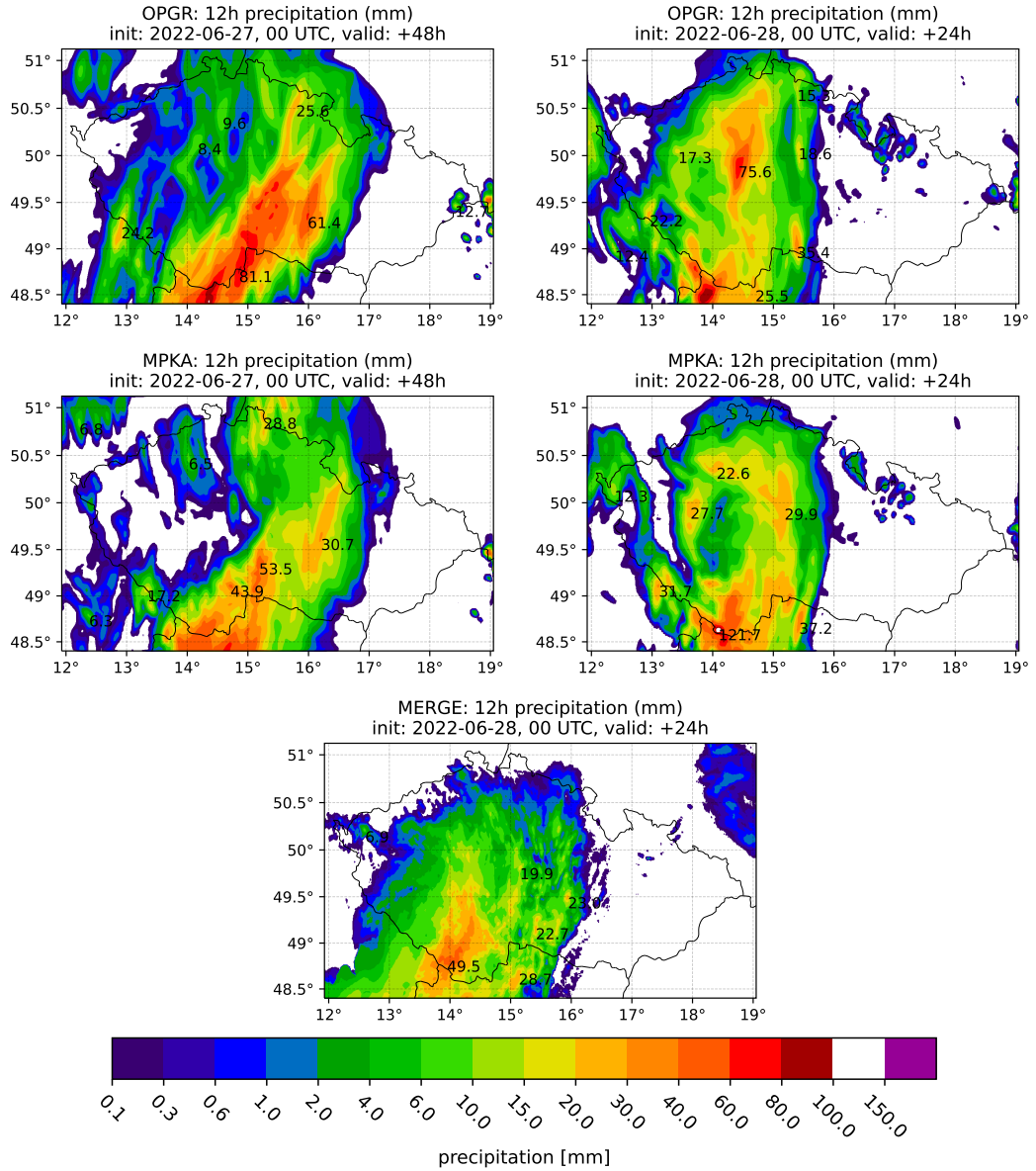


Figure 8.17: 12-hour precipitation accumulation on 2022-06-29 at 00 UTC. Model runs initialized on 2022-06-27 are on the left, model runs initialized on 2022-06-28 are on the right. The upper row is OPRG and the lower row is MPKA. In the bottom are observations by MERGE.

central Czechia in the case of MPKA and 132 mm in southern Czechia for OPRG. The position of precipitation maxima is almost perfect for MPKA. The maximum is overestimated by about 15 mm by MPKA. However, the rain continued during the night. For the precipitation accumulation between the 12th and 36th hour of integration, the total precipitation accumulation is slightly underestimated for MPKA, which predicted 124 mm compared to the observed 140 mm. Configuration OPRG delivered 130 mm. The difference between the two configurations is not large in this case.

Surprisingly, the run initialized at 12 UTC on the 24th of June does not deliver better results as various local precipitation accumulation maxima are

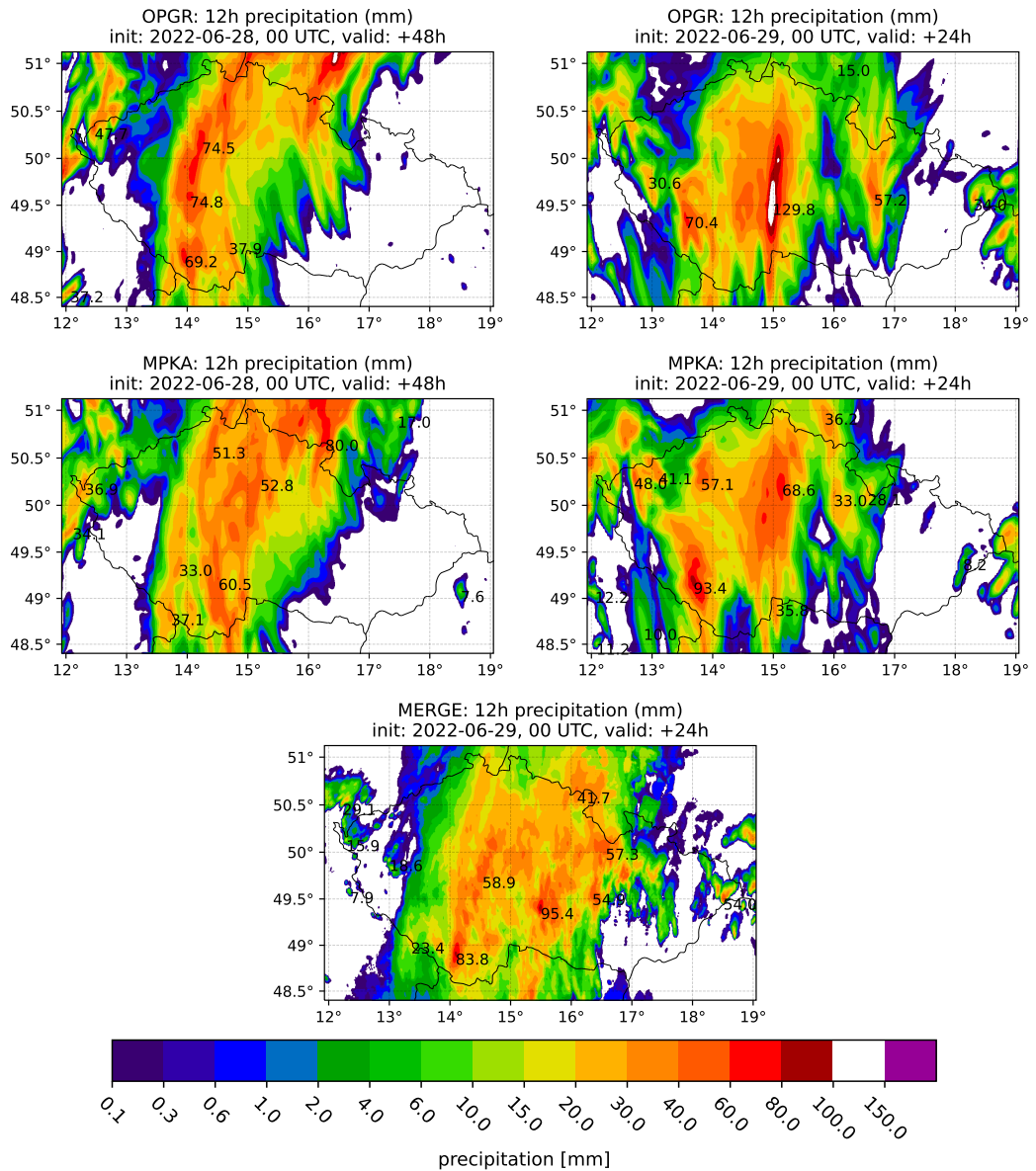


Figure 8.18: 12-hour precipitation accumulation on 2022-06-30 at 00 UTC. Model runs initialized on 2022-06-28 are on the left, model runs initialized on 2022-06-29 are on the right. The upper row is OPRG and the lower row is MPKA. In the bottom are observations by MERGE.

overestimated by OPRG. The configuration MPKN subtly reduces many spots of overestimated precipitation accumulation in this case.

2022-06-26 did not deliver much precipitation but 2022-06-27 did. For the model initialization on 2022-06-27 at 00 UTC, a better match is delivered by OPRG than MPKA regarding afternoon storms over western Czechia (Figure 8.16). Firstly, it delivers higher precipitation accumulations over western Czechia. Secondly, the precipitation band does not reach that far to the east of Czechia. Contrarily, MPKA delivers more precipitation over Silesia and Moravia, where storms developed overnight.

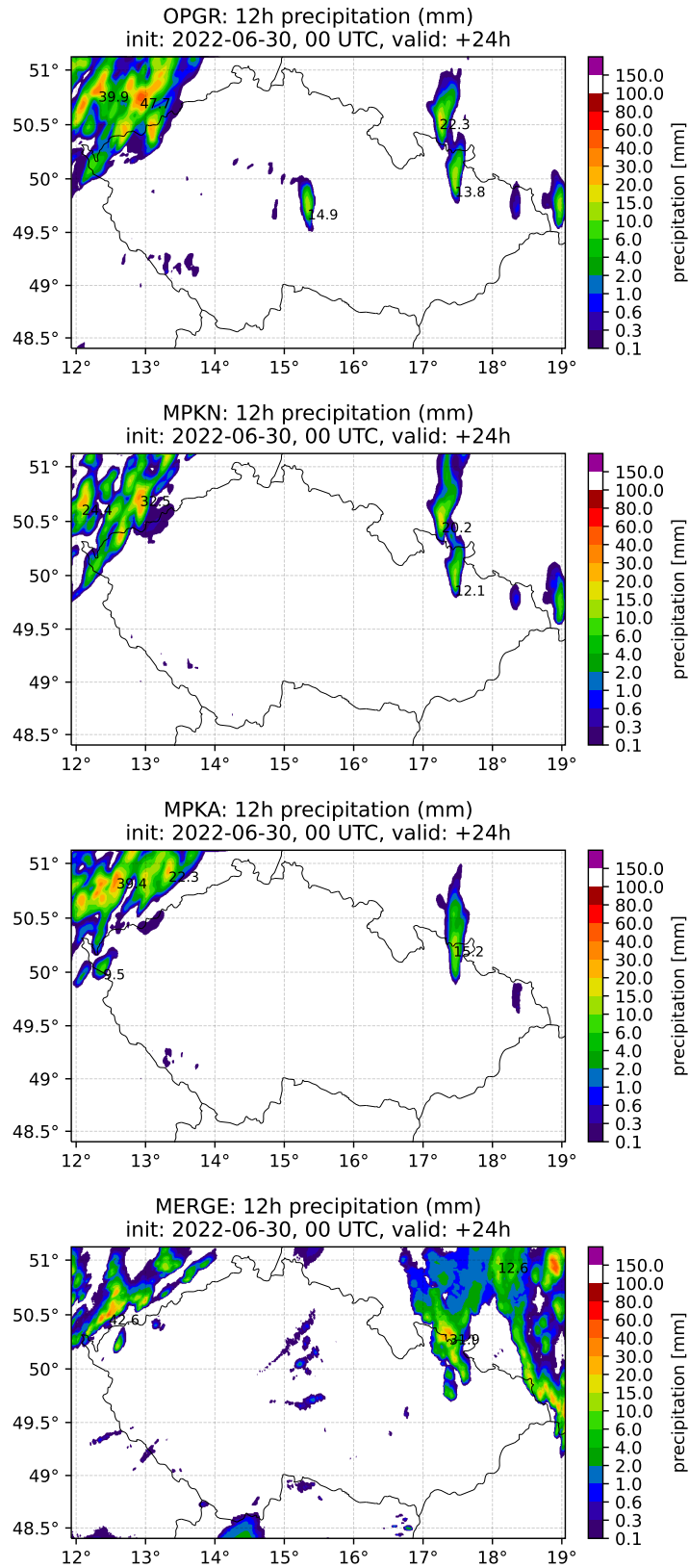


Figure 8.19: 12-hour precipitation accumulation on 2022-07-01 at 00 UTC. There are shown in descending order OPGR, MPKN, MPKA, and observations (MERGE).

Another interesting case was 2022-06-28, when another MCS crossed Czechia. For the forecast range 36-48 UTC for the run from 2022-06-27 00 UTC (Figure 8.17 left), both MPKA and MPKN (not shown) are in better agreement with observations as they reduce the precipitation accumulation predicted by OPGR, which overestimates the precipitation accumulation maxima by a factor of around two. The storm's position is shifted eastward, but the overall results are satisfactory, especially considering the long forecast range. For the model run from 2022-06-28 00 UTC (Figure 8.17 right), MPKA delivers locally extreme rainfall over the Bohemian Forest, which was caused by interaction with orography. However, precipitation accumulation is reduced compared to OPGR for the rest of the territory in better accordance with observations. So high maxima are not predicted by MPKN (not shown), but the reduction of precipitation remains. Thus, MPKN delivers the best results for this particular case.

Another MCS crossed Czechia on the 29th of June. Firstly, the run from 2022-06-28 00 UTC is validated (Figure 8.18 left). The area of precipitation of MPKA is broader compared to OPGR and is shifted to the east, which improves the forecast. On the other hand, the precipitation maxima are underestimated by both OPGR and MPKA; MPKA underestimates more. The model configuration MPKA improves the forecast of the MCS for the run initialized on 2022-06-29 at 00 UTC (Figure 8.18 right). Firstly, OPGR overestimates precipitation maxima by around 34 mm, while MPKA almost matches the maxima, although the position of the highest maxima is in a different location. Secondly, the precipitation accumulation in both bands, one in western Czechia and one in central Czechia, is comparable in the case of MPKA. At the same time, OPGR underestimates precipitation accumulations in western Czechia and overestimated precipitation accumulations over central Czechia.

The storm in the east of Czechia is not discerned by MPKA, which is a consequence of the modified physics in the assimilation cycle as MPKN captured it.

On 2022-06-30, there were only a few showers, one more intensive over the Hrubý Jeseník mountain range in the northeast of Czechia, and a weak precipitation echo was observed over central Czechia. However, it is purely based on the radar data, as no gauge captured any precipitation. Thus, it is possible that all precipitation evaporated before it reached the ground. The model forecast initialized that day at 00 UTC is shown in Figure 8.19. While OPGR predicts a relatively strong shower over central Czechia (with a precipitation accumulation of 15 mm), MPKA does not predict any precipitation in this area. Interestingly, this shower is not simulated by MPKN as well. Thus, it seems that it might be purely a consequence of the influence of the enhanced evaporation on the thermal stratification. The precipitation over Hrubý Jeseník is predicted similarly by all runs.

On 2022-07-01, when many single-cellular storms appeared, the precipitation maxima are reduced by MPKA compared to OPGR, as shown in Figure 8.20. Nevertheless, most of the territory still has a positive precipitation bias. However, there are two exceptions where observed rainfall accumulations are higher, one in southern Czechia, which OPGR very well captured, and one in Silesia, which is not captured by either model configuration. The latter case might be connected to local effects (of orography or land use) as the spatial extent of higher maxima is small.

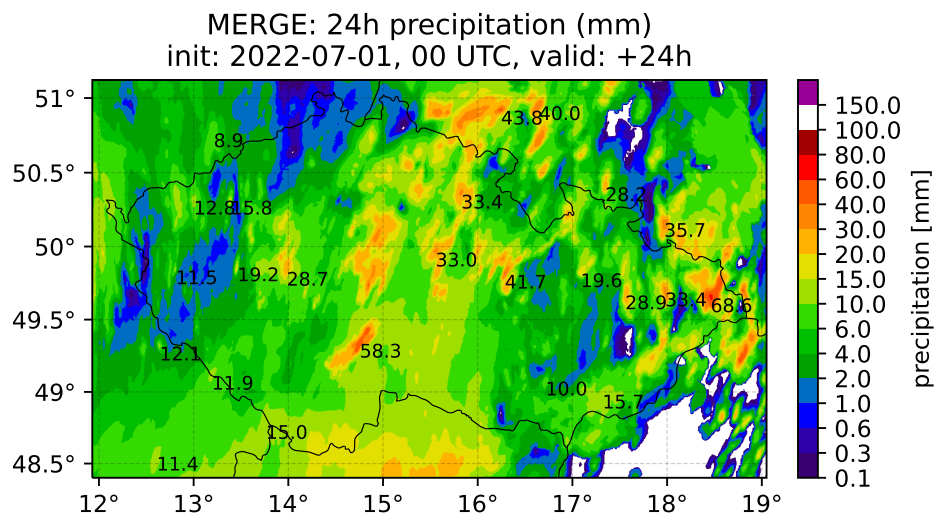
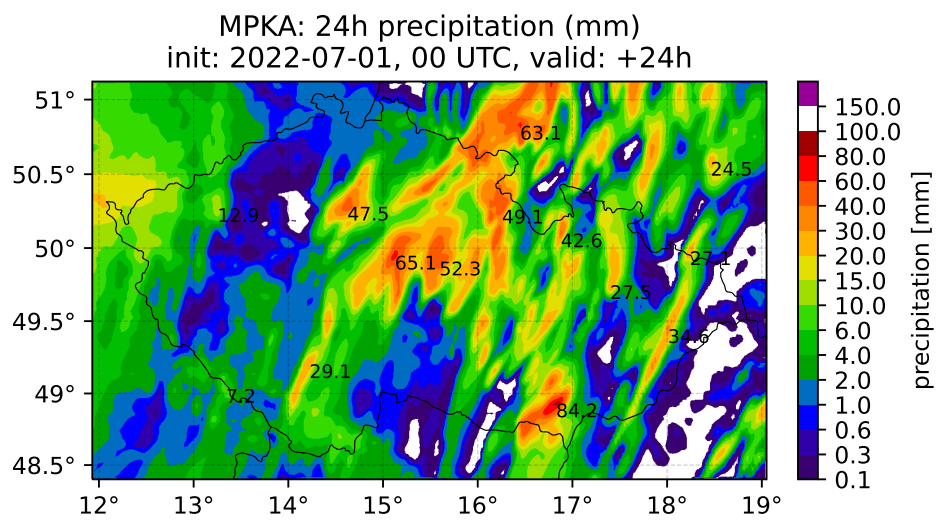
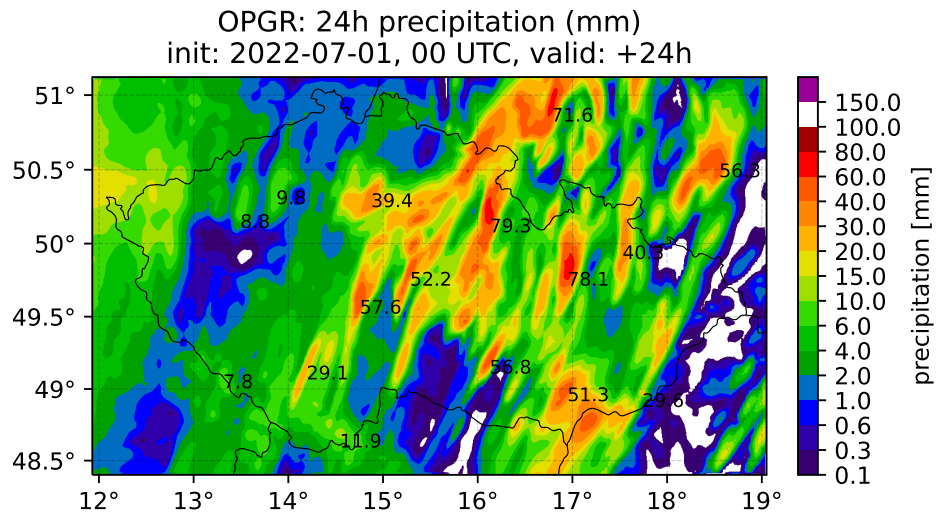


Figure 8.20: 24-hour precipitation accumulation on 2022-07-01, OPGR (top), MPKA (middle), and MERGE (bottom).

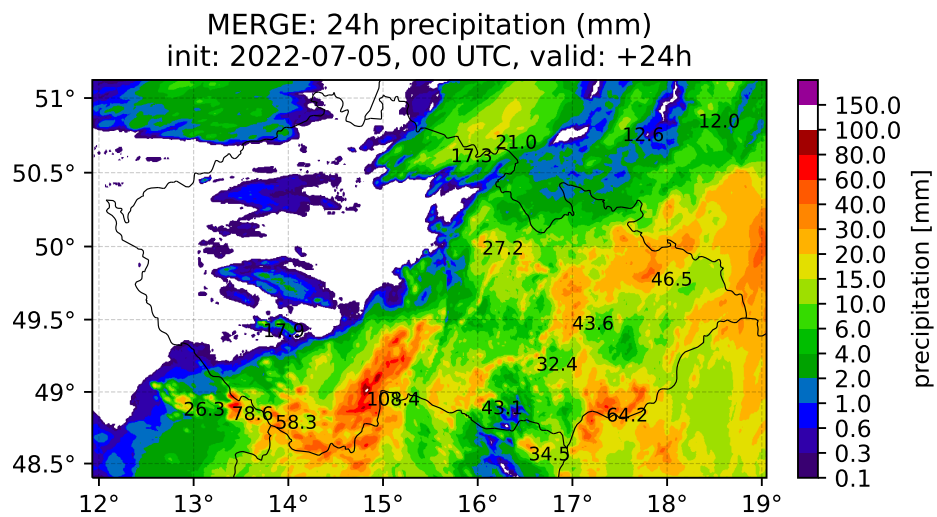
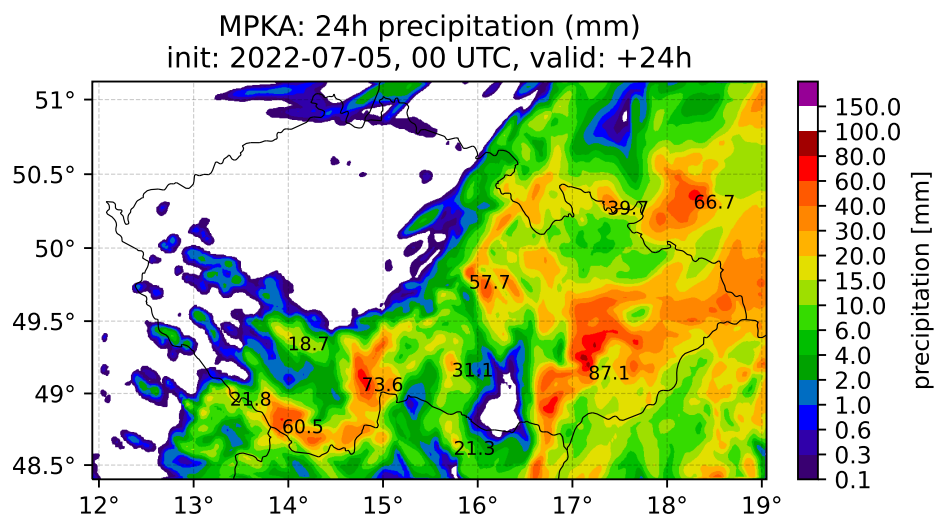
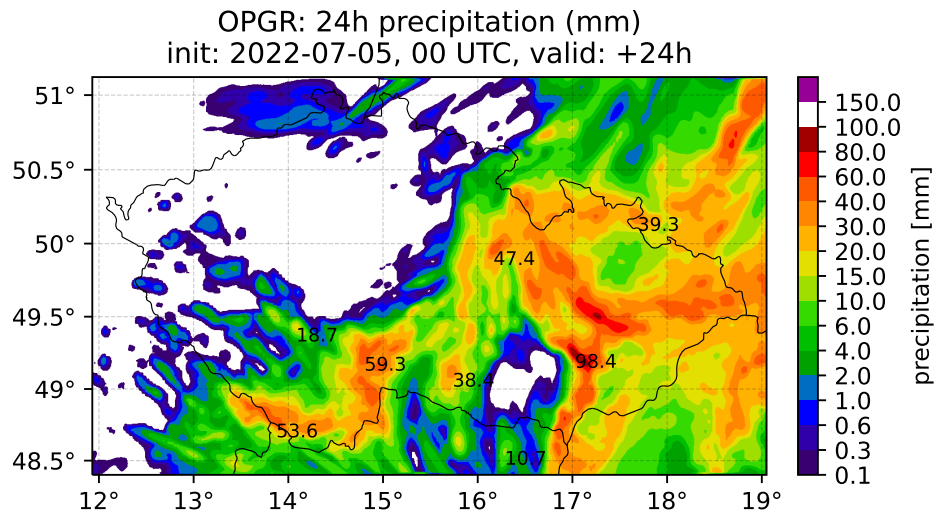


Figure 8.21: 24-hour precipitation accumulation on 2022-07-05, OPGR (top), MPKA (middle), and MERGE (bottom).

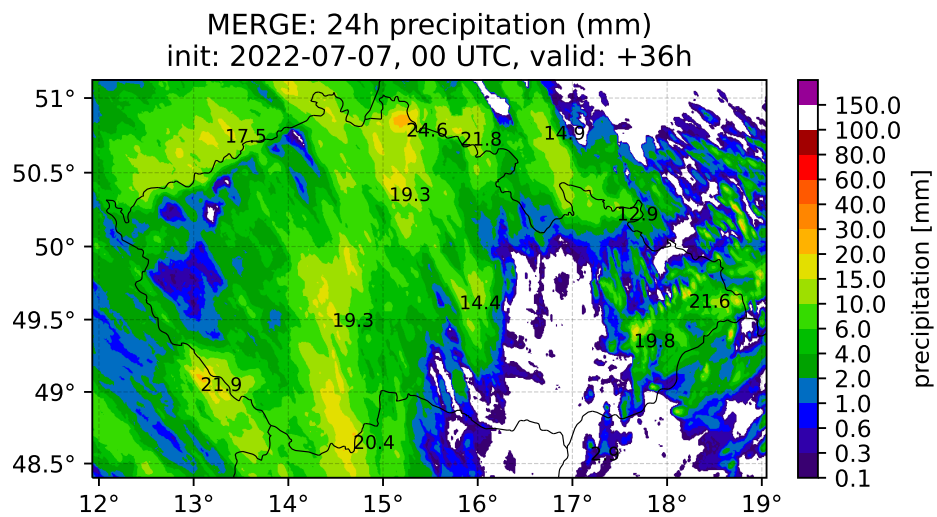
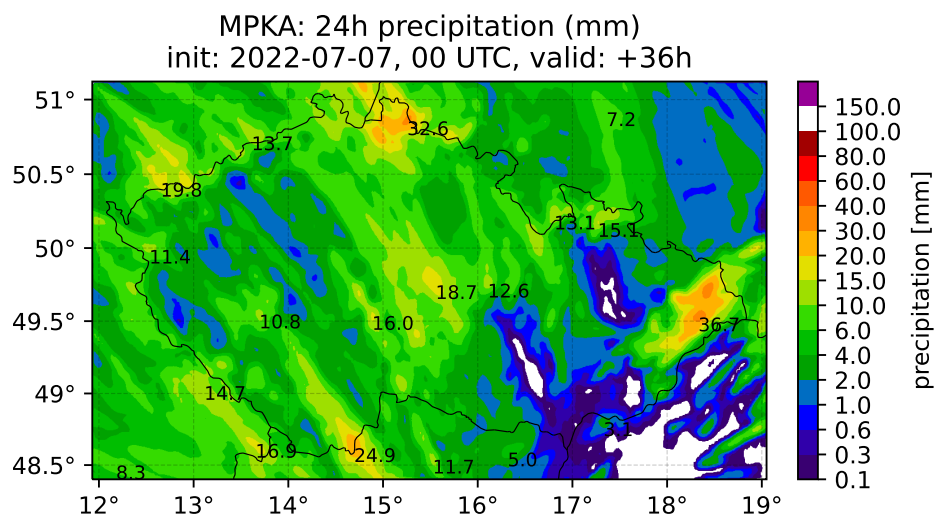
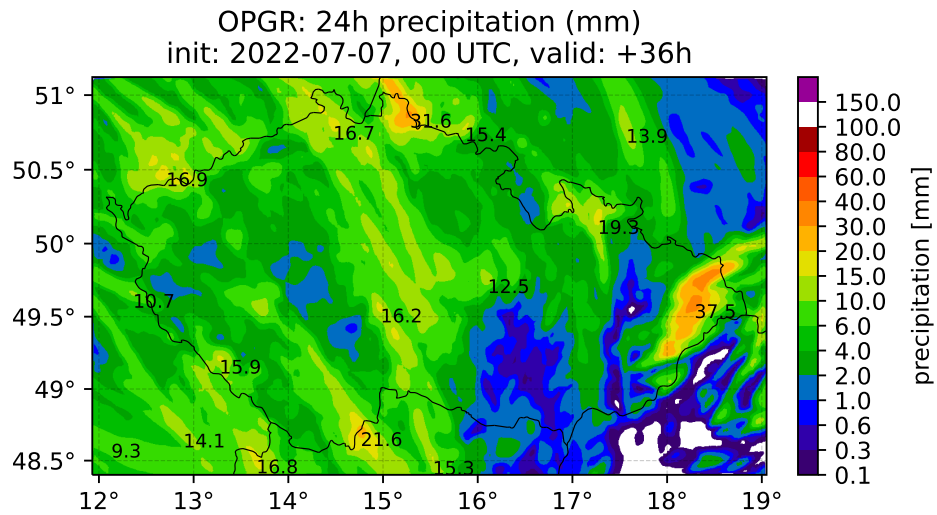


Figure 8.22: 24-hour precipitation accumulation on 2022-07-07, OPGR (top), MPKA (middle), and MERGE (bottom).

After two days without significant precipitation over Czechia, there were weaker storms over Czechia on 2022-07-04. Configuration **OPGR** delivers better results for that day than **MPKA**, which gives too little precipitation.

There were severe storms on 2022-07-05 in the southeastern part of Czechia (Figure 8.21). They are well-predicted by both **OPGR** and **MPKA**. However, **MPKA** delivers less precipitation over Moravia and slightly more over southern Czechia. Both changes are positive. Neither **MPKA** nor **OPGR** matches the high maxima over 100 mm/day in southern Czechia.

Very similar results were produced on 2022-07-06 when night showers appeared. On 2022-07-07, there were light showers in the morning, and a cold front crossed Czechia at night the day before. Only subtle differences between **OPGR** and **MPKA** are observed. The 24h precipitation accumulation (Figure 8.22) shows a more pronounced rain shadow downstream of the Ore Mountains. Changes between both simulations are small. The higher maxima predicted over the Jizera Mountains in northern Czechia were also captured by gauges (up to 38.1 mm), although the MERGE product does not depict them. Precipitation accumulations over central Czechia are slightly underestimated.

On 2022-07-08 and 2022-07-09, some weaker showers appeared. Both model configurations give very similar results; **MPKA** sometimes delivers slightly less precipitation, and the difference is up to around 5 %. On the last day of the extended period, 2022-07-10, there were relatively weak night showers created on 2022-07-09. In this case, the run of **MPKA** initialized on 2022-07-10 at 00 UTC underestimates the area fraction and intensity of showers compared to **OPGR**, which already slightly underestimates the area of precipitation. The differences are subtle and thus not shown.

8.2.4 Evaluation of this period

This period revealed these key characteristics:

- The negative bias of T2m remains.
- The upper air scores are slightly improved, while the surface scores are generally worsened.
- Precipitation maxima are reduced. That is mainly due to the new evaporation parameterization. However, there is also a small contribution from the different value of the autoconversion coefficient k_s .
- The FSS of precipitation is improved for six-hour accumulations at terms 18 and 24 UTC when the precipitation is heavy. On the other hand, weaker six-hour precipitation accumulations at 6 and 12 UTC are worsened, although they are more uncertain as the precipitation accumulations are generally lower.
- Based on the subjective evaluation of the forecast of precipitation in the previous subsection, the forecast of precipitation is subtly improved.

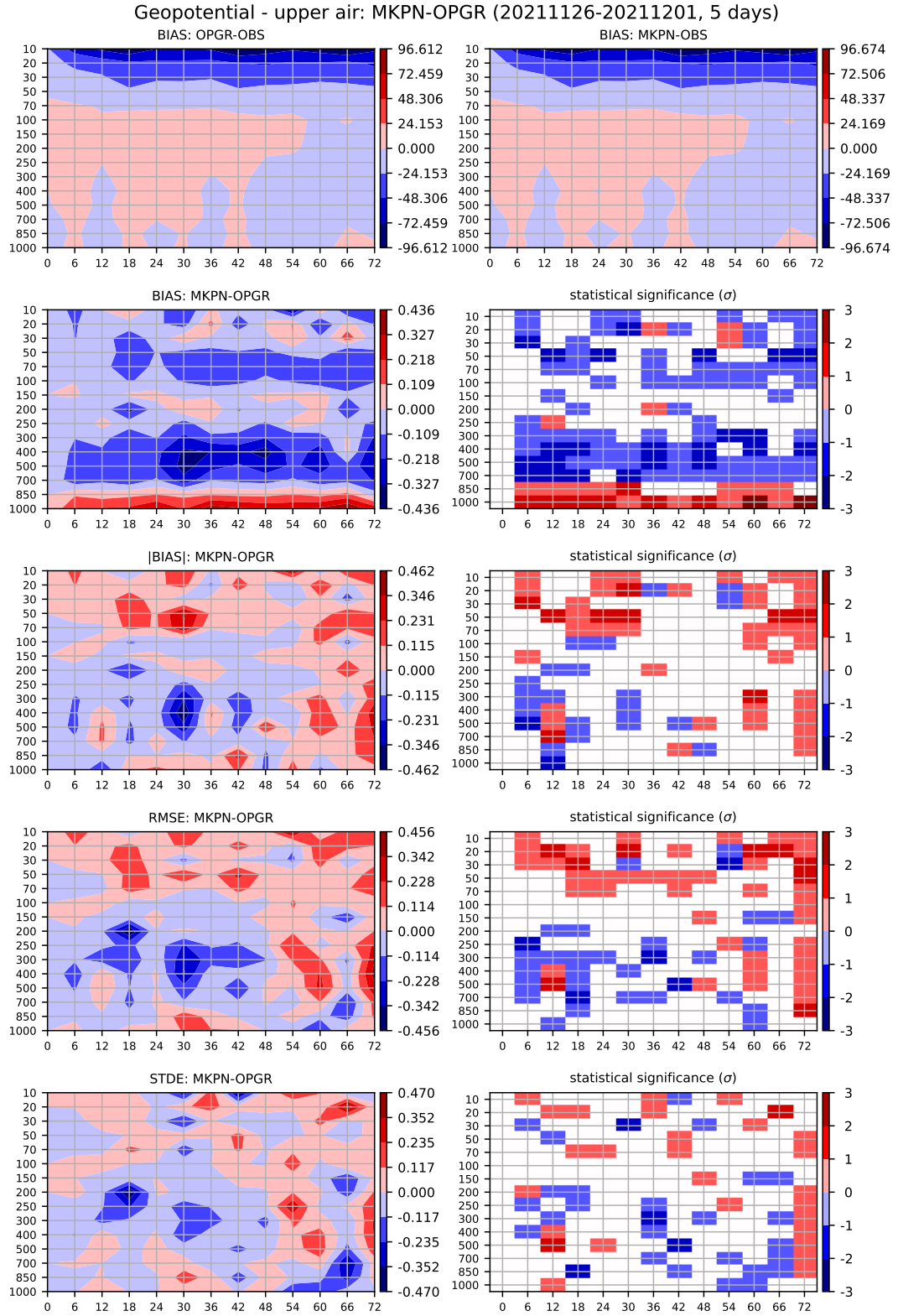


Figure 8.23: The upper air scores of geopotential for the winter precipitation period. Experiment MPKN is compared with OPGR, which is used as reference.

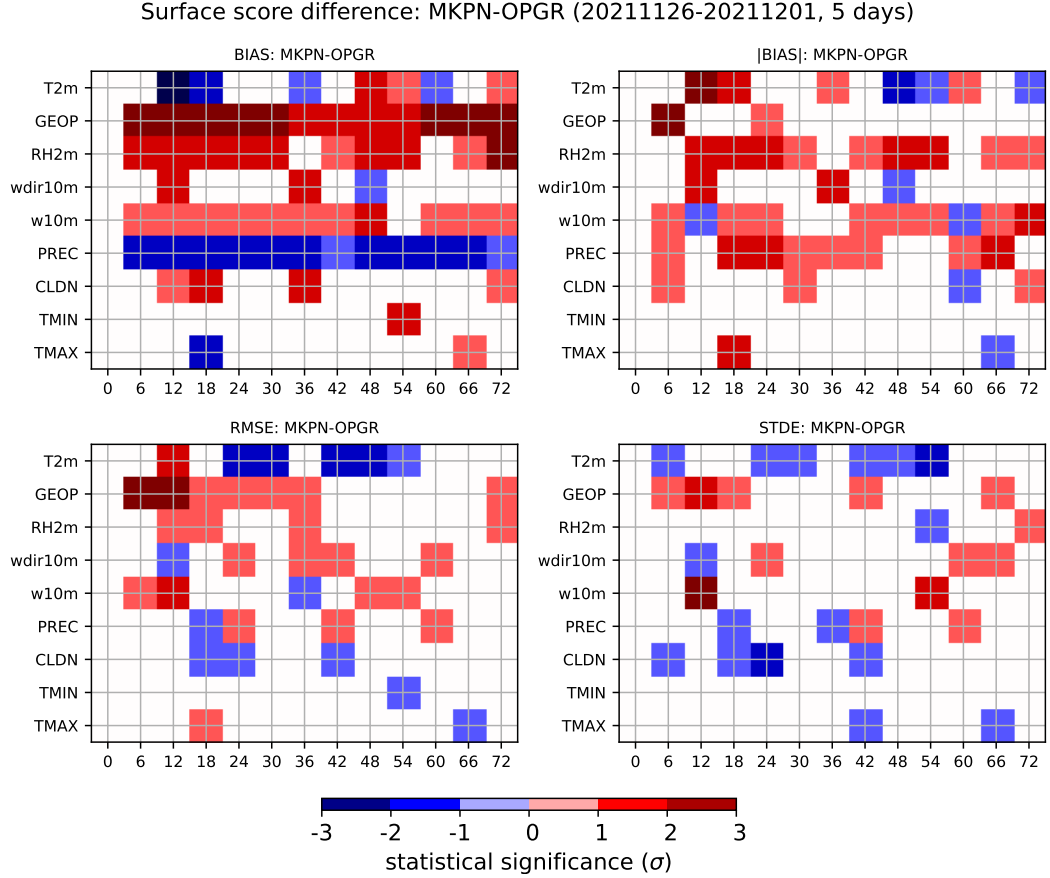


Figure 8.24: Surface scores for the winter precipitation period. Experiment MPKN is compared with OPGR, which is used as reference.

8.3 Winter precipitation period

The winter precipitation period was tested from 2021-11-26 to 2021-12-01. The upper air geopotential scores (Figure 8.23) show the typical dipole pattern when there is more mass below 850 hPa and less above. The borderline is lower than in summer due to lower temperatures. The RMSE and STDE of geopotential are slightly lowered above 700-850 hPa except for the last day of integrations. The difference for the last day is partially caused by one run (the run initialized on 2021-12-01 at 00 UTC), but the magnitude of the difference is not significant.

Temperature is lowered below 700 hPa, neutral higher, and raised from approximately 400 hPa to around 200 hPa. The RMSE and STDE of geopotential are neutral, maybe slightly worsened. However, the difference is subtle enough to be considered neutral.

Again, MPKN delivers more moisture below around 500 hPa and slightly less above. Its RMSE and STDE are improved throughout the troposphere except for a belt between 700 and 500 hPa. Scores of wind direction and wind speed are neutral.

The surface scores (Figure 8.24) show an improvement in the STDE and RMSE of T2m. However, its cold bias is more pronounced. Also, RH2m suffers from a positive bias. The positive bias of RH2m might be lowered if the modifi-

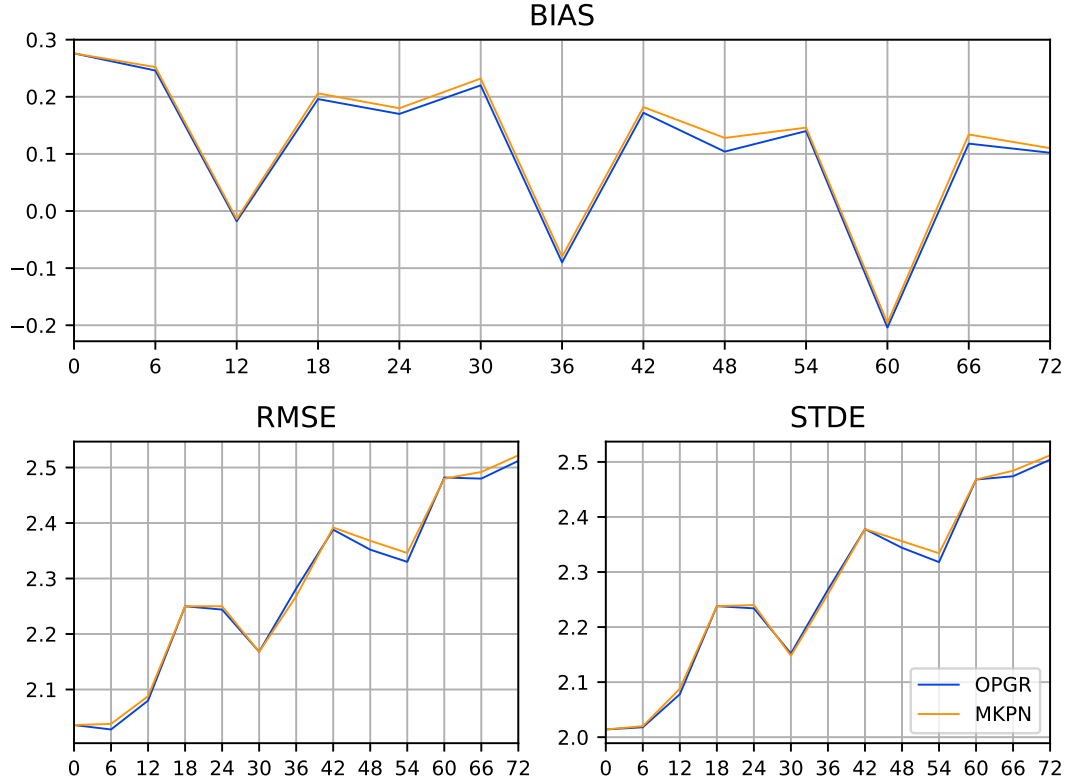


Figure 8.25: Surface scores of wind speed for the winter precipitation period from 2021-11-26 to 2021-12-01. Note the continuous positive bias of MPKN (orange) compared to OPGR (blue).

cation was tested with the assimilation cycle (not run) can lower the amount of groundwater and thus lower the evaporation rate from the surface, thus reducing the positive bias of RH2m. This might also improve 2-metre temperature. Interesting is also the positive bias of wind speed (Figure 8.25), which might be caused by the enhanced evaporation as it can cause more inhomogeneities in the atmosphere, which raise the wind speed. The bias of precipitation is lower for both experiments, which different from typical as the model usually overestimates precipitation accumulations. Thus, the reduction of precipitation is not beneficial for this particular period.

Overall, the magnitude of atmospheric score changes is lower than in summer cases. This corresponds with lower cloud bases, so the difference between evaporation parameterizations is not so pronounced.

The precipitation field is not much changed for all days. Experiment MPKN typically delivers slightly less weak precipitation. The difference in heavier stratiform precipitation is negligible in these cases. For example, Figure 8.26 shows a 24-hour accumulation of precipitation over Czechia, which depicts the subtle difference between model configurations.

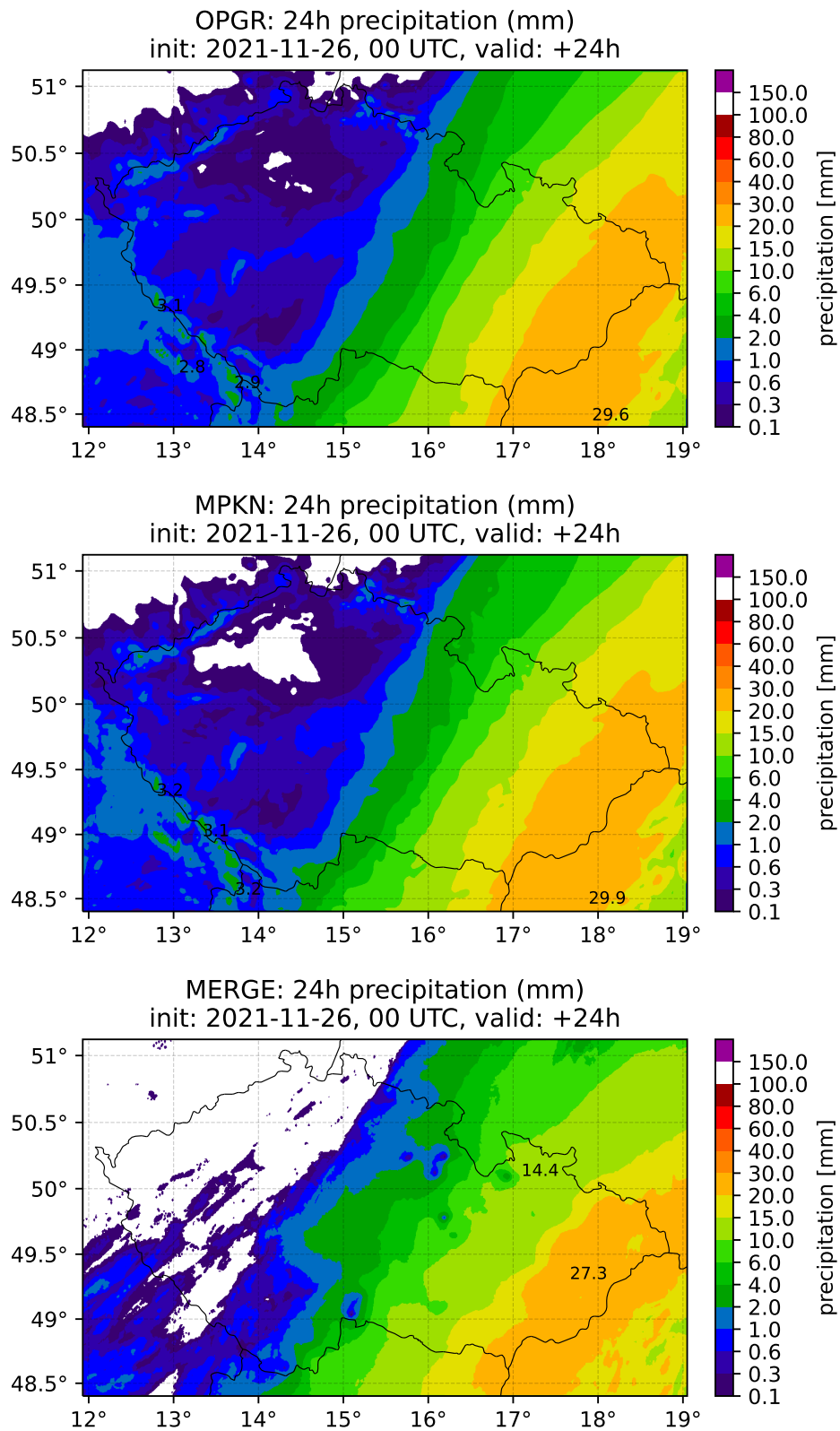


Figure 8.26: 24-hour precipitation accumulation on 2021-11-26. The difference between MPKN (middle) and OPGR (top) is small. Both fields are similar to observations (bottom).

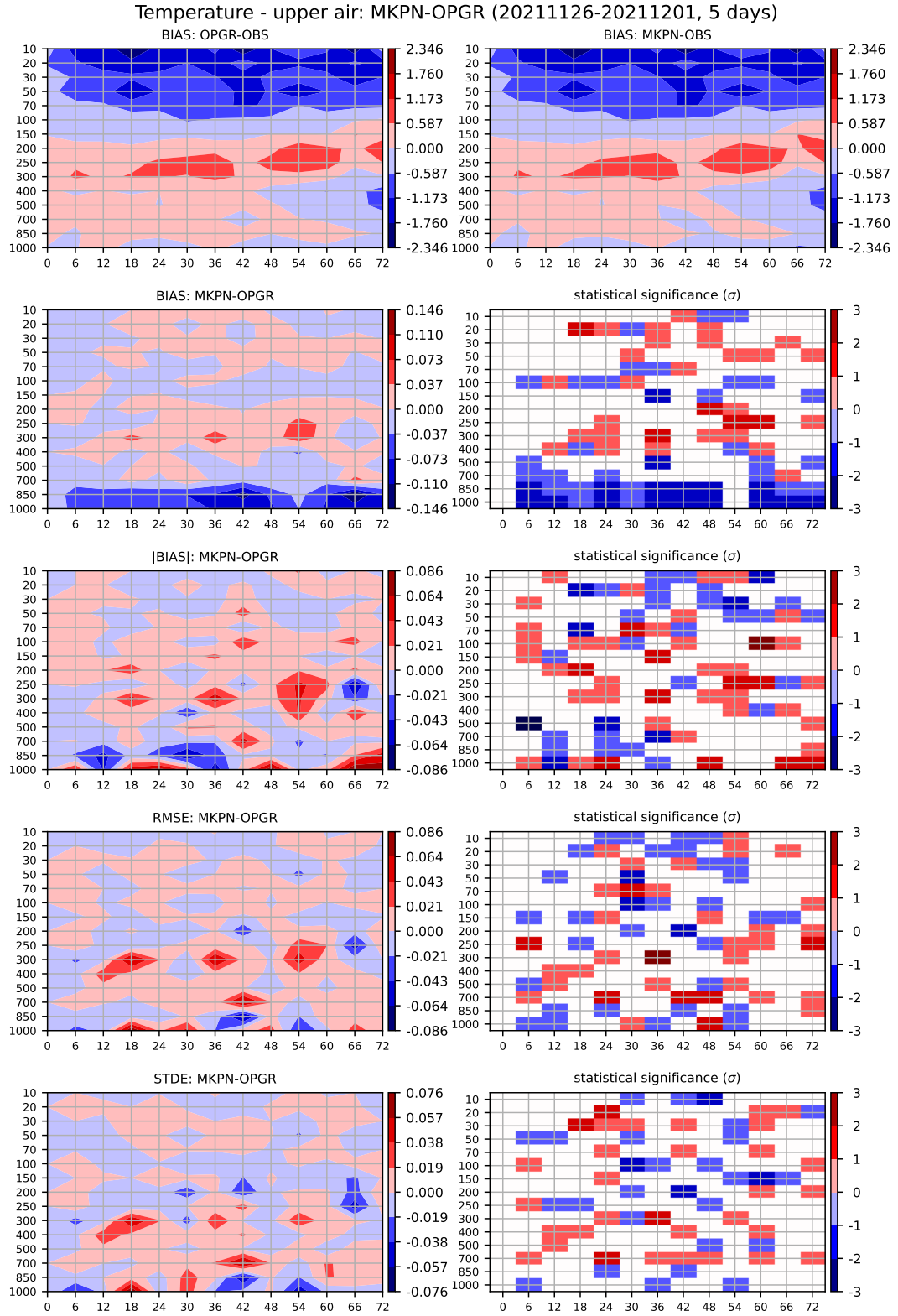


Figure 8.27: The upper air scores of temperature for the autumn stratocumulus period. Experiment MPKN is compared with OPGR, which is used as reference.

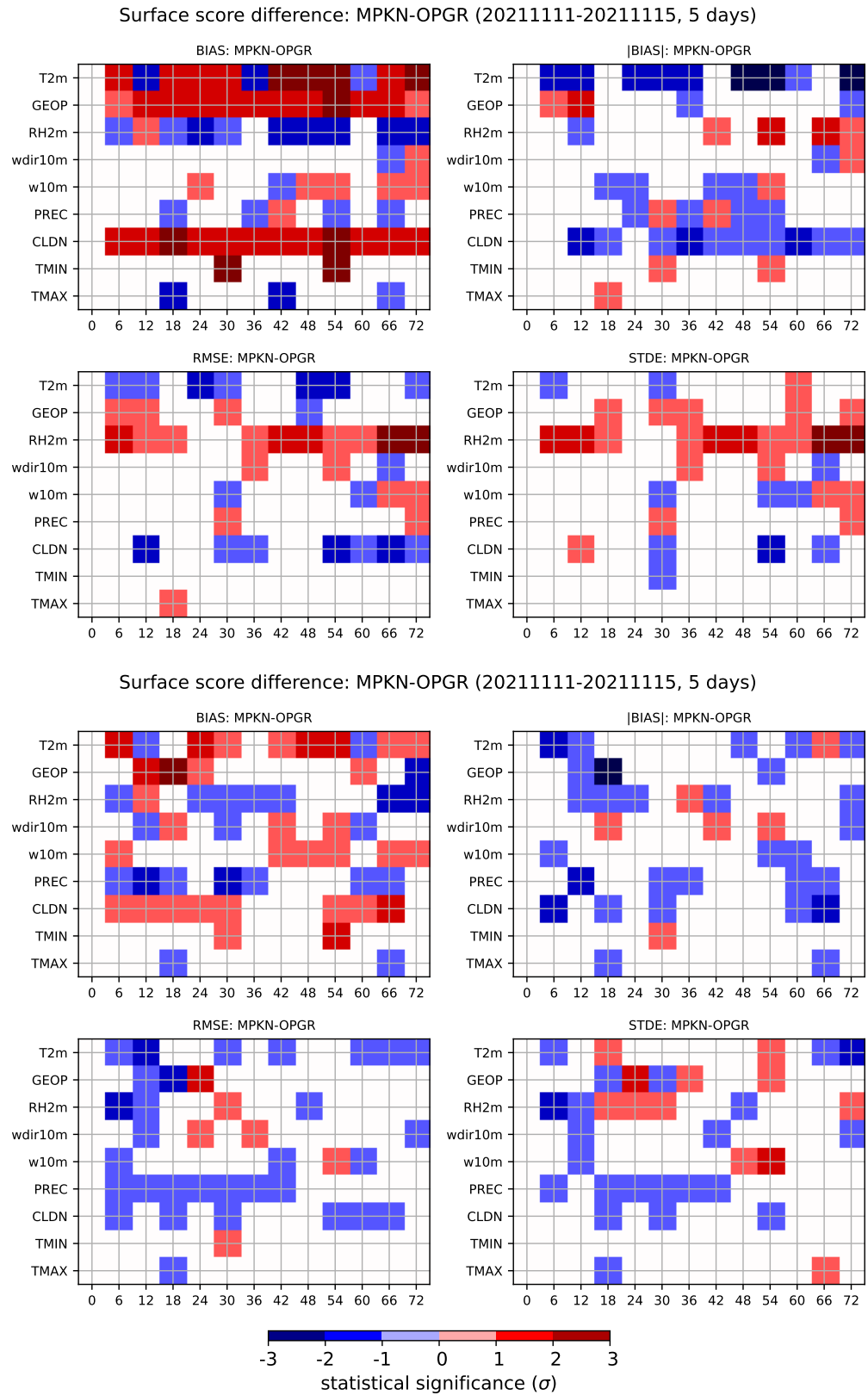


Figure 8.28: Difference of scores for the autumn stratocumulus period between MPKN and OPGR (reference). Lower is validation against Czech SYNOP stations.

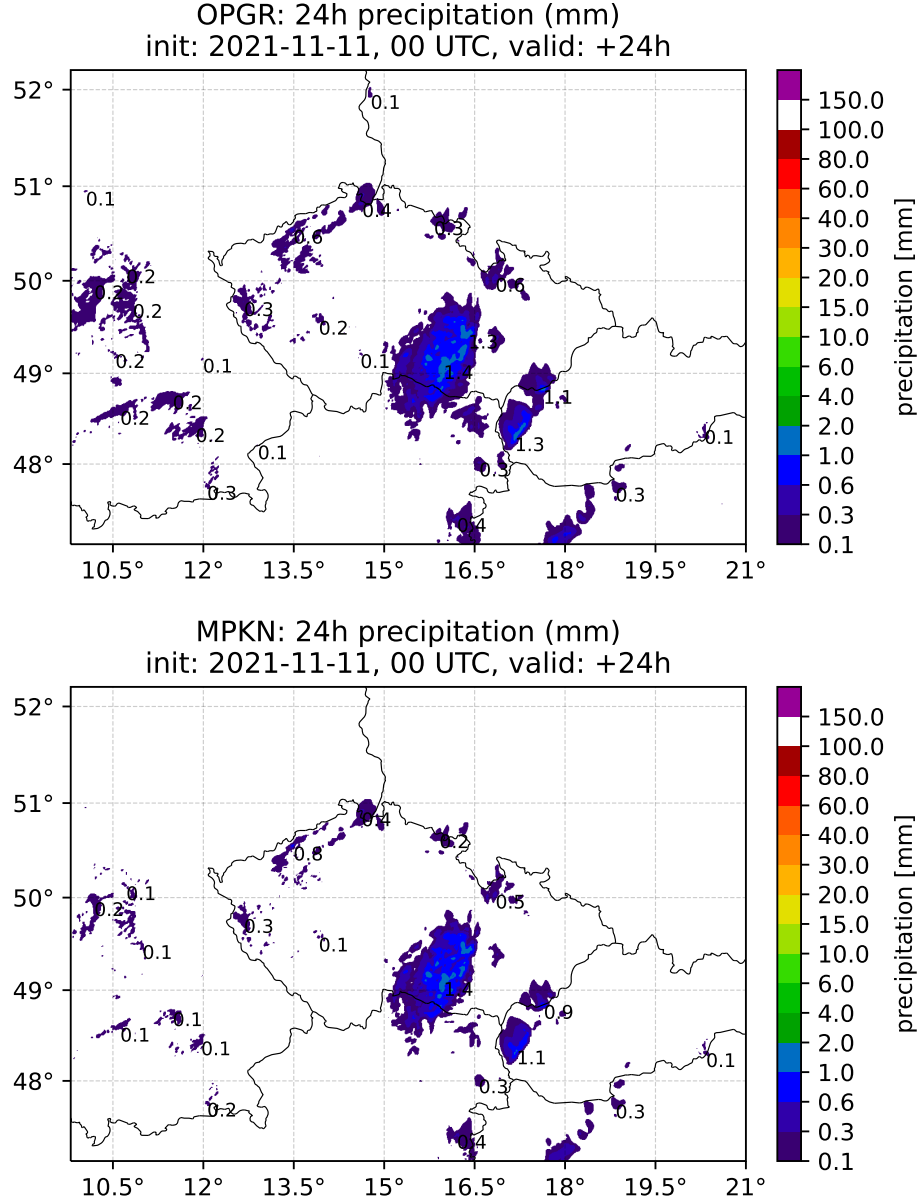


Figure 8.29: 24-hour precipitation accumulation on 2021-11-11, OPGR is upper and MPKN lower. MERGE is not shown as no precipitation was observed.

8.4 Autumn stratocumulus period

This period from 2021-11-11 to 2022-11-15 (a shortened version was tested) shows how well the model performs in the typical autumn inversion with stratocumulus over Czechia. Most of the period was without significant precipitation over Czechia. No assimilation cycle was run in this case. Thus, MKPN is compared to OPGR. All model integrations were initialized at 00 UTC.

The upper air scores of geopotential show the typical dipole pattern when there is more mass below 700 hPa and less above. Its statistics are improved mainly at later forecast ranges. The upper air scores of temperature are improved (Figure 8.27). The $|\text{BIAS}|$ of temperature is reduced for all levels except 400 hPa.

The STDE and RMSE of geopotential are statistically significantly improved or neutral except for level 500 hPa. The bias of upper air relative humidity is slightly reduced, and its STDE and RMSE are neutral or slightly worse. The changes in wind direction are insignificant. The wind speed bias is reduced, its RMSE is neutral, and its STDE is slightly worsened.

The surface scores are shown in Figure 8.28. This time, the surface temperature scores are also improved, except for the STDE. Geopotential is slightly worsened at the surface. Also, the STDE and RMSE of RH2m are worsened. Unusually, the bias of RH2m is negative compared to OPGR, which itself is further from neutral bias for this particular period. The positive bias of precipitation is reduced. The other surface scores are neutral.

The surface scores can also be validated against synoptic stations in Czechia only¹, which is convenient for the validation of the impact on the performance of the simulation of stratocumulus events.

The resulting surface scores are shown in the lower part of Figure 8.28. Surface scores are generally improved. This time, even the bias of geopotential is slightly reduced or neutral, while the RMSE and STDE of geopotential are neutral. The RMSE of temperature and its |BIAS| are reduced, while its STDE is neutral. Also, the bias of RH2m is improved. Crucially, the positive precipitation bias is lessened, although still positive.

Precipitation is only slightly reduced, as shown in Figure 8.29. There is some improvement, but the positive bias remains. Overall, MPKN performs better than OPGR for this particular period.

8.5 Snowfall on 2022-12-12

So far, no pure snow cases in Czechia have not been evaluated. One good case is the situation on 2022-12-12 when a cold front crossed Czechia and delivered snow even to the lowlands. Figure 8.30 shows that the precipitation accumulation is overestimated that day by OPGR. Nevertheless, the precipitation accumulation over central Czechia is sometimes even more overestimated by MPKN. That is caused mainly by the different split of solid precipitation between snow and graupel (Figure 8.31). After this modification, there is more graupel reaching the ground. It can be explained by the evaporation mechanism described in Section 7.2, which expects that as snow sublimates more efficiently, it leads to cloud water condensation allowing for graupel production. In reality, precipitation in the form of graupel is not expected as clouds were mostly stratiform. However, it is not possible to suppress graupel production under these weather conditions as graupel is produced via autoconversion from cloud water, which is present in clouds at such temperatures (a few Kelvins below the melting point of water).

Regarding the distribution of precipitation, an improvement is that there is a reduction of precipitation accumulation on the lee side of mountains in northern Czechia (Ore Mountains, Hrubý Jeseník, Krkonoše). The spatial distribution is much closer to observations in the case of MPKN than in the case of OPGR. This is caused by enhanced evaporation, which prevents precipitation from reaching the

¹The upper air scores might be validated over Czechia too from the technical point of view. However, it does not provide any value due to lack of observations

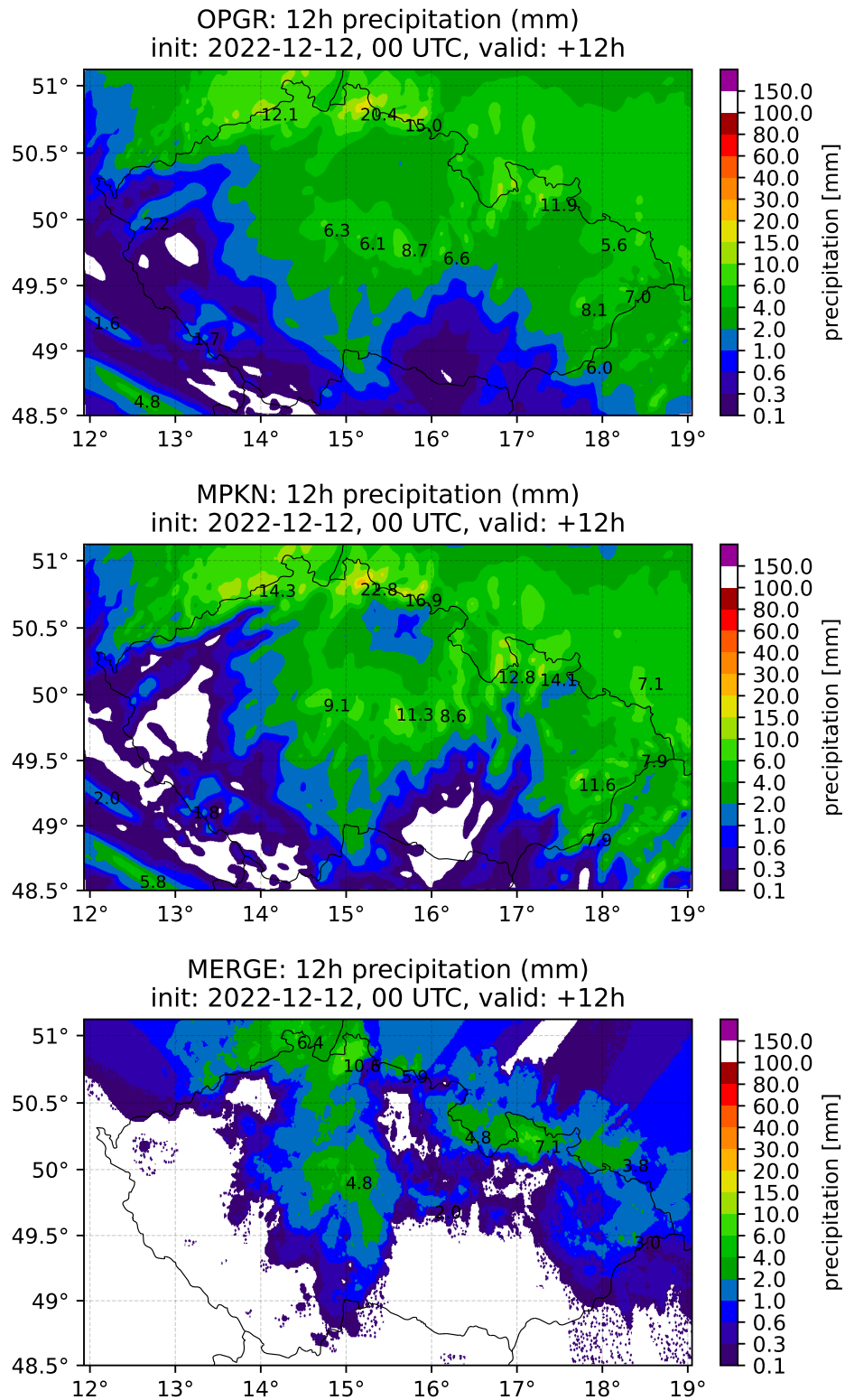


Figure 8.30: 12-hour precipitation accumulation on 2022-12-12 at 00 UTC, OPGR (top), MPKN (middle), and MERGE (bottom). In this case, the observed precipitation can be underestimated because snow has lower reflectivity and clouds can be low, so the radar beam is above them.

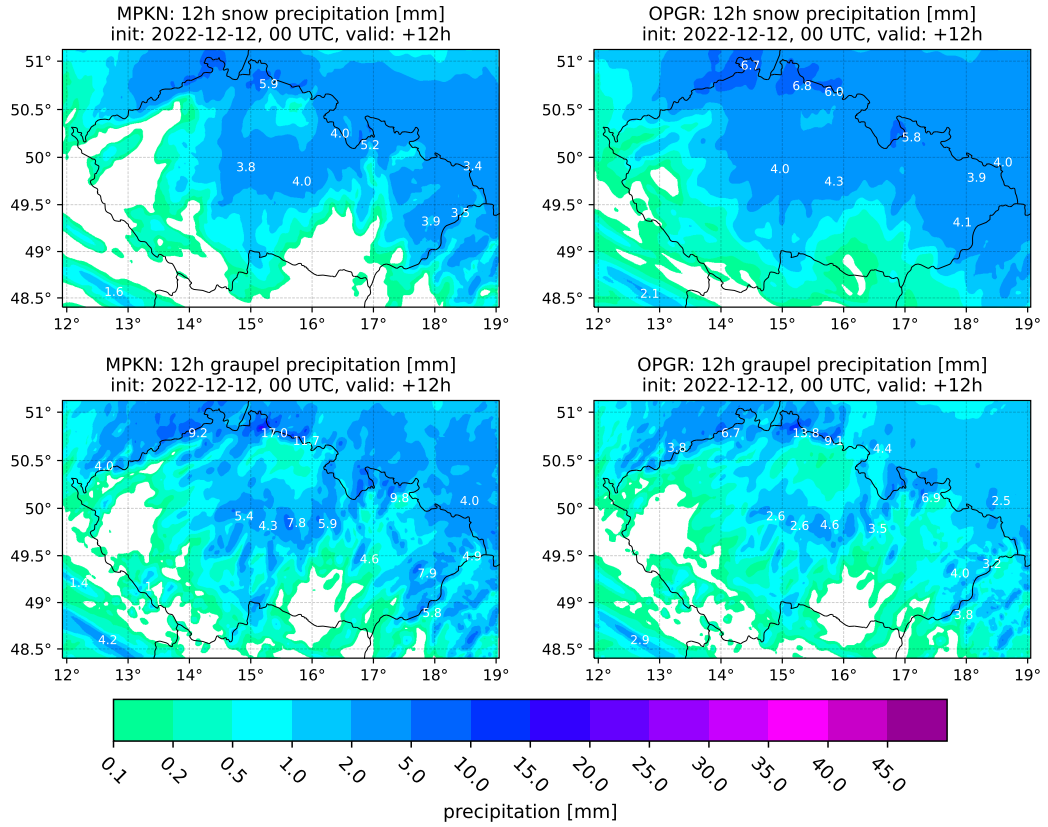


Figure 8.31: The precipitation accumulation in the form of snow (upper) and in the form of graupel (lower). MPKN is on the left and OPRG on the right.

ground when the cloud base is high above the surface, which is the case on the lee side of the mountains. This was confirmed by vertical cross sections of snow, which show that snow sublimates at small heights above the surface leeward of the mountains, although the cloud base is similarly high. This improvement is in accordance with the results obtained from the snowfall over the Alps and in Intal valley, discussed in Section 7.2.

On the other hand, there is a possible overestimation of precipitation over Jizerské hory, at least the comparison with MERGE suggests it. However, it can be tricky since the cloudiness was too low for radars to capture the amount of precipitation correctly, and the population of gauges is not so dense in this area to capture the possible effect of the circulation in the mountains. Moreover, not all snow falls into gauges due to wind. It seems that the precipitation accumulation over northern Czechia is slightly overestimated, as well as over central Czechia, where the uncertainty is lower.

9. Summary and discussion

The first aim of this thesis was to gather information about microphysics schemes with three prognostic ice hydrometeors. In the following stage, these findings were used for improving the parameterization of prognostic graupel.

The original parameterization of graupel was based on the idea that the mechanical properties (fall speed and collection) of graupel are that of rain, and its thermodynamical properties (evaporation and melting) are that of snow. A new set of parameters for graupel was introduced in this thesis as a more realistic approach to the parameterization of graupel. The new set of parameters primarily delivers a lower fall speed of graupel. The results of the upper air scores are slightly improved compared to the original parameterization of graupel. It tends to reduce the overestimated precipitation maxima in convection. Conversely, the proposed parameterization enhances the commonly observed cold bias at the surface due to more effective sublimation of graupel as its fall speed was reduced. The positive geopotential bias is also magnified. Thus, the main difference is that this approach is more physically based; the improvement of the model results is rather subtle.

The trial of the production of graupel from snow was not successful. When autoconversion from snow to graupel is implemented, graupel is produced in a horizontal layer below the layer where snow prevails. In reality, graupel is often located near updraughts. Another approach is to contribute to the graupel category in the case of heavy riming of cloud water onto snowflakes. However, it leads to sudden reflectivity drops when snow is abruptly converted to graupel. The drop of simulated reflectivity often happens in the central parts of storms, which is not observed. When this process is damped to prevent producing these artifacts, the influence of this proposal needs to be more significant to be beneficial. Thus, the production terms of graupel remain only the WBF process and the freezing of rain.

The second aim of this thesis was to improve the microphysical processes of the whole microphysics scheme. Firstly, the parameters of autoconversion of rain and snow were modified. Secondly, an alternative parameterization of evaporation was adjusted for the set of parameters for rain used in ALARO and for prognostic graupel.

Modifying the slope parameter of ice to snow autoconversion from $k_s = 2 \cdot 10^{-3} \text{ s}^{-1}$ to $k_s = 10^{-3} \text{ s}^{-1}$ improves surface scores. The influence on the meteorological fields is not substantial. However, precipitation maxima are slightly lowered in the case of convection and the simulated radiances are improved. This value ($k_s = 10^{-3} \text{ s}^{-1}$) is widely used across microphysics schemes. However, the autoconversion rates are often hardly known as they depend on many factors. Thus, this parameter remains a tunable one.

In addition, the computation of the temperature dependency of the threshold value of the specific content of cloud ice for autoconversion to snow q_i^{crit} was modified. The value of q_i^{crit} is set lower for all temperatures. The shape of the function and its coefficients were estimated by comparison with satellite measurements of tropical cirri by Chaboureaud and Pinty [2006]. Multiple values of coefficients of this computation were tested, but none of them improved the results. The result

of this modification is a better representation of Cumulonimbi anvils as feedback of the modified vertical temperature profile.

The threshold value of the specific content of cloud water for autoconversion to rain was changed from $q_l^{crit} = 3 \cdot 10^{-4} \text{ kg} \cdot \text{kg}^{-1}$ to $q_l^{crit} = 4 \cdot 10^{-4} \text{ kg} \cdot \text{kg}^{-1}$. This adjustment improves results in the case of autumn or winter inversions when there is often weak precipitation predicted, although no precipitation is observed. This value is a good compromise between lower precipitation accumulations and keeping the liquid water content of stratocumuli in realistic values.

The Khairoutdinov and Kogan [2000] autoconversion parameterization should deliver more realistic autoconversion rates than the Kessler autoconversion parameterization (Phillips and Yano [2015]). Thus, this approach was tested. However, simulations with this scheme delivers too high liquid water content of stratocumuli, which more than doubled the upper limit of the liquid water content based on the literature (Khvorostyanov and Curry [2014], Pruppacher and Klett [1997]). The main reason is that the model requires a certain rainwater specific content to onset precipitation. If the autoconversion rate is not high enough, all produced rain evaporates in one time step, and in the following step, cloud water is created again in the saturation adjustment. If the cloud water specific content is high enough, which is highly probable, autoconversion to rain delivers little rain again. This loop would be stopped if the water droplets' size distribution differed. The bigger the water drops, the higher the volume ratio to their surface. Thus, bigger particles deliver lower evaporation rates than smaller ones when stationary. However, the current model configuration uses the mass-size distribution of water drops following Abel and Boutle [2012], which should be more realistic than the mass-size distribution proposed by Marshall and Palmer [1948]. Moreover, the model suffers from too much precipitation in autumn. Thus, it is convenient to use this mass-size distribution as it assumes smaller drops in the case of drizzle and bigger ones in the case of heavy precipitation. Consequently, this autoconversion parameterization is not a favourable solution for keeping physical realism. Another possibility for avoiding high liquid water content in stratocumuli is implementing prognostic equations for aerosol concentrations. The number of aerosols modifies the number of cloud droplets. Thus, it influences the autoconversion rate of this autoconversion parameterization. The prognostic aerosol concentrations solved the problem for Wilkinson et al. [2013], so it might be an option to reduce the liquid water content in stratocumuli in ALARO.

Finally, the evaporation parameterization was changed. However, the results are controversial. On the one hand, precipitation forecasts are improved, mainly during convective storms and it delivers better representation of rain shadow. An explanation of the reduction of precipitation accumulation in convective storms might be that there is a narrower area of instantaneous precipitation. However, the maximal value in one time step is not reduced. Also, the enhanced evaporation modifies the temperature profile on local scales. Thus, the origin of new convective cells might be altered. The latter might explain why precipitation maxima are reduced in MCSs, unlike in single-cellular storms. Moreover, the movement of some storms is faster due to stronger cold pool. On top of that, enhanced evaporation causes stronger resolved downdrafts. Another positive is the general improvement of the upper air atmospheric scores.

On the other hand, the atmospheric scores are worsened at the surface as the existing cold bias and positive bias of relative humidity are enhanced. Both these deficiencies might be lessened when the microphysics modifications are incorporated into the assimilation cycle because less evaporation leads to lower filling of the groundwater reservoir, which does not support excessive evaporation from the surface during the day, which significantly lowers the temperature. This feedback through the assimilation cycle might be observed after a longer assimilation cycle because of the difference in precipitation accumulations. The model currently slightly overestimates the precipitation accumulations. Thus, less precipitation would be beneficial to forecasts of precipitation. The assimilation cycle would not change the positive bias of geopotential much as the lower troposphere remains colder even with different rates of heat fluxes at the surface. Thus, the effect of this modification must be thoroughly evaluated before meteorological services use it.

The final evaluation proved the primary influence of the alternative evaporation parameterization. It helped reveal the positive sides of the Lopez evaporation parameterization: improved upper air scores, better precipitation forecast, and lowered precipitation maxima. Contrarily, its deficiencies are the positive bias of geopotential, the negative bias of temperature, and the positive bias of RH2m. The assimilation cycle would partially compensate the latter two if extended, ideally for a few months. Nonetheless, the positive bias of geopotential at the surface is expected to remain. Thus, it is hard to say if the changes are positive or negative. It depends upon whether the improved forecast of precipitation outweighs the worsened surface scores.

Many factors influence the surface scores as the meteorological quantities are obtained by an interpolation between the lowermost model level and the parameterized surface. Consequently, the results are greatly influenced by radiation and turbulence. Thus, future work might focus on improving the model performance at the surface with this microphysical proposal.

Finally, the shape of the function for the Lopez evaporation parameterization might be problematic in the melting layer, where a small amount of rainwater might be produced from melting snow or graupel, which is then effectively evaporated. However, it is impossible to solve this problem with a single-moment scheme unless a particular variable with a different mass-size distribution is implemented. This approach is not used in any currently used single-moment microphysics schemes because the computational costs of such a solution exceed the possible gains. Double-moment schemes can solve this problem, as they also compute the number concentration of hydrometeors.

10. Conclusion

This thesis dealt with the microphysics schemes used in NWP and the consequent validation of the scheme used in the numerical weather prediction model ALADIN, used at the Czech Hydrometeorological Institute. The first three chapters described microphysical processes and their parameterization in various microphysics schemes. The fourth chapter described the NWP model ALARO and its parameterizations concerning the microphysics scheme. The fifth chapter introduced selected periods of various weather regimes, which are used for tests of adjustments of the microphysics scheme in chapters six and seven.

The first of the two main results of this thesis is a more physically correct parameterization of prognostic graupel. The proposed set of parameters is based on research on the treatment of graupel in various microphysics schemes. Graupel density was set to $\rho_g = 400 \text{ kg} \cdot \text{m}^{-3}$, and its shape is assumed spherical. The new fall speed relation delivers lower fall speeds. The collection efficiency of graupel is set to $E_{ff}^g = 0.15$, a value between the values used for rain and snow. This change decreases the temperature of the lower troposphere and occasionally slightly reduces precipitation accumulation maxima in convective storms.

The following part of this thesis focused on further developments of the ALARO microphysics. Coefficients of autoconversion to rain and snow were modified. The threshold value above which autoconversion from cloud water to rainwater occurs was raised to $q_l^{crit} = 4 \cdot 10^{-4} \text{ kg} \cdot \text{kg}^{-1}$, which reduces the positive bias of precipitation in autumn. The first coefficient of ice-to-snow autoconversion was decreased from $k_s = 2 \cdot 10^{-3} \text{ s}^{-1}$ to $k_s = 10^{-3} \text{ s}^{-1}$. This adjustment makes cumulonimbus anvils optically thicker. Finally, an alternative computation of the threshold value of the ice-to-snow autoconversion was implemented. It delivers more cloud ice to the higher troposphere and improves the shapes of cumulonimbi anvils.

Also, new relations respecting the values of the parameters of the fall speed relation and mass-size distribution of rain and graupel were derived. This package improves the forecast of precipitation and the performance of the model forecasts of upper air meteorological fields, namely, their biases and standard deviations. Contrarily, the performance at the surface is usually worsened for the same fields as the cold bias is more pronounced, as well as the positive bias of geopotential and relative humidity. Also, the standard deviation and root mean square error of wind speed and wind direction at the surface are often worsened. The deficiencies are partially reduced if the modifications are integrated into the assimilation cycle.

The possible further developments might focus on implementing prognostic aerosol computations, which may improve precipitation forecasts in all weather regimes. Another path might be the development of a multi-moment microphysics scheme.

Bibliography

- S. J. Abel and I. A. Boutle. An improved representation of the raindrop size distribution for single-moment microphysics schemes. *Quarterly Journal of the Royal Meteorological Society*, 138(669):2151–2162, 2012. doi: <https://doi.org/10.1002/qj.1949>. URL <https://rmets.onlinelibrary.wiley.com/doi/abs/10.1002/qj.1949>.
- C. Alexander, D. Dowell, M. Hu, J. Olson, T. Smirnova, T. Ladwig, S. Weygandt, J. Kenyon, E. James, H. Lin, G. Grell, G. Ge, T. Alcott, S. Benjamin, J. Brown, M. Toy, R. Ahmadov, A. Back, J. Duda, M. Smith, J. Hamilton, B. Jamison, I. Jankov, and D. Turner. Rapid Refresh (RAP) and High Resolution Rapid Refresh (HRRR) Model Development. Presentation. AMS 100th Annual Meeting., 01 2020. URL https://rapidrefresh.noaa.gov/pdf/Alexander_AMS_NWP_2020.pdf.
- American Meteorological Society. Glossary of Meteorology, 2023. URL <http://glossary.ametsoc.org>.
- S. Bae, S.-Y. Hong, and W.-K. Tao. Development of a Single-Moment Cloud Microphysics Scheme with Prognostic Hail for the Weather Research and Forecasting (WRF) Model. *Asia-Pacific Journal of Atmospheric Sciences*, 55, 10 2018. doi: 10.1007/s13143-018-0066-3.
- M. Baldauf, A. Seifert, J. Förstner, D. Majewski, M. Raschendorfer, and T. Reinhardt. Operational Convective-Scale Numerical Weather Prediction with the COSMO Model: Description and Sensitivities. *Monthly Weather Review*, 139(12):3887 – 3905, 2011. doi: 10.1175/MWR-D-10-05013.1. URL <https://journals.ametsoc.org/view/journals/mwre/139/12/mwr-d-10-05013.1.xml>.
- J.-W. Bao, S. Michelson, and E. Grell. Microphysical Process Comparison of Three Microphysics Parameterization Schemes in the WRF Model for an Idealized Squall-Line Case Study. *Monthly Weather Review*, 147:3093–3120, 09 2019. doi: 10.1175/MWR-D-18-0249.1.
- M. Batka. Optimalizace rozlišení LAM. Část II. Optimální volba parametrů Lambertova konformního zobrazení. *Meteorologické zprávy*, 55(2):33–39, 2002. URL <https://www.chmi.cz/files/portal/docs/reditel/SIS/casmz/assets/2002/Meteo-2002-02.pdf>.
- L. Bengtsson, U. Andrae, T. Aspelién, Y. Batrak, J. Calvo, W. de Rooy, E. Gleeson, B. Hansen-Sass, M. Homleid, M. Hortal, K.-I. Ivarsson, G. Lenderink, S. Niemelä, K. P. Nielsen, J. Onvlee, L. Rontu, P. Samuelsson, D. S. Muñoz, A. Subias, S. Tijn, V. Toll, X. Yang, and M. Ødegaard Kjøtzow. The HARMONIE–AROME Model Configuration in the ALADIN–HIRLAM NWP System. *Monthly Weather Review*, 145(5):1919 – 1935, 2017. doi: 10.1175/MWR-D-16-0417.1. URL <https://journals.ametsoc.org/view/journals/mwre/145/5/mwr-d-16-0417.1.xml>.

- E. X. Berry and R. L. Reinhardt. An analysis of cloud drop growth by collection: Part i. double distributions. *Journal of Atmospheric Sciences*, 31(7):1814 – 1824, 1974a. doi: 10.1175/1520-0469(1974)031<1814:AAOCDG>2.0.CO;2. URL https://journals.ametsoc.org/view/journals/atsc/31/7/1520-0469_1974_031_1814_aaocdg_2_0_co_2.xml.
- E. X. Berry and R. L. Reinhardt. An analysis of cloud drop growth by collection part ii. single initial distributions. *Journal of Atmospheric Sciences*, 31(7):1825 – 1831, 1974b. doi: 10.1175/1520-0469(1974)031<1825:AAOCDG>2.0.CO;2. URL https://journals.ametsoc.org/view/journals/atsc/31/7/1520-0469_1974_031_1825_aaocdg_2_0_co_2.xml.
- Y. Bouteloup, Y. Seity, and E. Bazile. Description of the sedimentation scheme used operationally in all météo-france nwp models. *Tellus A*, 63(2):300–311, 2011. doi: <https://doi.org/10.1111/j.1600-0870.2010.00484.x>. URL <https://onlinelibrary.wiley.com/doi/abs/10.1111/j.1600-0870.2010.00484.x>.
- I. A. Boutle and S. J. Abel. Microphysical controls on the stratocumulus topped boundary-layer structure during vocals-rer. *Atmospheric Chemistry and Physics*, 12(6):2849–2863, 2012. doi: 10.5194/acp-12-2849-2012. URL <https://acp.copernicus.org/articles/12/2849/2012/>.
- R. Brožková, A. Bučánek, J. Mašek, P. Smolíková, and A. Trojáková. New high-resolution operational configuration of the ALADIN model. *Meteorological Bulletin*, 72(5):129–139, 2019. URL http://portal.chmi.cz/files/portal/docs/reditel/SIS/casmz/assets/2019/chmu_mz_5-19.pdf.
- Radmila Brožková. Moist processes generalities. Presentation. ALARO Training Course, Radostovice., 03 2007. URL https://www.rclace.eu/File/ALARO/TCA0_Radostovice2007/L04_RB_Moist_Processes.pdf.
- Antonín Bučánek. Verification of the ALADIN precipitation forecast using Fraction Skill Score. *Technical note*, 11 2020.
- B. Catry, J.-F. Geleyn, M. Tudor, P. Bénard, and A. Trojáková. Flux-conservative thermodynamic equations in a mass-weighted framework. *Tellus A: Dynamic Meteorology and Oceanography*, 59(1):71–79, 2007. doi: 10.1111/j.1600-0870.2006.00212.x. URL <https://doi.org/10.1111/j.1600-0870.2006.00212.x>.
- B. Catry, J.-F. Geleyn, F. Bouyssel, J. Cedilnik, R. Brožková, M. Derková, and R. Mládek. A new sub-grid scale lift formulation in a mountain drag parameterisation scheme. *Meteorologische Zeitschrift*, 17:193–208, 04 2008. doi: 10.1127/0941-2948/2008/0272.
- Bart Catry. *Effects of moisture and mountains in Numerical Weather Prediction*. PhD thesis, University of Ghent, 2006.
- Bart Catry. Microphysical processes. Presentation. ALARO Training Course, Radostovice., 03 2007. URL https://www.rclace.eu/File/ALARO/TCA0_Radostovice2007/L05_BC_microphys2.pdf.

- Česká meteorologická společnost. Elektronický meteorologický slovník výkladový a terminologický (eMS)., 2023. URL <http://slovník.cmes.cz>.
- J.-P. Chaboureau and P. Bechtold. A simple cloud parameterization derived from cloud resolving model data: Diagnostic and prognostic applications. *Journal of the Atmospheric Sciences*, 59(15):2362 – 2372, 2002. doi: 10.1175/1520-0469(2002)059<2362:ASCPDF>2.0.CO;2. URL https://journals.ametsoc.org/view/journals/atsc/59/15/1520-0469_2002_059_2362_ascpdf_2.0.co_2.xml.
- J.-P. Chaboureau and J.-P. Pinty. Validation of a cirrus parameterization with meteosat second generation observations. *Geophysical Research Letters*, 33(3), 2006. doi: <https://doi.org/10.1029/2005GL024725>. URL <https://agupubs.onlinelibrary.wiley.com/doi/abs/10.1029/2005GL024725>.
- COSMO. Transition to icon, 2022. URL <http://www.cosmo-model.org/content/support/icon/default.htm>.
- R. J. Cotton, P. R. Field, Z. Ulanowski, P. H. Kaye, E. Hirst, R. S. Greenaway, I. Crawford, J. Crosier, and J. Dorsey. The effective density of small ice particles obtained from in situ aircraft observations of mid-latitude cirrus. *Quarterly Journal of the Royal Meteorological Society*, 139(676):1923–1934, 2013. doi: <https://doi.org/10.1002/qj.2058>. URL <https://rmets.onlinelibrary.wiley.com/doi/abs/10.1002/qj.2058>.
- G. Doms, J. Förstner, E. Heise, H.-J. Herzog, D. Mironov, M. Raschendorfer, T. Reinhardt, B. Ritter, R. Schrodin, J.-P. Schulz, and G. Vogel. *A Description of the Nonhydrostatic Regional COSMO-Model*, chapter Part II: Physical Parameterizations. Consortium for Small-Scale Modelling, 09 2021. doi: doi.org/10.5676/dwd_pub/nwv/cosmo-doc_6.00_II. URL https://www.cosmo-model.org/content/model/documentation/core/cosmo_physics_6.00.pdf.
- ECMWF. *IFS Documentation CY47R3 - Part III Dynamics and numerical procedures*. Number 3 in IFS Documentation. ECMWF, 10 2021. doi: [10.21957/b18qxs663](https://doi.org/10.21957/b18qxs663). URL <https://www.ecmwf.int/node/20197>.
- B. J. Engdahl, G. Thompson, and L. Bengtsson. Improving the representation of supercooled liquid water in the HARMONIE-AROME weather forecast model. *Tellus*, 72, 11 2019. doi: [10.1080/16000870.2019.1697603](https://doi.org/10.1080/16000870.2019.1697603).
- B. J. Engdahl, T. Carlsen, M. Kølitzow, and T. Storelvmo. The Ability of the ICE-T Microphysics Scheme in HARMONIE-AROME to Predict Aircraft Icing. *Weather and Forecasting*, 37(2):205 – 217, 2022. doi: [10.1175/WAF-D-21-0104.1](https://doi.org/10.1175/WAF-D-21-0104.1). URL <https://journals.ametsoc.org/view/journals/wefo/37/2/WAF-D-21-0104.1.xml>.
- European Severe Storms Laboratory. European severe weather database, 2023. URL <https://eswd.eu/cgi-bin/eswd.cgi>.

- Paul R. Field. Implementing double moment cloud microphysics into the regional configuration of the unified model. Presentation. Annual Seminar 2022. ECMWF, Reading., 9 2022. URL https://events.ecmwf.int/event/300/contributions/3282/attachments/1940/3499/AS2022_Field.pdf.
- M. F. Garvert, B. A. Colle, and C. F. Mass. The 13–14 december 2001 improve-2 event. part i: Synoptic and mesoscale evolution and comparison with a mesoscale model simulation. *Journal of the Atmospheric Sciences*, 62(10):3474 – 3492, 2005. doi: 10.1175/JAS3549.1. URL <https://journals.ametsoc.org/view/journals/atsc/62/10/jas3549.1.xml>.
- J.-F. Geleyn, B. Catry, R. Brožková, and C. Wittmann. APLMPHYS and its ingredients. *Technical note*, 2007. URL https://www.rclace.eu/media/files/ALARO/ACPLUIE_prog_septe.pdf.
- J.-F. Geleyn, R. Brožková, and J. Rio. Basic ideas about the use of a xu-randall-modified formula to find an equilibrium point for stratiform condensation-evaporation of prognostic cloud water. *Internal documentation*, 2008a.
- J.-F. Geleyn, B. Catry, Y. Bouteloup, and R. Brožková. A statistical approach for sedimentation inside a microphysical precipitation scheme. *Tellus A: Dynamic Meteorology and Oceanography*, 60(4):649–662, 2008b. doi: 10.1111/j.1600-0870.2007.00323.x. URL <https://www.tandfonline.com/doi/abs/10.1111/j.1600-0870.2007.00323.x>.
- J.-F. Geleyn, R. Brožková, L. Gerard, and C. Wittmann. Description of the microphysics used in the convective clouds part of the ALARO-0 physics ensemble. *Technical note*, 2011.
- J.-F. Geleyn, J. Mašek, R. Brožková, P. Kuma, D. Degrauwe, G. Hello, and N. Pristov. Single interval longwave radiation scheme based on the net exchanged rate decomposition with bracketing. *Quarterly Journal of the Royal Meteorological Society*, 143(704):1313–1335, 2017. doi: <https://doi.org/10.1002/qj.3006>. URL <https://rmets.onlinelibrary.wiley.com/doi/abs/10.1002/qj.3006>.
- L. Gerard, J.-M. Piriou, R. Brožková, Geleyn J.-F., and D. Banciu. Cloud and Precipitation Parameterization in a Meso-Gamma-Scale Operational Weather Prediction Model. *Monthly Weather Review*, 137(11):3960 – 3977, 2009. doi: 10.1175/2009MWR2750.1. URL <https://journals.ametsoc.org/view/journals/mwre/137/11/2009mwr2750.1.xml>.
- Luc Gerard. *Model resolution issues and new approaches in the convection-permitting regimes*, chapter Chapter 19, pages 113–134. 2015. doi: 10.1142/9781783266913_0022. URL https://www.worldscientific.com/doi/abs/10.1142/9781783266913_0022.
- S. Ghosh and P. Jonas. On the Application of the Classic Kessler and Berry Schemes in Large Eddy Simulation Models with a Particular Emphasis on Cloud Autoconversion, the Onset Time of Precipitation and Droplet Evaporation. *Annales Geophysicae*, 16, 05 1998. doi: 10.1007/s00585-998-0628-2.

- A. Heymsfield, M. Szakáll, A. Jost, I. Giammanco, and R. Wright. A comprehensive observational study of graupel and hail terminal velocity, mass flux, and kinetic energy. *Journal of the Atmospheric Sciences*, 75(11):3861 – 3885, 2018. doi: 10.1175/JAS-D-18-0035.1. URL <https://journals.ametsoc.org/view/journals/atsc/75/11/jas-d-18-0035.1.xml>.
- Viktória Homonnai. Initialization of aerosols in LIMA scheme for AROME. *RC LACE stay report*, 2016. URL https://www.rclace.eu/media/files/Physics/2016/homonnaiv_LACEreport_Nov2016_Toulouse.pdf.
- S. Hong and J. J. Lim. The WRF Single-Moment 6-Class Microphysics Scheme (WSM6). *Journal of the Korean Meteorological Society*, 42:129–151, 2006.
- ICON. Transition to icon, 2022. URL <https://code.mpimet.mpg.de/projects/iconpublic/wiki/Documentation>.
- A. L. Igel, M. R. Igel, and S. C. van den Heever. Make It a Double? Sobering Results from Simulations Using Single-Moment Microphysics Schemes. *Journal of the Atmospheric Sciences*, 72(2):910 – 925, 2015. doi: 10.1175/JAS-D-14-0107.1. URL <https://journals.ametsoc.org/view/journals/atsc/72/2/jas-d-14-0107.1.xml>.
- M. Ikawa and Kazuo Saito. Description of a Non-hydrostatic Model Developed at the Forecast Research Department of the MRI. *Technical Reports of the Meteorological Research Institute*, 28:238pp, 12 1991. doi: 10.11483/mritechrepo.28.
- Y. Ikuta, M. Satoh, M. Sawada, H. Kusabiraki, and T. Kubota. Improvement of the Cloud Microphysics Scheme of the Mesoscale Model at the Japan Meteorological Agency Using Spaceborne Radar and Microwave Imager of the Global Precipitation Measurement as Reference. *Monthly Weather Review*, 149(11): 3803 – 3819, 2021. doi: 10.1175/MWR-D-21-0066.1. URL <https://journals.ametsoc.org/view/journals/mwre/149/11/MWR-D-21-0066.1.xml>.
- M. Janoušek and R. Mládek. Verification package VERAL. Description and User’s Guide. *Internal technical note*, 2008.
- Japan Meteorological Agency. *Outline of the Operational Numerical Weather Prediction at the Japan Meteorological Agency. Appendix to WMO Technical Progress Report on the Global Data-processing and Forecasting System (GDPFS) and Numerical Weather Prediction (NWP) Research*, chapter Section 3.5.4: Cloud Microphysics. Japan Meteorological Agency, 03 2019. URL https://www.jma.go.jp/jma/jma-eng/jma-center/nwp/outline2019-nwp/pdf/outline2019_all.pdf.
- Japan Meteorological Agency. *Outline of the Operational Numerical Weather Prediction at the Japan Meteorological Agency. Appendix to WMO Technical Progress Report on the Global Data-processing and Forecasting System (GDPFS) and Numerical Weather Prediction (NWP) Research*, chapter Section 3.5.4: Cloud Microphysics. Number 3. Japan Meteorological Agency, 02 2022. URL https://www.jma.go.jp/jma/jma-eng/jma-center/nwp/outline2022-nwp/pdf/outline2022_all.pdf.

- M. Johnson, Y. Jung, D. Dawson II, T. Supinie, M. Xue, J. Park, and L. Yong-Hee. Evaluation of Unified Model Microphysics in High-resolution NWP Simulations Using Polarimetric Radar Observations. *Advances in Atmospheric Sciences*, 35:771–784, 07 2018. doi: 10.1007/s00376-017-7177-0.
- A. Joly, J.-M. Piriou, T. Kovacic, and J. Maziejewski. Diagnostics in Horizontal Domains (DDH). Guide for users and developpers. *Technical note*, 2019. URL <https://www.umr-cnrm.fr/gmapdoc/IMG/pdf/ddh.pdf>.
- Edwin Kessler. On the continuity of water substance. Technical report, Boulder, Colorado, USA, 04 1967.
- A. P. Khain, K. D. Beheng, A. Heymsfield, A. Korolev, S. O. Krichak, Z. Levin, M. Pinsky, V. Phillips, T. Prabhakaran, A. Teller, S. C. van den Heever, and J.-I. Yano. Representation of microphysical processes in cloud-resolving models: Spectral (bin) microphysics versus bulk parameterization. *Reviews of Geophysics*, 53(2):247–322, 2015. doi: <https://doi.org/10.1002/2014RG000468>. URL <https://agupubs.onlinelibrary.wiley.com/doi/abs/10.1002/2014RG000468>.
- M. Khairoutdinov and Y. Kogan. A New Cloud Physics Parameterization in a Large-Eddy Simulation Model of Marine Stratocumulus. *Monthly Weather Review*, 128(1):229 – 243, 2000. doi: 10.1175/1520-0493(2000)128<0229:ANCPPI>2.0.CO;2. URL https://journals.ametsoc.org/view/journals/mwre/128/1/1520-0493_2000_128_0229_ancppi_2.0.co_2.xml.
- V.I. Khvorostyanov and J. Curry. *Thermodynamics, kinetics, and microphysics of clouds*. Cambridge University Press, 01 2014. doi: 10.1017/CBO9781139060004.
- G. D. Kinzer and R. Gunn. The evaporation, temperature and thermal relaxation-time of freely falling waterdrops. *Journal of Atmospheric Sciences*, 8(2):71 – 83, 1951. doi: 10.1175/1520-0469(1951)008<0071:TETATR>2.0.CO;2. URL https://journals.ametsoc.org/view/journals/atsc/8/2/1520-0469_1951_008_0071_tetatr_2_0_co_2.xml.
- Yefim Kogan. A cumulus cloud microphysics parameterization for cloud-resolving models. *Journal of the Atmospheric Sciences*, 70(5):1423 – 1436, 2013. doi: <https://doi.org/10.1175/JAS-D-12-0183.1>. URL <https://journals.ametsoc.org/view/journals/atsc/70/5/jas-d-12-0183.1.xml>.
- C. G. Köhler and A. Seifert. Identifying sensitivities for cirrus modelling using a two-moment two-mode bulk microphysics scheme. *Tellus B: Chemical and Physical Meteorology*, 67(1):24494, 2015. doi: 10.3402/tellusb.v67.24494. URL <https://doi.org/10.3402/tellusb.v67.24494>.
- Laboratoire d’Aérodynamique et CNRM-GAME. *The Meso-NH Atmospheric Simulation System: Scientific Documentation.*, chapter Part III: Physics. Number 3. CNRM, 06 2022. doi: 10.21957/b18qxs663. URL http://mesonh.aero.obs-mip.fr/mesonh55/BooksAndGuides?action=AttachFile&do=view&target=scidoc_p3.pdf.

- René Laprise. The Euler Equations of Motion with Hydrostatic Pressure as an Independent Variable. *Monthly Weather Review*, 120(1): 197 – 207, 1992. doi: 10.1175/1520-0493(1992)120<0197:TEEOMW>2.0.CO;2. URL https://journals.ametsoc.org/view/journals/mwre/120/1/1520-0493_1992_120_0197_teeomw_2_0_co_2.xml.
- F. Lascaux, E. Richard, and J.-P. Pinty. Numerical simulations of three different MAP IOPs and the associated microphysical processes. *Quarterly Journal of the Royal Meteorological Society*, 132(619):1907–1926, 2006. doi: <https://doi.org/10.1256/qj.05.197>. URL <https://rmets.onlinelibrary.wiley.com/doi/abs/10.1256/qj.05.197>.
- H. Lee and J.-J. Baik. A Comparative Study of Bin and Bulk Cloud Microphysics Schemes in Simulating a Heavy Precipitation Case. *Atmosphere*, 9(12), 2018. ISSN 2073-4433. doi: 10.3390/atmos9120475. URL <https://www.mdpi.com/2073-4433/9/12/475>.
- J.-O. Lim, S.-Y. Hong, and J. Dudhia. The WRF-single-moment-microphysics scheme and its evaluation of the simulation of mesoscale convective systems. *Bulletin of the American Meteorological Society*, 01 2004.
- Y.-L. Lin, R. D. Farley, and H. D. Orville. Bulk Parameterization of the Snow Field in a Cloud Model. *Journal of Applied Meteorology and Climatology*, 22 (6):1065 – 1092, 1983. doi: 10.1175/1520-0450(1983)022<1065:BPOTSF>2.0.CO;2. URL https://journals.ametsoc.org/view/journals/apme/22/6/1520-0450_1983_022_1065_bpotsf_2_0_co_2.xml.
- Robert J. List. *Smithsonian Meteorological Tables*, volume 528. Smithsonian Miscellaneous Collections, 1951. ISBN 978-80-200-1505-1.
- Y. Liu and P. H. Daum. Parameterization of the Autoconversion Process. Part I: Analytical Formulation of the Kessler-Type Parameterizations. *Journal of the Atmospheric Sciences*, 61(13):1539 – 1548, 2004. doi: 10.1175/1520-0469(2004)061<1539:POTAPI>2.0.CO;2. URL https://journals.ametsoc.org/view/journals/atsc/61/13/1520-0469_2004_061_1539_potapi_2.0.co_2.xml.
- Y. Liu, P. Daum, R. McGraw, and R. Wood. Parameterization of the Autoconversion Process. Part II: Generalization of Sundqvist-Type Parameterizations. *Journal of the Atmospheric Sciences*, 63:1103–1109, 03 2006. doi: 10.1175/jas3675.1.
- J. D. Locatelli and P. V. Hobbs. Fall speeds and masses of solid precipitation particles. *Journal of Geophysical Research (1896-1977)*, 79(15):2185–2197, 1974. doi: <https://doi.org/10.1029/JC079i015p02185>. URL <https://agupubs.onlinelibrary.wiley.com/doi/abs/10.1029/JC079i015p02185>.
- Philippe Lopez. Implementation and validation of a new prognostic large-scale cloud and precipitation scheme for climate and data-assimilation purposes. *Quarterly Journal of the Royal Meteorological Society*, 128(579):229–257, 2002. doi: <https://doi.org/10.1256/00359000260498879>. URL <https://rmets.onlinelibrary.wiley.com/doi/abs/10.1256/00359000260498879>.

- Ekaterina Machulskaya. *Clouds and convection as subgrid-scale distributions*, chapter Chapter 25, pages 377–422. 2015. doi: 10.1142/9781783266913_0029. URL https://www.worldscientific.com/doi/abs/10.1142/9781783266913_0029.
- M. J. Manton and W. R. Cotton. Formulation of approximate equations for modeling moist deep convection on the mesoscale., 1977.
- J. S. Marshall and W. Mc K. Palmer. The distribution of raindrops with size. *Journal of Atmospheric Sciences*, 5(4):165 – 166, 1948. doi: 10.1175/1520-0469(1948)005<0165:TDORWS>2.0.CO;2. URL https://journals.ametsoc.org/view/journals/atsc/5/4/1520-0469_1948_005_0165_tdorws_2_0_co_2.xml.
- J. Mašek, J.-F. Geleyn, R. Brožková, O. Giot, H. O. Achom, and P. Kuma. Single interval shortwave radiation scheme with parameterized optical saturation and spectral overlaps. *Quarterly Journal of the Royal Meteorological Society*, 142 (694):304–326, 2016. doi: <https://doi.org/10.1002/qj.2653>. URL <https://rmets.onlinelibrary.wiley.com/doi/abs/10.1002/qj.2653>.
- J. A. Milbrandt and M. K. Yau. A Multimoment Bulk Microphysics Parameterization. Part I: Analysis of the Role of the Spectral Shape Parameter. *Journal of the Atmospheric Sciences*, 62(9):3051 – 3064, 2005. doi: 10.1175/JAS3534.1. URL <https://journals.ametsoc.org/view/journals/atsc/62/9/jas3534.1.xml>.
- A. K. Miltenberger, P. R. Field, A. A. Hill, P. Rosenberg, B. J. Shipway, J. M. Wilkinson, R. Scovell, and A. M. Blyth. Aerosol–cloud interactions in mixed-phase convective clouds – part 1: Aerosol perturbations. *Atmospheric Chemistry and Physics*, 18(5):3119–3145, 2018. doi: 10.5194/acp-18-3119-2018. URL <https://acp.copernicus.org/articles/18/3119/2018/>.
- Carl Rod Nave. Water Vapour and Vapor Pressure, 2023. URL <http://hyperphysics.phy-astr.gsu.edu/hbase/Kinetic/watvap.html>.
- J. Noilhan and S. Planton. A Simple Parameterization of Land Surface Processes for Meteorological Models. *Monthly Weather Review*, 117(3): 536 – 549, 1989. doi: 10.1175/1520-0493(1989)117<0536:ASPOLS>2.0.CO;2. URL https://journals.ametsoc.org/view/journals/mwre/117/3/1520-0493_1989_117_0536_aspols_2_0_co_2.xml.
- Petr Novák and Hana Kyznarová. Merge2 – the upgraded system of quantitative precipitation estimates operated at the czech hydrometeorological institute. *Meteorological Bulletin*, 69(5):137–144, 2016. URL http://portal.chmi.cz/files/portal/docs/reditel/SIS/casmz/assets/2016/chmu_mz_5-16.pdf.
- David Němec. Předpověď/simulace blesků numerickým předpovědním modelem ALADIN, 2021. Bachelor thesis. Supervisor: Žák, Michal.
- V.T.J. Phillips and J.-I. Yano. *Microphysics of convective cloud and its treatment in parameterization*, chapter Chapter 18, pages 75–112. 2015. doi: 10.1142/

- 9781783266913_0021. URL https://www.worldscientific.com/doi/abs/10.1142/9781783266913_0021.
- J.-P. Pinty and P. Jabouille. A mixed-phase cloud parameterization for use in mesoscale non-hydrostatic model: simulations of a squall line and of orographic precipitations. *Proc. Conf. of Cloud Physics, Everett, WA, USA, Amer. Meteor. soc.*, pages 217–220, 1998. URL http://mesonh.aero.obs-mip.fr/mesonh/dir_publication/pinty_jabouille_ams_ccp1998.pdf.
- H. Pruppacher and J. Klett. *Microphysics of clouds and precipitation*. Atmospheric and oceanographic sciences library ; 18. Kluwer Academic Publishers, Dordrecht, 1997. ISBN 0-7923-4211-9.
- D. Řezáčová, P. Novák, M. Kašpar, and M. Setvák. *Fyzika oblaků a srážek*. Academia, Praha, 2007. ISBN 978-80-200-1505-1.
- N. M. Roberts and H. W. Lean. Scale-selective verification of rainfall accumulations from high-resolution forecasts of convective events. *Monthly Weather Review*, 136(1):78 – 97, 2008. doi: 10.1175/2007MWR2123.1. URL <https://journals.ametsoc.org/view/journals/mwre/136/1/2007mwr2123.1.xml>.
- Daniel Rosenfeld. Deep convective clouds with sustained supercooled liquid water down to - 37.5 °C. *Nature*, 405:440–2, 06 2000. doi: 10.1038/35013030.
- S. A. Rutledge and P. V. Hobbs. The Mesoscale and Microscale Structure and Organization of Clouds and Precipitation in Midlatitude Cyclones. XII: A Diagnostic Modeling Study of Precipitation Development in Narrow Cold-Frontal Rainbands. *Journal of Atmospheric Sciences*, 41(20): 2949 – 2972, 1984. doi: 10.1175/1520-0469(1984)041<2949:TMAMSA>2.0.CO;2. URL https://journals.ametsoc.org/view/journals/atsc/41/20/1520-0469_1984_041_2949_tmamsa_2_0_co_2.xml.
- K. Sassen, K. N. Liou, S. Kinne, and M. Griffin. Highly Supercooled Cirrus Cloud Water: Confirmation and Climatic Implications. *Science*, 227(4685):411–413, 1985. doi: 10.1126/science.227.4685.411. URL <https://www.science.org/doi/abs/10.1126/science.227.4685.411>.
- A. Seifert and K. Beheng. A two-moment cloud microphysics parameterization for mixed-phase clouds. part 1: Model description. *Meteorology and Atmospheric Physics*, 92:45–66, 02 2006. doi: 10.1007/s00703-005-0112-4.
- A. Seifert and K. D. Beheng. A double-moment parameterization for simulating autoconversion, accretion and selfcollection. *Atmospheric Research*, 59-60: 265–281, 2001. ISSN 0169-8095. doi: [https://doi.org/10.1016/S0169-8095\(01\)00126-0](https://doi.org/10.1016/S0169-8095(01)00126-0). URL <https://www.sciencedirect.com/science/article/pii/S0169809501001260>. 13th International Conference on Clouds and Precipitation.
- Axel Seifert. A revised cloud microphysical parameterization for cosmo-lme. *COSMO News Letter No.7*, 4(7):25–28, 2008. URL http://www.cosmo-model.org/content/model/documentation/newsLetters/newsLetter07/cnl7_seifert.pdf.

- Y. Seity and S. Riette. Hail forecasts in AROME. Presentation. EWGLAM Meeting, Reading., 10 2017. URL http://srnwp.met.hu/Annual_Meetings/2017/download/tuesday/EWGLAM_2017_YS.pdf.
- B. J. Shipway and A. A. Hill. Diagnosis of systematic differences between multiple parametrizations of warm rain microphysics using a kinematic framework. *Quarterly Journal of the Royal Meteorological Society*, 138(669):2196–2211, 2012. doi: <https://doi.org/10.1002/qj.1913>. URL <https://rmets.onlinelibrary.wiley.com/doi/abs/10.1002/qj.1913>.
- A. J. Simmons and D. M. Burridge. An Energy and Angular-Momentum Conserving Vertical Finite-Difference Scheme and Hybrid Vertical Coordinates. *Monthly Weather Review*, 109(4):758 – 766, 1981. doi: 10.1175/1520-0493(1981)109<0758:AEAAMC>2.0.CO;2. URL https://journals.ametsoc.org/view/journals/mwre/109/4/1520-0493_1981_109_0758_aeaamc_2_0_co_2.xml.
- W. C. Skamarock, J. B. Klemp, J. Dudhia, D. O. Gill, Z. Liu, J. Berner, . . . , and X. yu Huang. A Description of the Advanced Research WRF Model Version 4.3 (No. NCAR/TN-556+STR). Technical report, 07 2021.
- Z. Sokol, R. Brožková, J. Popová, G. Bobotová, and F. Švábik. Evaluation of ALADIN NWP model forecasts by IR10.8 μm and WV06.2 μm brightness temperatures measured by the geostationary satellite Meteosat Second Generation. *Atmospheric Research*, 265:105920, 2022. ISSN 0169-8095. doi: <https://doi.org/10.1016/j.atmosres.2021.105920>. URL <https://www.sciencedirect.com/science/article/pii/S0169809521004762>.
- R. C. Srivastava and J. L. Coen. New Explicit Equations for the Accurate Calculation of the Growth and Evaporation of Hydrometeors by the Diffusion of Water Vapor. *Journal of Atmospheric Sciences*, 49(17):1643 – 1651, 1992. doi: 10.1175/1520-0469(1992)049<1643:NEEFTA>2.0.CO;2. URL https://journals.ametsoc.org/view/journals/atmsc/49/17/1520-0469_1992_049_1643_neefta_2_0_co_2.xml.
- L. Stašová and K. Sedláková. Červen 2022 na území ČR, 2022. URL <http://www.infomet.cz/index.php?id=read&idd=1657634285>.
- Jerry M. Straka. *Cloud and precipitation microphysics : principles and parameterizations*. Cambridge University Press, Cambridge, 2009. ISBN 0-511-69859-3.
- Hilding Sundqvist. A parameterization scheme for non-convective condensation including prediction of cloud water content. *Quarterly Journal of the Royal Meteorological Society*, 104(441):677–690, 1978. doi: <https://doi.org/10.1002/qj.49710444110>. URL <https://rmets.onlinelibrary.wiley.com/doi/abs/10.1002/qj.49710444110>.
- P. Termonia, C. Fischer, E. Bazile, F. Bouyssel, R. Brožková, P. Bénard, B. Bochenek, D. Degrauwe, M. Derková, R. El Khatib, R. Hamdi, J. Mašek, P. Potier, N. Pristov, Y. Seity, P. Smolíková, O. Španiel, M. Tudor, Y. Wang,

- C. Wittmann, and A. Joly. The ALADIN System and its canonical model configurations AROME CY41T1 and ALARO CY40T1. *Geoscientific Model Development*, 11(1):257–281, 2018. doi: 10.5194/gmd-11-257-2018. URL <https://gmd.copernicus.org/articles/11/257/2018/>.
- G. Thompson and T. Eidhammer. A Study of Aerosol Impacts on Clouds and Precipitation Development in a Large Winter Cyclone. *Journal of the Atmospheric Sciences*, 71(10):3636 – 3658, 2014. doi: 10.1175/JAS-D-13-0305.1. URL <https://journals.ametsoc.org/view/journals/atsc/71/10/jas-d-13-0305.1.xml>.
- G. Thompson, R. M. Rasmussen, and K. Manning. Explicit Forecasts of Winter Precipitation Using an Improved Bulk Microphysics Scheme. Part I: Description and Sensitivity Analysis. *Monthly Weather Review*, 132(2): 519 – 542, 2004. doi: 10.1175/1520-0493(2004)132<0519:EFOWPU>2.0.CO;2. URL https://journals.ametsoc.org/view/journals/mwre/132/2/1520-0493_2004_132_0519_efowpu_2.0.co_2.xml.
- G. Thompson, P. R. Field, R. M. Rasmussen, and W. D. Hall. Explicit Forecasts of Winter Precipitation Using an Improved Bulk Microphysics Scheme. Part II: Implementation of a New Snow Parameterization. *Monthly Weather Review*, 136(12):5095 – 5115, 2008. doi: 10.1175/2008MWR2387.1. URL <https://journals.ametsoc.org/view/journals/mwre/136/12/2008mwr2387.1.xml>.
- A. M. Tompkins and F. Di Giuseppe. An interpretation of cloud overlap statistics. *Journal of the Atmospheric Sciences*, 72(8):2877 – 2889, 2015. doi: 10.1175/JAS-D-14-0278.1. URL <https://journals.ametsoc.org/view/journals/atsc/72/8/jas-d-14-0278.1.xml>.
- Adrian M. Tompkins. A prognostic parameterization for the subgrid-scale variability of water vapor and clouds in large-scale models and its use to diagnose cloud cover. *Journal of the Atmospheric Sciences*, 59(12): 1917 – 1942, 2002. doi: 10.1175/1520-0469(2002)059<1917:APPFTS>2.0.CO;2. URL https://journals.ametsoc.org/view/journals/atsc/59/12/1520-0469_2002_059_1917_appfts_2.0.co_2.xml.
- G. J. Tripoli and W. R. Cotton. A Numerical Investigation of Several Factors Contributing to the Observed Variable Intensity of Deep Convection over South Florida. *Journal of Applied Meteorology and Climatology*, 19(9):1037 – 1063, 1980. doi: 10.1175/1520-0450(1980)019<1037:ANIOSF>2.0.CO;2. URL https://journals.ametsoc.org/view/journals/apme/19/9/1520-0450_1980_019_1037_aniosf_2_0_co_2.xml.
- UCAR. The official repository for the Weather Research and Forecasting (WRF) model, 2023. URL https://github.com/wrf-model/WRF/blob/master/phys/module_mp_thompson.F.
- J. Van den Bergh, J.-F. Geleyn, and R. Brožková. Improving the Cloud Overlap Scheme in APLMPHYS. Poster. 21st ALADIN Workshop, Norrköping, Sweden., 04 2011. URL http://www.umr-cnrm.fr/aladin/IMG/pdf/poster_vandenbergh.pdf.

- B. Vié, J.-P. Pinty, S. Berthet, and M. Leriche. LIMA (v1.0): A quasi two-moment microphysical scheme driven by a multimodal population of cloud condensation and ice freezing nuclei. *Geoscientific Model Development*, 9(2):567–586, 2016. doi: 10.5194/gmd-9-567-2016. URL <https://gmd.copernicus.org/articles/9/567/2016/>.
- C. E. Wainwright, D. T. Dawson, M. Xue, and G. Zhang. Diagnosing the Intercept Parameters of the Exponential Drop Size Distributions in a Single-Moment Microphysics Scheme and Impact on Supercell Storm Simulations. *Journal of Applied Meteorology and Climatology*, 53(8):2072 – 2090, 2014. doi: 10.1175/JAMC-D-13-0251.1. URL <https://journals.ametsoc.org/view/journals/apme/53/8/jamc-d-13-0251.1.xml>.
- D. Walters, A. J. Baran, I. Boutle, M. Brooks, P. Earnshaw, J. Edwards, K. Furtado, P. Hill, A. Lock, J. Manners, C. Morcrette, J. Mulcahy, C. Sanchez, C. Smith, R. Stratton, W. Tennant, L. Tomassini, K. Van Weverberg, S. Vosper, M. Willett, J. Browse, A. Bushell, K. Carslaw, M. Dalvi, R. Essery, N. Gedney, S. Hardiman, B. Johnson, C. Johnson, A. Jones, C. Jones, G. Mann, S. Milton, H. Rumbold, A. Sellar, M. Ujiie, M. Whittall, K. Williams, and M. Zerroukat. The Met Office Unified Model Global Atmosphere 7.0/7.1 and JULES Global Land 7.0 configurations. *Geoscientific Model Development*, 12(5):1909–1963, 2019. doi: 10.5194/gmd-12-1909-2019. URL <https://gmd.copernicus.org/articles/12/1909/2019/>.
- Weather Forecast Office Raleigh. WRF ARW Model Configuration at RAH, 2023. URL https://www.weather.gov/media/rah/arwwrf/WRF_ARW_%20Model_Configuration_%20RAH.pdf.
- J. M. Wilkinson, A. N. F. Porson, F. J. Bornemann, M. Weeks, P. R. Field, and A. P. Lock. Improved microphysical parametrization of drizzle and fog for operational forecasting using the Met Office Unified Model. *Quarterly Journal of the Royal Meteorological Society*, 139(671):488–500, 2013. doi: <https://doi.org/10.1002/qj.1975>. URL <https://rmets.onlinelibrary.wiley.com/doi/abs/10.1002/qj.1975>.
- D. R. Wilson and S. P. Ballard. A microphysically based precipitation scheme for the uk meteorological office unified model. *Quarterly Journal of the Royal Meteorological Society*, 125(557):1607–1636, 1999. doi: <https://doi.org/10.1002/qj.49712555707>. URL <https://rmets.onlinelibrary.wiley.com/doi/abs/10.1002/qj.49712555707>.
- World Meteorological Organization. International Cloud Atlas Manual on the Observation of Clouds and Other Meteors (WMO-No. 407)., 2017. URL <https://cloudatlas.wmo.int/en/home.html>.
- K.-M. Xu and D. A. Randall. A semiempirical cloudiness parameterization for use in climate models. *Journal of Atmospheric Sciences*, 53(21):3084 – 3102, 1996. doi: 10.1175/1520-0469(1996)053<3084:ASCPFU>2.0.CO;2. URL https://journals.ametsoc.org/view/journals/atsc/53/21/1520-0469_1996_053_3084_ascpfu_2_0_co_2.xml.

Yang Zhiyin. Large-eddy simulation: Past, present and the future. *Chinese Journal of Aeronautics*, 28(1):11 – 24, 2015. ISSN 1000-9361. doi: <https://doi.org/10.1016/j.cja.2014.12.007>. URL <http://www.sciencedirect.com/science/article/pii/S1000936114002064>.

I. Bašták Ďurán, J.-F. Geleyn, F. Váňa, J. Schmidli, and R. Brožková. A Turbulence Scheme with Two Prognostic Turbulence Energies. *Journal of the Atmospheric Sciences*, 75(10):3381 – 3402, 2018. doi: 10.1175/JAS-D-18-0026.1. URL <https://journals.ametsoc.org/view/journals/atsc/75/10/jas-d-18-0026.1.xml>.

List of Figures

1.1	Comparison of drop sizes approximated by the Marshall-Palmer distribution using the fixed value of $N_0 = 8 \cdot 10^6 \text{ m}^{-4}$ (MP), and with the modification proposed by Abel and Boutle [2012] (AB). Two rainwater specific contents are plotted. Note that while for $q_r = 0.1 \text{ g} \cdot \text{kg}^{-1}$ is more smaller particles estimated by AB, for $q_r = 1 \text{ g} \cdot \text{kg}^{-1}$ is more small particles estimated by MP.	12
2.1	Least square approximation of the first term in Equation (2.34) at $T = 20^\circ\text{C}$	25
2.2	Least square approximation of the second term in Equation (2.34) at $T = 20^\circ\text{C}$	25
4.1	Vertical dependence of HU_c used in microphysics in the standard atmosphere for a horizontal resolution of 2.325 km.	43
4.2	Temperature dependence of $(q_i/q_c)_{cond}$	44
4.3	Cloud and precipitation geometry. Symbols are explained in the main text.	50
5.1	Model domain in projection CRS84.	55
6.1	Vertical profiles of the specific content of hydrometeors for a winter case. The simulation without prognostic graupel is dashed.	61
6.2	The difference temperature budget for 2021-06-29. The version without prognostic graupel (NOGR) is used as a reference for a run with prognostic graupel (GRAU).	62
6.3	The difference water vapour budget for 2021-06-29. The version without prognostic graupel (NOGR) is used as a reference for a run with prognostic graupel (GRAU).	63
6.4	Vertical cross section of reflectivity through a multicellular storm of a run without prognostic graupel (left) and with prognostic graupel (right). Note the difference in the reflectivity above 4 km and also the difference in the top cloud height.	64
6.5	Dependence of the graupel fall speed on the precipitation rate for various proposals. The density of air is $\rho_a = 1 \text{ kg} \cdot \text{m}^{-3}$	65
6.6	The shape of the transition function of the ratio between snow and graupel production by snow collecting cloud water. The transition function used in ICE3 is compared to the function proposed for ALARO.	67
6.7	The cloud ice budget of the difference between a run with $E_{ff}^g = 0.1$ (EF10) and EF20 with $E_{ff}^g = 0.2$ (as a reference) for a summer convection case.	68

6.8	The difference of the upper air atmospheric scores of temperature for the period from 2021-06-21 to 2021-06-29 between OPGR and GRAU (reference). Terms 06 and 18 UTC are less reliable for the upper air observations as there is much less radiosondes released compared to terms 00 UTC and 12 UTC, which can make artefacts at 06 and 18 UTC.	71
6.9	The difference of the upper air atmospheric scores of geopotential for the period from 2021-06-21 to 2021-06-29 between OPGR and GRAU	72
6.10	The statistical significance of trends of various statistics at surface for the period from 2022-06-21 to 2022-06-29 (upper) and from 2021-11-25 to 2021-12-04 (lower). Configuration OPGR is compared to GRAU	73
6.11	12-hour precipitation accumulation ending on 2021-06-30 at 00 UTC. In descending order: NOGR , GRAU , OPGR , and MERGE (observations).	74
7.1	The area fraction of brightness temperature lower than a threshold value $T_{b,thr}$ for AKS1 and OPGR on 2022-06-24 at 21 UTC.	77
7.2	The statistical significance of trends of various statistics at the surface for the summer 2021 (upper) and winter precipitation (lower) periods for AKS1 with OPGR as the reference.	78
7.3	Temperature dependence of Equation 7.1 (ALARO) and Equation 7.2 (CP06).	79
7.4	The snow (top) and cloud ice (bottom) budget difference between CP06 and AKS1 for a summer convection case.	81
7.5	Multiple tested coefficients for the autoconversion parameterization following Khairoutdinov and Kogan [2000]. The number in the name of the experiment denotes the value of the multiplication coefficient. Black line roughly denotes the empirically discovered (from various simulations) required autoconversion rate at which stratocumuli typically start to precipitate with the operational collection parameterization in the current ALARO configuration. Thus, the black dashed line roughly denotes the specific water content of thick stratocumuli.	82
7.6	Comparison of the 24-hour precipitation accumulation ending on 2021-11-19 at 00 UTC of OPGR (upper) and KK00 (lower).	84
7.7	Comparison of the precipitation bias of OPGR (blue) and KK00 (orange) for the period from 2021-11-26 to 2021-12-01.	85
7.8	The temperature budget difference between KK00 and OPGR for an autumn case.	86
7.9	Bias, STDE and RMSE of temperature for the period from 2021-06-21 to 2021-06-26. Configuration OPGR in blue and KK00 in orange.	87
7.10	Vertical cross section of the specific content of cloud water through a stratocumulus cloud, which produced very little precipitation in the case of OPGR (upper) and no precipitation in case of KK00 (lower).	88

7.11	The shape of the Lopez evaporation function for rain with the Abel-Boutle size distribution (AB) and with the Marshall-Palmer distribution (MP).	90
7.12	The water vapour budget difference between TLOP and AKS1 for a summer convection case.	91
7.13	The temperature budget difference between TLOP and AKS1 for a summer convection case.	92
7.14	Vertical profiles of the specific content of hydrometeors for the convection case 2022-06-24 at 18 UTC. Solid lines are used for TLOP and dashed lines for AKS1.	93
7.15	Evolution of the leading edge of the MSC on 2021-06-29. Configuration OPGR is denoted by red lines, ELOP by blue lines. Note that ELOP moves a little bit faster.	94
7.16	24 hour precipitation accumulation for the case of snowfall over Austria.	95
7.17	Temperature budget difference between CLOV and AKS1 for a summer convection case.	96
7.18	Precipitation bias, RMSE and STDE of CLOV and AKS1 for the summer period from 2021-06-21 to 2021-06-30.	97
8.1	The diurnal cycle of precipitation in the summer period of 2009 from June 24 th to July 4 th . Model configurations MPKA (orange) and OPGR (blue) are compared to MERGE (green).	99
8.2	The upper air scores of temperature for the period from 2009-06-24 to 2009-07-04. Experiment MPKA is compared with OPGR, which is used as reference.	100
8.3	The upper air scores of geopotential for the period from 2009-06-24 to 2009-07-04. Experiment MPKA is compared with OPGR, which is used as reference.	101
8.4	Surface scores for the period from 2009-06-24 to 2009-07-04. Experiment MPKA is compared with OPGR, which is used as reference.	102
8.5	Bias, RMSE and STDE of precipitation in the summer period of 2009 between 2009-06-24 and 2009-07-04.	103
8.6	The difference of components of the surface energy budget between MPKA and OPGR (used as reference) on 2009-07-02. The flux towards the surface is positive. Data are averaged over the domain.	104
8.7	The evolution of the ratio of the amount of groundwater in MPKA to the amount of groundwater in OPGR during the assimilation cycle. Values are spatially averaged over the domain. Values over sea are filtered out.	105
8.8	The upper air scores of geopotential for the period from 2022-06-20 to 2009-07-10. Experiment MPKA is compared with OPGR, which is used as reference.	106
8.9	The diurnal cycle of precipitation in the summer period of 2022 from June 21 st to June 29 th . Model configurations MPKA (orange) and OPGR (blue) are compared to MERGE (green).	107
8.10	The mean FSS of precipitation accumulation for the forecast range 12-18 UTC.	108

8.11	The mean FSS of precipitation accumulation for the forecast range 18-24 UTC.	109
8.12	The mean FSS of precipitation accumulation for the forecast range 24-30 UTC.	110
8.13	The mean FSS of precipitation accumulation for the forecast range 30-36 UTC.	111
8.14	12-hour precipitation accumulation ending on 2022-06-23 at 00 UTC. In descending order: OPGR, MPKN, MPKA, and observations (MERGE).	113
8.15	12-hour precipitation accumulation on 2022-06-25 at 00 UTC predicted by model runs initialized on 2022-06-23 at 00 UTC (left) and model runs initialized on 2022-06-24 at 00 UTC (right). Left column is OPGR, right MPKA. Observations are shown in the lowermost row.	114
8.16	24-hour precipitation accumulation on 2022-06-28 at 06 UTC. There are shown OPGR (top), MPKA (middle), and MERGE (bottom). . .	115
8.17	12-hour precipitation accumulation on 2022-06-29 at 00 UTC. Model runs initialized on 2022-06-27 are on the left, model runs initialized on 2022-06-28 are on the right. The upper row is OPGR and the lower row is MPKA. In the bottom are observations by MERGE. .	116
8.18	12-hour precipitation accumulation on 2022-06-30 at 00 UTC. Model runs initialized on 2022-06-28 are on the left, model runs initialized on 2022-06-29 are on the right. The upper row is OPGR and the lower row is MPKA. In the bottom are observations by MERGE. .	117
8.19	12-hour precipitation accumulation on 2022-07-01 at 00 UTC. There are shown in descending order OPGR, MPKN, MPKA, and observations (MERGE).	118
8.20	24-hour precipitation accumulation on 2022-07-01, OPGR (top), MPKA (middle), and MERGE (bottom).	120
8.21	24-hour precipitation accumulation on 2022-07-05, OPGR (top), MPKA (middle), and MERGE (bottom).	121
8.22	24-hour precipitation accumulation on 2022-07-07, OPGR (top), MPKA (middle), and MERGE (bottom).	122
8.23	The upper air scores of geopotential for the winter precipitation period. Experiment MPKN is compared with OPGR, which is used as reference.	124
8.24	Surface scores for the winter precipitation period. Experiment MPKN is compared with OPGR, which is used as reference.	125
8.25	Surface scores of wind speed for the winter precipitation period from 2021-11-26 to 2021-12-01. Note the continuous positive bias of MPKN (orange) compared to OPGR (blue).	126
8.26	24-hour precipitation accumulation on 2021-11-26. The difference between MPKN (middle) and OPGR (top) is small. Both fields are similar to observations (bottom).	127
8.27	The upper air scores of temperature for the autumn stratocumulus period. Experiment MPKN is compared with OPGR, which is used as reference.	128

8.28	Difference of scores for the autumn stratocumulus period between MPKN and OPGR (reference). Lower is validation against Czech SYNOP stations.	129
8.29	24-hour precipitation accumulation on 2021-11-11, OPGR is upper and MPKN lower. MERGE is not shown as no precipitation was observed.	130
8.30	12-hour precipitation accumulation on 2022-12-12 at 00 UTC, OPGR (top), MPKN (middle), and MERGE (bottom). In this case, the observed precipitation can be underestimated because snow has lower reflectivity and clouds can be low, so the radar beam is above them.	132
8.31	The precipitation accumulation in the form of snow (upper) and in the form of graupel (lower). MPKN is on the left and OPGR on the right.	133

List of Tables

2.1	Description of various microphysical processes. References are abbreviated for readability: AMS for American Meteorological Society [2023], PK97 for Pruppacher and Klett [1997], KC14 for Khvorostyanov and Curry [2014] and eMS for Česká meteorologická společnost [2023]	15
2.2	Coefficients of the approximation of the first term in Equation (2.34).	24
2.3	Coefficients of the approximation of the second term in Equation (2.34). Values of $\rho_{v,sat}$ are taken from Nave [2023]	24
3.1	Coefficients for Equation (3.1) used in the ICE3 scheme (Pinty and Jabouille [1998]).	29
4.1	ALARO parameterizations, according to Termonia et al. [2018].	42
5.1	List of abbreviations used for contributors in graphs in the DDH diagnostics.	57
6.1	The proposed set of parameters for graupel.	69
7.1	Experiments with Sundqvist autoconversion.	89
7.2	List of parameters used in the evaporation parameterization following Lopez [2002]. Superscripts r , s and g stand for the corresponding parameters of rain, snow (unchanged), and graupel, respectively. MP stands for the Marshall-Palmer size distribution and AB for the modification of the intercept parameter by Abel and Boutle [2012]. New graupel is graupel with the new set of parameters introduced in Chapter 6 and old graupel is graupel parameterized in the original way; that is, mechanical properties of rain and thermodynamic of snow.	90

List of symbols

$\Delta_{process}^{j_1+j_2 \rightarrow j_3+j_4}$, where j_1 and j_2 are sinks and j_3 and j_4 are sources.

Processes can be:

fre	freezing
eva	evaporation
melt	melting
melt,enhcd	enhanced melting by liquid water collection
aco	autoconversion
col	collection
cond	condensation
dep	deposition
het	heterogeneous freezing
hom	homogeneous freezing
shed	shedding
HM	Hallet-Mossop process of secondary ice production
convmel	conversion melting
wet	wet growth of graupel
dry	dry growth of graupel

Sources and sinks can be these water species:

v	water vapour
l	cloud water
i	cloud ice
r	rain
s	snow
g	graupel
a	aqueous aerosols.

List of remaining symbols:

a	radius
a_{lt}	threshold radius of cloud droplets
a_i	radius of the ice core of a melting spherical particle
a_l	radius of droplets (collected)
a_r	radius of drops (collectors)
a_{crit}	critical diameter
a_1	first coefficient for mass-size relation
a_2	second coefficient for mass-size relation
$a(3, T)$	first temperature dependent function for the intercept parametr of snow
b_1	first coefficient for fall speed relation
b_2	second coefficient for fall speed relation

b_3	third coefficient for fall speed relation
b_4	fourth coefficient for fall speed relation
$b(3, T)$	second temperature dependent function for the intercept parameter of snow
c	coefficient for the mass-size relationship
c_w	specific heat capacity of water
C	cloud fraction (nebulosity, cloudiness)
C^*	cloud fraction at the top of a model layer
C_w	heat capacity of water
C_{cv}	moist deep convection cloud fraction
C_{res}	resolved cloud fraction
\mathcal{C}	crystal capacitance
D	diameter of a particle
$\overline{D_j^V}$	mean volume diameter of hydrometeor species j
$\overline{D_{j,0}^V}$	reference mean volume diameter of hydrometeor species j
D_v	diffusivity of air
\mathcal{D}	
e_w	water vapour pressure
$e_{w,sat}$	saturation water vapour pressure with respect to water
$e_{w,sat,a}$	saturation water vapour pressure with respect to water at the droplet's surface
$e_{w,sat,\infty}$	saturation water vapour pressure with respect to water in the infinite distance limit
E	collection efficiency
E_{coal}	coalescence efficiency
E_{colli}	collision efficiency
E_g	collection efficiency of graupel
E_s	collection efficiency of snow
E_r	collection efficiency of rain
E_{gi}	collection efficiency of graupel collecting cloud ice
E_{gl}	collection efficiency of graupel collecting cloud water
E_{gs}	collection efficiency of graupel collecting snow
E_{s+g}	collection efficiency of snow with diagnostic graupel
E_{si}	collection efficiency of snow collecting cloud ice
E_g^{max}	maximal collection efficiency of graupel
E_l	collection efficiency of water droplets
E_s^{max}	maximal collection efficiency of snow
E_2	second exponential integral
E_3	third exponential integral
E_{vap}	coefficient for evaporation
f_{agg}	variable for the diagnostic split of the ice category into aggregates and cloud ice
$\overline{f_c}$	the average ventilation factor of mass
$\overline{f_h}$	the average ventilation factor of heat
F	dimensionless factor for Kessler evaporation
F_{WBF}^a	first coefficient for the WBF process
F_{WBF}^b	second coefficient for the WBF process
F_{ont}	coefficient for melting

F_{SO}	precipitation flux in the seeded cloudy part
F_{RO}	precipitation flux in the non-seeded cloud part
F_{SE}	precipitation flux in the seeded clear sky part
F_{RE}	precipitation flux in the non-seeded clear sky part
F_{SO}	precipitation flux in the seeded cloudy part at the top of a model layer
F_{RO}	precipitation flux in the non-seeded cloud part at the top of a model layer
F_{SE}	precipitation flux in the seeded clear sky part at the top of a model layer
F_{RE}	precipitation flux in the non-seeded clear sky part at the top of a model layer
g	gravity of Earth
H_w	Howell factor for liquid water
HU_c	critical relative humidity
$\mathcal{H}(\cdot)$	Heaviside step function
\vec{j}_v	flux density of water vapour
k_a	thermal conductivity of air
k_{huc}	coefficient in the computation of the critical relative humidity
k_g	coefficient for autoconversion to graupel
k_r	coefficient for autoconversion to rain
\tilde{k}_r	modified coefficient for autoconversion to rain
k_w	thermal conductivity of water
\mathcal{K}	
K	collection kernel
l_v	specific latent heat of evaporation
l_f	specific latent heat of fusion
L_v	latent heat of evaporation
L_f	latent heat of fusion
m	mass
m_d	mass of dry air
m_v	mass of water vapour
m_l	mass of cloud water
\bar{m}_l	mean mass of water droplets
m^*	threshold mass beyond which a significant number of droplets does not occur
$M(p)$	p-th moment of a distribution
M_w	molar mass of water
N	number concentration of particles
N_j	number concentration of hydrometeor species j
N_T	total number of particles
N_0	the intercept parameter of the generalized gamma distribution
N_0^r	the intercept parameter of the generalized gamma distribution for rain
N_0^s	the intercept parameter of the generalized gamma distribution for snow
N_0^g	the intercept parameter of the generalized gamma distribution for graupel

N_1	upper intercept limit
N_2	lower intercept limit
N_l	number concentration of cloud droplets
p	pressure
p_0	reference atmospheric pressure
p^*	pressure at the top of the model layer
P_0	first probability function for sedimentation
P_1	second probability function for sedimentation
P_2	third probability function for sedimentation
P'_2	temporary third probability function for sedimentation
P_3	fourth probability function for sedimentation
q_c	sum of specific contents of cloud ice and cloud water
q_v	specific content of water vapour
q_v^{sat}	specific content of saturated water vapour
q_l	specific content of cloud water
q_i	specific content of cloud ice
q_r	specific content of rain
q_s	specific content of snow
q_g	specific content of graupel
q_w	equilibrium water content in the case of exact saturation
q_l^{crit}	threshold specific content of cloud water for autoconversion
q_i^{crit}	threshold specific content of cloud ice for autoconversion
q_s^{crit}	threshold specific content of snow for autoconversion
r_v	mixing ratio of water vapour
r_l	mixing ratio of cloud water
r_i	mixing ratio of cloud ice
r_r	mixing ratio of rain
r_{r0}	transition mixing ratio of rain of the intercept parameter of rain in the Thompson scheme
r_s	mixing ratio of snow
r_g	mixing ratio of graupel
$\widetilde{r_g}$	ratio of the precipitation flux of diagnostic graupel to the total snow precipitation flux
$\widetilde{r_g}'$	modified ratio of the precipitation flux of diagnostic graupel to the total snow precipitation flux
r_l^{crit}	threshold mixing ratio of cloud water for autoconversion
r_i^{crit}	threshold mixing ratio of cloud ice for autoconversion
r_s^{crit}	threshold mixing ratio of snow for autoconversion
r_r^{thres}	threshold mixing ratio of rain for WSM6
r_s^{thres}	threshold mixing ratio of rain for WSM6
R^*	universal gas constant
R_v	specific gas constant of water vapour
Re	Reynolds number
\mathcal{R}	precipitation flux
\mathcal{R}	precipitation flux
\mathcal{R}_{top}	precipitation flux at the top of the layer
\mathcal{R}_{bot}	precipitation flux at the bottom of the layer
s	supersaturation (with respect to water)

s_a	equilibrium supersaturation over the drop (with respect to water)
S	surface area
Sc	Schmidt number
t	time
T	temperature
T_a	temperature at the droplet's surface
T_f	temperature of fusion
T_t	temperature of the triple point of water
T_x	temperature of the maximum difference between the saturation vapor pressures with respect to ice and to liquid
T_w	wet-bulb temperature
T_∞	temperature in the infinite distance limit
\vec{u}	relative velocity of the drop to the surrounding flow
V	volume
w	terminal fall velocity
w_r	terminal fall velocity of rain
w_s	terminal fall velocity of snow
w_g	terminal fall velocity of graupel
w_l	terminal fall velocity of cloud water
w_L	water liquid content
x_1	first coefficient of the Abel-Boutle size distribution
x_2	second coefficient of the Abel-Boutle size distribution
Z	inverse Courant number
z	vertical coordinate
\mathcal{Z}	test variable to decide the regime of the cloud overlap scheme
α	seeded part of the clear-sky part
α^*	seeded part of the clear-sky part at the top of a model layer
β	seeded part of the cloudy part
β^*	seeded part of the cloudy part at the top of a model layer
$\Gamma(\cdot)$	gamma function
δ	parameter for cloud scheme in ALARO
δz	model layer thickness
ΔT	positive temperature difference from the cloud top
ϵ	decorrelation depth for cloud geometry
ι	first parameter of the generalized gamma distribution
λ	slope parameter of the generalized gamma distribution
μ	dynamic viscosity
ν	second parameter of the generalized gamma distribution
ρ_0	reference density
$\rho_{v,a}$	water vapour density at the drop's surface
$\rho_{v,sat}$	saturation water vapour density
$\rho_{v,\infty}$	water vapour density in the infinite distance limit
ρ_w	density of water
ρ_g	density of graupel
ρ_i	density of ice
ρ_a	density of air
ρ_l	density of cloud water in air volume
ρ_{lt}	threshold density of cloud water in air volume

ρ_v	density of water vapour
σ	exponent used in the Sunqvist autoconversion
τ_c	time constant for melting
v	equivalent thickness of the transition shell outside the drop
ϕ_v	fractional relative humidity of air
χ	absolute humidity deficit
χ	diffusivity of water vapour in the air
ψ	decorrelation parameter for cloud geometry
ζ_r	first coefficient in ventilation factor for raindrops
ζ_s	first coefficient in ventilation factor for ice
ξ_r	second coefficient in ventilation factor for raindrops
ξ_s	second coefficient in ventilation factor for ice

List of abbreviations

3MT	Microscale Modular Microphysics and Transport
ACRANEb2	Actif Calcul de RAYonnement et NÉBulosité 2
ALADIN	Aire Limitée Adaptation Dynamique Développement International
ALARO	ALadin-AROMe
AROME	Application of Research to Operations at Mesoscale
CASIM	Cloud AeroSol Interacting Microphysics
CFL	Courant-Friedrichs-Lewy (condition)
CHMI	Czech Hydrometeorological Institute
CRS84	Coordinate reference system 84
DDH	Diagnostics in horizontal domain
FSS	Fractional skill score
GM	global model
HRRR	High Resolution Rapid Refresh
ICE3	3 ice scheme in AROME
ICON	Icosahedral Nonhydrostatic (model)
IFS	Integrated Forecast System
IN	ice nuclei
IN	ice nuclei
ISBA	Interaction Sol-Biosphère-Atmosphère
JMA-LSM	Japan Meteorological Agency - Land Surface Model
LAM	limited area model
LCC	Lambert conformal conical
LES	large-eddy simulation
LIMA	Liquid Ice Multiple Aerosols
MCS	mesoscale convective system
MERGE	combination of precipitation estimates from radar and gauges used at CHMI
NCEP	National
NWP	numerical weather prediction
PDF	probability density function
PPI	Plan Position Indicator
RAP	Rapid refresh
RH2m	2-metre relative humidity
RHI	Range Height Indicator
RMSE	root mean square error
STDE	standard deviation
T2m	2-metre temperature
TOUCANS	Third Order moments Unified Condensation Accounting and N-dependent Solver for turbulence and diffusion
UM	Unified Model
UTC	Coordinated Universal Time
w10m	wind at 10 meters above the ground
WBF	Wegener-Bergeron-Findeisen (process)
wdir10m	wind direction at 10 meters above the ground

WDM	WRD double moment
WRF-ARW	Weather Research and Forecast
WRF	Weather Research and Forecast
WSM	WRF single moment

A. Appendix

A.1 Mass-weighted relation for fall speed

The derivation of the mean fall speed in the mass-weighted framework starts from

$$\bar{w} = \frac{\int_0^\infty w(D) N_0 e^{-\lambda D} \frac{\pi D^3}{6} \rho_h dD}{\int_0^\infty N_0 e^{-\lambda D} \frac{\pi D^3}{6} \rho_h dD} = a \frac{\Gamma(\alpha + 4)}{\Gamma(4) \lambda^\alpha} \quad (\text{A.1})$$

where $w(D)$ is computed as

$$w(D) = a D^\alpha \left(\frac{\rho_0}{\rho_a} \right)^b, \quad (\text{A.2})$$

where a , α , and b are tunable parameters, ρ_h the density of the hydrometeor, ρ_a is the density of air, and ρ_0 is the density of air at the atmospheric pressure in the standard atmosphere.

Substituting Equation A.2 into A.1 yields

$$\bar{w} = \frac{\int_0^\infty a D^\alpha N_0 e^{-\lambda D} \frac{\pi D^3}{6} \rho_h dD}{\int_0^\infty N_0 e^{-\lambda D} \frac{\pi D^3}{6} \rho_a dD} = a \frac{\Gamma(\alpha + 4)}{\Gamma(4) \lambda^\alpha}. \quad (\text{A.3})$$

For the precipitation flux we have

$$\begin{aligned} \mathcal{R} &= \int_0^\infty w(D) N(D) m(D) dD = \int_0^\infty a D^\alpha N_0 e^{-\lambda D} \frac{\pi D^3}{6} \rho_w dD \\ &= \frac{\Gamma(\alpha + 4) a N_0 \rho_w \pi}{6 \lambda^{\alpha+4}} \rightarrow \frac{1}{\lambda^\alpha} = \left[\frac{6R}{\rho_h \Gamma(\alpha + 4) a N_0 \pi} \right]^{\frac{\alpha}{4+\alpha}}, \end{aligned} \quad (\text{A.4})$$

which allows us to substitute for λ into Equation A.3

$$\begin{aligned} \bar{w} &= \frac{1}{\Gamma(4)} [a \Gamma(\alpha + 4)]^{\frac{4}{4+\alpha}} \left[\frac{6R}{\pi \rho_h N_0} \right]^{\frac{\alpha}{4+\alpha}} \\ &= \frac{1}{\Gamma(4)} \left[a_0 \left(\frac{\rho_0}{\rho_a} \right)^b \Gamma(\alpha + 4) \right]^{\frac{4}{4+\alpha}} \left[\frac{6R}{\pi \rho_h N_0} \right]^{\frac{\alpha}{4+\alpha}} \\ &= \frac{1}{\Gamma(4)} [a_0 \Gamma(\alpha + 4)]^{\frac{4}{4+\alpha}} \left[\frac{6R}{\pi \rho_h N_0} \right]^{\frac{\alpha}{4+\alpha}} \left(\frac{\rho_0}{\rho_a} \right)^{\frac{4b}{4+\alpha}}. \end{aligned} \quad (\text{A.5})$$

A.2 Collection

The derivation of the equation for collection is highly based on Geleyn et al. [2007], although the general formula is derived originally. In ALARO, as well as in many other models, the parameterization of collection follows the continuous growth model. Thus, collection starts from the equation of the mass relation. The only variable parameter is the collection efficiency (here denoted by E). It is a hardly known quantity; thus, its value significantly differs across microphysics schemes.

Generally, the collection follows the following relation:

$$\frac{dM}{dt} = \Delta A w \rho_a q_j, \quad (\text{A.6})$$

where q_j is the mass fraction of given hydrometeor (r,s,g), w the fall speed of this hydrometeor and A the surface of the hydrometeor.

In ALARO, we have for collection of q_l by q_r

$$\begin{aligned} \frac{dm(D)}{dt} &= \frac{\pi D^2}{4} a D^\alpha \rho_a q_l \\ -\frac{dR}{dz} &= \int_0^\infty N_0 e^{-\lambda D} \frac{\pi D^2}{4} a D^\alpha \rho_w q_l dD \quad [\text{kg} \cdot \text{m}^{-3} \cdot \text{s}^{-2}] \\ \frac{dR}{dp} &= \frac{\pi a N_0 \Gamma(\alpha + 3)}{4g \lambda^{\alpha+3}} q_l \quad [\text{s} \cdot \text{m}^{-1}] \\ \frac{dR}{dp} &= \left(1 - \frac{\alpha + 3}{\alpha + 4}\right) \frac{\Gamma(\alpha + 3) \pi a N_0}{4g} \left(\frac{6R}{\rho_r \Gamma(\alpha + 4) a N_0 \pi}\right)^{\frac{\alpha+3}{\alpha+4}} q_l \\ &= C^{\frac{1}{4+\alpha}} E R^{\frac{\alpha+3}{\alpha+4}} q_l. \end{aligned} \quad (\text{A.7})$$

The general formula for the time derivative of the specific content of cloud water is:

$$\begin{aligned} \frac{dq}{dt} &= -\frac{\Gamma(\alpha + 3) E \pi a_0 \rho_0^{\frac{b}{\alpha+4}} N_0}{4} \left(\frac{6}{\rho_r \Gamma(\alpha + 4) a_0 N_0 \pi}\right)^{\frac{\alpha+3}{\alpha+4}} R^{\frac{\alpha+3}{\alpha+4}} \rho_a^{\frac{-b}{\alpha+4}} q_l \\ &= -\frac{\Gamma(\alpha + 3) E \left(\pi a_0 N_0 \rho_0^b\right)^{\frac{1}{\alpha+4}}}{4} \left(\frac{6}{\rho_r \Gamma(\alpha + 4)}\right)^{\frac{\alpha+3}{\alpha+4}} R^{\frac{\alpha+3}{\alpha+4}} \rho_a^{\frac{-b}{\alpha+4}} q_l \\ &= -C_E^r E R^{\frac{\alpha+3}{\alpha+4}} \rho_a^{\frac{-b}{\alpha+4}} q_l \end{aligned} \quad (\text{A.8})$$

The density dependency is often neglected as the typical value of the power is small (around 0.2).

A.3 Evaporation in ALARO

The derivation of evaporation in ALARO tightly follows its derivation in Geleyn et al. [2007]. ALARO uses a fit of data from the Smithsonian meteorological tables. The fit is performed on both parts in square brackets:

$$\frac{dM}{dt} = \left[2\pi D \left(1 + \frac{Fa}{s} \right) \right] \left[d_v \left(\rho_v^{sat} - \rho_v \right) \right], \quad (\text{A.9})$$

where s is the equivalent thickness of the drop.

ALARO uses the following expressions for the fall speed relation and the evaporation (only rewritten Equation (A.9)): The loss of mass due to evaporation can be written as

$$\frac{dm(D)}{dt} = b(T, p) D^\beta \rho_a (q - q_w), \quad (\text{A.10})$$

where the specific humidity q_w at the wet-bulb point is considered rather than q_v^{sat} as it allows to hide the thermodynamical effects in the Physics-Dynamics interface (Catry [2006]).

The conservation of mass yields (due to that all change of the precipitation flux is done through the change of the mass of precipitating particles)

$$\frac{d\mathcal{R}}{dz} = \int_0^\infty b D^\beta \rho_a (q_w - q) N_0 e^{-\lambda D} dD = \rho_a (q_w - q) \frac{b N_0 \Gamma(\beta + 1)}{\lambda^{\beta+1}}, \quad (\text{A.11})$$

A transition to the pressure coordinate gives

$$\frac{dR}{dp} = (q_w - q) \frac{b N_0 \Gamma(\beta + 1)}{g \lambda^{\beta+1}} = (q_w - q) \frac{b N_0 \Gamma(\beta + 1)}{g} \left(\frac{6R}{\Gamma(\alpha + 4) a N_0 \rho_w \pi} \right)^{\frac{\beta+1}{\alpha+4}} \quad (\text{A.12})$$

or

$$\frac{d}{dp} R^{1-\frac{\beta+1}{\alpha+4}} = \left(1 - \frac{\beta+1}{\alpha+4} \right) (q_w - q) \frac{b N_0 \Gamma(\beta + 1)}{g} \left(\frac{6}{\Gamma(\alpha + 4) a N_0 \rho_w \pi} \right)^{\frac{\beta+1}{\alpha+4}} \quad (\text{A.13})$$

According to the fit of the data in List [1951] is $\alpha = 0.7706$ and $\beta = 1.614$, giving $R^{0.4521}$, which is for the sake of lower computational cost approximated to \sqrt{R} and refitted values of a (used in the derivation of the fall speed relation) and b are (Geleyn et al. [2007]):

$$\begin{aligned} a(p, T) &= 654.5 \left(\frac{p_0}{p} \right)^{0.7706} \left(\frac{T}{T_*} \right)^{0.7706} = 654.5 R \left(\frac{\rho_0}{\rho_a} \right)^{0.7706} \\ b(p, T) &= 0.005655 \left(\frac{p_0}{p} \right) \left(\frac{T}{T_*} \right)^{7.095}, \end{aligned} \quad (\text{A.14})$$

which using equation (A.13) gives

$$\frac{d\sqrt{R}}{dp} = (q_w - q) \frac{b N_0 \Gamma(\beta + 1)}{2g} \sqrt{\frac{6}{\Gamma(\alpha + 4) a N_0 \rho_w \pi}} = A (q_w - q), \quad (\text{A.15})$$

which leads to

$$A = 4.146 \cdot 10^{-4} \left(\frac{p_0}{p} \right)^{0.6147} \left(\frac{T}{T_*} \right)^{7.4803}. \quad (\text{A.16})$$

After eliminating the temperature dependency using the standard atmosphere:

$$p_0 = 101325 \text{ Pa}, T_* = 288.16, \frac{dT}{dz} = -0.0065 \text{ K/m},$$

it leads to

$$\frac{d\sqrt{R}}{d(1/p)} = E_{vap}(q_w - q), E_{vap} = 4.8 \cdot 10^6. \quad (\text{A.17})$$

For snow, the same relation is used, but it is multiplied by the ratio of the specific latent heat of evaporation of liquid water to the specific latent heat of sublimation of ice water.

A.4 Melting

The derivation of the formula for melting follows Geleyn et al. [2007]. Melting is treated similarly to evaporation. Again, the loss of mass due to melting is

$$\left(\frac{dM}{dt}\right)_f = b'(T, p) D^\beta \rho_a (T_t - T), \quad b' = bB, \quad B = \frac{\gamma C_{pd}}{\Delta L_f} = 2.5 \cdot 10^{-3}. \quad (\text{A.18})$$

with Δ the molecular diffusion of water vapour, γ the molecular diffusion of heat, C_{pd} the heat capacity of dry air at the standard atmospheric pressure, L_f the latent heat of fusion, and T_t the temperature of the triple point.

For $i=1,2$ we have $R_i = m_i R$ and $M_i = m_i M$, thus

$$\frac{dR_i}{dz} = m_i \frac{dR}{dz} + R \frac{dm_i}{dz} = \underbrace{-\frac{dM_i}{dt}}_{\text{decrement in time}} = \underbrace{-m_i \frac{dM}{dt}}_{m_i = \text{const.}} - \underbrace{\left(\frac{dM_i}{dt}\right)_f}_{\substack{m_i \neq \text{const.} \\ \Rightarrow \\ \text{change due to fusion}}} = m_i \frac{dR}{dz} - \left(\frac{dM_i}{dt}\right)_f \quad (\text{A.19})$$

So we have

$$R \frac{dm_i}{dz} = b'(T, p) D^\beta \rho_a (T_t - T) \quad (\text{A.20})$$

and

$$\begin{aligned} \frac{dm_i}{dp} &= \frac{6b'}{\rho_a g a \pi} (T_t - T) \frac{\int_0^\infty N_0 e^{-\lambda D} D^\beta dD}{\int_0^\infty N_0 e^{-\lambda D} D^{3+\alpha} dD} \\ &= b'(T, p) D^\beta \rho_a (T_t - T) \frac{\Gamma(\beta + 1)}{\Gamma(\alpha + 4)} \left(\frac{6R}{\rho_w \Gamma(\alpha + 4) a N_0 \pi} \right)^{\frac{\beta+1}{\alpha+4}-1} \\ &= \frac{AB}{1 - \frac{\beta+1}{\alpha+4}} R^{\frac{\beta+1}{\alpha+4}-1} (T_t - T). \end{aligned} \quad (\text{A.21})$$

Using values from the evaporation part, we get

$$\frac{dm_i}{dp} = \frac{2AB}{\sqrt{R}} (T_t - T) \quad (\text{A.22})$$

and because $A \sim p^{-2}$

$$\frac{dm_i}{d(1/p)} = \frac{F_{ont}}{\sqrt{R}} (T_t - T) \quad (\text{A.23})$$

with $F_{ont} = 2.4 \cdot 10^4$.

A.5 Derivation of the Lopez evaporation parameterization for rain

We assume rain to follow the Abel-Boutle size distribution in the form

$$N(D) = x_1 \lambda^{x_2} e^{-\lambda D}, \quad (\text{A.24})$$

where $x_1 = 0.22$ and $x_2 = 2.2$. This is a negative exponential distribution with prognostically computed intercept parameter $x_1 \lambda^{x_2}$, which is often kept constant and denoted by N_0^r (Marshall-Palmer size distribution).

The change of mass of a raindrop due to evaporation can be expressed as:

$$\begin{aligned} \frac{dm}{dt} &= \frac{2\pi D(1 - RH)(1 - C)f_c}{\mathcal{K}_r + \mathcal{D}_r} \\ &= \frac{2\pi D(1 - RH)(1 - C)}{\mathcal{K}_r + \mathcal{D}_r} \left[\zeta_r + \xi_r \left(\rho_a \mu^{\frac{1}{2}} \chi \right)^{-\frac{1}{3}} \left(\rho_a D b_1 \left(\frac{\rho_0}{\rho_a} \right)^{0.7706} D^{b_2} \right)^{\frac{1}{2}} \right] \\ &= \frac{2\pi D(1 - RH)(1 - C)}{\mathcal{K}_r + \mathcal{D}_r} \left[\zeta_r + \xi_r \left(\mu^{\frac{1}{2}} \chi \right)^{-\frac{1}{3}} \rho_a^{-\frac{1}{3} + \frac{1}{2} - \frac{0.7706}{2}} \rho_0^{0.385} b_1^{\frac{1}{2}} D^{\frac{1+b_2}{2}} \right] \\ &= \frac{2\pi(1 - RH)(1 - C)}{\mathcal{K}_r + \mathcal{D}_r} \left[\zeta_r D + \xi_r \left(\mu^{\frac{1}{2}} \chi \right)^{-\frac{1}{3}} \rho_a^{-0.21} \rho_0^{0.385} b_1^{\frac{1}{2}} D^{\frac{3+b_2}{2}} \right], \end{aligned} \quad (\text{A.25})$$

where

$$\begin{aligned} \mathcal{K}_r &= \frac{l_v}{k_a T} \left(\frac{l_v}{R_v T} \right) \\ \mathcal{D}_r &= \frac{R_v T}{\chi e_{w,sat}}. \end{aligned} \quad (\text{A.26})$$

and the other quantities are (all values are in SI units):

D	particle diameter
RH	relative humidity
C	cloud cover
f_c	ventilation factor
$\zeta_r = 0.78$	first coefficient in ventilation factor for raindrops
$\xi_r = 0.31$	second coefficient in ventilation factor for raindrops
ρ_a	density of air
$\mu = 1.69 \cdot 10^{-5}$	dynamic viscosity of air
$\chi = 2 \cdot 10^{-5} \frac{p}{p_0}$	diffusivity of water vapour in the air
p	atmospheric pressure
$p_0 = 10^5$	reference atmospheric pressure
$b_1 = 654.5$	first coefficient in fall speed relation
$b_2 = 0.7706$	second coefficient in fall speed relation
$\rho_0 = 1.2 \text{ kg} \cdot \text{m}^{-3}$	reference density of air.
l_v	latent heat of evaporation
$e_{w,sat}$	saturation vapour pressure of water
$k_a = 2.31 \cdot 10^{-2}$	thermal conductivity of air
T	temperature
$R_v = 461.5$	specific gas constant for water vapour.

The evaporation rate can be written as

$$\frac{dq_r}{dt} = \frac{1}{\rho_a} \int_0^\infty \frac{dm(D)}{dt} N(D) dD, \quad (\text{A.27})$$

where $N(D)$ is the number concentration of raindrops following the Abel-Boutle size distribution. Substituting Equation (A.24) and Equation (A.25) into Equation (A.27) yields

$$\begin{aligned} \frac{dq_r}{dt} &= \frac{1}{\rho_a} \int_0^\infty x_1 \lambda^{x_2} \frac{dm(D)}{dt} e^{-\lambda D} dD \\ &= \frac{x_1 \lambda^{x_2}}{\rho_a} \int_0^\infty \frac{2\pi(1-RH)(1-C)}{\mathcal{K} + \mathcal{D}} \\ &\quad \left[\underbrace{\zeta_r D e^{-\lambda D}}_{\text{first term}} + \underbrace{\xi_r \left(\mu^{\frac{1}{2}} \chi\right)^{-\frac{1}{3}} \rho_a^{-0.21} \rho_0^{0.385} b_1^{\frac{1}{2}} D^{\frac{3+b_2}{2}} e^{-\lambda D}}_{\text{second term}} \right] dD \end{aligned} \quad (\text{A.28})$$

For the first term we have:

$$\frac{1}{\rho_a} x_1 \lambda^{2.2} \zeta_r \int_0^\infty D e^{-\lambda D} dD = \frac{1}{\rho_a} x_1 \lambda^{2.2} \zeta_r \frac{1}{\lambda^2} = \frac{1}{\rho_a} x_1 \zeta_r \lambda^{2.2-2} = \frac{1}{\rho_a} x_1 \zeta_r \left(\frac{\rho_a q_r}{x_1 \pi \rho_w} \right)^{\frac{2-2.2}{4-2.2}}, \quad (\text{A.29})$$

since

$$\lambda_{\text{AB12}} = \left[\frac{\pi \rho_w x_1 \Gamma(4 + \nu)}{6 \rho_a q_r} \right]^{\frac{1}{4-x_2}}, \quad (\text{A.30})$$

where ρ_w is the density of water and ν is the shape parameter of the gamma distribution. Since the exponential distribution is assumed, $\nu = 0$. This leads to values of

$$\begin{aligned} C_1 &= 2\pi x_1 \zeta_r \left[\frac{\pi \rho_w x_1 \Gamma(4)}{6} \right]^{\frac{x_2-2}{4-x_2}} = 2.229 \\ C_2 &= \frac{2-x_2}{4-x_2} = \frac{2-2.2}{4-2.2} = -1/9. \end{aligned} \quad (\text{A.31})$$

Indeed, using the Abel-Boutle size distribution leads to a negative exponent $C_2 = -1/9$. It means that very little rain evaporates very quickly since droplets are very small. However, one can rewrite Equation (A.29) to the part of λ coming from Equation (A.24) and the part originating from the integration above. The formula can be separated, and the λ -part of the intercept parameter can be put in front of this computation, so the evaporation itself is proportional to the flux. This can be written as

$$\frac{1}{\rho_a} \underbrace{x_1 \lambda^{2.2}}_{\text{intercept}} \underbrace{\frac{1}{\lambda^2}}_{\text{integration}} \sim \underbrace{x_1 q_r^{-2.2}}_{\text{intercept}} \underbrace{q_r^2}_{\text{integration}}, \quad (\text{A.32})$$

from which is apparent why C_2 is negative.

The second term becomes:

$$\begin{aligned}
& \frac{x_1 \lambda^{x_2}}{\rho_a} \frac{2\pi(1-RH)(1-C)}{\mathcal{K} + \mathcal{D}} \xi_r b_1^{\frac{1}{2}} \rho_0^{0.385} \rho_a^{-0.21} \left(\mu^{\frac{1}{2}} \chi\right)^{-\frac{1}{3}} \int_0^\infty D^{\frac{b_2+3}{2}} e^{-\lambda D} dD \\
&= \gamma \frac{\lambda^{x_2}}{\rho_a} \rho_a^{-0.21} \Gamma\left(\frac{b_2+5}{2}\right) \frac{1}{\lambda^{\frac{b_2+5}{2}}} \\
&= \gamma \frac{1}{\rho_a} \rho_a^{-0.21} \Gamma\left(\frac{b_2+5}{2}\right) \lambda^{\frac{2x_2-b_2-5}{2}} \\
&= \gamma \frac{1}{\rho_a} \rho_a^{-0.21} \Gamma\left(\frac{b_2+5}{2}\right) \left[\frac{\pi \rho_w x_1 \Gamma(4)}{6 \rho_a q_r} \right]^{\frac{2x_2-b_2-5}{2 \cdot (4-x_2)}} \\
&= \gamma \Gamma\left(\frac{b_2+5}{2}\right) \rho_a^{-1-0.21+\frac{-2x_2+b_2+5}{2 \cdot (4-x_2)}} \left[\frac{\pi \rho_w x_1 \Gamma(4)}{6} \right]^{\frac{2x_2-b_2-5}{2 \cdot (4-x_2)}} \left[\frac{1}{q_r} \right]^{\frac{2x_2-b_2-5}{2 \cdot (4-x_2)}},
\end{aligned} \tag{A.33}$$

where

$$\gamma = x_1 \frac{2\pi(1-RH)(1-C)}{\mathcal{K} + \mathcal{D}} \xi_r b_1^{\frac{1}{2}} \rho_0^{0.385} \left(\mu^{\frac{1}{2}} \chi\right)^{-\frac{1}{3}}. \tag{A.34}$$

One can approximate $\rho_a^{-0.21} \approx 1$ (the error is less than the uncertainty of other processes, for example, turbulent mixing or the size distribution of raindrops). Thus, we get the form:

$$\underbrace{\frac{(1-RH)(1-C)}{\rho_a(\mathcal{K}_r + \mathcal{D}_r)}}_{C_3} [\rho_a q_r]^{\frac{5+b_2-2x_2}{2 \cdot (4-x_2)}} p^{\frac{1}{3}}, \tag{A.35}$$

where $p^{1/3}$ comes from $\chi = 2 \cdot 10^{-5} p_0/p$ and

$$C_3 = 2\pi \xi_r b_1^{\frac{1}{2}} \rho_0^{0.385} \left(\mu^{\frac{1}{2}} \cdot 2 \cdot 10^{-5} p_0\right)^{-\frac{1}{3}} \Gamma\left(\frac{b_2+5}{2}\right) \left[\frac{\pi \rho_w x_1 \Gamma(4)}{6} \right]^{\frac{2x_2-b_2-5}{2 \cdot (4-x_2)}} = 8.738. \tag{A.36}$$

Finally, the exponent

$$C_4 = \frac{5+b_2-2x_2}{2 \cdot (4-x_2)} = \frac{5.7706-4.4}{2 \cdot 1.8} = 0.3807, \tag{A.37}$$

which leads to $q_r^{0.3807}$, so the evaporation rate delivered by this term is proportional to the amount of q_r .

A.6 Derivation of the Lopez evaporation parameterization for graupel

In the case of graupel, the size distribution with the new graupel option follows the Marshall-Palmer distribution

$$N_g(D) = N_0^g e^{-\lambda_g D}, \tag{A.38}$$

where $N_0^g = 4 \cdot 10^6 \text{ m}^{-4}$. The fall speed relation $w_g = b_1 D^{b_2} (\rho_0/\rho_a)^{0.4}$ has coefficients $b_1 = 124$ and $b_2 = 0.66$ in SI units. Also, graupel is assumed spherical with

a constant density of $\rho_g = 400 \text{ kg}\cdot\text{m}^{-3}$, so the derivation of the Lopez evaporation must start from an equation for spherical particles taken from Lopez (2002). Thus, the only difference between the computation of coefficients for rain and graupel is that one needs to assume the ventilation coefficients of ice (ζ_s and ξ_s) instead of that of liquid water (ζ_r and ξ_r), and also the computation of \mathcal{K} and \mathcal{D} must be changed since they depend on the phase of given hydrometeor (subscript i for ice), mathematically speaking:

$$\frac{dm}{dt} = \frac{2\pi D(1 - RH)(1 - C)}{\mathcal{K}_i + \mathcal{D}_i} \left[\zeta_s + \xi_s \left(\rho_a \mu^{\frac{1}{2}} \chi \right)^{-\frac{1}{3}} \left(\rho_a D b_1 \left(\frac{\rho_0}{\rho_a} \right)^{0.5} D^{b_2} \right)^{\frac{1}{2}} \right], \quad (\text{A.39})$$

where the meaning of symbols is the same as in the case of rain.

These assumptions lead to

$$\frac{dq_g}{dt} = \frac{N_0^g}{\rho_a} \int_0^\infty \left[\underbrace{\zeta_s D e^{-\lambda D}}_{\text{first term}} + \underbrace{\xi_s \left(\mu^{\frac{1}{2}} \chi \right)^{-\frac{1}{3}} \rho_a^{-\frac{1}{12}} \rho_0^{0.2} b_1^{\frac{1}{2}} D^{\frac{3+b_2}{2}} e^{-\lambda D}}_{\text{second term}} \right] dD \quad (\text{A.40})$$

For the first term we have

$$\zeta_s \frac{N_0^g}{\rho_a} \int_0^\infty D e^{-\lambda D} dD = \zeta_s \frac{N_0^g}{\rho_a} \frac{1}{\lambda^2} = \zeta_s \left(\frac{\rho_a q_g}{\pi \rho_g N_0^g} \right)^{\frac{1}{2}}, \quad (\text{A.41})$$

which yields

$$\begin{aligned} C_1 &= \frac{2\pi\zeta_s}{\rho_g\pi} = 0.115 \cdot (N_0^g)^{1-C_2} \\ C_2 &= 0.5. \end{aligned} \quad (\text{A.42})$$

The second term can be derived in a similar fashion as in the case of rain (again, the weak dependency of ρ_a is neglected), leading to the following set of coefficients:

$$\begin{aligned} C_3 &= 1.75 \cdot (N_0^g)^{1-C_4} \\ C_4 &= 0.7075. \end{aligned} \quad (\text{A.43})$$

In the case of the old graupel option, the fall speed relation as well as the size distribution function of graupel is the same as of rain, so the relation for graupel and rain evaporation are the same except that it is necessary to use the ventilation factor for ice. Therefore, coefficients C_1 and C_3 become

$$\begin{aligned} C_1 &= \frac{\zeta_s}{\zeta_r} \cdot C_1^r = 0.833 \cdot C_1^r \\ C_3 &= \frac{\xi_s}{\xi_r} \cdot C_3^r = 1.419 \cdot C_3^r. \end{aligned} \quad (\text{A.44})$$

and C_2 and C_4 remain unchanged from the rain ones.